Mechanosensitive protein-protein interactions in nascent focal adhesions determined by three-colour FRET sensing using Multiphoton Fluorescence Lifetime Imaging Microscopy

Treacy, Conor

Awarding institution:
King's College London

Mechanosensitive protein-protein interactions in nascent focal adhesions determined by three-colour FRET sensing using Multiphoton Fluorescence Lifetime Imaging Microscopy

Authored by:

Conor A. Treacy, BSc *(Hons)*, MRes

Supervised by:

Professor Simon M. Ameer-Beg BSc (Hons), MSc, PhD

&

Professor Maddy Parsons BSc (Hons), PhD

This dissertation is submitted for the degree of

Doctor of Philosophy

in

Cell & Molecular Biophysics

Supervised by:
Prof. Simon M. Ameer-Beg & Prof. Maddy Parsons
Work conducted between October 2017 - March 2022
at New Hunt's House
The Randall Centre for Cell and Molecular Biophysics
Kings's College London

"Scientific knowledge is a body of statements of varying degrees of certainty – some most unsure, some nearly sure, none absolutely certain."
Richard P Feynman, 1918 - 1988

ABSTRACT

Focal Adhesions (FA) are large sub-cellular structures comprised of macromolecular assemblies that anchor cells to the extracellular matrix and play a key role in force transduction and intracellular mechano-signalling pathways. Understanding how mechanical signalling influences specific molecular and cellular mechanisms is crucial in progressing our knowledge of how the external environment affects normal cell physiology and pathology.

In this project, we have used a tension-sensitive biosensor to detect real-time changes in applied force across the mechanosensitive FA protein vinculin. The biosensor contains two fluorescent proteins joined by a short-coiled linker that extends when force is applied. When the biosensor is under tension, the two fluorescent proteins separate, decreasing the amount of Förster Resonance Energy Transfer (FRET) observed. By measuring FRET using time-correlated single-photon counting fluorescence lifetime imaging microscopy (TCSPC-FLIM), we observe the loss of FRET, compared to a control, as a direct consequence of an applied intracellular force across the biosensor. By transiently transfected vinculin null mouse embryonic fibroblasts (MEFs) with a vinculin construct encoding the Tension Sensing Module (TSM), we can demonstrate how force-transduction changes within maturing adhesions in both fixed and live cells.

In addition, we have also shown through biochemical and biophysical assays that RIAM (Rap1-interacting Adapter Molecule) interacts with vinculin through an N-terminal binding domain. Furthermore, by developing a novel three-colour FRET sensing methodology, we have been able to describe the spatiotemporal relationship between several components assembled in nascent adhesions, namely talin, vinculin and RIAM. We have combined live cell fluorescence lifetime imaging with three-colour FRET sensing to determine the order of assembly for a multimeric complex as a function of time.

ACKNOWLEDGEMENTS

I want to thank my primary project supervisor, Professor Simon Ameer-Beg, for allowing me to conduct my research project in his group and for all his expert advice, guidance, and encouragement throughout my time there, especially while writing this thesis. I am very grateful for the opportunity to expand my knowledge in advanced optical microscopy, particularly the fascinating worlds of Fluorescence Lifetime Imaging Microscopy and Super-Resolved, Single-Molecule Localisation Microscopy.

I would also like to thank my second supervisor, Professor Maddy Parsons, for her support and guidance throughout my Ph.D.

There have been many people who have taken their time to not only train me in specific techniques but who have also supported my development throughout my PhD, and I would like to take this opportunity to thank them. I want to thank Dr Mark Pfuhl and Dr Ambrish Kumar for their help and support with protein expression and purification; Dr Elisabeth Storck, Dr Stephen Terry, and Dr José Vicencio for their support in my training in cell and molecular biology techniques; Dr Simon Poland and Dr James Levitt for their guidance and insight with advanced imaging techniques and basic optics training. Without their continued support in and out of the lab, I would certainly not have been as successful or productive. I would also like to thank the members of the Ameer-Beg group, both past and present, who have supported me throughout my journey during my PhD and time at King's College London.

A very special thanks to Cooper for being a very good boy and keeping me company while I wrote my thesis.

Finally, and most importantly, I would like to thank my wife, Claire Treacy, for all her help, support, and dedication through the ups and downs of the last four and half years of PhD life. There is no way I would have accomplished nearly as much without her inspiring commitment and perseverance.

ABBREVIATIONS

bp	Base pairs
BSA	Bovine Serum Albumin
Conc.	Concentration
COT	Cyclooctatetraene
Da	Daltons
DABCO	1,4-Diazobicyclo -2,2,2-octane
ddH_2O	Double Distilled Water
DMEM	Dulbecco's Modified Eagle's media
dNTPs	Deoxynucleoside triphosphate
E. coli	Escherichia coli
EDTA	Ethylenediaminetetraacetic acid
EGTA	Ethylene glycol-bis(β-aminoethyl ether)-N,N,N,N-tetraacetic acid)
FA	Focal Adhesion
FBS	Foetal Bovine Serum
FCS	Fluorescence Correlation Spectroscopy
FLIM	Fluorescence Lifetime Imagining Microscopy
FP	Fluorescent Protein
FRET	Förster Resonance Energy Transfer
g	Acceleration due to gravity $\approx$ 9.81 ms^{-2}
Glox	Glucose Oxidase
HEPES	4-(2-hydroxyethyl)-1-piperazineethanesulfonic acid
6xHis-tag	Hexa-Histidine purification tag
HPM	Hybrid Photomultiplier
IMAC	Immobilised Metal-ion Affinity Chromatography
LB	Luria-Bertani broth
LB Agar	Luria-Bertani Agar
L-Glut	L-Glutamine
MOPS	3-Morpholinopropane-1-sulfonic acid
n	Refractive index
N	Avagadro's Constant $\approx$ 6.022x10^{23} mol^{-1}
NA	Nascent Adhesion

N_A	Numerical Aperture
NEAA	Non-Essential Amino Acids
Noc.	Nocodazole
PAGE	Polyacrylamide Gel electrophoresis
PALM	Photoactivatable Localisation Microscopy
PBS	Phosphate Buffered Saline
PBS-Tw	Phosphate Buffered Saline with 0.2% Tween
Pen/Strep	Penicillin/Streptomycin
PFA	Paraformaldehyde
PIPES	1,4-Piperazinediethanesulfonic acid
PMT	Photomultiplier Tube
Qy	Quantum Yield
RAP1	RAS-Related Protein 1
RESOLFT	Reversible Saturable Optical Fluorescence Transitions
RIAM	Rap1-GTP Interacting Adapter Molecule
ROCK	Rho Associated Protein Kinase
rSAP	Recombinant Shrimp Alkaline Phosphatase
SDS	Sodium Dodecyl sulphate
SEC	Size Exclusion Chromatography
SMLM	Single Molecule Localisation Microscopy
SPAD	Single Photon Avalanche Diode
SR-M	Super-Resolution Microscopy
STEAD	Stimulated Depletion
STORM	Stochastic Optical Reconstruction Microscopy
SWARM	Swept Array Microscopy
TC	Tissue Culture
TCSPC	Time-Correlated Single Photon Counting
TEV	Tobacco Etch Virus Protease
Ti:Sapph	Titanium-Sapphire
TIRF-M	Total Internal Reflection Microscopy

LIST OF FIGURES

LIST OF TABLES

LIST OF EQUATIONS

CONTENTS

1

INTRODUCTION

1.1 Thesis Overview

Conventionally, Fōrster Resonance Energy Transfer (FRET) is extensively used to detect direct interactions between pairs of fluorescently labelled proteins or to detect changes in the internal environment of cells through biosensors. However, by multiplexing the FRET interactions, more information is gained by looking at the bigger picture, not just considering one event in isolation but putting that event in context with when or where another cellular event occurs. In this thesis, I set out to determine if a putative vinculin-RIAM interaction can be detected in cells and whether this interaction may have a physiological function. I then develop a three-colour FRET methodology to determine if a vinculin tension sensor is in an open or closed conformation when RIAM interacts with vinculin. Specifically, does RIAM only associate with the auto-inhibited form of cytoplasmic vinculin?

The first chapter of this thesis is an introduction chapter which I have split into two halves; in the first half, I review the current literature relating to Focal Adhesion (FA) assembly, its regulation and the proteins that adhesions are comprised. Specifically, I discuss the recruitment of talin by the activated rap1-RIAM complex and how it is actively recruited to the plasma membrane, which is activated and forms a core element of nascent adhesions. I then discuss a putative binding interaction between vinculin and RIAM which is a core focus of this thesis. In the second half of this chapter, I review FRET imaging techniques with specific attention given to three-colour FRET imaging techniques and TCSPC-FLIM, both of which are used extensively throughout this thesis.

Chapter 2 describes the materials and methods I used during my PhD to accomplish the results described herein.

Chapter 3 focuses on detecting and characterising the putative vinculin-RIAM interaction in vinculin null mouse embryonic fibroblasts (vinculin -/-MEFs), which has been proposed only from in vitro N-terminal binding studies. So far, this interaction has only been reported in vitro and has not been previously characterised in cells. I will show by using several biochemical and biophysical assays that two-photon TCSPC-FLIM can detect the interaction. The interaction is further interrogated by investigating whether the vinculin-RIAM interaction is actin-dependent, which was achieved using a specific Rho-associated kinase (ROCK) inhibitor, H-1152. I further characterised the interaction by investigating whether the interaction affects FAs turning over. Lastly, in this chapter, I explore the relationship between the intracellular mechanical force acting on vinculin by using a vinculin Tension Sensing biosensor.

In Chapter 4, I describe the development of a new three-colour FRET-based assay using two-photon TCSPC-FLIM to determine the interaction between multiple fluorescently labelled proteins in a single complex at a specific time point and location in a cell. This chapter is focused on discussing the production of a model system comprising purified fluorescent proteins and their biophysical characterisation. The new methodology for determining multi-protein complex formation is an analytical approach used in conjunction with TCSPC-FLIM to identify the individual FRET components in a complex system and show which fluorescently tagged proteins are directly interacting at specific locations in the cell and how this evolves over time.

In Chapter 5, I combine the objectives set in the previous results chapters and apply the three-colour FRET model to answer questions relating to vinculin-RIAM binding and intracellular tension, specifically across vinculin in developing focal adhesions. I also explore our understanding of how FA proteins are recruited to lamellipodium and to what extent the putative vinculin-RIAM interaction plays in recruitment and adhesion assembly.

Finally, in Chapter 6, I thoroughly discuss all aspects of the thesis research, draw conclusions for the work, and indicate where interesting work may take the project in the future.

1.2 A Brief Introduction to Cellular Mechanotransduction.

The Extracellular Matrix

The Extracellular Matrix (ECM) is a vast three-dimensional network of intertwined and interlocking fibrous proteins such as collagen, fibronectin and elastin, glycoproteins such as proteoglycan, and a vast array of polysaccharides [1, 2]. The composition and structure of the ECM is tightly regulated and maintained by the same cells that live within it. Significant changes in its composition are strongly associated with the progression of many degenerative diseases such as cancer [2, 3], cardiac dysfunction, and liver damage [4]. It has been known for some time that cells respond to changes in their environment brought about by mechanosensing-dependent signalling [1, 5]; however, the exact molecular mechanism of these pathways is still not fully understood. For this reason, understanding how cells detect mechanical stimuli and ultimately alter the ECM in response is the subject of intense investigation. Several intracellular molecules have been identified that can react to mechanical stimulation and - in turn – modify cell function [5].The nature and the extent of the changes caused by mechanical stimuli on the cell can vary drastically, such as proteins deforming through stretching or unfolding in response to mechanical stimuli [6] or the formation of new, novel interactions at the cell membrane [7]. Regardless of how the cell receives the stimulus, the detected signal is first detected and then transduced from the ECM to the nucleus via the cell membrane through a molecular process is collectively known as mechanotransduction [1]. Essentially, cells constantly sense and respond to the physical world surrounding them by detecting mechanical and biochemical stimuli through the interactions made by membrane-bound proteins that project into the ECM. Stimuli cause changes at the cell membrane in a diverse set of mechanosensitive proteins that include integrins, G-protein coupled receptors or stretch-activated ion channels, all of which activate different downstream pathways that lead to significant downstream changes [8]. Integrins act as active sensors responding to cues and signals from the ECM [9], along with other signalling molecules such as kinases, phosphatases, and adaptor proteins. Studies using magnetic tweezers to transfer force directly from integrins to the local cytoskeleton shows that the mechanical deformation of one or more FA proteins is a crucial step in an intracellular signalling cascade that leads to global cytoskeletal rearrange-

ments and mechanotransduction at multiple, distant sites within a cell [10].

Focal Adhesions

Focal adhesions (FAs) are large intracellular macromolecular assemblies that anchor cells to the ECM and are the primary site of mechanical force transduction. FAs are unique in directly connecting the cell membrane and ECM through integrins and so are crucially involved in sensing and responding to mechanical stimuli from the external environment [11, 12]. The act of mechanosensing depends on identifying and transmitting mechanical signals from the extracellular milieu into the cell. Cells achieve this through their adhesions comprising two halves, an outward-facing transmembrane domain and an inward-facing intracellular domain. In the transmembrane domain, integrins reach out into the ECM and connect the cell to the exterior world; this is where extracellular sensing and communication occur. The intracellular domain, in contrast, is where proteins like talin, vinculin, FAK, paxillin and many others are located and recruited by proteins such as Ras GTPase, Rac, and RIAM [13–16]. Integrins are recruited first and assemble along with talin as the first nascent adhesions before other proteins like actin, and vinculin are recruited and stabilise the increasingly enlarged complex, which grows into mature FAs. It is within the intracellular domain where scaffolding, docking, and signalling proteins collectively serve as an interface between transmembrane components directly contacting the ECM (integrins) and the actin cytoskeleton. The precise molecular composition of FAs is constantly changing in response to the ECM composition, mechanical forces, and integrin binding. Small changes in external stimuli have been shown to strongly influence the pattern of integrin clustering. Differences in the spacing and availability of ECM adhesion sites have been shown to strongly affect the recruitment of FA proteins to these binding sites [16–18]. Most of the proteins that assemble in adhesion are not involved in outside-in signal transduction, but two heavily involved proteins, talin and vinculin, are of particular interest.

The assembly of these proteins within FAs and how these form distinct layers with specific functions (figure 1.2.1-1) [19]. As cells remodel the matrix or shape tissue, they must apply forces to respond to changes in their physical environment. Cells must contact neighbouring cells and the matrix to modify local tissue morphology. Over 200 different proteins have been identi-

fied within the integrin-mediated adhesome, many identified through mass spectrometry, and a further 400 proteins that associate with FAs in a force-dependent manner [20, 21]. Cell adhesions are vast complex assemblies easily identified through conventional widefield microscopy techniques. The large adhesion complex extends for several micrometres from integrins at the leading edge of migrating cells and is easily identified through fluorescence microscopy techniques. With such critical functions and many constituent components, FA assemblies and the large family of interactors have received considerable attention. FAs have been shown to play a role in many facets of normal cell physiology, from regulating correct cell motility to wound healing and the spread and development of cancer. FAs transmit intracellular, myosin-generated forces from the cytoskeleton to the extracellular matrix (ECM), generating traction forces that pull the cell body forward during cell migration [22, 23]. The position of vinculin within FAs means that it is ideally placed to mediate the transmission of intracellular forces [24].

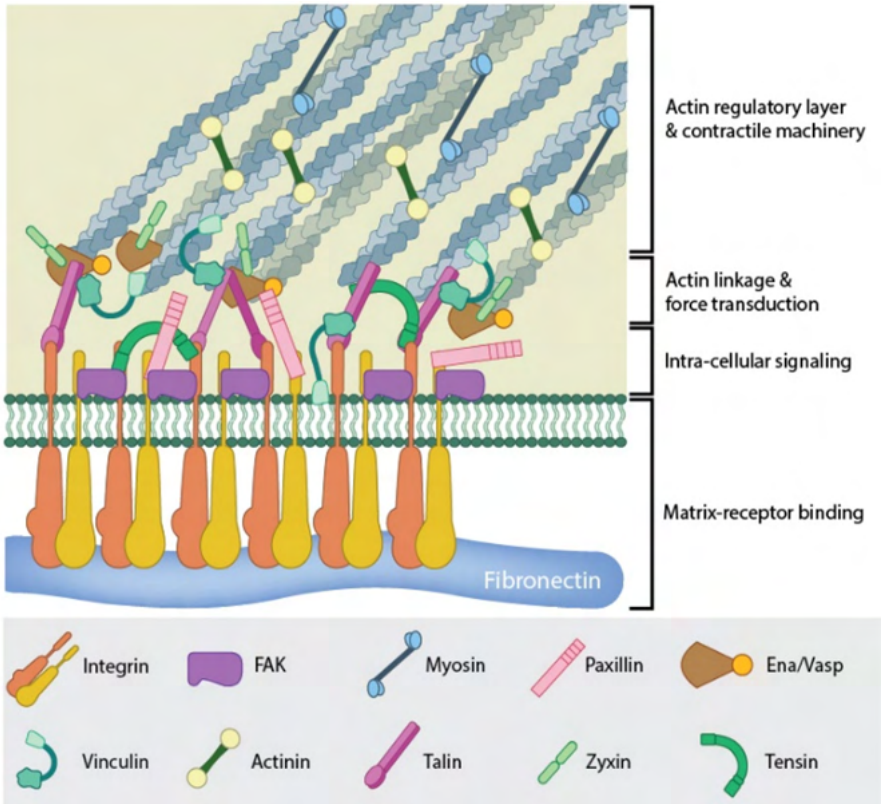

Figure 1.2.0.1: ***A diagram of a Focal Adhesion assembly:*** *A diagram showing the major components of a typical mature focal adhesion (adapted from Changede & Sheetz, 2016).*

FA research is vital in understanding how cells respond to their external environment and how this can manifest in diseases like cancer. Proteomic

analysis has identified over 2,400 proteins that have some involvement with the integrin-mediated adhesome. These proteins have been grouped into four critical families: FAK-Paxillin, talin-Vinculin, α-Actinin-Zyxin-VASP and ILK-PINCH-Kindlin pathways [25]. Although these pathways have been well studied in cancer cell lines, not all constituents have been identified. Alterations in gene expression of these proteins seem to be critical in determining the FA size, shape, and density of each cell-matrix contact [2]; this has been demonstrated by FAK, Integrin-linked kinase (ILK), talin and Zyxin knockdowns in MCF-7 breast cancer cell lines [26, 27]. These knockdown cell lines have shown an increase in FA size, which corresponds to an increase in the anchoring of breast cancer cells to the ECM and, therefore, a reduced rate of FA disassembly [28].

Cancerous cells must migrate through the ECM during metastasis before entering the blood and lymphatic vessels through intravasation. The early stages of this highly ordered and complex process involving the coordination of intracellular signals with the external environment to facilitate the detachment of the cell from its primary location. The initial steps require a sizeable morphological change where the cell becomes densely packed and rounded. Protrusions are lost as the cells break their attachment points through FAs and detach from the matrix [2, 3]. Furthering our understanding of this highly complex, integrated process and its regulation is a primary aim of this PhD.

Vinculin

Since its discovery in 1979 [29], the 124 kDa protein *vinculin* (from the Latin vinculum meaning "bond", "tie", or "link") has been one of the most studied proteins found in cellular adhesions to date [12, 29]. Vinculin is localised within the cytoplasmic layer of integrin-mediated, cell–ECM junctions [30] and appears early in nascent adhesion assembly. It is considered a core protein as it is universally localised within FAs as a well-characterised binding partner of talin [31].

Vinculin consists of two domains, a 90.6 kDa head domain (V_H) which is made of five sub-domains D1-5, each consisting of between five and eight helix-turn-helices and a 33.1 kDa vinculin tail (V_T) domain. The V_H and V_T domains have been shown to interact independently from each other when vinculin is in its fully functional conformation. They are joined by a 52 amino acid

proline-rich flexible linker with binding sites for Arp2/3 and vinexin, which directly interact with and regulate actin [32]. In vinculin's inactive, autoinhibited conformation (as shown in figure 1.2-2 panels A and B), the D1 sub-domain of the V_H domain binds to and occludes the V_T domain preventing the V_T domain from interacting with its primary binding partner, actin [33], as shown in panel B below. The occlusion of V_T by V_H results in a tightly bound, autoinhibited conformation before recruitment and activation [34]. Vinculin

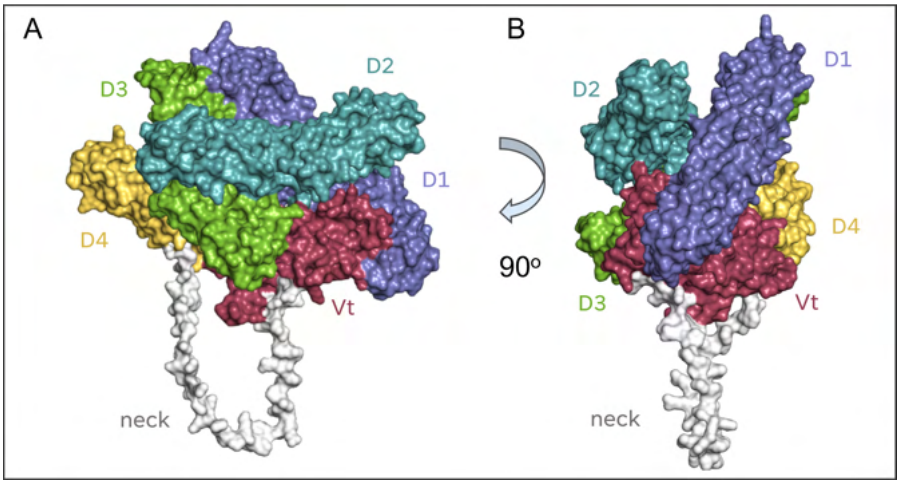

Figure 1.2.0.2: ***Vinculin structure and autoinhibition:*** *Vinculin structure and autoinhibition: A) Shows a surface view of the crystal structure of vinculin in its autoinhibited conformation. B) Shows the vinculin molecule rotated 90^0 demonstrating how the D1 sub-domain of the VH domain prevents the VT l domain from interacting with its binding partners in its autoinhibited conformation. Alpha fold model AF-Q64727-F1 was used and modelled in Pymol.*

recruitment and activation is regulated by force (figure 1.2.-3) to the extent that recruitment and localisation of vinculin to maturing FAs depends upon actomyosin contraction [6]. Vinculin is one of the core components of FAs, and its recruitment to nascent adhesion requires talin activation by mechanical forces [22, 34]. There is evidence to suggest that talin and vinculin are pre-complexed through vinculin binding to rod domain 8 (R8) of talin, and talin actively shuttles vinculin to the site of FA assembly [35]. Regardless of the mechanism that drives vinculin enrichment of the lamellipodium, it has been demonstrated that vinculin localisation within developing FAs is directly correlated with mechanical force measured within the same FAs such that vinculin recruitment is force-driven [36]. The current vinculin recruitment and activation model suggests that the talin binding site in the D1 sub-domain of the vinculin head domain first associates with the mechanosensitive compact N-terminus of talin through rod domains 2 and 3 (see figure 1.2-4 for further details on the structure of talin) [37]. Once vinculin is bound to talin, a signifi-

cant conformational change occurs in the tertiary structure of vinculin that releases the auto-inhibited conformation described in figure 1.2-2, allowing the vinculin tail domain to associate with actin. Once vinculin is bound to both actin and talin, additional vinculin molecules are recruited force-dependently to the developing adhesion [6, 38, 39].

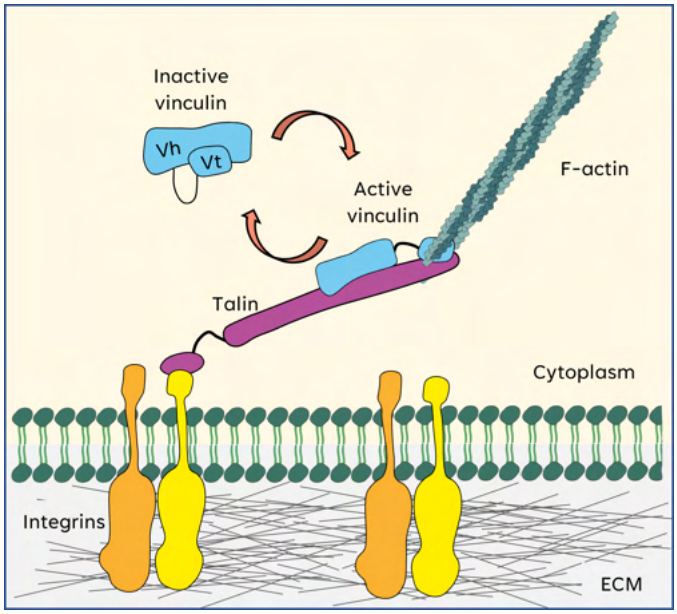

Figure 1.2.0.3: ***Activation of vinculin requires talin and actin:*** *Activation of vinculin requires talin and actin. The diagram shows a cartoon which lllustrates the activation of vinculin through the binding of talin and f-actin vinculin – not drawn to scale.*

Several models have been proposed relating to the mechanisms of vinculin mechanosensitivity. One model proposes mechanosensitivity of vinculin is dependent upon functional actin binding the tail domain. Vinculin null MEFs have been found to have significantly reduced myosin contractility, as a loss of the V_T domain prevents vinculin association with actin [36]. This phenotype is successfully rescued by transfecting the same vinculin null MEFs with the tail domain but crucially was not rescued by transfecting in the vinculin head domain alone [36]. It has been suggested that this was most likely due to the tail domain facilitating the cyclic association and dissociation of vinculin from FA complexes. There seems to be some evidence of this as cells expressing V_T mutants have been shown to have reinforced FA stability, something usually only seen for wild-type cells grown on stiffer surfaces [40]. An alternative model described a more complex system where V_H domain increases adhesion strength by stabilising ECM-integrin complexes independently from the interactions the V_T domain forms with the actomyosin cytoskeleton [36].

The presence of talin is essential for vinculin localisation [22,41] Without talin, the necessary actomyosin-mediated forces critical for vinculin localisation and activation within maturing mature adhesion complexes are not present. The vinculin mutant A50I, located in the talin binding domain within the V_H, has been shown to inhibit the talin binding and, by extension this has been found to actively de-stabilise adhesion complexes [7]. During cell migration, vinculin activation occurs at the protruding cell edge, where nascent focal complexes mature into tension-dependent FAs. It has been shown that where tension is insufficient to retain vinculin in an extended active conformation, FAs become unstable and dissemble; this explains the transient nature of adhesion formation in migrating cells, as adhesion sites grow in specific locations of a cell's leading edge where both rho GTPase activity and tension are greatest [39]. Conversely, FAs typically disassemble in the lamella ahead of the cell's nucleus where rho GTPase activity and tensional forces are at their lowest [42], suggesting that vinculin-mediated signalling remains active only in regions where tension is maintained.

Cell motility studies have shown that constitutive activation of vinculin leads to unpolarised, protrusive morphology usually associated with mislocalised rac1 activity [39], strongly indicating that cycles of vinculin activation and inactivation are required for correct FA protein recruitment, activation, and disassembly, crucial for efficient cell polarised migration. Indicating mutations in vinculin prevent correct FA morphology formation and could increase the propensity of a cell to migrate unpolarised, as seen in many metastatic cancer cell lines [39].

Talin

Talin is a very large 270 kDa (2,541 amino acids) protein first discovered in 1983 [43]. Talin comprises an N-terminal FERM (**F**our-point-one-protein, **E**zrin, **R**edixin, **M**oesin) domain (≈50 kDa) and a long flexible C-terminal rod domain (≈220 kDa), the two domains much like vinculin, are connected by an unstructured flexible linker. The The N-terminal FERM domain consists of F1-F3 domains arranged in a linear rather than the usual clover leaf arrangement [44] with an additional domain, F0, packed against the F1 domain. Basic side chains distributed along one face of the FERM domain interact with acidic phosphate heads of phospholipids found in the plasma membrane and are essential for integrin activation [44, 45]. The FERM domain is a widespread protein module that localises proteins to the plasma membrane. The F3 FERM

domain found in talin has been shown to bind to the β-subunit of cytoplasmic integrin tails and is chiefly responsible for the strength of integrin binding; however, F0 and F1 FERM domains have also been shown to be necessary for maximal integrin activation [46]. The interaction between talin and the cytoplasmic β-subunit of integrin is necessary to activate integrins to bind ECM proteins with sufficient affinity. Integrin-mediated adhesion mechanosensitivity allows cells to tune their gene expression and function to mechanical cues from their external environment [47]

The talin rod has three actin-binding sites, five RIAM binding sites and 11 vinculin binding sites; however, not all are accessible simultaneously. Due to the mechanosensitive nature of talin, many of the VBS remain cryptically hidden until forces pulling on talin cause widespread conformational changes, which reveal these cryptic sites and allow vinculin to bind [48, 49].

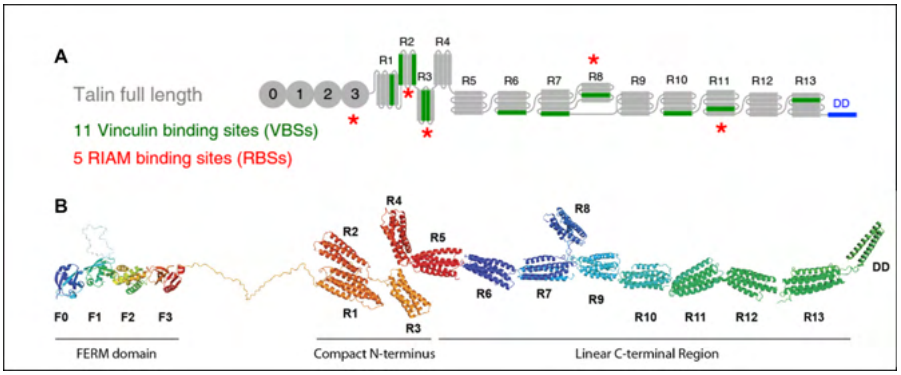

Figure 1.2.0.4: ***Multidomain structure of full-length talin:*** *Multidomain structure of full-length talin: A) Domain organisation of talin 1. The N-terminal domain comprises of the typical F0, F1, F2 and F3 FERM domains, this is joined to the rest of flexible α-helical rod structure by an unstructured 80 amino acid linker. The rod is comprised of a total of 62 α-helices arranged into thirteen 4- or 5- helical bundles (R1-R13) with the last two α-helices forming a single helical dimerization domain (DD) at the C-terminal. The 11 VBS and 5 RIAM binding sites are annotated. Adapted from Vigouroux et al, 2020. B) A structural model showing all 13 domains of the 250 kDa talin protein assembled from X-Ray crystallography and nuclear magnetic resonance (NMR) structures (adapted from Goult et al, 2013).*

Talin is of specific importance as changes in tension across the protein cause conformational changes, specifically, the extension of flexible linkers that join helical bundles. The extension of these coiled coils causes the rearrangement of the helical bundles, revealing specific binding sites that recruit other proteins to the FAs [50, 51]. The initiation of biochemical pathways by mechanical signalling is vital in furthering our understanding of how cell motility and stimuli by external forces are linked to the spread of cancer. These vinculin binding sites (VBS) are found buried deep with 4- and 5- helical bundles occluded when talin is under low tensional force [52] but once the tension has applied, a series of force-dependent conformational changes occur that reveal these VBS. Applied force actively reinforces the interaction with F-actin through vinculin binding as vinculin binds to actin via its ABS in its tail, V_H domain [26, 50]. This tension-dependent cooperativity is of great interest as it shows how tensional forces interact with the external environment and influence intracellular processes.

Without mechanical force, the talin rods remain in tightly coiled auto-inhibited conformation where none of the 11 VBS are available; under low-force situations, weaker rod domains and helical bundles unfold and reveal the first VBSs on talin [52]. This allows vinculin to bind, releasing it from its autoinhibited state. It also further alters the tertiary 3D structure of talin, facilitating further vinculin molecules to bind as increasingly more force is applied to talin [6, 52]. This occurs as vinculin can bind to actin, which equally responds to mechanical force, working synergistically in activating an increasing number of vinculin molecules. This process is described as talin-vinculin mechanosensitivity [6, 52, 53].

RIAM

RIAM was first named in 2004 when it was identified through yeast two-hybrid screens used to find novel effectors of the small GTPase Rap1, hence - **R**ap1-GTPase **I**nteracting **A**dapter **M**olecule or RIAM [54]. However, the RIAM protein was first discovered in 1997 as a binding partner of the amyloid β (A4) precursor protein-binding family B_{55}, member 1, otherwise known as APBB1 (alternatively as Fe65). As RIAM was identified as a binding partner of APBB1, it was appropriately given the name APBB1IP (or amyloid β (A4) precursor protein-binding family B, member 1 interacting protein1). This interaction is facilitated by a small W-W (tryptophan-tryptophan) domain of Fe65, which interacts with the two proline-rich regions of RIAM [55]. In a separate

study, RIAM was also identified as an interactor of the Enabled/vasodilator-stimulated (Ena/VASP) family of proteins involved in cell motility and actin polymerization. As a result, the protein is also known as **P**roline-**R**ich **E**VH1 **L**igand 1 or PREL1 [56]. The study showed that RIAM colocalized with Ena/-VASP at the leading edge of lamellipodia and in focal adhesions in response to epidermal growth factor (EGF) treatment. The same study also showed that RIAM/PREL1 directly binds to activated Ras in a phosphoinositide-dependent manner, linking Ras signalling to cytoskeletal remodelling via Ena/VASP proteins during cell migration and spreading [56].

Rap1 is a vital molecule, too, as it is a member of the Ras super family of small GTPases; it was first identified as a Ras-related protein back in 1989 [57] and is the closest relative of Ras. It was initially identified in a screen for revertant (cells with genetic alterations that reverse the effect of mutations) of genetically transformed cells by mutant Ras [58]. The close association of RIAM with the small GTPase Rap1 has been of particular interest as Rap1 is known to be linked to cell proliferation, secretion, and migration [58]. This is of significant interest as irregular Rap1 activity has been linked to integrin hyperactivity which is correlated to tumour development and metastasis in several different cancers [59]. Furthering our understanding of how cells sense their environment and respond through these and other pathways is critical, as it often leads to tumour growth and metastasis when misregulated.

We have so far only discussed how cells sense their external environment through an ECM > Integrin > FA signalling cascade, which ends in the activation of effectors in the cytoplasm. This type of integrin-mediated signal transduction is known as outside-in signalling. However, this is not the only direction in that information flows, as signal transduction can occur in both directions [18]. We also know that Rap1 GTPase can initiate that integrin signalling through an inside-out pathway requiring the recruitment of the Rap1 effector, RIAM and talin to the the plasma membrane, which binds to integrins and activates FA formation [15, 54, 60, 61].

Structurally, RIAM is a 74 kDa protein comprising four separate binding domains or regions; these are the N-terminal talin Binding Sites (TBS), the Proline-Rich (PR) regions, the Ras Associated (RA) domain and the Pleckstrin Homology (PH) domain. The TBSs are encoded between amino acids 7-30 for TBS I and 50-85 for TBS II, and they have been shown to bind and recruit talin by binding to the FERM domains on talin, specifically the F2 and F3 [15].

Separate studies have shown that TBSs on RIAM are also associated with auto-inhibited conformations of the R2/R3 and R8 rod domains of talin [44]. The binding of RIAM to talin is thought to be self-inhibitory as this action blocks RA-PH domain localization to plasma membrane [44,45,62]. As previously described, RIAM interaction with Rap1 initiates inside-out integrin signalling. RIAM interacts with Rap1 GTPase via the RA domain on RIAM; after being activated by Rap1, the complex is then translocated to the plasma membrane, where RIAM disassociates from rap1 and binds to the membrane-associated moiety, phosphoinositide di-phosphate (PIP2) via the PH domain on RIAM [63]. The RA and PH domains of RIAM form an integrated RA–PH structural module that has also been found in the Grb7/10/14 family and MRL (**M**ig-10/**R**IAM/**L**amellipedian) family of proteins [37,60]. In addition to the domains described already, RIAM contains two putative coiled-coil motifs (CC) and at least six proline-rich (PR) motifs organised into two regions interacting with cytoskeletal proteins Ena/VASP [55] see figure 1.2-5 panel A for details structure of RIAM. RIAM recruits talin to the leading edge of the cell through TBS I [64–66]. As the RIAM TBSs can recognise and bind to multiple sites within the talin FERM domain, F2 and F3, as well as rod domains R2/R3 and R8, it is thought that multiple RIAM molecules can and are required for effective recruitment of talin by RIAM [67].

One of the primary sites of vinculin binding occurs at the atypical R2/3 talin rod domain; this is considered atypical as these helical bundles comprise only four and not the usual five helices per bundle, and R2/3 binds up to two vinculin molecules in a force-dependent manner [51]. Even though the talin rod domains bind RIAM, R2/3, R8 and R11 have been found to also bind vinculin, RIAM and vinculin binding is thought to be largely mutually exclusive [37,68]. This is primarily due to RIAM and vinculin having very different modes of interacting with talin, as RIAM has been shown to intercalate its single TBS α-helix within the folded auto-inhibited form of talin [37]. NMR studies showed that this intercalation causes only minor changes in the positioning of the helical rods in talin and does not require any large-scale unfolding of auto-inhibited talin to bind [37]. Mutations in the VBS which dramatically reduce the affinity vinculin has for talin, had little effect on the ability of RIAM to successfully bind to talin despite their respective binding sites overlapping [37]. Showing that even though the same surface of talin is used for both of their interactions, different levels of re-modelling and conformational

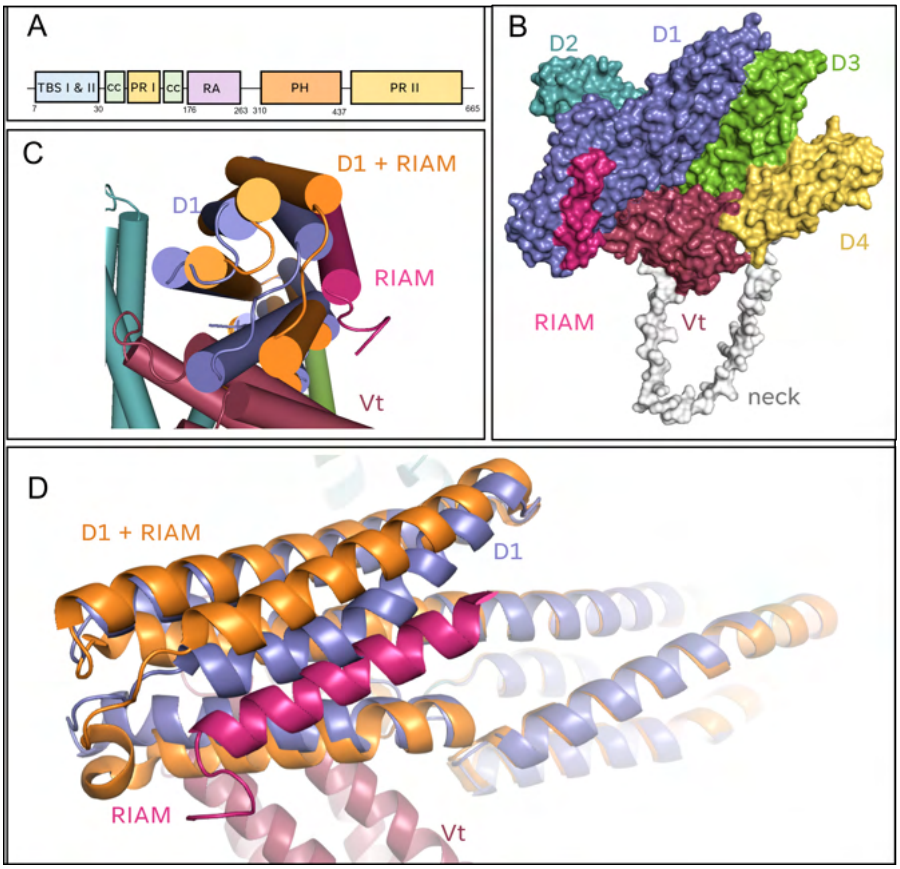

Figure 1.2.0.5: ***RIAM Structure and binding Partners:*** *RIAM Structure and binding Partners. A) RIAM, comprising of talin-binding sites I & II (TBS), coiled-coil domain (CC), proline-rich domain I (PR I), Ras-Association domain (RA), Pleckstrin Homology domain (PH), and proline-rich domain II (PR II). B) Shows auto-inhibited vinculin (D1-5 + Vt) with RIAM bound to the D1 sub-domain of the vinculin head domain. Image produced in Pymol from Alpha fold model AF-Q64727-F1. C) A diagram illustrating the re-positioning of vinculin VH D1 alpha helices in the presence (orange) and absence (purple) of RIAM (pink). D) Ribbon diagram of the N-terminus of RIAM binding to D1 of the vinculin head domain; alpha fold model (AF-Q64727-F1) in purple, bound RIAM in pink and D1 complexed with RIAM in orange PDB file 3zd1.*

change are sufficient to lead to different activation modes, ultimately leading to their binding to talin being described as mutually exclusive [37].

Several recent studies have explored the mechanism of RIAM activation from an autoinhibited homodimer [65, 69–71]. In some instances, RIAM molecules have been found to dimerise with an association via their respective PH domains [65, 70, 71]. This interaction obfuscates the binding of RIAM to PIP [1] (Phosphatidylinositol 4,5-bisphosphate) located on the plasma membrane and, therefore, must be disrupted for the proper function of RIAM as it associates with the plasma membrane [65, 69, 70]. The same studies reported that Src-family kinases were required to phosphorylate tyrosine residues Y267 and Y427 to disrupt PH-mediated RIAM-RIAM interactions. At the same

time, another has also shown that focal adhesion kinase (FAK) is also required for the successful phosphorylation of residue Y45 [69,70]. While it has been shown [72] that an autoinhibited RIAM requires phosphorylation, which remodels the PH domain and allows for binding of RIAM to the plasma membrane, it is still unclear if this is also strictly required for talin-RIAM binding. Canonical activation of RIAM has been achieved through binding by Rap1 via the Ras association domain within RIAM [61,63,71]. Once Rap1 is bound to RIAM, the complex translocates to the plasma membrane, where RIAM associates with PIP_2 molecules via its PH domain [54]. Src family kinases are a group of non-receptor tyrosine usually located with cell membranes such as the plasma membrane, endosomal membrane, and perinuclear membrane [73,74]. If src family kinases are required for successful association of RIAM to the plasma membrane, then it would suggest that RIAM would only become phosphorylated after it had already translocated to the plasma membrane complexed with rap1 and talin.

The N-terminus of RIAM was expressed and purified and was shown to interact with a vinculin-talin complex *in vitro*. Specifically, the first 127 amino acids of RIAM were incubated in a 1:1 ratio with respect to a vinculin-talin complex comprised of talin R2/3 + the D1 V_H sub-domain (amino acids 1-258) and was found to be sufficient to cause some of the vinculin-talin complex to dissociate and instead form a vinculin + RIAM complex, which was identified through gel filtration [37]. D1 of the V_H domain (1-258) was then shown in the same study to readily crystallise with the TBS I of RIAM (1-30), this is shown in panel B (figure 1.2-5) as a space-filling surface model of the auto-inhibited vinculin with RIAM, and in panel D, a cartoon model is shown. The surface model in panel B shows how the auto-inhibited form of vinculin is maintained by binding the D1 sub-domain, locking the vinculin head domain in place and preventing the activation of vinculin by inhibiting the release of the vinculin tail. We can further see how the biding of the N-terminus of RIAM does not affect this in a significant way. Panels C and D of the same figure show in blue the D1 sub-domain in the absence of RIAM and orange in the presence of RIAM, it is interesting to see the displacement of the α-helices within the D1 bundle, but this is insufficient to cause any significant changes or activation of vinculin. The hydrophobic face of the TBS domain on RIAM is seen embedded within the hydrophobic groove formed between α-helix 1 and 2 of the four helical D1 bundles. Leading to the supposition that this interaction is relatively weak due to hydrophobic-hydrophobic intermolecular

forces holding the two proteins together. This idea is further supported by isothermal titration calorimetry (ITC) data that reported the binding affinity between the R3 talin and the vinculin N-terminal domain; a K_D of 0.8 μM was experimentally determined. The same study also reported on the binding affinity between the same R3 talin domain and the TBS of RIAM, which was found to be 5 μM, approximately 6-fold weaker [37].

The current model of Nascent and Focal Adhesion assembly

The current model of nascent adhesion assembly describes how signalling pathways activate Rap1-GTPase, which in its active state binds RIAM through its RA-PH double domain, which translocates to the plasma membrane with talin bound to RIAM. Only in the absence of force can RIAM bind synergistically to the R2/3 talin rod domains via TBS I & II [37]. Once at the plasma membrane, talin engages with integrin tails and anionic phospholipids like PIP2 through its FERM domain, forming the nascent adhesion [63] and activating integrin [75]. It has also been suggested that the talin-RIAM-Rap1 complex may also recruit other proteins that regulate actin polymerisation at the leading age [54, 76]. Once talin is bound, competition between vinculin and RIAM for talin binding sites begins the process of adhesion maturation. It has been shown that tensile forces on talin drive the unfolding of the cryptic VBS on talin (figure 1.2-6). This can only occur if the C-terminal of talin can bind actin and then captures the retrograde flow of actin filaments, which generates the tension across the talin rod. Increased tension pulls apart the helical bundles revealing the cryptic VBS and allowing more vinculin molecules to bind to talin. Vinculin binding to stretched RIAM-binding sites prevents the simultaneous binding of RIAM to talin in the presence of both vinculin and force (figure 1.2-6). The exchange of RIAM for vinculin, as the tensile force acting on talin increases, causes the rod structure of talin to be remodelled as the adhesion site matures. During the maturation process, further assembly of FA proteins and applied mechanical force drive the maturation of nascent adhesions enriched in RIAM to become first adhesion complexes and finally stable, vinculin-enriched mature FAs.

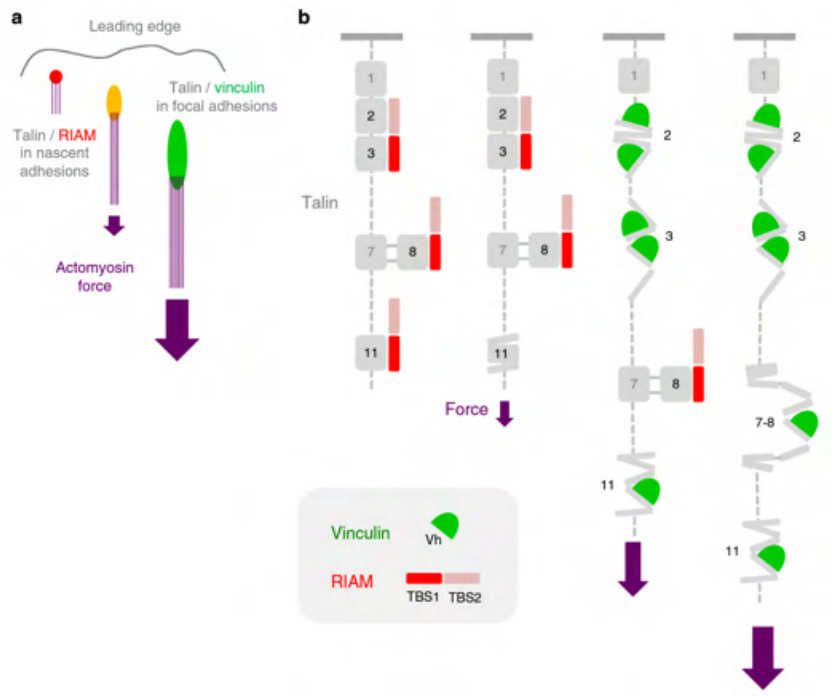

Figure 1.2.0.6: ***Model for the actomyosin-dependent binding of RIAM and vinculin to talin:*** *Model for the actomyosin-dependent binding of RIAM and vinculin to talin. A diagram illustrating the change between RIAM-dominated, low-force nascent adhesions and vinculin-enriched mature FAs in response to mechanical force exerted by the actomyosin stress fibres. b Model describing how talin dissociates from RIAM and associates to vinculin sequentially in response to the actomyosin force. Image adapted from Vigoroux et al, 2020.*

Cytoskeletal drugs

Since the 1970s, the effects of several actin and microtubule disruptors on the cytoskeleton have been identified and studied. The table below (1.2-1) lists some of the more common compounds, their targets, and their effects.

Actin effecting drugs

One group of compounds known as cytochalasins consist of around 20 known fungal metabolites that bind and cap the growing, barbed end of filamentous actin (F-actin), preventing further polymerisation of actin [77]. Cytochalasins inhibit polymerisation without directly affecting depolymerisation, subsequently causing disassembly of actomyosin cytoskeleton [77]. Specifically, cytochalasin B and D are known for their high specificity for binding the barbed end (plus end) of F-actin and causing rapid inhibition of cytoplasmic ruffling and loss of filopodial extension in growth cones [78]. These changes occur fast, within minutes, but are reversed when the toxins are

Table 2: *Cytoskeletal drugs and their effects.*

Cytoskeletal Drug	Drug Target	Action/Effect
Cytochalasins	Actin	Prevents polymerisation
Latrunculin	Actin	Prevents polymerisation
Jasplakinolide	Actin	Enhances polymerisation
Phalloidin	Actin	Stabilises filaments
ROCK inhibitors		
-H1152	Actin	Prevents polymerisation
-Y27632	Actin	Prevents polymerisation
Demecolcine	Microtubule	Depolymerases
Nocodazole	Microtubule	Prevents polymerisation
Paclitaxel (taxol)	Microtubule	Stabilises microtubules preventing mitosis
Rotenone	Microtubule	Prevents polymerisation
Vinblastine	Microtubule	Prevents polymerisation

removed [78]. Another group of compounds involved in actin depolymerisation are the Latrunculins; these are a class of molecules purified from the Red Sea sponge *Negombata magnifica* (formerly *Latrunculia magnifica*) [79]. These compounds have been shown to bind to globular actin monomers (G-actin), sequestering the free monomers preventing further polymerisation of actin and subsequently enhancing its depolymerisation [80]. Both groups of compounds act directly on actin, and their effects are seen primarily in highly dynamic regions of actin turnover.

Alternatively, some proteins maintain the cytoskeleton and its regulation, which are effective indirect targets for actin depolymerisation. One such protein is the Rho-associated protein kinase (ROCK). ROCK is a kinase belonging to the PKA/PKC family of serine-threonine specific protein kinases and is primarily involved in the regulation of morphology and turnover of the cytoskeleton [81]. One of the canonical functions of ROCK is to stabilise actin filaments by inhibiting depolymerisation indirectly. This effect is achieved as ROCK phosphorylates and activates LIM kinase, which phosphorylates cofilin. Whereas dephosphorylated cofilin acts to sever F-actin, resulting in depolymerisation at the pointed (minus end) of filaments and subsequently preventing their reassembly [81–83]. Canonical ROCK phosphorylates cofilin preventing actin depolymerisation [82,83]. The converse occurs by activating ROCK with a specific inhibitor such as Y27632 or H-1152, and actin is actively depolymerised (figure 1.2-7 below). Additionally, ROCK is also involved in the regulation of myosin light chain-phosphatase, which ROCK inhibits; in doing so, this promotes more of the phosphorylated Myosin Light Chain (MLC-P),

which is associated with stress fibre assembly [81]. Again, we see more active MLC-phosphatase inhibiting ROCK, which promotes stress fibre disassembly and contraction (see Figure 1.2-7 for details).

Of the two ROCK inhibitors discussed here, the Y27632 compound is the most widely used and understood inhibitor of ROCK [81]. This pyridine derivative is the oldest synthesised and reported specific inhibitor of Rho-kinase family enzymes. The Y27632 compound inhibits ROCK activity by competing for the catalytic ATP binding domain [84]. The newer H-1152 compound is an *isoquinoline-sulfonamide* derivative [84], a more specific and membrane-permeable inhibitor of Rho kinases. Compared to the Y27632 compound, the H1152 compound is a poorer inhibitor of the serine/threonine kinases, PKA, PKC and MLCK, and so acts with increased specacifity [85].

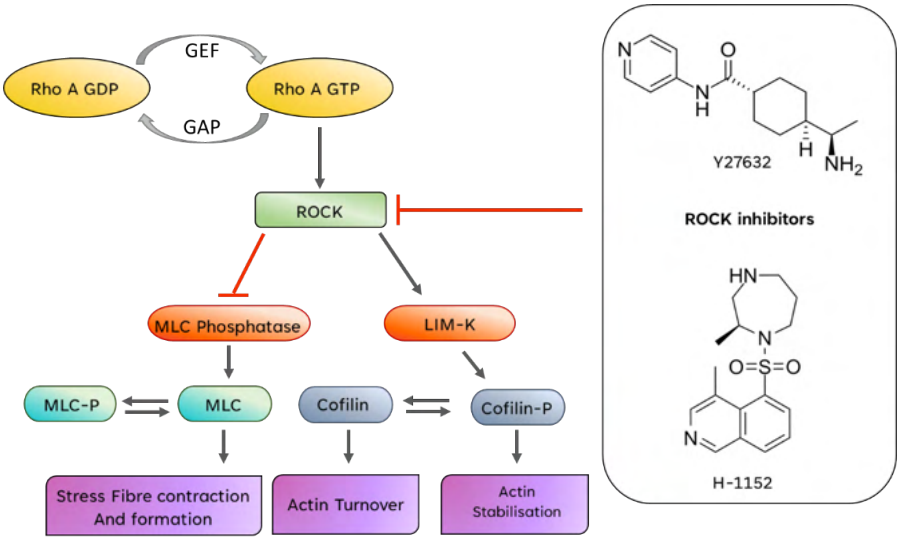

Figure 1.2.0.7: ***ROCK Targets:*** *ROCK Targets: Rho A GDP is activated by guanine nucleotide exchange factors (GEFs) which are themselves activated in response to lysophosphatidic acid (LPA) binding to G-protein-coupled receptors (GPCRs) on the plasma membrane. GTP-bound Rho A subsequently activates ROCK to phosphorylate several substrates leading to numerous cellular responses involving focal adhesions, actin network assembly intermediate filament disruption and many more. Two of note are the phosphorylation and activation of LIM-K which in turn phosphorylates cofilin, leading to actin stabilisation and the phosphorylation of the myosin binding subunit of myosin light chain phosphatase which inhibits the dephosphorylation of myosin light chain (MLC), thereby increasing myosin II activity and stress-fibre formation and contractility.*

Why inhibit actin with Rho kinases? Both latrunculin and cytochalasin principally prevent further actin polymerisation by obstructing further growth of actin filaments without directly disassembling existing actin filaments. While advantageous, directly inhibiting the polymerisation of new actin filaments in the lamellipodia, actin within stress fibres which are tightly crosslinked [86]

does not turn over as quickly and so remains within the cell for longer [87,88]. Direct inhibition of polymerisation is an issue when studying actin-dependent protein-protein interactions within mature adhesions, which are associated with stress fibres. In comparison, the ROCK inhibitors cause direct and rapid disassembly of stress fibres and their bound focal adhesions within minutes. While stress fibres located in the periphery of the cell are not severely affected due to nascent adhesions actin independence [89].

Phalloidin is an actin stabilisation compound; phalloidin belongs to a class of toxins known as phallotoxins. These are a group of bicyclic heptapeptides derived from poisonous mushrooms, such as the death cap mushroom (Amanita phalloides), from where these molecules get their name (Wieland et al., 1978). Phalloidin, the most well-known from this class of compounds, binds to actin filaments with much great affinity than actin binds to its monomers [90]. This causes a shift in the equilibrium towards filaments, lowering the critical concentration for polymerisation by 10 to 30-fold under various conditions [90]. The lower critical concentration is due to a decrease in the rate constant for the dissociation of actin subunits from filament ends [90,91].

Another actin-stabilising compound, jasplakinolide, is a cyclic peptide consisting of three amino acid residues, l-alanine, N-methyl-2-bromotryptophan and β-tyrosine joined in a 15-carbon macrocyclic ring [92]. Jasplakinolide is isolated from the marine sponge, *Jaspis johnstoni*, which has previously been shown to bind to and stabilise filamentous actin [93]. The effect of jasplakinolide on actin filaments is less well understood than that of phalloidin. It is known that jasplakinolide binds to F-actin competitively (see figure 1.2-8) in a similar way to phalloidin [93] and that jasplakinolide acts to accelerate actin polymerisation by inducing more nucleation events [93,94]. Jasplakinolide has also been shown to promote actin polymerisation under non-polymerising and lowers the critical concentration of actin assembly in vitro [95].

Microtubule effecting drugs

Microtubules are elongated, rigid polymers made of monomers of α and β-tubulin that assemble into highly dynamic, structurally, and functionally important components of the eukaryotic cytoskeleton (see figure 1.2-10). Microtubules are the largest and one of the most significant cytoskeletal components and play a vital role in nearly every cellular event; microtubules

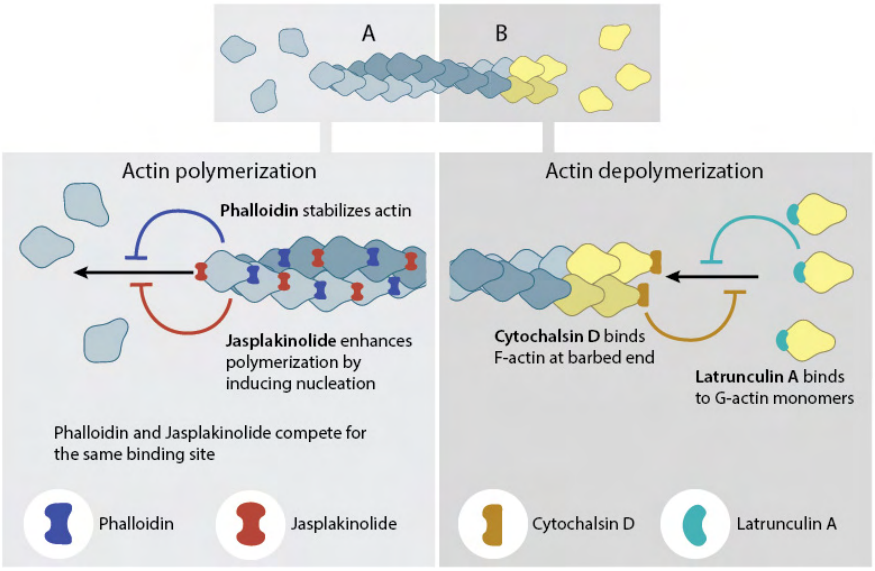

Figure 1.2.0.8: ***Actin Dynamics:*** *Actin Dynamics. A diagram to illustrate how the different compounds act to either actively enhance actin polymerisation or depolymerisation and their mechanisms. (Adapted from https://www.mechanobio.info/cytoskeleton-dynamics/)*

are an essential component in an interconnected intracellular "highway" where many cellular cargos are shuttled across the cell by a dynamic network of molecular motors. During the prometaphase of mitosis, microtubes are of paramount importance in the formation of mitotic spindle fibres, which provide the force necessary to divide chromosomes producing two identical daughter cells.

One of the drugs which specifically affects microtubules is Nocodazole; Nocodazole is a well-known anti-mitotic agent that reversibly disrupts the polymerisation and growth of microtubules. Nocodazole achieves this by binding to beta-tubulin monomers preventing association with alpha-tubulin molecules and thus frustrating further polymerisation and microtubule assembly [96]. Impaired microtubule dynamics and failed microtubule assembly significantly affect the cell as this prevents the formation of metaphase spindle fibres during mitosis [96]. Poorly assembled spindle fibres cause cells to become arrested in mitosis by inducing a G2/M-phase arrest which subsequently induces apoptosis. Spindle fibres not attached to kinetochores will otherwise bind to MAD2, preventing progression from prometaphase to metaphase and, subsequently, anaphase of mitosis [97]. It has been suggested that kinetochore-bound MAD2 promotes the up-regulation of Cdc2 and cyclin B1 in cells arrested in prometaphase. The increase of these two cell cycle checkpoint proteins in prometaphase cells, particularly their accumulation, is

thought to be primarily responsible for developing characteristic phenotypes. Following a prolonged prometaphase arrest, nocodazole-treated cells are seen to undergo cell death via intrinsic apoptosis pathways [97]. For this reason, nocodazole has been used as a chemotherapy drug for rapidly dividing cells such as tumour cells [98].

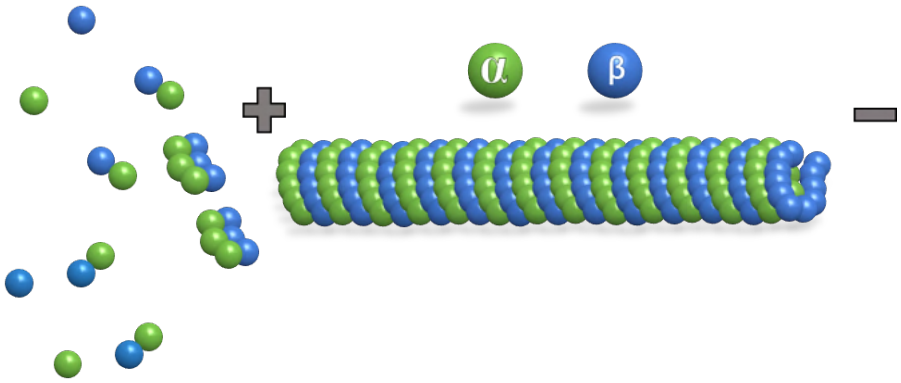

Figure 1.2.0.9: *Microtubule Dynamics:* *Microtubule Dynamics: A diagram illustrating Microtubule assembly and disassembly. Microtubules are assembled at the plus end where GTP-bound α and β tubulin monomers bind together to assemble the growing tubule. Conversely, at the minus end, α and β monomers disassemble.*

Paclitaxel is a microtubule-stabilising drug also known as Taxol; this is due to its discovery, being isolated from *Taxus brevifolia*, the Pacific yew tree [99]. Paclitaxel is a well-known drug used to treat various cancers such as ovarian, breast, lung, gastroesophageal, endometrial, cervical, prostate, and head and neck cancer [99]. This is because, like nocodazole, paclitaxel can induce mitotic arrest, leading to cell death in a subset of the arrested cells. However, the mechanism of this is achieved from that of nocodazole. Where nocodazole binds to β-tubulin and blocks the formation of new microtubules, paclitaxel stabilises microtubules by reducing the critical threshold concentration necessary for tubulin heterodimers to polymerise [99, 100]. Furthermore, microtubules assembled in the presence of paclitaxel are protected from disassembly induced by cold or calcium treatment due to the lower threshold required for polymerisation [99–101].

1.3 A Brief Introduction to Fluorescence, FRET and FLIM

What is Fluorescence?

Microscopy has always played an essential and pivotal role in studying cellular processes. From van Leeuwenhoek's and Hooke's earliest endeavours in the 17th century to the 2014 Nobel prize in chemistry for *developments in super-resolved fluorescence microscopy,* so much of recent advancement in modern biomedical research has only been made possible with the development of fluorescence microscopy. Whether cells are stained with fluorescent dyes or have been genetically engineered to express fluorescent-tagged proteins to molecules of interest, our understanding of the fundamental basics of the living world has exponentially expanded with the advent of modern fluorescence microscopy and related techniques. Fluorescence microscopy has revealed many secrets of the microscopic and, in recent years, the nanoscopic worlds, from which our understanding of the molecular basis of many diseases, such as cancer, heart disease, and many neurodegenerative diseases have all vastly benefitted.

Various descriptions of unexplained phenomena concerning solutions containing what we now know as flavonoids emitting a strange blue glow were reported as far back as the 16th century. Although, it was not until the beginning of the 19th the century that we started to examine these unusual phenomena more scientifically. Sir David Brewster found a similar effect while investigating chlorophyll solutions in 1833, and Sir John Herschel stumbled upon the same effect with sulphates of quinine [102]. It was in 1852 that the Anglo-Irish scientist George Gabriel Stokes published his seminal paper *"On the change of refrangibility of light"* [102], where he also described the same phenomena as others had previously done. Crucially, he also described how a particular mineral of Calcium Fluorite (CaF_2), known as fluorspar, exhibited a deep blue glow when irradiated with non-visible wavelengths of ultraviolet light. A brief footnote introduces Fluorescence as Stokes describes this new form of light emission [103].

"I am almost inclined to coin a word and call the appearance fluorescence from fluor-spar, as the analogous term opalescence is derived from the name of a mineral." [103]

Fluorescence is a specific type of luminescence: the phenomenon of light production where light is emitted from a substance that has not been directly heated. Essentially, luminescence describes the emission of photons from any excited state where an excited electron is returned to the ground state in a radiative process. This phenomenon contrasts with the other form of light production, incandescence. Incandescence is seen in the operation of a lightbulb where a filament is heated to glow white-hot, emitting energy as mostly heat and only a small percentage as light. Luminescence produces photons without heat through a radiative relaxation of electrons in the excited electronic state. This relaxation can occur in nanoseconds with fluorescence or more slowly over a timescale ranging from several milliseconds to minutes as with phosphorescence [104].

In fluorescence, an electron is promoted from the S_0 ground state to the excited S_1 state, known as an S_0 to S_1 transition [105] (see figure 1.3.1). The rapid de-excitement from the S_1 state occurs, causing the return of the excited electron to the ground state simultaneously with the emission of a photon [106]. Electronic transitions such as these are particularly favourable because the process (excitation and return) only takes a few nanoseconds—the resulting emission produces rates of $\approx 10^8$ photons per second for most fluorescent species [107].

In contrast, phosphorescence requires an electronic transition from the ground singlet state to the excited singlet state ($S_0 \rightarrow S_1$) before an intersystem crossing event occurs ($S_1 \rightarrow T_1$). This event transitions the excited electron from the singlet to the excited triplet state before the emission of a photon can occur, and the electron can finally return to the ground singlet state ($T_1 \rightarrow S_0$) [104]. The lifetime of the triplet state is considerably longer than that of the excited electron in the singlet, as phosphorescence, requires an intersystem crossing event that is not particularly favourable. During the intersystem crossing, the excited electron becomes uncoupled with the ground state electron and therefore has the same parallel spin (see figure 1.2-1). The uncoupling of the ground, and excited electrons occur when an excited singlet state electron goes through a non-radiative process, where the spin of the excited electron is coupled with the net orbital angular momentum. The outcome is a reduction in the emission rate to between 10^3 and 10^0 photons per second [104].

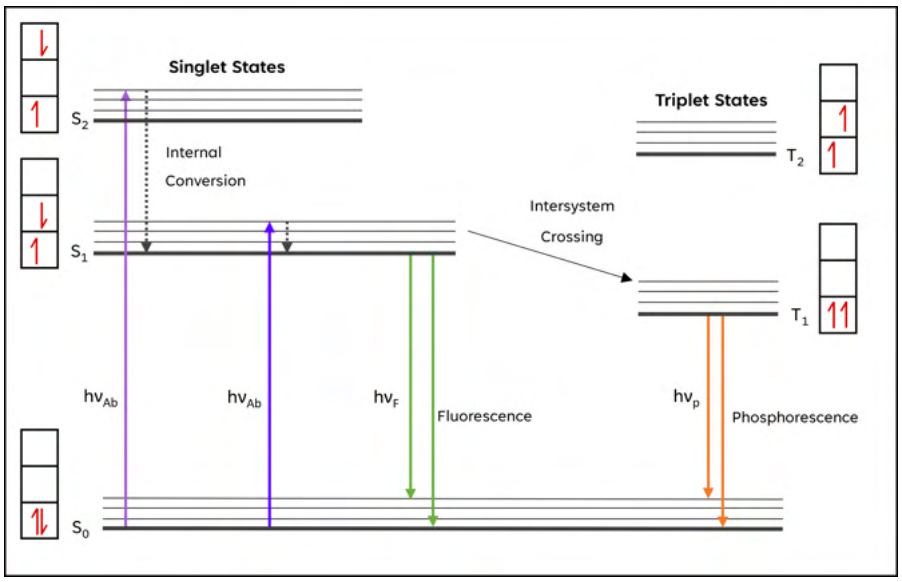

Figure 1.3.0.1: ***Classic Jablonski Diagram:*** *A diagram illustrating the possible electronic transition from the ground singlet state to the excited singlet and triplet states*

The chromophore is the part or moiety of a fluorescent molecule that absorbs light, and for a fluorescent molecule, it is the specific moiety responsible for the emission of photons by fluorescence [108]. Promoted electrons to the excited singlet state (S_1) are usually promoted with more than the minimum energy to overcome the quantised energy gap, such that newly promoted electrons usually relax initially from a position of higher vibronic energy within the S_1 state to the lowest vibronic state within the excited singlet [104]. This process is known as Kasha's rule, named after American spectroscopist Michael Kasha proposed the rule in 1950 [95]. The excess energy the electron loses typically produces a small amount of kinetic energy or heat (see equations 1.3.1-1 – 1.3.1-3). Even though the energy loss is small, it is still essential as the photon that caused the ground state electron to become excited will always have more energy than the photon emitted. The more energy a photon has, the shorter its wavelength will be, such that the emitted photon is always red-shifted from (or has a longer wavelength than) the excitation photon. This phenomenon was first demonstrated by George Gabriel Stokes in 1852 and is now known as Stokes shift in his honour [104]. A repercussion of Kasha's rule is the associated Vavilov rule (named after the Soviet optical physicist Sergey Vavilov), which states that the quantum yield of a fluorophore is independent of the excitation wavelength [104].

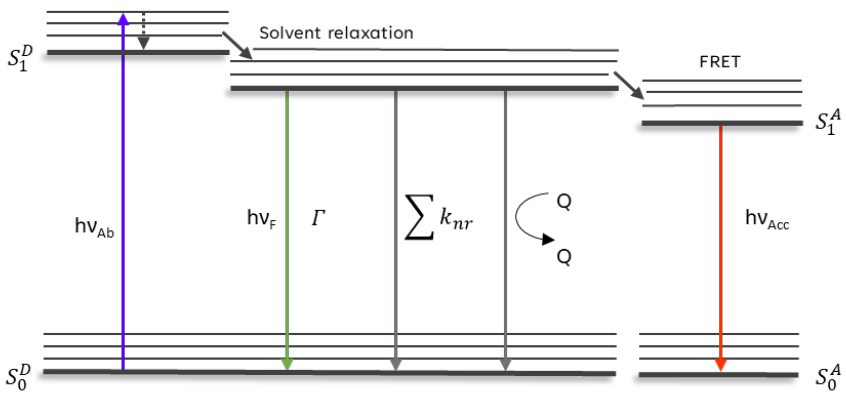

Figure 1.3.0.2: ***Jablonski Diagram Illustrating FRET:*** *A scheme illustrating the possible energy transfers pathways which depopulates an excited donor fluorophore*

What is FRET, and why do we use it?

Fōrster (or Fluorescence) Resonance Energy Transfer (FRET) is a quantum phenomenon describing an energy transfer between two fluorophores that are sufficiently close together. FRET describes the energy transfer from a donor fluorophore that is initially electronically excited to a nearby accepting fluorophore through a non-radiative dipole-dipole coupling event. This energy transfer depopulates the donor fluorophore's excited state while simultaneously populating the excited state of the acceptor fluorophore [109]. The efficiency of this energy transfer is inversely proportional to the sixth power of the distance that separates the two fluorophores, a consequence of which is that FRET only occurs across very short distances, typically only 2-10 nm for most pairs of fluorophores [104]. There are several possible depopulation pathways of the excited fluorophore (figure 1.3-2); these include the emission of a photon through fluorescence (shown in green), non-radiative (in grey) describes the mechanisms that depopulate the excited state of the fluorophore, which does not emit photons. Quenching (shown in pink) describes how energy is transferred to other molecules in a non-radiative manner but crucially also does not cause the emission of a photon. FRET is the last mechanism of depopulation described in the figure (shown in red); this is where a neighbouring compatible fluorophore accepts energy from the excited state of an electron located in the donor fluorophore and depopulates the donor through the emission of a photon from the acceptor fluorophore. The theory of Resonance Energy Transfer was established first by Theodor Fōrster with his seminal paper on the topic entitled *"Zwischenmolekulare Energiewanderung und Fluoreszenz"* published in 1948 [109] for his contri-

bution to this subject; the photophysical phenomenon is named in his honour. As described by the Fōrster equation, energy transfer efficiency is inversely proportional to the sixth power of the separation distance between two fluorophores. The Fōrster equation (equation 1.2-1) describes the relationship between the FRET efficiency E, separation distance, r and the Fōrster radius, R_0. The Fōrster radius is the distance at which there is 50% energy transfer between two fluorophores; for this reason, the Fōrster radius is often used over other metrics to compare the energy transfer efficiency between different pairs of fluorophores.

$$E = \frac{{R_0}^6}{r^6 + {R_0}^6} \tag{1}$$

For instance, FRET-based microscopy techniques such as FLIM and FCS (Fluorescence Correlation Spectroscopy) are compelling for their nanoscale proximity detection and have been used extensively to study Protein-Protein interactions over the last 40 years [110]. Even though other biophysical techniques have been developed with much greater resolution, such as X-Ray crystallography, Cryo-EM, NMR, and super-resolution microscopies such as STEAD or STORM 10-40 nm, to name a few, these techniques are generally far less accessible. They require much more complex sample preparation and restrictions regarding what can be imaged. NMR, for instance, has an upper limit on the molecule size that it can image (≈30 kDa), and X-Ray crystallography requires the sample to be crystalline. Whereas with FRET-based techniques, these can all be achieved with live cell imaging or even *in vivo,* providing us with experimental conditions more comparable to physiological conditions.

$$R_0 = \sqrt[6]{\frac{9000 \cdot \ln(10) \cdot \kappa^2 \cdot \Phi_D \cdot J_\lambda}{128 \cdot \pi^5 \cdot N_A \cdot n^4}} \tag{2}$$

The Fōrster radius depends on many factors, as outlined in equation 1.3-2 above. Briefly, where, κ^2 is the orientation factor, Φ_D is the quantum yield of the donor, J_λ is the overlap integral, N_A is the Avogadro constant and is equal to 6.022 x10^{23} (to 3 sig. fig), and $\mathbf{n}$ is the refractive index of the imaging medium. The Fōrster radius is an essential tool when considering which pairs of fluorophores to use in a FRET or FLIM experiment, and as such, I will expand

a little on each term in the Fōrster equation as this is vital in understanding what factors affect the efficiency of energy transfer.

The orientation factor, κ^2, describes the relative orientation of the two coupled dipoles between the donor and acceptor fluorophores and is of great significance in understanding energy transfer efficiency. In the same way as the relative position of a radio antenna can affect its reception, the relative orientation of the two fluorophores has a significant effect on the ability of the acceptor to receive the transmitted energy from the donor [111, 112]. If the donor and acceptor are aligned perpendicular to one another, energy transfer efficiency will be zero. Conversely, if the angle between the two coupled fluorophores is parallel, then the energy transfer efficiency will be maximal (see figure 13.-3). Even though κ^2 can theoretically vary between 0 and 4 for nearly all isotropic systems; this is assumed to be 2/3 [112, 113]. Dynamic averaging is used to create this approximation which assumes that

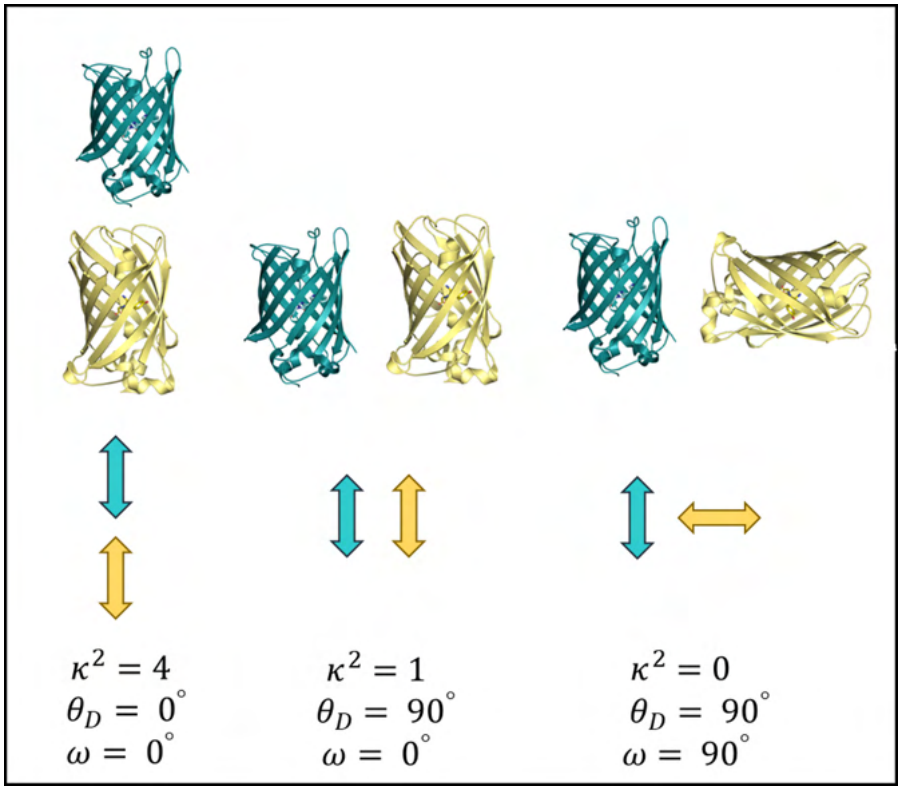

Figure 1.3.0.3: ***Orientation Factor:*** *A diagram illustrating the relationship between the kappa-squared, the orientation factor and the relative positions of the fluorophores. Maximal FRET is observed when the two dipoles are orientated end on end with a κ^2 of 4. However, when orientated in a parallel manner the κ^2 drops to 1 and will be equal to 0 if arranged in a perpendicular orientation.*

the rotational diffusion timescale of a FRET pair is much shorter than the fluorescence lifetime of the donor. In any given FLIM experiment, the fluo-

rophores are rotating freely and with sufficient speed that any anisotropy would be averaged out over the lifetime of the donor [111,114]. This is generally accepted for ergodic systems as a distribution of kappa-squared values will be expected to with a mean centred around 2/3, representing an isotropic system. However, in systems where single FRET interactions are being studied or in systems where fluorophores are either tightly constrained in 3D complex or are orientated regularly, it might well be the case that one or even both fluorophores are not as free to rotate on this timescale [111–114].

Studies from single-molecule FRET (smFRET) experiments with fluorophores labelled directly to DNA bases have yielded exciting results due to the rigid structure and the natural helical twist of the DNA, causing the fluorophores to stack in a parallel arrangement. This stacking arrangement resulted in very low FRET efficiencies of $\approx 0\%$ due to a very low experimental kappa-squared value [115,116].

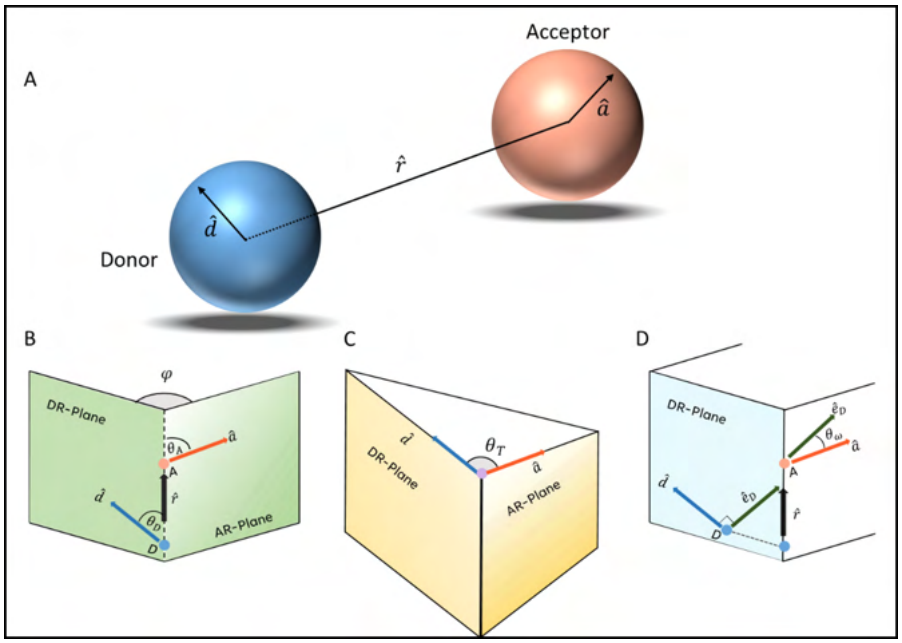

Figure 1.3.0.4: ***Kappa-squared Visualized:*** *A) $\hat{d}$ and $\hat{a}$ are unit vectors along the emission and absorption diploes and $\hat{r}$ is the vector which connects the of the centres two diploes. B-D) are diagrams which illustrate the relationships between the vectors $\hat{d}, \hat{a}$ and $\hat{r}$ with respect to the donor-r plane and acceptor-r plane yielding separation angles, $\varphi, \theta_A, \theta_D, \theta_T$ and θ_ω.*

Where the angle φ, is the angle between the projections of $\hat{d}$ and $\hat{a}$ on a plane perpendicular to $\hat{r}$ (panel B). The angle θ_T, is the angle between the plane bound by the donor-dipole, $\hat{d}$ and the vector $\hat{r}$, and the plane bound by acceptor-dipole $\hat{a}$, and $\hat{r}$ (panel C). The angle ω is the angle between the

acceptor dipole, $\widehat{a}$ and the electric field dipole that is perpendicular to the donor dipole, $\widehat{d}$ (panel D).

Visualising kappa-squared, for a single pair of fluorophores, the orientation factor is dependent upon the direction of the emission transition moment of the donor and the subsequent orientation of the absorption transition moment of the acceptor and the the direction of the connecting line between the centres of the donor and acceptor (figure 1.3-4). A 2D diagram is generally insufficient to represent the 3D relationship between the various vectors and angles which describe the orientation factor. Equations 1.3.-3 outline the angles and planes one needs to consider when visualising the diploe-dipole interaction between fluorophores in 3 dimensions.

$$\begin{aligned}\kappa^2 &= (\cos\theta_T - 3cos\theta_D \cos\theta_A\ )^2 \\ \kappa^2 &= (\sin\theta_D \sin\theta_A \cos\varphi - 2\cos\theta_D \cos\theta_A)^2 \\ \kappa^2 &= \cos^2\omega \left(1 + 3\cos^2\theta_D\right)\end{aligned} \tag{3}$$

The quantum yield of a fluorescent dye can change upon the addition of a label as fluorophores are very sensitive to their local environment; the labelling position, the conformational state of the molecule and the binding of ligands can also affect the quantum yield [117]. For example, the quantum yield of Cy3B can vary between 0.19 to 0.97 when labelled at different positions on dsDNA; this results in a substantial difference in the R_0 value for the Cy3B-ATTO 647N FRET pair between 5.48 nm and 6.59 nm [117–119]. This is why the independent quantum yield determination at different labelling positions is strongly recommended for fluorescent dyes and proteins.

The refractive index $\mathbf{n}$, describes the optical density of the medium in which the fluorophores are dissolved; this is typically between $1.33 \approx 1.5$ [117]. This will vary as the precise concentration of dissolved solutes, such as proteins, lipids and even nucleic acids will often affect the refractive index. There is a considerable degree of variation in refractive indices, which depend on many factors, the most significant of which is the viscosity of the local environment of the fluorophores. Intracellular refractive indices typically vary, from the primarily aqueous cytosol of 1.36 to 1.42 for lipid and protein-rich mitochrondria [120]. An intermediate value of 1.4 was previously suggested [102] for use in these calculations. However, different values may be more

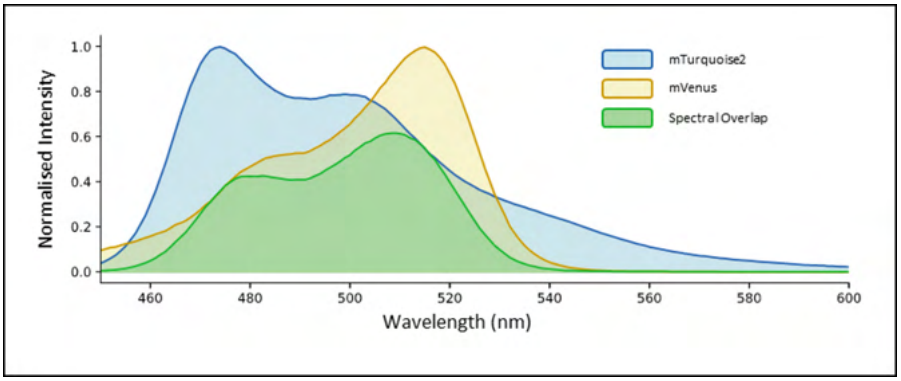

Figure 1.3.0.5: ***Spectral overlap for the mTurquoise2 and mVenus Fluorescent Proteins:*** *A graphical illustration of the spectral overlap required for efficient resonance energy transfer between fluorescent proteins. The area in green represents the total potential energy that mTurquoie2 can transfer to mVenus.*

appropriate when investigating FRET interactions within specific organelles [121].

The overlap integral J_λ , describes the degree of spectral overlap between the donor fluorophore's emission spectra and the acceptor fluorophore's absorption spectra and is measured in M^{-1} cm^{-1} nm^4. The overlap integral is equal to the area under the donor's emission spectra, which is also under the area for the excitation spectra of the acceptor and scaled by the donor fluorophores quantum yield (see figure 1.3-5). The greater the degree of overlap between two spectra, the more efficient the fluorescence transfer is between the two fluorophores [104].

Measuring FRET by Sensitised Emission.

Ratiometric FRET, also known as sensitised emission FRET, is one of the simplest methods of detecting FRET and can be used on a wide range of microscopes. In this case, the donor fluorophore is excited at a specific wavelength the emitted light is filtered through emission filters before reaching either a camera (widefield) or detector (confocal). This method would function perfectly in an ideal world where bleed-through and crosstalk were absent, but it does not. In the real world, we must consider the crosstalk between fluorophores which is a significant issue and extensive control experiments are usually required to establish the presence or absence of FRET. This is mainly due to the degree that which different fluorophores' excitation spectra overlap, meaning that when we excite GFP at 488 nm, we are also exciting the acceptor mCherry, albeit at a lower intensity of $\approx 5\%$. This issue becomes a significant difficulty when we realise the amount of undesired excitation

is approximately equal to the magnitude of increased fluorescence due to FRET. The control experiments for ratiometric FRET experiments can be extensive as they require different combinations of emission filters and excitation wavelengths with different samples that contain either the donor only, the acceptor only, or the potential FRET sample labelled with both the donor and acceptor. It is often necessary to undertake considerable image processing to subtract unwanted components to remove much of the cross-talk and spectral bleed-through incurred through ratiometric FRET experiments. However, this often decreases the signal-to-noise level and increases the uncertainty in the FRET measurements. This is why obtaining quantitatively accurate FRET data with this approach is somewhat challenging and why other FRET-based techniques are often used instead.

FLIM: Measuring Lifetimes and Molecular Interactions.

Fluorescent Lifetime Imaging Microscopy, or simply FLIM, is an advanced imaging technique where the fluorescence lifetime (τ) of an emitted fluorophore is directly measured. This is usually achieved concurrently with acquiring a widefield, confocal or multiphoton intensity image. Conventionally, fluorescence lifetime is defined as the average time a fluorophore remains in the excited (S_1) state before it returns to its ground and emits a photon. Within this interval, the intensity $I(t)$ will have decreased by 36.79% (e^{-1}) of its original value [120]. The relationship between the decay intensity, time (t) and the fluorescence lifetime can be described with a first-order kinetics equation summed for all fluorophores, i, within a given sample; see equation 1.3-3 below. Where α_i is the amplitude of the respective intensities for each fluorophore (pre-exponential factor).

$$I(t) = \sum_i \alpha_i e^{\frac{-t}{\tau_i}} \tag{4}$$

Fluorescence lifetime can either be measured using frequency-domain or time-domain instrumentation. For time-domain FLIM, a pulsed laser source such as a Ti-sapphire laser used to create a short excitation pulse followed by a more extended exponential decay emission from the sample. The decay profile is calculated directly from the arrival times of emitted photons binned into a histogram as with Time Correlated Single Photon Counting (TCSPC)

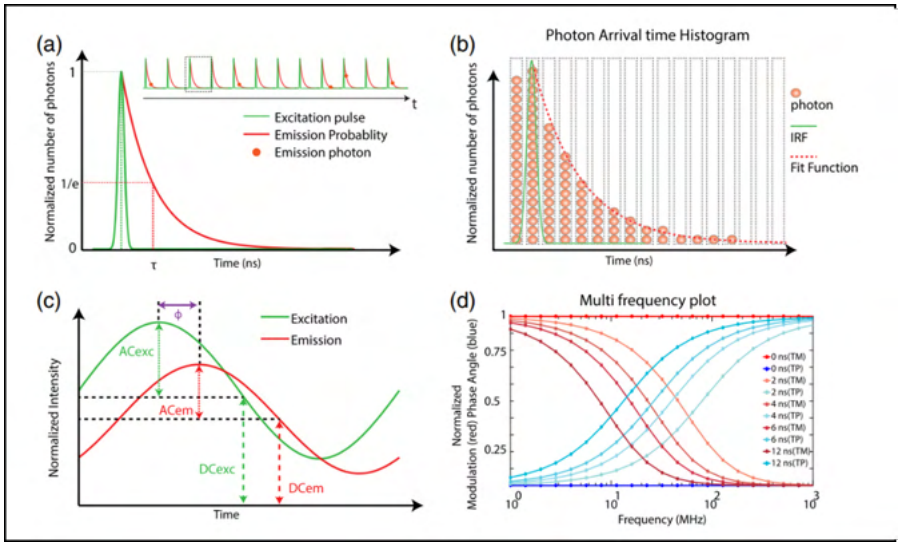

Figure 1.3.0.6: ***A scheme illustrating the fundamental concepts of time-domain (TCSPC) and frequency-domain FLIM:*** *A) TCSPC FLIM acquisition showing the excitation pulse (green), the probability emission decay (red solid line) and the estimation of the fluorescence lifetime from e-1. B) Following a short excitation pulse (green peak) photon arrivals times (red balls) are temporally binned (grey boxes) with an exponential decay curve fitted (red dotted line). (C) a diagram depicting frequency-domain FLIM measurements with sinusoidally modulated excitation (exc) and the resulting phase-shifted emission (em) signal. (D) Modulation and phase versus frequencies for different lifetimes. TM, modulation lifetime; TP, phase lifetime. Adapted from Datta et al, 2020.*

or through time-gated or pulse sampling techniques (see panels A and B of Figure 1.3.7 below [120]. If multiple species are present in the sample, both fluorescent emissions are binned together and during the analysis, a bi-exponential fitting can be used to separate the contribution of the two fluorescent lifetimes for the two fluorescent species. In frequency-domain methods, each photon measured is represented as a phase delay with respect to the excitation photon (see panels C and D of figure 1.3.7 below) [122, 123]. For multiple species, this phase distribution is analysed in Fourier space to extract the modulation and demodulation parameters that separate multiple species [104, 120]. Both methods have advantages and disadvantages in different imaging conditions and scenarios, including low photon budget, high spatial resolution, high dynamic range, or short temporal resolution [120].

Details of the optical set-up for Two-Photon TCSPC-FLIM, which was used extensively throughout this project, can be seen in figures 1.3-6 below. The system uses a pulsed multiphoton Titanium-sapphire solid-state laser, which is pulsed at a frequency of 80 MHz (8×10^7). Essentially, a pulse of laser light with an FWHM of approximately 200 fs (200×10^{-15} s) is emitted from the laser

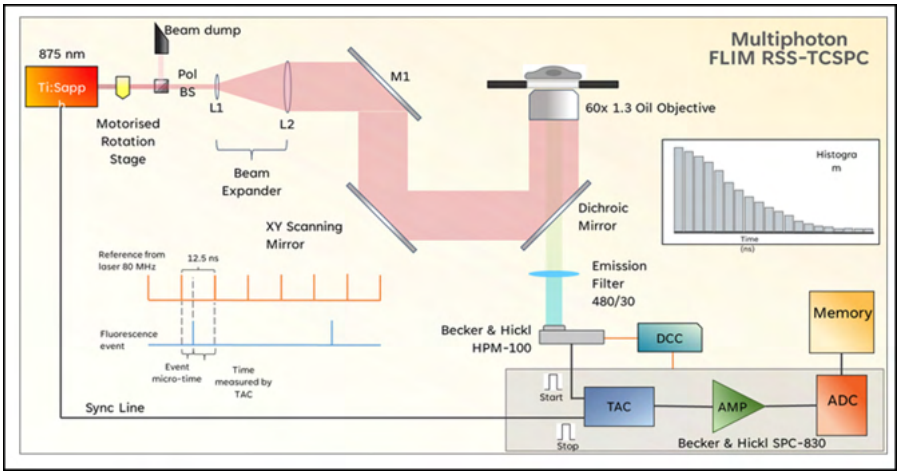

Figure 1.3.0.7: ***A scheme illustrating Multiphoton TCSPC-FLIM optical configuration:*** *The diagram illustrates the optical set-up used for Two-Photon TCSPC-FLIM imaging throughout this PhD.*

every 12.5 ns. A pulsed laser source is required to perform time-resolved fluorescence lifetime imaging as the pulses of light from the laser, and the emitted pulses from the sample are used as the stop and start signals in the timing circuit. The sub-type of TCSPC-FLIM that I used is known as reverse-Start/Stop or RSS-TCSPC-FLIM. In this mode, the timing circuitry is activated when a photon of light emitted from the sample is detected, and the "timer" or Time-Amplitude capacitor (TAC) will run until the next pulse from the laser is detected from a reference line. Measuring the length of time an electron remains in the excited S_1 state after it is excited by a pulse of light and before it falls back to the ground, S_0 state and emits a single photon is how the fluorescence lifetime of a fluorophore is measured. A pulsed laser source is essential and just not possible with a continues-wave laser source; at the time of building this imaging system, not many pulsed lasers were commercially available with the power output that was needed; it was for this reason, above many others, the multiphoton Ti-sapphire laser was chosen. An added benefit is that this laser is tuneable, so only one laser is needed to excite fluorophores between single photon excitations between 400 and 600 nm.

The rest of the FLIM system was built around a Nikon Eclipse Ti-E microscope fitted with a 60× 1.30 NA Nikon Plan-Fluor oil objective and an 80 MHz Ti-sapphire laser (Chameleon Vision II, Coherent) tuned to 875 nm (two-photon excitation wavelength for the donor mTFP1). Photons were collected using a 482 ± 25 nm emission filter (FF01-482/25-25, Semrock™) and an HPM 100-40 hybrid detector (Becker & Hickl). Laser power was adjusted to give average photon counting rates of the order 10^4 to 10^5 photons s^{-1} with peak

rates approaching 8x10^5 photons s^{-1}. Acquisition times of 300 seconds at low excitation power were used to achieve sufficient photon statistics for fitting while avoiding either pulse pile-up or significant photobleaching. Pulse pile-up is caused when the sample emits multiple photons during a single excitation pulse. Pulse pile-up is a real problem as only the arrival time of the first emitted photon is counted, and all others are not recorded. This has the effect of reducing the measured lifetime and should be avoided where possible. The practical solution is to reduce the laser power such that the probability of an emitted photon from the sample is roughly 0.01; this is typically achieved by reducing the laser power such that the emitted photon count is two orders of magnitude less than the laser pulse rate of 8 x 10^7 to less than 8 x 10^5. All FLIM data were analysed using *TRI2* [124], a time-resolved image analysis package, and were fitted with a mono-exponential Levenberg-Marquardt model. The data were further processed using a Python script (see §7.2) to produce graphical representations of the fluorescence lifetime and FRET efficiencies using the following equation as previously described [125].

Equation 1.3-5 FRET efficiency Equation

$$\eta_{fret} = \left(\frac{{R_0}^6}{{R_0}^6 + r^6} \right) = 1 - \frac{\tau_{DA}}{\tau_D} \tag{5}$$

Three-Colour and Multiplexed FRET

Most FRET, and FLIM experiments are limited in scope to only investigating one signalling or binding event with one FRET biosensor at a time [126]. A typical intramolecular FRET biosensor is a single molecule, usually a protein, encoding at least one fluorescent protein (FP) and a sensing domain that detects a specific cell change. The detected change can be as simple as the binding of a ligand [127, 128], cleavage of a molecule [129] or the conformational change of the sensing domain responding to mechanical force [50, 130]. Regardless of how this cellular change occurs, the change is reported either through changes in the emission intensity or a reduction in the fluorescence lifetime of the donor FP [104, 126].

Intermolecular FRET often consists of two interacting proteins [131], each labelled with either a donor or acceptor fluorophore often used for detecting protein complex formation. Both sensor types, intra- and inter-molecular, can

be used to extend the scope of an investigation by interrogating not just one event in isolation but by putting that event in context with when or where another cellular event occurs by multiplexing the FRET interactions [126]. This is particularly interesting and necessary when considering how interconnected the cellular world is. Often the systems, interactions, and molecules we are trying to explore involve many interconnected and overlapping pathways. Understanding that two molecules directly bind together is essential but being able to contextualise that interaction with another interaction at the same time is of great importance and interest to many [131,132]. Do we need to use multiplex FRET to investigate multiple interactions or signalling events simultaneously? We could engineer multiple cell lines expressing a different biosensor in each and then attempt to correlate the different FRET-based responses from each into a single model. Whilst this would yield a single model, which could be used to describe the many interwoven interactions, it may not be the most useful or reliable. The correlation of many events in different systems would likely be very problematic, complicated by the innate heterogeneity observed in cellular activity and responses across multiple cells and cell lines [126,133].

Over the last 20 years, many have used multiplexed FRET, where two and even three intra-molecular FRET biosensors have been expressed in the same cell to report the interplay between different cellular events [133]. The first to do so successfully was Pilji and Schultz in 2008, who successfully imaged cells using ratiometric FRET containing three separate FRET biosensors to monitor three different calcium-dependent signalling events. This was possible through spatial separation of the biosensors and spectral unmixing [133]. A graphical explanation of this multiplexed FRET experiment can be seen in panel A of figure 1.3-8.

Using a multi-parameter imaging methodology has given significant insight into the precise timings and interactions of specific cellular events within the same cell [131, 133]. This is possible if there is a sufficient spectral distance between selected FPs or if the sensors used are tightly segregated to specific locations in the cell. If one or more biosensors are expressed in the same cellular compartment, then spectral unmixing and adequate spectral filtering is required to separate similar fluorescence emission wavelengths. Spectral unmixing has been used to simultaneously image CFP/YFP and GFP-based biosensors in pancreatic β-cells. A separate study demonstrated through Image Mapping Spectrometry (IMS), a technique that collects high-

resolution hyperspectral spectral data, that two FRET biosensors excited at the same wavelength, one for cAMP and the other for Caspase-3, could be simultaneously imaged within the same cell [134]. Another study used fluorescence anisotropy with spectral unmixing to provide adequate spectral separation of the FP pairs [135].

Three fluorophores or two-step -cascade FRET is an approach where one donor (the FP with the shortest excitation wavelength) is excited and transfers energy to an acceptor; this acceptor then acts as the donor for a second acceptor in the cascade (figure 1.3-8b). This sequential FRET or two-stepping method has been used to investigate multiple conformational states with a single protein [108, 126, 136]. A proof of principal model illustrating how cascade-FRET could be utilised was created through three-fluorophore labelling oligonucleotides of known distances. A different study applied a similar model using three temperature-sensitive fluorescently labelled proteins imaged in live cells [137]. They used a ratiometric FRET cascade approach to successfully investigate the relationship between intracellular temperature and complex formation [137].

Single-molecule three-colour FRET has been used to probe Holliday junctions (four-way DNA junctions) as a model system that underwent two-state conformational fluctuations, where the three arms of the four-way junction were labelled with Cy3, Cy5 and Cy5.5 fluorophores and, the distance changes between the FPs were measured simultaneously [138]. A separate study used two spectrally identical photo-switchable acceptors (Cy5) with a single donor (Cy3B) to dramatically reduce the experimental and analytical complexity. This allowed for the direct monitoring of multiple distances within dynamic Holliday junctions. Panel C of figure 1.3-8 illustrates how this arrangement would work, except that no FRET would occur between the acceptors [139].

A 2004 study, (Galperin et al., 2004) was the first to use separately fluorescently labelled proteins to determine how a protein complex was assembled in live cells [131]. While others have shown binary binding of three or more proteins to a single protein complex, these approaches were established *in vitro* before being applied to cultured mammalian cells [140].

Another primary application of three-colour FRET is determining stoichiometries for protein complexes using spectral unmixing and FRET coupling in mixed donor-acceptor pairs and complexes [141]. Some challenges and lim-

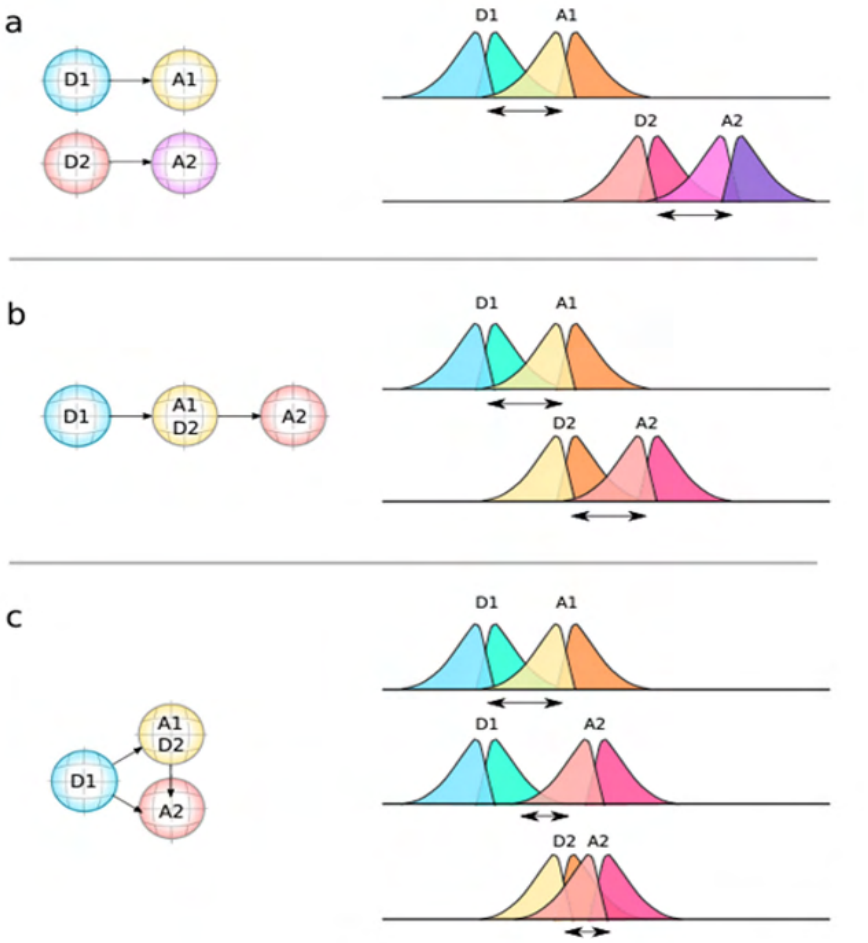

Figure 1.3.0.8: ***Examples of the Types of Multiplexed FRET:*** *A) Parallel FRET assays where two or more spectrally different biosensors are expressed in the same cell. B) Two-step or Cascade FRET, where there are three FPs expressed in the cell in such a way that the FRET interaction is sequential. The D1-A2 FRET can span larger distances than traditional two-colour FRET can. C) Three-fluorophore FRET is used often to detect multiple interactions in a complex. Adapted from Bunt and Wouters, 2017.*

itations in successfully multiplexing FRET lie in expanding the number of fluorophores that can be expressed and combined in a single cell. The interpretation of the combined FRET data may also be problematic if reliant upon intensity-based or ratiometric FRET techniques. Whilst single-molecule FRET has its challenges, at least the obstacle of heterogeneity is not one of the many hurdles to overcome when imaging single molecules and going beyond one donor and one acceptor, as previously outlined. There are many alternative ways that three-colour FRET can be achieved, either with pairs of non-spectrally overlapping biosensors or with sequential cascade FRET. Both imaging approaches rely on only one available donor and acceptor pair at a time. It is usually quite challenging to deconvolve or segregate competing FRET interactions with the same donor. However, it is possible to go beyond this one-to-one limit. By analysing the individual energy transfer rates between fluorophores, we can model the three-colour multiplexed interaction between any number of fluorophores. In practice, this is best suited to looking at no more than four FPs but could be extended theoretically. In the next part of this section, I will describe how energy rate transfer analysis can be used to describe the FRET interactions of three fluorescently labelled proteins.

The energy transfer rate (Γ_{DA}), (s^{-1}) describes the rate of energy transfer (FRET) from the donor to the acceptor. It can also describe the probability of the donor de-excitation or 'decay' occurring through FRET [126]. There are two other decay paths which occur on all fluorophores; these are the radiative decay path k_r where the fluorophore emits a photon and the non-radiative decay path, where energy is lost by interactions with the environment, as given by the non-radiative rate k_{nr}. There is a reciprocal relationship between fluorescence lifetime and energy transfer rates such that:

$$\frac{1}{\tau_D} = k_r + k_{nr} \qquad and \qquad \frac{1}{\tau_{DA}} = \Gamma_{DA} + k_r + k_{nr} \tag{6}$$

The two equations in (6) above can be substituted into the classic FRET efficiency equation (equation 1.3-4) to yield the following equation, equation 1.3-6:

$$E = 1 - \frac{\Gamma_D + k_r + k_{nr}}{k_r + k_{nr}} \tag{7}$$

Equation 7 can be further simplified yielding (8) below:

$$E = \frac{\Gamma_{DA}}{\Gamma_{DA} + k_r + k_{nr}} \tag{8}$$

Equation 1.3-7 describes the same FRET efficiency discussed previously within this chapter but now in terms of the energy transfers for two-fluorophores undergoing FRET instead of the usually measured lifetimes. We can then extend this single equation into a set of equations that can be used to determine interaction rates:

$$\begin{aligned} E_{AB} &= \frac{\Gamma_{AB}}{\Gamma_{AB} + k_r + k_{nr}} \\ E_{BC} &= \frac{\Gamma_{BC}}{\Gamma_{BC} + k_r + k_{nr}} \\ E_{AC} &= \frac{\Gamma_{AC}}{\Gamma_{AC} + k_r + k_{nr}} \end{aligned} \tag{9}$$

Where AB describes the FRET transfer between the first donor (A) and the first acceptor (B), BC describes the FRET transfer between the second donor (B) and the second acceptor (C), and AC describes the FRET transfer between the first donor (A) and the second acceptor (C) (figure 1.3-9).

As the donor fluorescence lifetimes scale with the FRET efficiencies, the total transfer rate increases as the FRET transfer rate increases proportionally. The time the donor electron spends in the excited state before being emitted decreases [107]. Thus, lifetime measurements provide a valuable tool for elucidation of the de-excitation rates acting on the donor. Measured FRET rates are linear and cannot be added to lifetimes as the radiative, and non-radiative decay pathways do not scale with increased FRET [107]. However, from the measured lifetimes of the donor alone and donor + acceptors 1 and 2 in isolation, we can construct a theoretical transfer rate which should be the reciprocal of the lifetime measured for the construct with one donor and two acceptors [126].

$$E_{A|ABC} = \frac{\Gamma_{AB}}{\Gamma_{AB} + (k_r + k_{nr})} + \frac{\Gamma_{AC}}{\Gamma_{AC} + (k_r + k_{nr})} \tag{10}$$

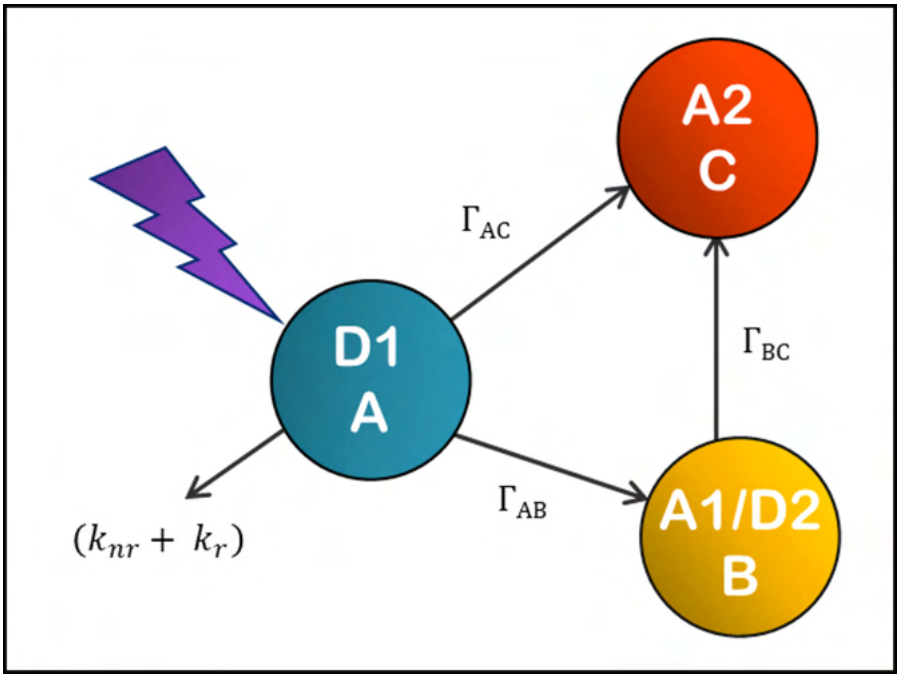

Figure 1.3.0.9: ***One-donor, two-acceptor Three-colour FRET model:*** *A Scheme to illustrate the energy transfers within a one donor-two acceptors three-colour FRET system.*

Where $A|ABC$ describes the lifetime of the first donor mTFP1 or mTurq2 in the three-colour system, $E_{A|ABC}$ describes the total FRET efficiency of the two FRET interactions which simultaneously occur on the donor, and Γ_{AB} and Γ_{AC} are the two coupled FRET interactions between the first donor and the two acceptors, respectively.

Tension Sensing and Force Measurement with FRET

Cells must generate mechanical forces while simultaneously sensing, adapting, and responding to mechanical signals, which are vital for many developmental, homeostatic, and physiological processes [142, 143]. In this dynamic, physical world, cells have evolved various mechano-sensitive strategies and mechanical signalling networks to respond to various challenges. Evidenced in the numerous cellular pathways which force sensing and responding to are just as crucial as protein interactions in pathways such as cell migration, motility, mitosis, and cytokinesis. Failure of critical force-dependent interactions have been linked directly to the dysregulation of a wide range of developmental and homeostatic pathways [143, 144]. A key issue in understanding the molecular mechanisms, which, when fail, give rise to disease and pathological conditions are essential for developing a more precise and

informed understanding of how mechanobiology plays a crucial role in the normal physiology of cells and tissue [145]. Crucial as these processes are, the underlying mechanisms of how cells continuously sense and respond to the various physical stimuli they are exposed to are often not well understood. Several novel techniques have been developed to visualise and quantify the intra- and inter-molecular forces that act between proteins within cells. This has been primarily achieved with advances in the last 20 years of genetically encoded molecular tension sensors which have allowed for the direct detection and quantification of piconewton scale (pN) forces between proteins in living cells [142, 145, 146].

The most used techniques for force sensing include atomic force microscopy (AFM), traction force microscopy (TFM), and optical tweezers. AFM and optical tweezers have been used extensively to elucidate specific mechano-sensitive conformational changes within purified proteins *in vitro (*Figure 1.3-10 panel b). Several studies have used optical trap and AFM-based techniques to pull on entrapped proteins, yielding a force measurement of tensile strength as protein domains are pulled apart [146]. TFM techniques have been utilised to show how much tractional force motile cells apply to specific surfaces [145, 147]. Fluorescence-based techniques which utilise FRET as an indicator of protein-protein inactions, such as FLIM, have also been extensively used and have the added advantage of being used in live cells; these are required to be genetically encoded and therefore have a predefined force-sensing range. The combination of several approaches generally offers the most effective methodology; for example, simultaneous AFM and TFM [148] measurements, but co-applications with genetically encoded probes [5, 130, 149] can obtain the most detailed insights into complex dynamic mechanobiological processes.

Genetically encoded molecular tension sensors are designed around a central tension sensor module (TSM) comprising a flexible linker separating two fluorescent proteins or dyes *(*Figure 1.3-12 panel a). The TSM is then typically encoded within a force-sensitive molecule such as vinculin or talin in FAs [50, 130, 149]. When the TSM containing mechano-sensitive protein experiences an applied force, the distance between the FPs extends reversibly in response to mechanical force as they separate. The FRET efficiency decreases, which can be determined with various microscopy methods, most notably ratiometric FRET imaging and FLIM [50, 149, 150].

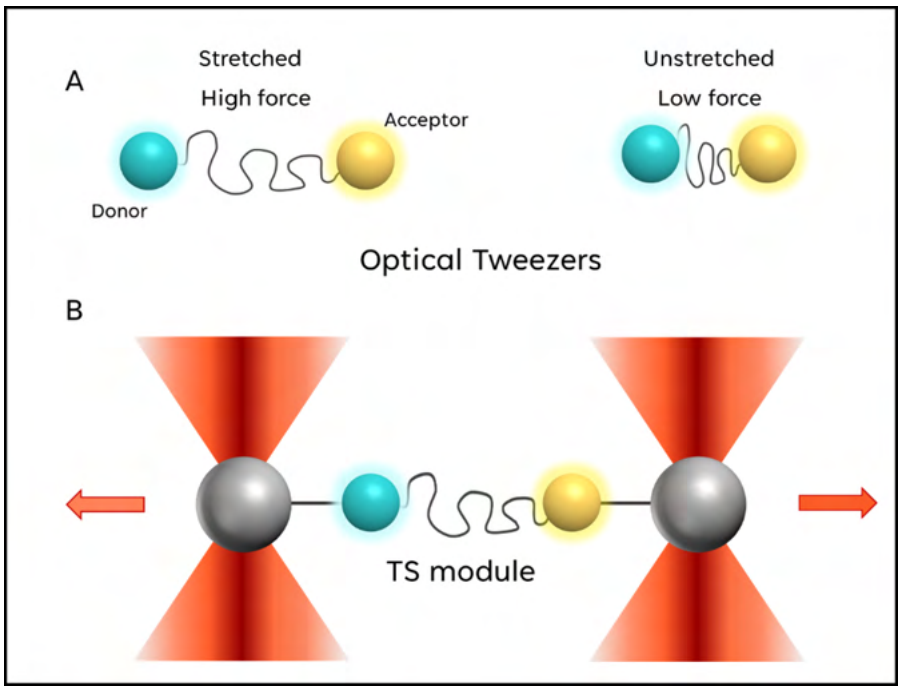

Figure 1.3.0.10: ***Basic design principle of genetically encoded FRET-based Tension sensing Modules:*** *A) A TSM comprising of a mTurq2-mVenus FRET pair connected by a force-sensitive linker peptide, that extends applied mechanical force. (B) Optical tweezer–based single-molecule experiment, which can be used to characterise force-dependent unfolding of TSMs.*

A broad selection of force-sensing linkers is required to sufficiently cover the total spectrum of force sensitivities within force-transducing molecules (see Table 1.3-1 below for details). Early genetically encoded molecular tension sensors were based on initial observations of elastic molecules such as single-stranded DNA (ssDNA) [150], which can act as a pN force sensor when inserted between fluorescence dyes. Other linkers were later found and developed that used short, comparably stiff peptide linkers with similar pN force ranges, mainly comprising α-helixes or spectrin repeats [151]. One of the most popular tension sensors is the TSMod, based on a 40-amino acid peptide linker comprising a 5 amino acid sequence repeated eight times; this linker was derived from the spider silk protein flagelliform. The flagelliform linker (or TSMod-F40) gives TSMod spring-like reversible qualities and enables force measurements at 1-6 pN [130, 149]. This linker and other similar flagelliform-based linkers have been well-calibrated using optical trap experiments [130, 149] this knowledge allows for a simple equation to convert the distance between the two FPs in the TSMod to determine the applied force acting upon the mechano-sensitive protein of interest [130].

The force sensitivity range is adjusted by varying the length of the flagelliform sequence, with more repeats of the five-amino acid sequence (GGPGA) yielding a lower force and narrower range, only 1-5 pN for the F50 TSMod. In contrast, the F25 has the broadest dynamic range at 2–11 pN [130]. These spring-like sensors are ideally suited to determine molecular forces in single-molecule measurements, where a distinct FRET efficiency for a single FRET pair is easily correlated with a distinct force value. However, in cells, many hundreds to thousands of TSMod encoded molecules are detected in ensemble measurements, in which signals are averaged to obtain a mean FRET efficiency and force value. This is a significant and relevant limitation because most current applications, including ratiometric FRET imaging or FLIM, determine FRET based on bulk measurements. The problem is that it usually remains unknown how many molecules are present and in what stoichiometry during a given force transduction process. A key advantage of using genetically encoded TSMs is that these can be inserted into almost any protein of interest and subsequently expressed either transiently or stably in a cell line of choice and are then used to determine how much mechanical force acts on the target molecule. Care is required when regarding the placement of the TSM within the protein of interest such that the original function of the protein is not detrimentally affected.

Table 3: *Force sensitives for common tension Sensing modules*

Name	Tension-sensitive element	Force range (pN)	Reference
F25	Flagelliform $(GPGGA)_5$	2-11	[133]
F40 (TSMod)	Flagelliform $(GPGGA)_8$	1-6	[152,153]
F50	Flagelliform $(GPGGA)_{10}$	1-5	[133]
FL	Ferredoxin-like peptide	3-5	[152]
HP35	villin headpiece peptide	6-8	[158]
HP35st	Mutated villin headpiece peptide	9-11	[158]
sstFRET	Spectrin repeats	1-5	[156]
TSMod-like	$(GGSGGS)_n$	Low pN range	[159]
StFRET	α-Helix	pN range	[160]
cpYFP	Chromophore & pN range	Low pN range	[161]
cpstFRET	Conformation sensitve	5-7 pN	[160]

The vinculin Tension Sensing Module (Vinculin-TSMod) was the tension sensing biosensor used extensively in this thesis and is shown below (figure 1.3-11). The vinculin-TSMod was a kind gift of Prof. Carsten Grashoff [149] (University of Münster) in which Teal and An extendable 40 amino acid flagelliform linker $(GPAGGA)_8$ derived from spider silk [130] separates Venus

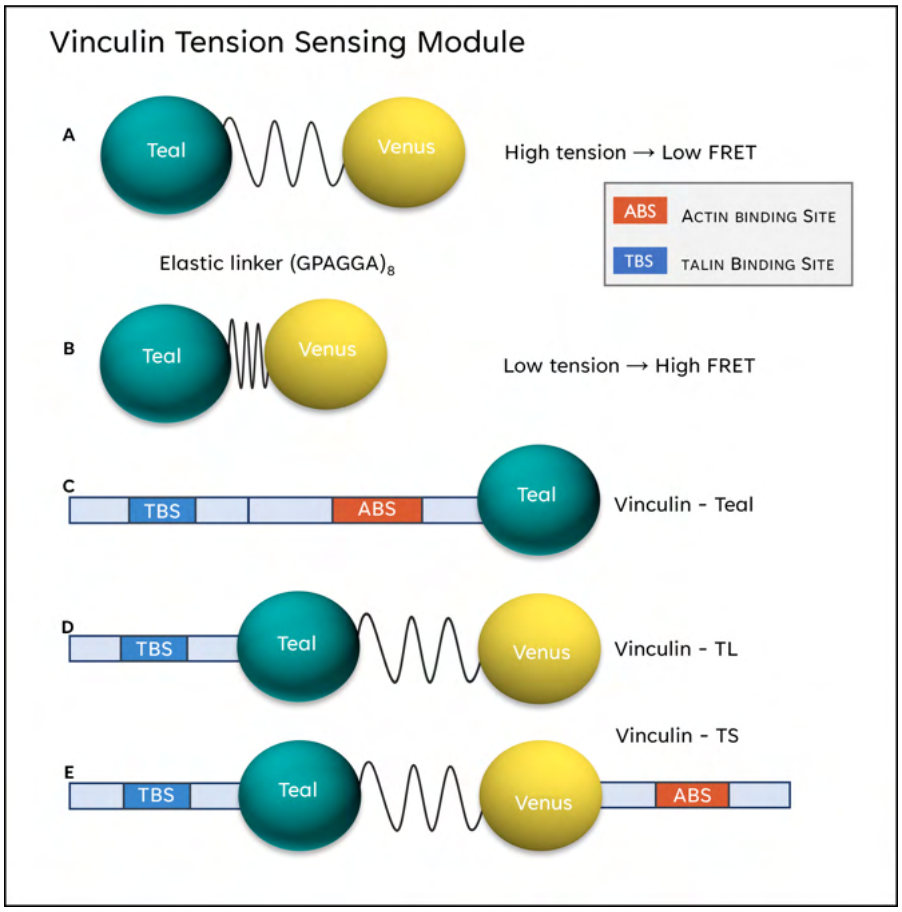

Figure 1.3.0.11: ***Illustration of the Vinculin Tension Sensing Constructs:*** *Diagram showing the structural components of the three Vinculin Tension Sensing biosensors. A) depicts the Vinculin-Tension Sensing Module Vinc-TSMod, which is comprised of Teal and mVenus Fluorescent proteins separated by Flagelliform linker (GPAGGA)8 in a high-tension, low FRET conformation. B) shows the same Teal-Venus TSMod but in low tension, high FRET conformation. C) illustrates the C-terminal labelling of vinculin with a teal FP as a donor-alone control. D) shows the same Teal-Venus TSMod cloned within a truncated 'Tensionless' vinculin construct. E) Shows the Teal-Venus TSMod inserted within full-length Vinculin at amino acid 883 (within domain 3).*

Fluorescent proteins. The flagelliform linker comprises a a repetitive motif that forms an entropic nanospring capable of measuring forces between 1-6 pN while extending from 2.1 to ≈10.0 nm [130, 152]. The TSMod was inserted into vinculin at amino acid 883 to produce the Vinculin-TS construct (panel E in Figure 3.2.7-1) and inserted into a truncated (tail-less) vinculin control construct to produce the Vinculin-TL construct (panel D of the same figure). The basic concept is straightforward, vinculin must bind to talin at its N-terminus and actin at its C-terminus, and mechanical force loaded onto vinculin causes the autoinhibited, coiled protein to extend. Extending separates the two fluorophores, which will be observed as a reduction in FRET as the distance between the FPs increases.

1.4 Aims of the thesis

There are three core aims of this thesis that I am determined to research, explore, and investigate. The first is to determine if the *in vitro* interaction between RIAM and vinculin can be detected and characterised *in vivo* using a range of biochemical and biophysical assays. Work published by the Goult group [37] (the University of Kent at Canterbury) identified a real interaction between the N-terminus of RIAM and the N-terminus of vinculin via gel filtration of purified N-terminal domains. Nevertheless, this interaction has not been characterised *in vivo,* nor do we know if this is physiological. My first objective is to conduct a series of co-immunoprecipitation and FLIM experiments to see if an *in vivo* interaction can be found. I then intend to investigate whether vinculin-RIAM binding requires actin by using a specific Rho-associated kinase (ROCK) inhibitor, H-1152. I want to determine if, by turning over the FAs, I can detect an increase in the interaction. I also want to explore the relationship between the intracellular mechanical force acting on vinculin and if it is required for RIAM binding.

The second aim is to develop a new FRET-based assay that would be used to determine whether multiple fluorescently labelled proteins are bound together in a single complex at a specific time point and location. Essentially, a methodology for determining multi-protein complex formation, FRET-Cascade. FRET-Cascade is an analytical approach used with TCSPC-FLIM to identify the individual FRET components in a complex system and show which fluorescently tagged proteins are directly interacting at specific locations in the cell and how this evolves over time. This will be achieved by purifying the fluorescent proteins alone, in pairs and as a triplet; additionally, through site-directed mutagenesis, I will create a non-fluorescent mVenus protein which does not fluorescence and cannot function as a FRET acceptor either. I hope to use a broad range of biophysical and biochemical techniques to fully characterise the three-colour model before expressing the same constructs in mammalian cells.

The third aim is to combine the two previous sets of objectives and apply the multi-colour FRET model to solve questions set around intracellular tension, specifically across vinculin, in developing focal adhesions while concurrently furthering our understanding of FA proteins are recruited to the lamellipodium. Additionally, to better understand to what extent the putative vinculin-RIAM interaction plays in recruitment and adhesion assembly.

There are several questions I aim to answer in this manuscript. I want to determine if the vinculin Tension Sensor is in an open or closed conformation when RIAM is bound to vinculin. Specifically, does RIAM only associate with the auto-inhibited form of cytoplasmic vinculin? This will be achieved chiefly through TCSPC-FLIM imaging of fixed cells and ideally through live-cell TCSPC-FLIM imaging. Furthermore, by applying the three-colour model to the Vinculin-TS + mScarlet-RIAM data, I hope to formulate a new hypothesis concerning where and when RIAM and vinculin occur in the cell.

2

MATERIALS AND METHODS

2.1 Cell Culture, Transfections, and Pull-downs

2.1.1 Cell Lines and Passaging

Vinculin null Mouse Embryonic Fibroblasts, MEFs were cultured in a complete growth media DMEM (Table 18). The MEFs were a kind gift from Prof. Maddy Parsons and were grown typically in a T75 flask and incubated in a water-jacketed incubator at 37 °C and 5% CO_2. The MEFs were routinely tested for mycoplasma and were passaged at approximately 70% confluency, aspirating the old growth media and washing the cells thoroughly with 8 mL of sterile Dulbecco's phosphate-buffered saline (PBS) (Table 18). The cells were then incubated with 2 mL of (0.25%) Trypsin-EDTA (Thermofisher) for 5 minutes at 37 °C. Once detached, the trypsin was inactivated with 8 mL of fresh growth media. The cell-media solution was thoroughly mixed to prevent aggregation. If a precise cell count was required, a 10 μL sample was taken and introduced to a disposable haemocytometer. The observable window on the haemocytometer had a volume of 1 μL. A Leica DM IL LED microscope was used to view the cells in the haemocytometer; a cell count was conducted. The total cell count was then multiplied by 1,000 to give a concentration of cells in one mL. If a simple 1:10 or 1:5 dilution was required, either 1 or 2 mL of cell solution was removed from the flask of detached cells and added to a fresh T75 containing 9 or 8 mL of fresh growth media.

2.1.2 Cell Seeding

Round coverslips (13 mm diameter, Type 1.5, VWR) were washed in 70% ethanol and then rinsed in 1x PBS (Thermofisher) before being placed into each well of a 24-well TC plate, fibronectin-PBS solution (10 μg/mL) was added to each of the wells (approximately 30 μL) and incubated for 90 minutes before being removed and washed once with PBS. Adherent cells treated with trypsin and fresh growth media (described in §2.1.1) were added to the fibronectin-coated coverslips at a density of 50,000 cells per well. A further

1 mL of growth media was added to each well before mixing the cell solution with a Gilson P1000 to prevent clumping. All cells are returned to the incubator and cultured at 37 °C and 5% CO_2.

2.1.3 Lipofectamine 3000 Transfection

This protocol follows the culturing and seeding protocol and assumes that 50,000 cells per well of a 24-well tissue culture plate have already been seeded 24 hours before transfection on fibronectin-coated glass coverslips. Lipofectamine 3000 (Thermofisher) was used to transiently transfect constructs into vinculin null MEFs. Two wells were used per construct for the following protocol. In a fresh microcentrifuge tube, 2 μg of plasmid DNA was diluted in Opti-MEM (Thermofisher) before the P3000 reagent was added at 2 μL/μg of DNA; this was mixed thoroughly and incubated for 5 minutes at room temperature. In a separate microcentrifuge, a Lipofectamine 3000 master mix was made by diluting 4 μL of Lipofectamine 3000 reagent in 100 μL of Opti-MEM (4% v/v solution) for each construct used. Co-transfections were performed for FRET pairs with a 3:1 ratio of acceptor to donor DNA - see table 2.1.3-1.

Table 4: *2.1.3-1 Lipofectamine 3000 reagents and volumes:*

Construct	DNA (ng)	Conc. (ng/μL)	Vol. (μL)	P3000 (μL)	Vol. OM (μL)
GFP-vinculin	2000	715.9	2.8	4.0	93.2
Teal-vinculin	2000	500.0	4.0	4.0	92.0
GFP-Vinc + mScarlet-RIAM	3000	251.6	12.5	6.0	87.5

DNA Ratio 1: 3	Donor			Acceptor		
Construct	DNA (ng)	Conc. (ng/μL)	Vol (μL)	DNA (ng)	Conc. (ng/μL)	Vol (μL)
GFP-Vinc + mScarlet-RIAM	1000	715.9	1.4	2000	190	10.5
Teal-Vinc + mScarlet-RIAM	1000	500.0	2.0	2000	190	10.5

DNA Ratio 1: 3	Combined		
Construct	DNA (ng)	Conc. (ng/μL)	Vol (μL)
GFP-Vinc + mScarlet-RIAM	3000	251.6	12.5
Teal-Vinc + mScarlet-RIAM	3000	239.5	12.5

This was done to achieve an excess of acceptor protein to donor protein which is desirable for FRET experiments. The expectation is that adding more plasmid DNA will produce more protein. Once complete, 100 μL of the diluted Lipofectamine solution was added to 100 μL of the DNA-Opti-MEM-P3000 mix and left to incubate for 15 minutes. After which, 100 μL of the transfection solution was added to the appropriate wells (two per construct) dropwise and left to incubate for 6 hours at 37 °C. After incubation, transfection media was removed, cells were washed in PBS, and regular growth media was added. The cells were further incubated for 24 hours post-transfection before the cells were fixed and mounted.

2.1.4 Fixing Cells for TCSPC FLIM

All volumes are calculated for a 24-well tissue culture plate containing transfected cells that adhere to fibronectin-coated borosilicate glass coverslips (13 mm diameter, Type 1.5, VWR). After 24 hours of growth post-transfection, the growth media was removed, and the cells were washed once with PBS, 1000 μL per well. The PBS was aspirated, and 500 μL of fixing solution (4% PFA (Thermofisher) in PBS) was added and incubated for 15 minutes at room temperature. Once complete, the fixing solution was removed, and the well was washed with PBS before 500 μL of 0.2% Triton X-100 was added and incubated for 10 minutes at room temperature. Cells were washed with PBS before 500 μL of freshly prepared $NaBH_4$ (Sigma-Aldrich) was added at 1 mg/mL and left to incubate for 10 minutes at room temperature. This step is crucial in minimising the autofluorescence induced by PFA fixing. Once done, the cells were washed three times in PBS to ensure all traces of PFA, Triton-X 100 and $NaBH_4$ had been removed.

2.1.5 Mounting on Coverslips with Mowiol

Microscope slides were cleaned with denatured ethanol to remove any dirt or dust negatively affecting imaging and allowed to air dry. The coverslips were carefully removed from their wells and were briefly washed in a large (1000 mL) beaker of ultrapure water. This was done by dipping the coverslips in the water and briefly washing them; not removing all the PBS from the coverslips before mounting will cause phosphate crystals to form, which obscures the cells. After carefully drying the coverslips on a paper towel, 10 μL of Mowiol Mounting Solution (see Table 18) was added to the clean

microscope slide where the coverslip was to be mounted. The coverslips were then carefully placed on the slide, cells-side down. Tweezers were used to remove air bubbles by gently applying pressure to the top of the coverslip. Once all the coverslips were mounted, the slides were left to cure at 4 °C for 12 hours in the dark before imaging.

2.1.6 DNA Plasmids

All the fluorescently tagged vinculin plasmids were kindly gifted by Professor Maddy Parsons (*King's College London*) but are available on Addgene (www.Addgene.org) (Addgene reference numbers are listed in Table 2.1.6-1). The pEGFP plasmid was also provided by Dr Stephen Terry (*University College London*). The mScarlet-RIAM and mTurquoise2-talin constructs were designed by myself but were produced on my behalf by Vectorbuilder® . Table 2.1.6-1 details the origins of the plasmids used for the FRET-FLIM experiments (for additional constructs developed for our three-colour in-vitro model, see § 2.3.8).

Table 5: *2.1.6-1 Table of constructs used and their origins*

Construct	Description	Resistance	Origin
GFP-Vinculin	N-terminally labelled vinculin with GFP	Kanamycin	Addgene/ 67935
RIAM-mScarlet	C-terminally labelled RIAM with mScarlet	Ampicillin	Prof. Maddy Parsons
mScarlet-RIAM	N-terminally labelled RIAM with mScarlet	Ampicillin	C.Treacy/Vector builder
Teal-Vinculin	N-terminally labelled vinculin with mTFP1	Ampicillin	Addgene/ 55516
Vinculin-TL	Vinculin Head only with tension sensing module	Ampicillin	Addgene/ 26020
Vinculin-TS	Full-length vinculin with tension sensing module	Ampicillin	Addgene/ 26019
mVenus-Vinculin	N-terminally labelled vinculin with mVenus	Ampicillin	Addgene/ 56625
pEGFP-N1	Empty EGFP vector	Ampicillin	Dr Stephen Terry
mTurq2-talin	mTurquiose2 cloned into the neck of talin1	Ampicillin	C.Treacy/Vector builder

2.1.7 Immunoprecipitation by GFP-Trap

MEFs were seeded at 2,000,000 cells per 100 mm diameter round tissue culture dishes 24 hours before transfection. In a typical experiment, four

dishes would be prepared and two transfected with an empty vector GFP-only plasmid and two other dishes with GFP-vinculin. Transfections were carried out as outlined in §2.1.3 (Table 2.1.7 1).

Table 6: *2.1.3-1 Lipofectamine 3000 reagents and volumes:*

Construct	DNA (ng)	Conc. (ng/μL)	DNA Vol. (μL)	P3000 (μL)	Vol. OM (μL)
GFP-Vinc.	28,000	636	44.0	14	442.0
EGFP	28,000	750	37.3	14	448.7

Vol. Opti-MEM (μL)	Vol. Lipofectamine (μL)	Total .vol (μL)
1880	120	2000

Approximately 24 hours post-transfection (or once the cells had reached 60-70% confluency), one of the two dishes transfected with the GFP empty vector, and one of the two dishes transfected with GFP-vinculin were incubated for 30 minutes with 20 μM nocodazole (Abcam). All four dishes were washed in ice-cold PBS twice before adding 750 μL of fresh lysis buffer (Table 18). The lysis buffer was combined with a cell scraper to detach the cells from the dish's surface. Once liberated, the cell solution was transferred to a pre-chilled microfuge tube, which was incubated on ice for 30 minutes to allow time for the chemical lysis of the cells. During this time, a 25-gauge needle and 2 mL syringe were used to encourage cell lysis through mechanical force by pipetting the solution through the narrow-gauge needle. The cell lysate solution was centrifuged at 17,100 g for 10 minutes at 4 °C, the resulting cleared lysate was kept on ice, and the cell-debris pellet was discarded. The *Total Input* sample was made by taking 20 μL of the cleared lysate for each pull-down reaction and mixing it with 20 μL of 2x Laemmli buffer (Table 18). These were then boiled at 95 °C for 10 minutes before running out on an SDS-PAGE.

In parallel, 25 μL of ChromoTek GFP-Trap® Magnetic Agarose beads were washed in 500 μL of dilution buffer (Table 18) before being aspirated; this was done three times for each 25 μL aliquot of magnetic beads. For each pull-down reaction, 500 μL of cleared cell lysate was added to 25 μL of washed GFP-Trap® magnetic beads and 500 μL of dilution buffer. The bead-lysate solution was left to mix on a rotational mixer for 2 hours. Once the incubation period had finished, magnetic beads were separated from the cell-lysate solution using a magnetic rack, the cell-lysate solution was discarded, and the beads were washed three times with wash buffer (7-1). Finally, 20 μL of

2x Laemmli buffer was added to the washed beads; these were boiled for 10 minutes before running out on a 3-8% gradient SDS-PAGE for analysis.

2.1.8 SDS-PAGE & Western Blot

The following was (in part) adapted from Laemmli [153], who originally demonstrated the principle of polyacrylamide gel electrophoresis (PAGE) for the separation of proteins by molecular weight. Towbin [154] originally demonstrated the principle of electrophoretic transfer of proteins from a polyacrylamide gel to a nitrocellulose membrane. A single pre-cast 3-8% Tris-Acetate NuPAGE gradient gel was used to separate proteins isolated from an immunoprecipitation experiment. However, a pre-cast 10% Bis-Tris gel was used when separating purified proteins. Both were loaded the same way into an XCell SureLock^{TM} mini-cell (Invitrogen) electrophoresis tank and filled with either Tris-Acetate SDS running buffer or MOPS SDS-PAGE running buffer for either Tris-Acetate or Bis-Tris gels respectively, (Table 18). Samples prepared in 2x Laemmli buffer were boiled at 95°C for 10 minutes and, once cooled to room temperature the samples were loaded onto the SDS-PAGE. Once all samples were loaded onto the gel, the gel was then run initially at 120 V for 20 minutes until the gel front had exited the stacking gel when the voltage was increased to 200 V and ran for a further 60 minutes or until the dye front had exited the resolving gel. After the SDS-PAGE had run, gels not blotted were removed from their cassettes and emerged in Coomassie Blue colloid stain for 1 hour before washing in warm water and imaged on a G-sys Bioimager. Gels that were to be transferred as part of a western blot was disassembled, and the gel containing the separated proteins was removed and sandwiched between blotting paper and a 7.5 x 8.5 cm sheet of 0.45 μm nitrocellulose membrane. Once the transfer cassette had been loaded with the gel, membrane and blotting sheets and placed in the XCell SureLock^{TM} electrophoresis tank, tank was filled with NuPAGE transfer buffer and run at 100 V, 4 °C for 120 minutes. After the transfer was complete, the nitrocellulose membrane was initially washed in 0.1% TBS-Tween (TBS-Tw); the membrane was then placed into a solution of 5% milk in TBS-Tw (w/v) blocking solution for one hour while under gentle agitation (rocking at 60 rpm, orbital shaker). Once complete, the blocking solution was removed, and the primary antibodies were added (Table 19) before returning to the rocker for approximately 16 hours (overnight). The primary antibodies were removed, and the membrane was thoroughly washed in TBS-Tw three times before fluorescently tagged secondary anti-

bodies were added (Table 2.1.8) and incubated at room temperature for 1 hour at 60 rpm. Once complete, the secondary antibody was also removed, and the membrane was washed three times in TBS-Tw before a final wash in TBS and then imaged with the Odyssey CLX (Li-Cor) imaging system.

2.1.9 Protein Assay (Lowry method)

This protocol was adapted from Lowry [155], who originally introduced this method of protein concentration determination using the Folin–Ciocalteu reagent (a mixture of phosphotungstic acid and phosphomolybdic acid) with BSA standards. BSA standards were prepared in triplicate, from which a standard curve was made, facilitating a method to determine the concentration of our unknown samples. Determining the total protein concentration of a cell lysate sample is typically done to ensure a consistent loading concentration of total protein in each well of the gel and any differences in protein expression levels are not due to inadequate loading of cell lysates.

Into a single well of a 96-well tissue culture plate, 10 μL of each BSA standard was loaded in triplicate. In separate wells, 10 μL of each sample to be tested was also loaded in triplicate. From the DC (detergent compatible) protein assay kit (Bio-Rad), 1000 μL is taken from solution A (an alkali solution of Cu^{2+} ions) and is mixed with 20 μL from reagent S; this is enough for reactions 40 reactions (13 cell lysate or fluorescent protein samples in triplicate). Once mixed, 25 μL of this mixture is added to each well containing either a BSA standard or a protein sample. 200 μL of DC protein assay solution B (containing the Folin–Ciocalteu reagent) is added to each well containing a testing sample. The samples are then incubated at room temperature for 15 minutes. The POLARstar Omega plate reader was then used to quantifiably measure the protein in all the samples at an excitation wavelength of 750 nm. Lastly, a standard curve from the BSA samples is produced and used to calculate the amount of protein in each sample.

2.2 Imaging techniques and Microscopy

2.2.1 Live cell imaging on the Spinning Disc Microscope

MEFs were cultured in 35 mm tissue culture dishes (Ibidi) that were seeded at 200,000 cells per dish; these were transfected with GFP-vinculin using lipofectamine 3000 (see §2.1.3 for details on transient transfections with lipofectamine 3000). Once transfected, live cell dyes were then added: either SiR-Tubulin (Spirochrome) at 500 nM and Hoechst-33342 at 500 ng/mL or SiR-Actin (Spirochrome) at 500 nm and Hoechst-33342 at 500 ng /mL, these were incubated at 37°C, 5% CO_2 for 90 minutes before the cells were washed in cTBS, and then 3 mL of complete live cell imaging media was added (Table 19).

Live cell images were collected at the Nikon Imaging Centre on a Spinning Disk confocal imaging system built around a Nikon Eclipse-TI inverted microscope (Nikon) equipped with a Yokogawa CSU-X1 disk head, and an sCMOS camera (Andor, Neo), a 60x 1.40 NA Plan Apochromat VC DIC N2 oil immersion objective and a Perfect Focus System used for continuous maintenance of focus. Hoechst was excited with a 405 nm laser source, GFP-vinculin with a 488 nm laser, and the two silicon-rhodamine labelled dyes (SiR-Tubulin and SiR-Actin) were excited with a 640 nm laser. NIS-Elements (Nikon, version 5.21.03) was used for microscope control and image acquisition.

Tubulin dynamics were imaged both pre and post-the addition of 20 μM nocodazole (Abcam), and actin dynamics were similarly imaged pre and post-the addition of 10 μM ROCK inhibitor H-1152 (Invitrogen). Timelapse image series were collected at intervals of 30 seconds for a total of 30 minutes per series following the addition of the drugs, using an exposure time of 200 ms and 2x2 binning, with illumination light, shuttered between acquisitions. Images were then processed using ImageJ (FIJI).

2.2.2 Multiphoton TCSPC FLIM imaging

Transfected cells were cultured on borosilicate glass coverslips (VWR, Thickness No. 1.5) and fixed in 4% PFA 48 hours post-transfection. Subsequently, the cells were treated with 0.2% Triton-X and 1 mg/mL $NaBH_4$ before mounting onto coverslips with Mowiol® -188 (see §2.1.1-2.1.5).

The Multiphoton-FLIM TCSPC (Time-Correlated Single Photon Counting) imaging system was built around a Nikon Eclipse Ti-E microscope fitted with a

60x 1.30 NA Nikon Plan-Fluor oil objective and an 80 MHz Ti-sapphire laser (Chameleon Vision II, Coherent) tuned to 875, 925 or 950 nm for two-photon excitation of mTFP1, GFP or mVenus.

Photons were collected using a 482/25 nm emission filter for mTFP1 (FF01-482/25-25, Semrock™), 515/17 nm emission filter for GFP (FF01-517/20-25, Semrock™) or a 525/25 nm emission filter for mVenus (FF01-524/24-25, Semrock™) and detected using a hybrid Photomultiplier detector (HPM 100-40 hybrid, Becker & Hickl GmbH). Laser power was adjusted to give average photon counting rates of the order 10^4 to 10^5 photons/second with peak rates approaching 10^6 photons/second. Acquisition times of 300 seconds at low excitation power was used to achieve sufficient photon statistics for fitting while avoiding either pulse pile-up or significant photobleaching. All FLIM data were analysed using [124], a time-resolved image analysis package, and were fitted with either a mono-exponential or bi-exponential Levenberg-Marquardt algorithm.

2.2.3 FLIM Data Analysis

Lifetime data was processed in *TRI2*, a Time-Resolved Imaging software package developed in house [124] that produced histograms of pixel frequencies against photon arrival times (ns) for every FP imaged in each cell condition and experiment. A simple Python script (written by me, §7.2) was used to import the histograms for each cell in each experiment into a single data frame, and an intensity-weighted average lifetime was calculated for each cell imaged. An average of 10 cells per cell condition were imaged for each experiment, where each cell imaged in each condition was given an equal weighting. Average lifetimes per condition were then calculated and finally normalised to produce a distribution of fluorescent lifetimes. The average peak lifetime was then picked, and from that value, the average lifetime of the condition across several (usually 3 or 4) experiments was determined.

Mean lifetimes were used to produce graphs illustrating the difference specific acceptors had on donor lifetimes and for statistical testing. Specifically, the *Shapiro-Wilk* test for normality was used first to show that the lifetime distributions were not suitable for parametric testing such as T-tests or ANOVA, but non-parametric tests would be more suitable. Following this, a Two-Sample *Kolmogorov-Smirnov* test (non-parametric) was applied to each donor and acceptor pair in an experiment. This statistical test was used to

compare a test distribution (donor + acceptor) to a reference distribution (donor alone) and test the (null) hypothesis: "What is the probability that collection of samples could have been drawn from the same distribution?". In practice, this statistical test is susceptible to small changes in the two samples and is very likely to conclude that two sample distributions drawn from the same population distribution are from different populations where the distributions are under-sampled. A *Wilcoxson Rank* Sum Test is also calculated for each FRET pair in each experiment within the Python script (§7.2). This statistical test differs from the 2-sample KS in that only shifts in the peaks of the sample distributions (donor alone or donor + acceptor) are required to reject the null hypothesis.

The Python script uses the average lifetimes to calculate the FRET efficiencies for each donor-acceptor pair in each experiment, which are then presented graphically and used to calculate the energy transfer rate between donor-acceptor pairs (see §7.2). The FRET efficiencies were then used to determine the inter-molecular distances between FPs in the FRET cascade model and to calculate the FRET cascade transfer rates.

2.2.4 Statistical testing

The *Kruskal-Wallis* [156] test (alternatively, one-way ANOVA on ranks), which is a non-parametric alternative to a one-way ANOVA was selected as this is the most appropriate statistical test for testing the difference between two or more non-parametric distributions, i.e., the difference between the donor only and the donor-acceptor FRET efficiency or Lifetime distributions. The *Kruskal-Wallis* is particularly beneficial as a test as used it can be used to compare several independent distributions simultaneously, which is extremely useful when comparing multiple donor-acceptor conditions with a single donor-only data set. However, it should be noted that for a single donor, donor + acceptor scenario, the *Mann-Witney* (alternatively known as the *Wilcoxon Rank-Sum* test is the most appropriate statistical test to use as this is the non-parametric equivalent to the unpaired t-test. A significant advantage of using the *Mann-Witney* or
textitKruskal-Wallis tests is that they calculate the average shift between the test distribution (donor + acceptor) and a control distribution (donor alone) [156]. In contrast to alternative non-parametric test, the two-sample *Kolmogorov-Smirnov* (KS) test compares only the cumulative distributions of the two data sets and computes a P-value dependent on, and is strongly

influenced by, the most significant discrepancy between the two. Making the 2-sample KS test overly sensitive to minor differences between the two data sets and any substantial differences in the shape, spread, or median will result in a smaller P-value, which can result in a rejection of the null hypothesis. Subsequently, this leads to the conclusion that the two data sets come from the same population or condition and are significantly different when they are not. This is a common issue associated with under-sampling, which can be a particular issue when analysing imaging data from a relatively small number of cells (10-20). One way to overcome this problem is to image more cells, as the central limit theorem would suggest that the more measurements we have per condition, the more likely the data would be normally distributed. If we were to image more than 50 cells per image, then it is likely that a simple t-test or ANOVA would be the most appropriate statistical test to use. However, this is not always practical when a FLIM image and accompanying data set of a single cell can take more than 5 minutes. If we were to take 50 images per condition with 3 conditions per experiment across only three technical repeats, we would need to image 450 cells. It is not impossible to imagine fast and with a large field of view with widefield or confocal microscopies. Nevertheless, if we are only imaging individual cells and each takes 5 minutes, then the total imaging time per data set would be more than 37 hours -hence, why there is a need to develop methods that require either the analysis of fewer cells per condition or a faster FLIM-imaging system.

3

RESULTS CHAPTER I:
CHARACTERISING THE FORCE-DEPENDENT VINCULIN-RIAM INTERACTION

3.1 Introduction to characterising the force-dependent vinculin-RIAM interaction

This chapter will introduce a novel interaction between the focal adhesion protein vinculin and the cytoskeletal protein RIAM. Previous work by the Goult group (the University of Kent at Canterbury) identified a possible interaction between the N-terminus of RIAM (amino acids 1-127) and the N-terminus of vinculin (1–258) via gel filtration of the purified N-terminal domains [37]. Using Isothermal titration calorimetry (ITC), the same group also showed that the RIAM-vinculin interaction was approximately five-fold weaker than the mutually exclusive vinculin-talin interaction [37]. They postulated that the interaction might not be biologically significant and maybe an artefact of the structural similarities found in the proteins N-termini [37].

chapter characterises the interaction of full-length, fluorescently tagged vinculin and RIAM transiently transfected in MEFs in both fixed and live cells through TCSPC-FLIM. Furthermore, immunoprecipitation methods are used to "pull down" the vinculin-RIAM protein complex from MEFs, showing that the interaction, despite its alleged weak binding affinity, is of biological relevance. Next, the orientation of the interaction is characterised to better understand how and crucially where in the cell vinculin and RIAM associate (see figure 3.1-1 below). Following this, the actin and FA dependency of the vinculin-RIAM binding is investigated, as an integral element of the actinomycin cytoskeleton, using a specific Rho-associated kinase (ROCK) inhibitor H-1152 and whether turning over FAs promotes the interaction. Inhibiting ROCK has many downstream effects, one of which is that LIM kinases activity decreases; this is significant as LIM kinases phosphorylate cofilin, which in a phosphorylated state stabilises actin filaments. A loss of functional ROCK will ultimately lead to less stabilised actin filaments, which will cause a loss

of the actomyosin cytoskeleton. This cascade is interesting as we would like to know if the vinculin-RIAM interaction is present outside FAs, nascent or otherwise. Following depolymerisation of the actomyosin cytoskeleton, if we are still able to see a FRET interaction, this would indicate that the interaction is predominantly cytoplasmic or at least not wholely exclusive to FAs. The highly selective H-1152 Rho-associated protein kinase (ROCK) inhibitor compound was used [85].

Lastly, the relationship between intracellular mechanical force, vinculin activation and RIAM binding is investigated. It is well documented that the binding availability of vinculin dramatically changes when vinculin is in an activated "high-tension" state compared to its zero-tension auto-inhibited conformation [52, 149, 157]. Using the latest literature in this field and the data presented in this chapter will allow for formulating a hypothesis for the possible mechanism through which RIAM interacts with vinculin. I then hope to refine and shape this hypothesis in later chapters to explain how the putative interaction fits into the latest thinking surrounding nascent adhesion formation and maturation.

3.2 Results I: Characterising the force-dependent vinculin-RIAM interaction

3.2.1 Co-Immunoprecipitation Studies of EGFP-vinculin binding-partners

The input fractions (whole-cell lysates harvested from the transfected MEFs) were blotted along with the proteins co-immunoprecipitated (or pulled down) with either EFGP or EGFP-vinculin (figure 3.2.1-1 panel A-C). Before harvesting, 20 μM nocodazole was added to selected dishes and incubated for 30 minutes. Nocodazole was added to investigate whether increasing FA assembly would cause a significant increase in the amount of pulled-down RIAM, suggesting that vinculin-RIAM interaction is predominantly associated with nascent adhesions. Whereas a reduction in pulled-down RIAM could suggest the opposite effect, that the interaction is primarily not in FAs (nascent or otherwise) and is predominantly associated away from the lamellipodium.

Western blotting showed, as expected, that talin is present in the MEF whole-cell lysates for both cells transfected and not transfected with EGFP-vinculin and EGFP-vinculin pull-downs but not in the control EGFP lanes (figure 3.2.1-1A). This result is expected as talin is a well-known binding partner for vinculin. Analysis of the immunoblots showed a significant increase in the mean band intensity of EGFP-vinculin transfected cells (panel E of the exact figure). There was also a slight decrease for the nocodazole-treated cells, but this was not to be significant).

Results for the RIAM co-IP (figure 3.2.1-1B) are similar; however, blotting with an α-RIAM primary antibody produced a faint band for the EGFP controls. Western blot analysis (figure 3.2.1-1F) showed a significant difference between the negative controls and the bands for RIAM in the EGFP-vinculin transfected lanes. The intensity of the RIAM band for EGFP-vinculin transfected cells treated with nocodazole is reduced compared to cells that were not treated. Potentially an important and profound result as it would suggest that de-stabilising microtubules (as a direct consequence of nocodazole) are detrimental to the RIAM-vinculin interaction, as previously discussed. This could point to the interaction being away from the lamellipodium, or at least FA-associated vinculin cannot interact directly with RIAM in the same manner as cytoplasmic vinculin. Control experiments (figure 3.2.1-1C) show using α-GFP in western blots, bands for EGFP-vinculin transfected cells bands at

approximately 150 kDa corresponding to the size of EGFP-vinculin and bands at approximately 27 kDa corresponding to EGFP alone. A second control was also undertaken, where a primary antibody for α-tubulin was added to the blot to show that the beads were not cross-reacting with the primary antibodies non-specifically (figure 3.2.1-1D). The data (figure 3.2.1) indicates a specific biochemical interaction between vinculin and RIAM in MEFs. However, this interaction appears relatively weak, as indicated by *in vitro* studies of the same interaction [37]. In the next section, I will further, interrogate this interaction through another biophysical assay, two-photon TCSPC FLIM, which allows us to observe the spatiotemporal evolution of the interaction.

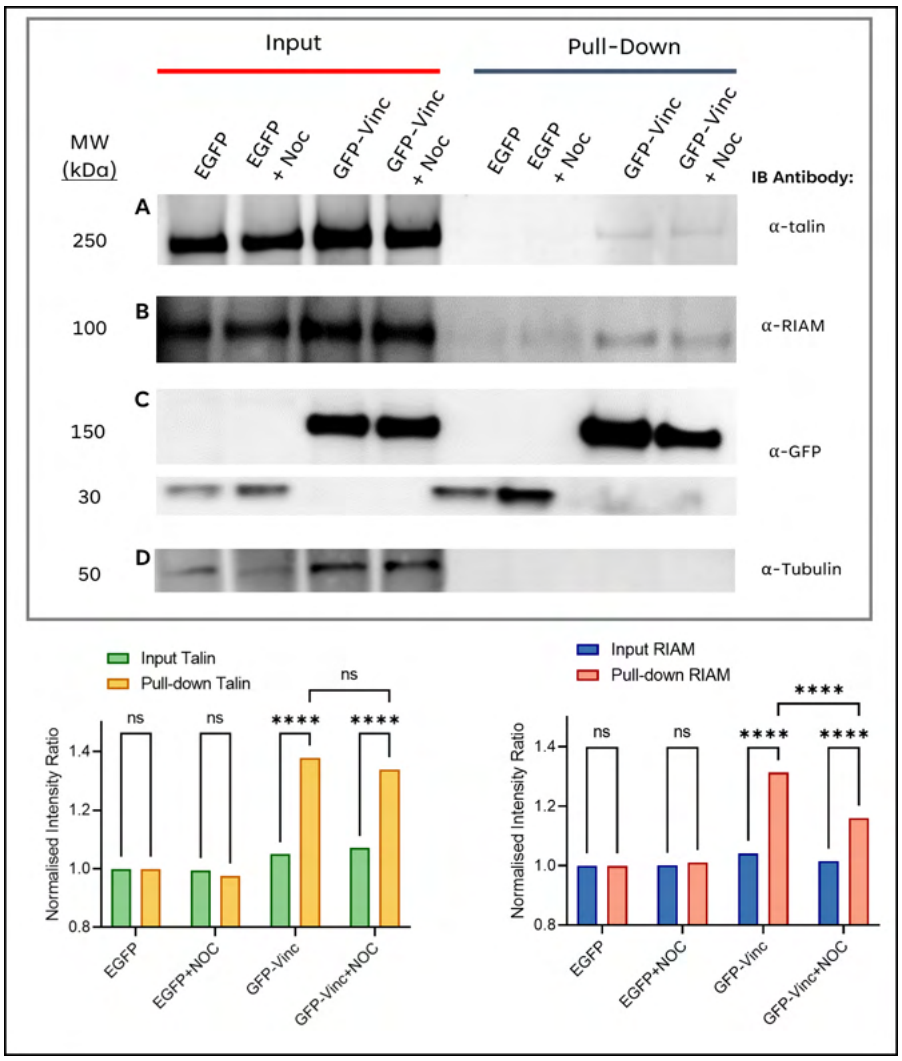

Figure 3.2.1.1: ***Co-Immunoprecipitation studies of GFP-vinculin binding partners:*** *A) co-IP of GFP-vinculin with talin, using GFP-Trap-agarose beads in the +/- 20 μM nocodazole. Immunoprecipitation (IP): α-GFP immunoblot analysis (IB) mouse α-talin primary and goat anti-mouse-HRP secondary antibody. B) co-IP of GFP-vinculin with RIAM, using GFP-Trap-agarose beads +/- 20 μM nocodazole. IP: α-GFP and IB: sheep α-RIAM primary and DAS-HRP secondary antibody. C) Control co-IP of GFP-vinculin against a GFP antibody, GFP-Trap-agarose beads +/- 20 μM nocodazole. IP: α-GFP and IB rabbit α-GFP primary and goat anti-rabbit -HRP secondary antibody. D) Control IP and blot of mouse α-tubulin primary and goat anti-mouse-HRP secondary antibody in the +/- 20 μM nocodazole. For all Co-IPs cells expressing EGFP only were used as control +/- 20 μM nocodazole. E) Graph of showing the ratio of normalised band intensity for the co-IP blotted for RIAM against the various transfected cell conditions. F) Graph showing the ratio of normalised band intensity for the co-IP blotted for talin against the various transfected cell conditions. For both graphs E and F, the blots were repeated three times and the error bars represent the standard deviations. Independent t-test, n=3, P-values ≥ 0.123 ns, ≤ 0.0332 (*), ≤ 0.0021 (**), ≤ 0.0002 (***), ≤ 0.0001 (****)*

3.2.2 FRET by FLIM of EGFP-vinculin with RIAM-mScarlet and mScarlet-RIAM

In this section, I seek to determine whether the N-terminus of vinculin interacts with the N or C terminus of RIAM. To do this via quantitative FRET imaging by FLIM, I decided to use two different FRET constructs, specifically, EGFP-vinculin with mScarlet-RIAM and EGFP-vinculin with RIAM-mScarlet. The only difference between the two FRET pairs is which termini of RIAM the mScarlet is labelled; this is important in understanding if this biochemical interaction is as previously described *in vitro* between RIAM (amino acids 1-127) and the N-terminus of vinculin (1–258).

Results are summarised and presented in figure 3.2.2-2; panels G with H and I show lifetime data and that the average fluorescence lifetime is longest in panel G, representing the donor alone (control) condition, than either of the two donor-acceptor conditions indicating that FRET occurs between the EGFP-vinculin donor and the two mScarlet labelled RIAM acceptors. This can be seen in the blue colour of the FAs in the donor alone (panel G) compared to both the acceptors (panels H and I) and the longer average lifetime presented in the summary table (panel N). A table summarising the critical values taken from further analysis of the fluorescence lifetime data is presented in panel N. This data indicates that cells co-transfected with both EGFP-vinculin and mScarlet-RIAM had the shortest fluorescence lifetime compared to cells transfected with EGFP-vinculin alone. FRET efficiencies were calculated for the two donor-acceptor pairs; the EGFP-vinculin & mScarlet-RIAM FRET pair exhibited a greater FRET efficiency (12.36 ± 1.48 %) compared to the EGFP-vinculin & RIAM-mScarlet FRET pair (18.99 ± 2.34 %). This is a crucial finding since FRET efficiency is related to separation distance and enables us to conclude that the separation distance between the EGFP and mScarlet FPs must be shortest for the FRET pair with greater FRET efficiency. The distribution of average FRET efficiencies (figure 3.2.2-2 panel M) illustrates the significant difference between the donor alone and both donor + acceptor FRET pairs.

Furthermore, there is a significant difference between the mScarlet-RIAM and RIAM-mScarlet transfected cells, demonstrating, through differential labelling of the acceptor, identification of the orientation of the interaction. Therefore, the N-terminus of RIAM is more likely to be in direct contact with the vinculin N-terminus, previously indicated [37]. This finding strengthens the argument for a biological interaction between vinculin and RIAM between the

N-terminal head domain (amino acids 1–258) of vinculin and the N-terminal talin binding domain of RIAM (amino acids 1-127).

It should be noted that the position where the FP tag is placed can significantly affect the binding of a tagged protein to another protein, especially one in complex with many others. There is a danger of adding an FP, which is usually sizeable at approx. 40 kDa can have a significant and undesirable effect in preventing an interaction or, worse, possibly weakening that interaction due to the introduced steric hindrance that the FP can place on the binding within a busy, crowded local environment. This potentially could result in a false positive, such that we might conclude that there is more significant energy transfer between donor-acceptor FRET pairs when we have only perturbed the original system in such a way that a lower FRET efficiency is observed because of poor FP placement and not due a greater distance between FPs. However true, I do not believe this to be the case here as there is already evidence of an N-terminal to N-terminal interaction between vinculin and RIAM, which would result in a shorter distance between tagged FPs which would subsequently yield a greater FRET efficiency compared to a C-terminally tagged RIAM.

FRET efficiency distributions (Figure 3.2.2-3A) for the EGFP-vinculin, EGFP-vinculin & mScarlet-RIAM, and EGFP-vinculin & RIAM-mScarlet conditions were produced from the normalised weighted lifetime histograms. These distributions were used to conduct a test for normality; this was required to select the correct statistical test to determine the significance between sampled conditions. The graphical results of a QQ plot (figure 3.2.2-3 panels B and D) and a *D'Agostino and Pearson's* test for normality, this data showed that none of the selected distributions are likely to be normally distributed with P-values < $1x10^{-6}$ for all but one. Consequently, a non-parametric test, such as a one-way ANOVA with Tukey corrections was required to test if the differences in fluorescence lifetimes were significant.

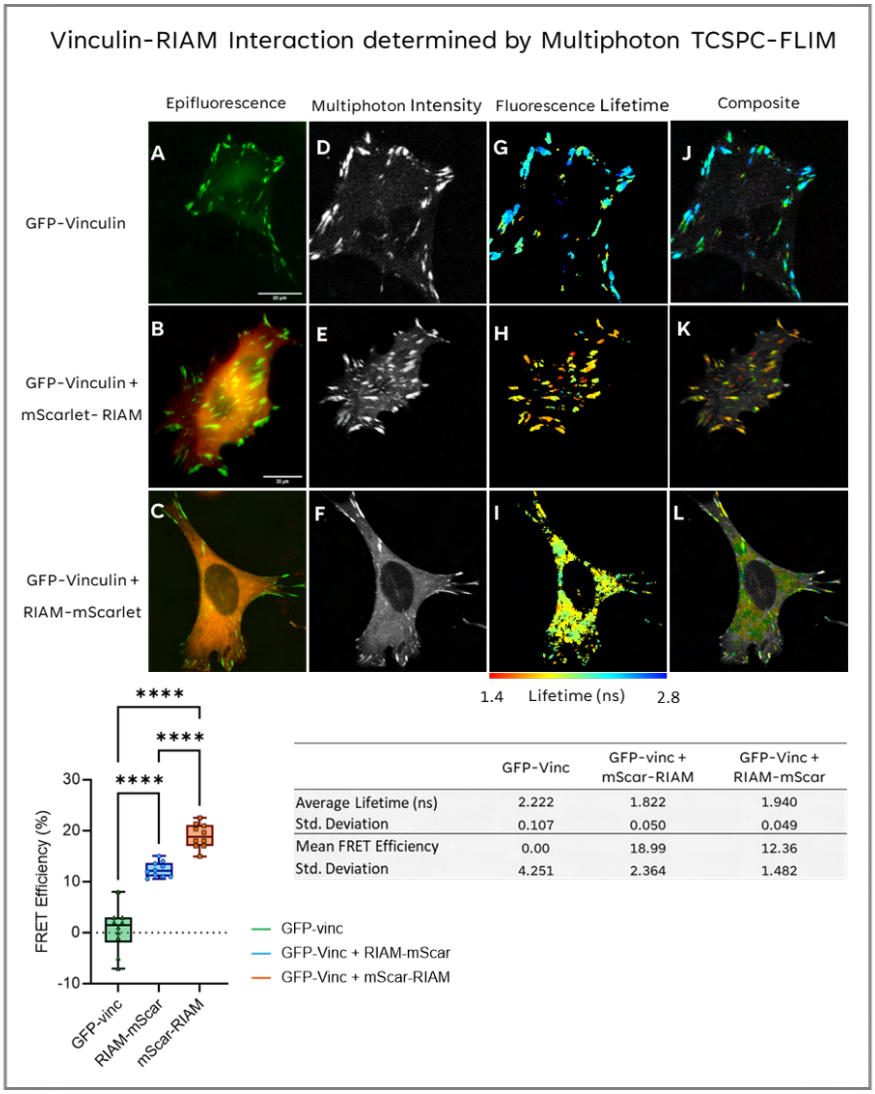

	GFP-Vinc	GFP-vinc + mScar-RIAM	GFP-Vinc + RIAM-mScar
Average Lifetime (ns)	2.222	1.822	1.940
Std. Deviation	0.107	0.050	0.049
Mean FRET Efficiency	0.00	18.99	12.36
Std. Deviation	4.251	2.364	1.482

Figure 3.2.2.1: ***Vinculin-RIAM Interaction determined by TCSPC-FLIM:*** *The donor GFP-vinculin was excited at 920 nm (TPE) for GFP. A-C) show widefield epi-fluorescence images of MEF transfected with a GFP-vinculin in isolation or with one of the two acceptors. Panels D-F) shows two-photon Intensity images, G-I) show the lifetime distribution in a typical transfected cell. Panels J-L) show a composite image of lifetime and two-photon fluorescence intensity image. M) Box and whisker plot of the average FRET efficiencies per construct. Significance was determined through a one-way ANOVA with Tukey corrections for multiple tests. N) A summary table of lifetimes, standard deviation, and FRET efficiencies. N= 10 cells imaged per condition, with P-values* $\geq$ *0.123 ns,* $\leq$ *0.0332 (*),* $\leq$ *0.0021 (**),* $\leq$ *0.0002 (***),* $\leq$ *0.0001 (****)*

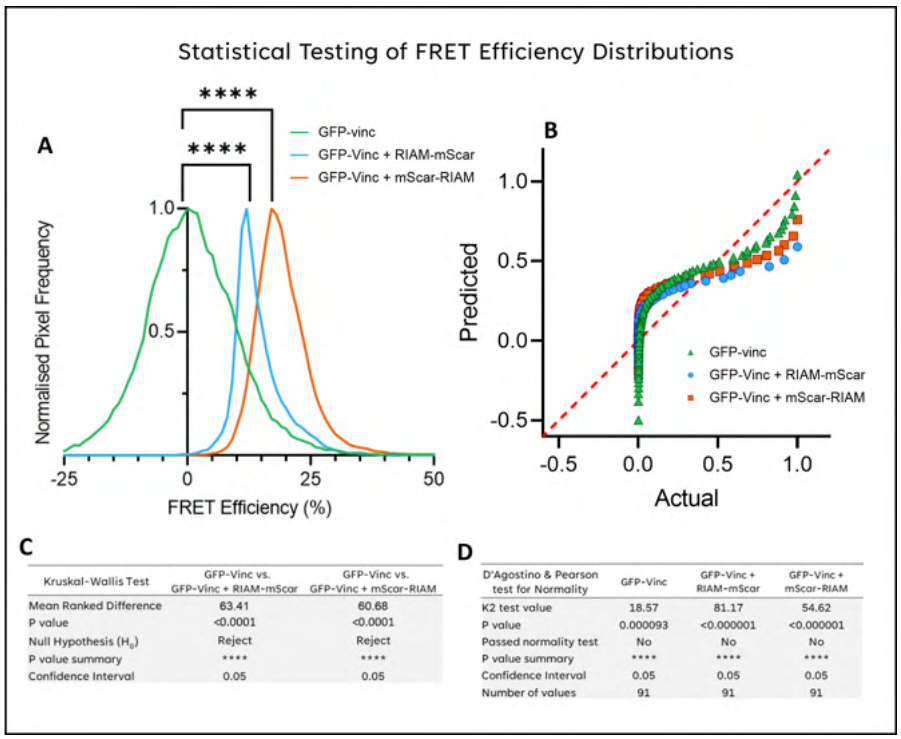

Kruskal-Wallis Test	GFP-Vinc vs. GFP-Vinc + RIAM-mScar	GFP-Vinc vs. GFP-Vinc + mScar-RIAM
Mean Ranked Difference	63.41	60.68
P value	<0.0001	<0.0001
Null Hypothesis (H_0)	Reject	Reject
P value summary	****	****
Confidence Interval	0.05	0.05

D'Agostino & Pearson test for Normality	GFP-Vinc	GFP-Vinc + RIAM-mScar	GFP-Vinc + mScar-RIAM
K2 test value	18.57	81.17	54.62
P value	0.000093	<0.000001	<0.000001
Passed normality test	No	No	No
P value summary	****	****	****
Confidence Interval	0.05	0.05	0.05
Number of values	91	91	91

Figure 3.2.2.2: ***Statistical Testing of FRET Efficiency Distributions:*** *Panel A Shows the distribution of FRET efficiencies, significant differences between the peaks determined by the Kruskal-Wallis test. B) QQ-plot showing graphically predicted versus observed measurements for the three FRET efficiency distributions. Significant deviation from the red dotted line indicates a non-normal distribution. C) The results of the Kruskal-Wallis test. D) D'Agostino & Pearson test for normality results, generating a P-value for the likely hood that the distributions are normal. Averages were calculated from three independent repeats of 10 cells imaged per condition per experiment. P-values* $\geq$ *0.123 ns,* $\leq$ *0.0332 (*),* $\leq$ *0.0021 (**),* $\leq$ *0.0002 (***),* $\leq$ *0.0001 (****)*

3.2.3 Localising the Vinculin-RIAM Interaction with two-photon TCSPC FLIM

There is a significant difference in the fluorescence lifetimes between the donor alone (EGFP-vinculin) and the three masked regions of the RIAM-mScarlet acceptors (figure 3.2.3-1, panels A-C). We can see from the summary table (panel J) that the fluorescence lifetimes and FRET efficiencies for the Focal Adhesion, Inverted Focal Adhesion and Whole-cell masks exhibit approximately the same FRET efficiencies of $\approx$ 10% (8.34 $\pm$ 3.82 %, 9.78 $\pm$ 1.84 % and 10.50 $\pm$ 1.39 % respectively, panel I). This data demonstrates that in all three masked conditions, FRET is detected between vinculin and RIAM, indicating that the interaction is not limited to the FAs but also occurs throughout the cytoplasm. This data also shows no significant difference in the amount of FRET for the three conditions. There is undoubtedly a difference in the variance between the FA-associated FRET efficiencies and the whole cell masked, but this is not significant. This finding could indicate that the interaction occurs first in the cytoplasm where RIAM associates with vinculin before shuttling its vinculin towards the leading edge of the cell within the lamellipodia where vinculin disassociates from RIAM and joins talin and the rest of the focal adhesion machinery in forming nascent complexes.

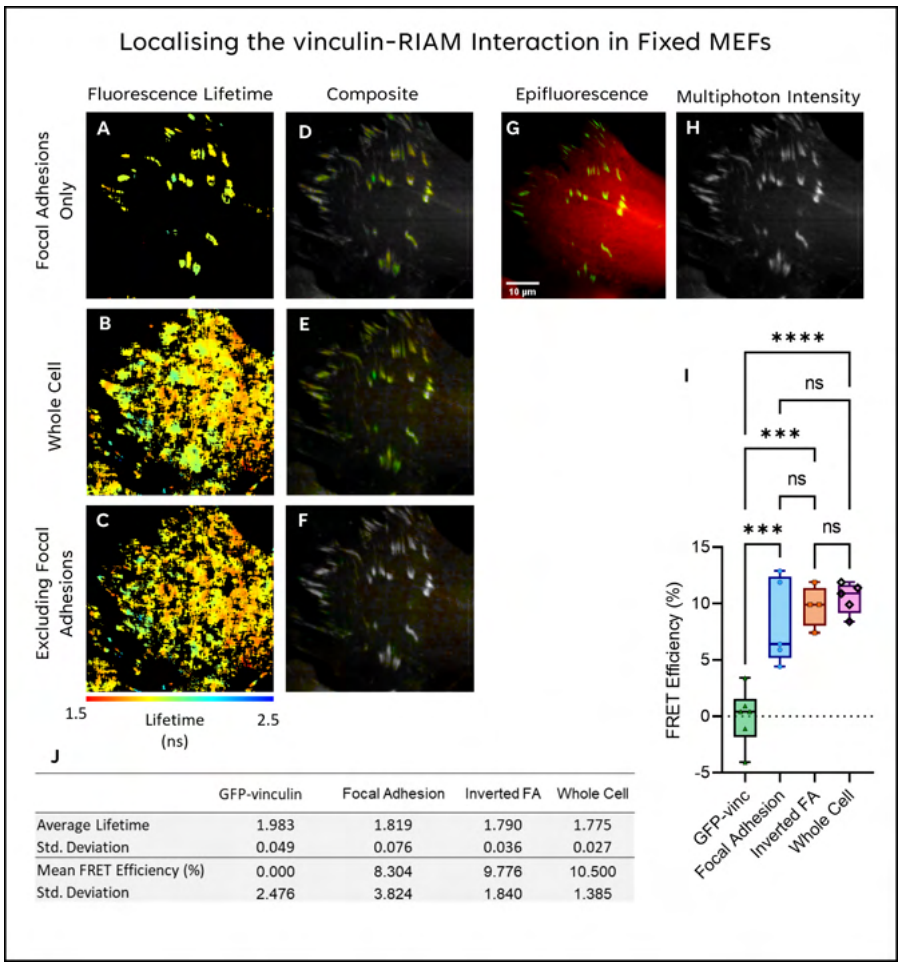

	GFP-vinculin	Focal Adhesion	Inverted FA	Whole Cell
Average Lifetime	1.983	1.819	1.790	1.775
Std. Deviation	0.049	0.076	0.036	0.027
Mean FRET Efficiency (%)	0.000	8.304	9.776	10.500
Std. Deviation	2.476	3.824	1.840	1.385

Figure 3.2.3.1: ***Localising the vinculin-RIAM Interaction in Fixed MEFs:*** *A-C) show Fluorescence Lifetime images for the same cell masked through thresholding of the two-photon intensity map for the three separate conditions: Focal Adhesions only, Whole Cell and Focal Adhesions Excluded for EGFP-vinculin + mScarlet-RIAM. Panels D-F) shows composite images for the Multiphoton Intensity images merged with the lifetime images. G) Shows the epifluorescence widefield image of the sample cell. This cell was transfected with both EGFP-vinculin and mScarlet-RIAM. H) shows the two-photon Intensity image for the same cell. I) Shows the average FRET efficiencies as a Box plot for each condition. Significance was determined through a one-way ANOVA with Tukey corrections for multiple tests. J) A summary table of lifetimes, standard deviation, and FRET efficiencies. Averages were calculated from three independent repeats of 10 cells imaged per condition per experiment. N= 10 cells imaged per condition, with P-values $\geq$ 0.123 ns, $\leq$ 0.0332 (*), $\leq$ 0.0021 (**), $\leq$ 0.0002 (***), $\leq$ 0.0001 (****).*

3.2.4 Immunofluorescence of Cytoskeletal and Focal Adhesion Proteins in the presence of Nocodazole and ROCK Inhibitor H-1152

The effect of the inhibitor can be seen in figure 3.2.4-1A which shows a cell transfected with EGFP-vinculin in green and stained with Silicon-Rhodamine-Actin (SiR-Actin) red, Hoechst-33342 blue and treated with 10 μM H-1152 for 30 minutes during live-cell imaging with a Nikon Spinning Disc Confocal imaging system (NIC@King's). We can see from panel B images that the actin filaments begin to contract and disassemble rapidly, with a notable change in appearance within the first, 5 minutes of the drug being added. As the time course proceeds, the size of the FAs reduced while the matured FAs throughout the lamella decreased in size, disappearing entirely in many places by the end of the 30-minute time-lapse. The addition of H-1152 is sufficient to reduce the size of FAs and can be used to disrupt a vinculin-RIAM interaction in FAs.

A second cytoskeletal-affecting drug was also used Nocodazole. Nocodazole is known to disrupt microtubule assembly; this has the added effect of driving the enlargement of FAs as more FA-associated proteins assemble at the leading edge. The rationale behind using this drug is to see if we get a change in the proportion of vinculin molecules interacting with RIAM when nocodazole is present. If we see more vinculin-RIAM interacting, this could mean that the vinculin-RIAM interaction is likely to occur in developing nascent adhesions, and if we do not see an increase, then it is unlikely that the interaction is formed first in the adhesion complex but may instead be formed elsewhere in the cytoplasm. Evidence of this can be seen in figure 3.2.4-1B, which shows two cells transfected with EGFP-vinculin (green) and stained with SiR-Tubulin (red), Hoechst (Blue) and treated with 20 μM nocodazole for 30 minutes during live-cell imaging with a Nikon Spinning Disc Confocal imaging system (NiC@King's). In panel B, we can see the loss of the finer microtubule network over time, especially at the leading edges of the two cells imaged. The SiR-tubulin dye only stains polymerised tubulin, so we do not see an increase in free tubulin throughout the cytoplasm; another feature to mention is that the FAs in the treated cell are enlarged after 30 minutes than those seen at the start of the time course. This is what we expect to see as FA assembly is upregulated as a direct consequence of the added drug.

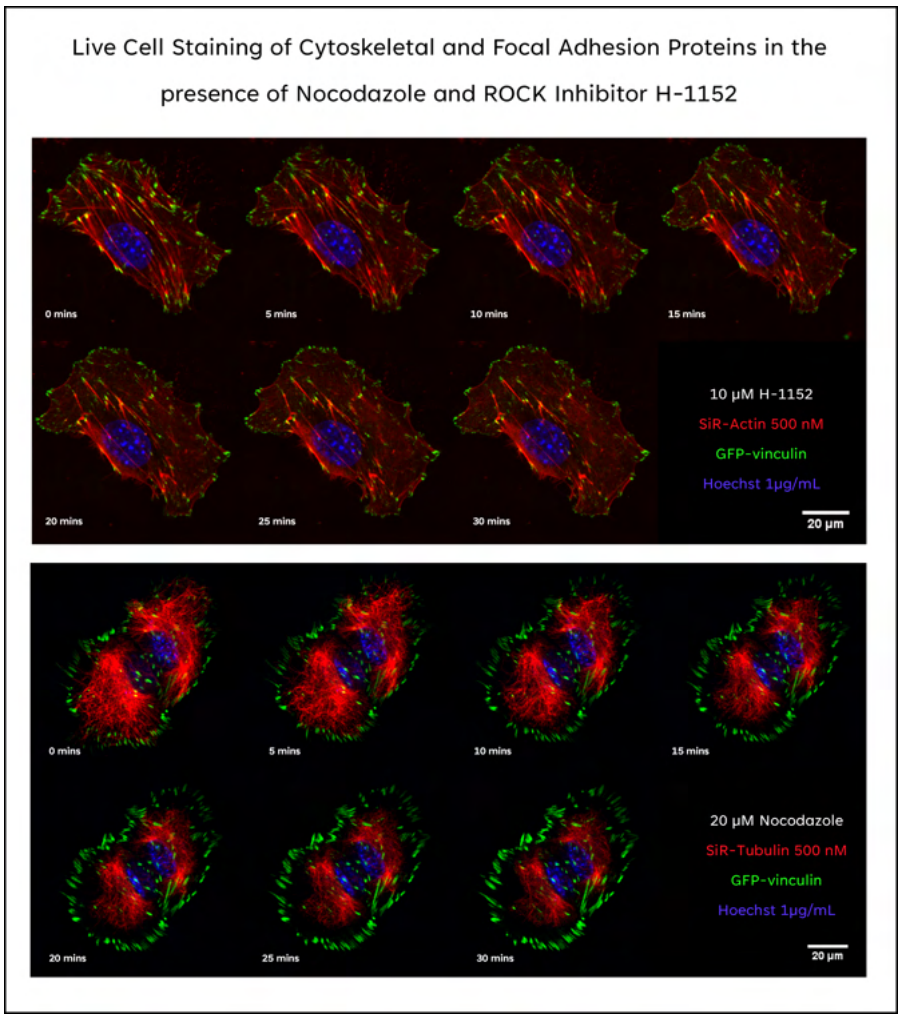

Figure 3.2.4.1: ***Live cell staining of cytoskeletal and focal adhesion proteins in the presence of Nocodazole and ROCK Inhibitor H-1152:*** *MEFs transfected with GFP-vinculin and stained either with A) SiR-Actin or B) SiR-Tubulin at 500 nM, and Hoechst nuclear stain at 1 µg/mL. Cells were treated either with 10 µM ROCK inhibitor (H-1152) or 20 µM nocodazole for 30 minutes during live-cell imaging. Imaging was conducted on a Spinning Disc Confocal imaging system (NIC@King's).*

3.2.5 Effect of Rho Associated Protein Kinase Inhibitor on the Putative Vinculin-RIAM Interaction Determined by TCSPC-FLIM

Following the live cell imaging of the previous section, two-photon TCSPC-FLIM was used to determine whether the vinculin-RIAM FRET interaction described in §3.2.2 would persist in the presence of the ROCK inhibitor, H-1152. Fluorescence lifetime images (figure 3.2-5, panels G-I) show that the FAs are bluer in colour for the donor alone panel compared to the donor + acceptor conditions (panels H and I). Indicative of a FRET interaction between EGFP-vinculin + mScarlet-RIAM with and without the ROCK inhibitor. Furthermore, we can see from the summary table (panel N) of the fluorescent lifetimes and FRET efficiencies that for the untreated cells, an average FRET efficiency of 25.09 ± 2.67 %, and for the treated cells, an average of 26.75 ± 2.56 % was calculated. This data shows a significant FRET interaction between EGFP-vinculin + mScarlet-RIAM and that the FRET efficiency for the treated cells are not significantly different to the average FRET efficiency for the untreated cells. The addition of the ROCK inhibitor has not significantly changed the lifetimes and subsequent FRET efficiencies recorded for the EGFP-vinculin + mScarlet-RIAM interaction.

Furthermore, the size of the FAs are smaller in the H-1152 treated cells compared to the control cell (panel H). This is because actin is required for nascent adhesions to mature into the larger FAs, as seen in the control cell image. Without actin, the adhesions which were present before treatment disassemble. The lack of actin stress fibres in the imaged cell is a strong indicator of inhibition, and the effects seen in the FRET interactions are because of the activity of H-1152.

The data presented in this section suggest that the vinculin-RIAM interaction is actin independent and is either a predominantly cytoplasmic interaction or that the interaction only occurs at the very leading edge of the cell, where nascent actin-independent adhesions are found. One possibility is that RIAM acts as a shuttling protein, recruiting vinculin from the cytoplasm and shuttling it to the very leading edge of the cell. It has already been shown that RIAM plays a similar role in talin recruitment [37, 64] where it binds to the auto-inhibited form of talin in the cytoplasm, recruits talin to integrins, and RIAM is believed to detach from talin once talin begins to become activated through a series of mechanosensitive conformational changes in its 3D struc-

ture. These changes in the rod structure of talin allow vinculin to bind to an active talin molecule.

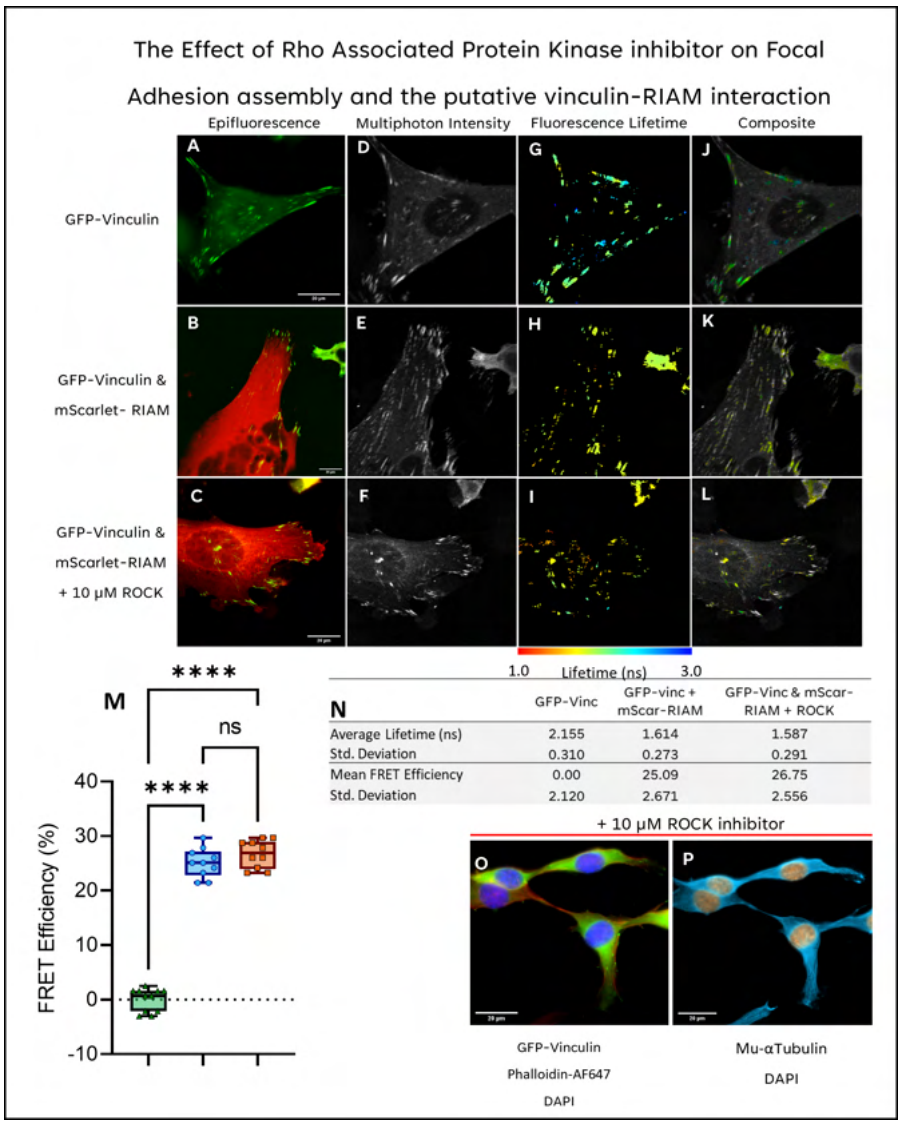

Figure 3.2.5.1: ***Vinculin-RIAM Interaction determined by TCSPC-FLIM:*** *The donor GFP-vinculin was excited at 920 nm (TPE) for GFP. A-C) show widefield epi-fluorescence images of MEF transfected with a GFP-vinculin in isolation or with one of the two acceptors. Panels D-F) shows two-photon Intensity images, G-I) show the lifetime distribution in a typical transfected cell. Panels J-L) show a composite image of lifetime and two-photon fluorescence intensity image. M) Box and whisker plot of the average FRET efficiencies per construct. Significance was determined through a one-way ANOVA with Tukey corrections for multiple tests. N) A summary table of lifetimes, standard deviation, and FRET efficiencies. N= 10 cells imaged per condition, with P-values* $\geq$ *0.123 ns,* $\leq$ *0.0332 (*),* $\leq$ *0.0021 (**),* $\leq$ *0.0002 (***),* $\leq$ *0.0001 (****)*

3.2.6 Effect of nocodazole on the putative vinculin-RIAM interaction

Two-photon TCSPC-FLIM was used to determine whether the vinculin-RIAM FRET interaction would remain in the presence of nocodazole, a microtubule inhibitor. Data collected demonstrated a FRET-based interaction for both EGFP-vinculin + mScarlet-RIAM with and without nocodazole. This data (figure 3.2.6-1) shows the average fluorescence lifetimes and FRET efficiencies (panel N) and shows the untreated cells have an average FRET efficiency of 16.83 ± 3.95 % and the treated cells an average of 18.03 ± 2.36 %. This data would suggest a significant FRET interaction between EGFP-vinculin + mScarlet-RIAM and the FRET efficiency for the treated cells is not significantly different to the average FRET efficiency for the untreated cells.

The addition of nocodazole has not significantly changed the lifetimes and FRET efficiencies recorded for the EGFP-vinculin + mScarlet-RIAM interaction. The FAs in the treated cells (panel O) are much larger than those seen in the control cell in panel A. This is because nocodazole has been shown to disrupt the assembly/disassembly of microtubules while concurrently causing the rapid assembly of FAs [158]. It has been shown that the disruption caused by nocodazole activates the integrin-dependent signalling cascade, which leads to the assembly of new FAs [158, 159].

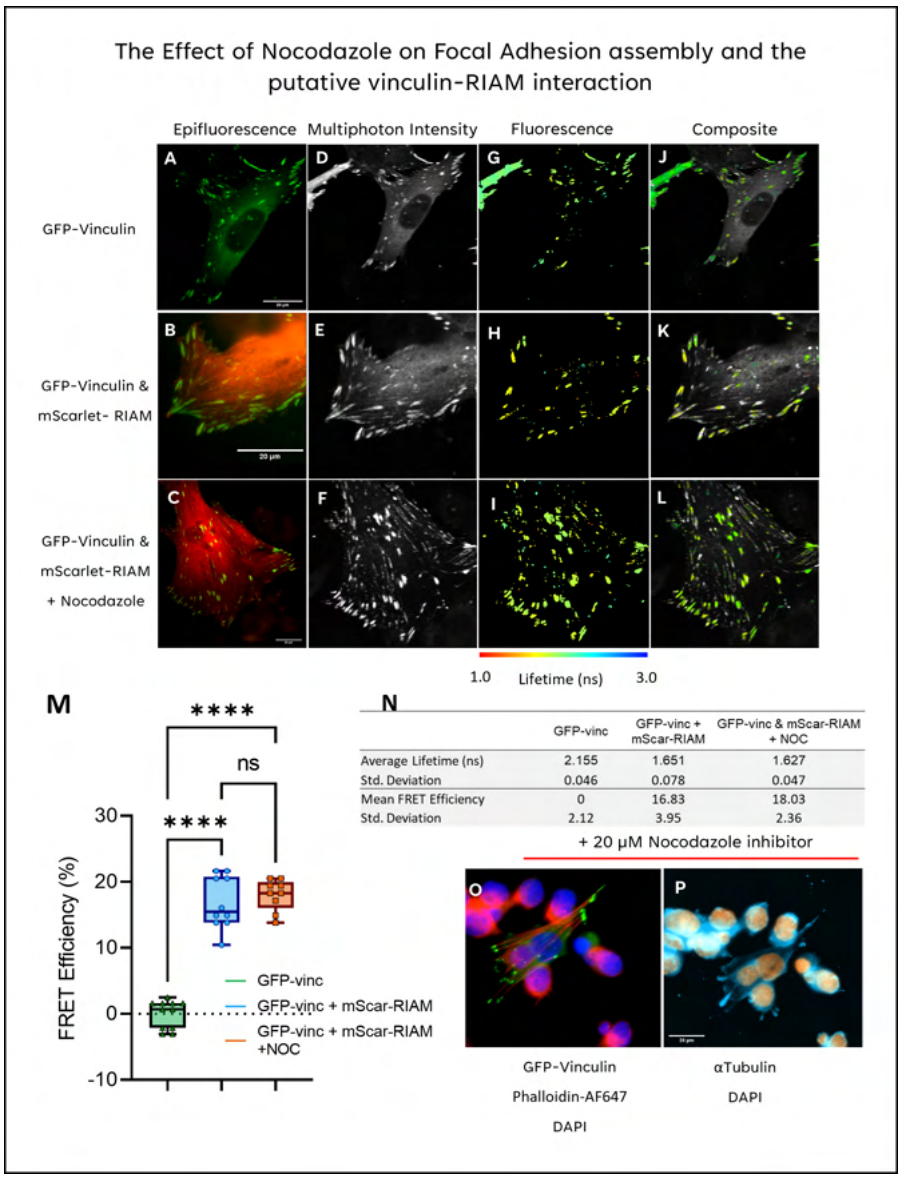

Figure 3.2.6.1: ***Vinculin-RIAM Interaction determined by TCSPC-FLIM:*** *. A-C) show epi-fluorescence images of MEF transfected with a GFP-vinculin in isolation or with one of the two acceptors. Panels D-F) shows Multiphoton Intensity images, G-I) show the lifetime distribution in a typical transfected cell. Panels J-L) show a composite image of lifetime and multiphoton intensity image. M Box and whisker plot of the average FRET efficiencies per construct. Significance is determined through a one-way ANOVA with Tukey corrections for multiple tests. N) A summary table of lifetimes, standard deviation, and FRET efficiencies. O-P) Images show MEFs transfected GFP-vinculin (O) which were then fixed in 4% PFA in PHEM buffer, permeabilised in 0.1% Triton x-100 and blocked in 4% BSA in TBS. Cells were stained with a mouse primary anti-α Tubulin antibody at a 1:50 dilution followed by a goat anti-mouse Alexa Fluor® 568 (shown in P). Phalloidin-Alexa Fluor® 647 was (red) at a 1:40 dilution (O). Cells were treated with 20 µM nocodazole inhibitor 30 minutes prior to fixing and imaging. N= 10 cells imaged per condition, P-values* $\geq$ *0.123 ns,* $\leq$ *0.0332 (*),* $\leq$ *0.0021 (**),* $\leq$ *0.0002 (***),* $\leq$ *0.0001 (****).*

3.2.7 Vinculin Tension Sensor in Fixed MEFs

The teal-vinculin (donor alone) transfected cells exhibited a longer average fluorescence lifetime than either the vinculin-TS or vinculin-TL transfected cells, indicating that these cells displayed some degree of constitutive FRET is absent in the donor alone. This is further evidenced when the average lifetimes were converted to FRET efficiency; the dynamic, active vinculin-TS transfected cells had an average FRET efficiency of 11.15 ± 3.99 % and the high FRET vinculin-TL transfected control cells had the greatest average FRET efficiency, 17.99 ± 3.66 %. The distributions for the vinculin-TL and vinculin-TS transfected cells were significantly different, with a P-value of 0.0037.

These results would suggest that these FAs are in a relatively low force state on average, as FRET is detected for the vinculin-TS transfected cells, which only occurs when the two FPs are close together, exclusively when there is little to no applied force on vinculin, separating them apart. A relatively large spread of values for both the vinculin-TS and vinculin-TL lifetimes also suggest much more heterogeneity in the cells sampled, which may not be much of a surprise when imaging force-sensitive proteins which have been fixed.

Previous experiments using the same tension sensor have shown that in live cells, static FAs were shown to have an average force of ≈ 2.5 pN. We would expect to see a more extensive spread of mean cellular lifetimes for the vinculin-TS construct as this construct responds to the intramolecular forces applied to vinculin in the cell. As individual vinculin molecules turn over within adhesions, bind to new partners and diffuse in and out of the adhesome, we expect a full range of possible FRET values. A loss of FRET is only observed in high-tension events, and an event that produces a short lifetime indicates high FRET, which corresponds to a low-tension force acting on the biosensor. The average force applied per cell is calculated using the formula below [130, 149]. This a simple application of Hook's law which states that the extended distance a spring will be displaced by (FP separation distance) by an external force is directly proportional to the magnitude of the applied force. The proportionality constant describes the stiffness of the nanospring.

$$Force = R_0 \cdot \frac{\left(\frac{1}{E_{vinTS}} - 1\right)^{\frac{1}{6}} - \left(\frac{1}{E_{vinTL}} - 1\right)^{\frac{1}{6}}}{0.01196 \cdot N + 0.0001255} \tag{11}$$

Where, $R_0$is the Forster radius for the mTFP1-mVenus FRET pair, E_{vinTS} and E_{vinTL} are the FRET efficiencies for the vinculin-TS and vinculin-TL constructs, respectively, and N is the linker amino acid count of 40. Both *in vitro* and *in vivo* studies of the spider silk linker have shown that the FL-40 linker used in the vinculin-TS and vinculin-TL constructs is elastic and has an intracellular compliance of approximately 0.478 nm/pN [130,149,152]. Applying equation 3.2.7-1, we can calculate an applied intracellular tensile force of 1.57 ± 0.97 pN.

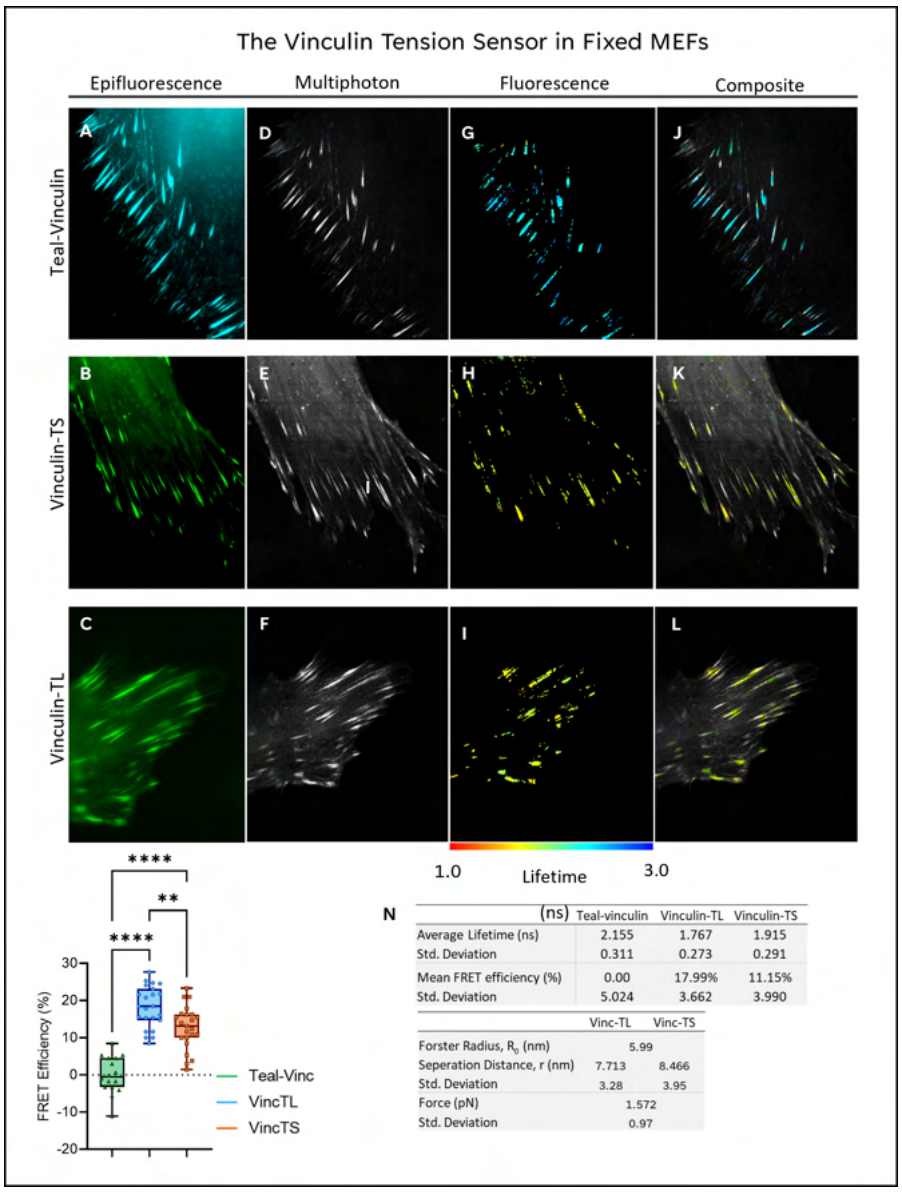

Figure 3.2.7.1: ***The Vinculin Tension Sensor determined by TCSPC-FLIM:*** *A-C) show epifluorescence images of MEF transfected with an EGFP-vinculin in isolation or with one of the two acceptors. Panels D-F) shows two-photon Intensity images, G-I) show the lifetime distribution in a typical transfected cell. Panels J-L) show a composite image of lifetime and two-photon intensity image. M) Box plot of the average FRET efficiencies per construct. Significance was determined through a one-way ANOVA with Tukey corrections for multiple tests. N) Summary tables of lifetimes, standard deviation, FRET efficiencies, separation distances and intramolecular Force. N=30 cells imaged per condition across three separate technical repeats with P-values* $\geq$ *0.123 ns,* $\leq$ *0.0332 (*),* $\leq$ *0.0021 (**),* $\leq$ *0.0002 (***),* $\leq$ *0.0001 (****).*

3.3 Results Chapter I Conclusions

Co-immunoprecipitation studies of EGFP-vinculin (described in §3.2.1) showed that it is possible to pull down both talin and RIAM from a GFP-trap, talin is a known binding partner to vinculin, so seeing a successful pull-down for this protein is no surprise. However, detecting RIAM on the same blot strongly supports the notion that a specific biochemical interaction occurs between vinculin and RIAM in MEFs. This interaction may not be particularly strong, as previous studies [37] have suggested. Consequently, the interaction may be a more transient transaction, which could explain why the band intensities for the RIAM pull-down were not strong. In addition, I have also shown an unambiguous FRET interaction between vinculin and RIAM which further supports the conclusion that vinculin and RIAM are involved in a biochemical interaction.

The vinculin-RIAM interaction was further investigated using two FRET pairs, one where RIAM was genetically encoded to mScarlet at RIAMs N-terminus and the other where mScarlet is placed at RIAMs C-termini. In both cases, EGFP-vinculin is kept the same as the donor. To recap, the EGFP-vinculin + RIAM-mScarlet FRET pair was calculated to have a FRET efficiency of 12.36 ± 1.48 %, and the FRET efficiency for the EGFP-vinculin + mScarlet-RIAM FRET pair was determined to be 18.99 ± 2.34 %. As FRET efficiency is inversely related to the distance separating the two fluorophores, the FRET pair with the highest FRET efficiency must have the shortest separation distance. In this case, the EGFP-vinculin + RIAM-mScarlet FRET pair with a FRET efficiency of almost 19 % would equate to a separation distance of 7.23 nm compared to 7.91 nm* for the other pair. This is an important finding as it suggests the N-terminus of RIAM is more likely to be in direct contact with the N-terminus of vinculin, as was previously indicated from *in vitro* studies of the N-terminal domains in isolation [37]. These data also strengthen the argument for a biological interaction between vinculin and RIAM; as previously outlined, this is a significant aim of this chapter. The N-terminus of vinculin (head domain) is between amino acids 1–258, including a talin binding site. Similarly, the N-terminus of RIAM between amino acids 1-127 also includes RIAMs talin binding domain. It could be possible that this interaction occurs through both of their respective talin-binding domains as they have similar features. Still,

*Förster radius of 56.75 used and online calculated from FPbase.org/fret/

without creating a series of constructs, each with their point mutations, it would be challenging to say for sure.

The third objective I sought to investigate involved determining the primary location of the vinculin-RIAM interaction. In §3.2.3, I described how I used different thresholds to mask high and low-intensity regions, excluding different background levels to isolate pixels from the whole cell and FAs. I then inverted the FA mask maintaining the low-intensity threshold to ensure no extra-cellular background crept in to produce a cytosolic mask. The FRET efficiencies calculated for the separate regions were all approximately the same. This result demonstrated no significant difference in the interaction between vinculin and RIAM in the different masked regions. Some differences in variance could be exciting and might, for the FA-only mask, indicate that the FRET pair could be in a mixed population, at least for some cells. It could be conjectured that the vinculin-RIAM interaction we have seen so far is part of a separate pathway, one where RIAM actively recruits and shuttles vinculin to the leading edge of the lamellipodium, where we would expect RIAM to release vinculin and return to the cytoplasm where it could pick up more vinculin and cycle through. If this occurs, we could expect a situation where only a certain percentage of all the vinculin and RIAM molecules interact in the FAs, as we expect to see a certain amount of dissociation. We also know that RIAM does a similar role for talin and that talin cannot simultaneously bind to both RIAM and vinculin on the R4 domain of talin [37]. The specific location of the interaction is likely confined to the cytoplasm and not exclusively to the focal adhesions, as I had initially thought when I began working on this interaction.

Further investigation is required to look at the intracellular on-off rates at specific cell locations, cytoplasm versus FAs, for instance. A better understanding of the equilibrium between the two proteins and whether there is a meaningful change at various locations could be valuable. One might find that in the cytoplasm, the situation is in dynamic equilibrium. In contrast, in the FAs, the concentration of vinculin and talin is such that the equilibrium for the vinculin-RIAM interaction shifts from mostly bound to unbound. A simple Michaelis-Menten model could be built if we could accurately measure *in vivo* the protein concentrations within the two compartments.

The possibility that the vinculin-RIAM interaction is not solely FA based is further evidenced by data presented in §3.2.4, which suggests the interaction

is also actin independent, as cells treated with the ROCK inhibitor H-1152 still exhibit FRET between the EGFP-vinculin and mScarlet-RIAM constructs. A similar effect is also observed when nocodazole is added to the cells where there is no further change in the FRET efficiencies between vinculin and RIAM. The simplest explanation is that the two proteins do not require actin to associate, so they are unlikely to bind once vinculin has bound to actin in the mature FAs but are more likely to associate in the cytoplasm, where actin dynamics do not play a significant role in the association probability. When nocodazole is added to the cells, and vinculin is recruited to nascent adhesions where we could find RIAM playing a vital role in the recruitment and transport of vinculin, but again, no change in the interaction would be expected.

Data presented (in §3.2.4) suggested that the vinculin-RIAM FRET interaction is not affected when microtubules depolymerise, which is not unsurprising. As we do see larger adhesions after the addition of nocodazole (figure 3.2.4-1 panel B) due to vinculin (amongst other proteins) being recruited to nascent adhesions where we might find RIAM playing a vital role in the recruitment and transport of vinculin, but no change in the interaction would be expected. Nocodazole may increase the proportion of vinculin molecules undergoing FRET with RIAM, but the interaction is unaffected. Without a robust quantitative method to determine how much of the vinculin population is undergoing FRET with RIAM and precisely where in the cell this is occurring, it is impossible to draw any concrete conclusions at this stage.

One possible way to achieve this would be to use a bi-exponential Levenberg-Marquardt [160, 161] fitting algorithm described by the Ameer-Beg group [124]. The bi-exponential fit would yield two lifetimes, one associated with the donor alone and the other with the donor-acceptor condition. If a global analysis approach was used for each image, a single average-weighted lifetime was calculated for each fluorescent lifetime, tau, a ratio of tau 1 and 2 could be derived for each image. The ratio of tau1:tau2 would be equivalent to the fraction of FRET occurring in any masked or segregated cell area. Many groups have done this in the past, and it could be utilised here to achieve more meaningful quantified conclusions regarding where there is more of the vinculin-RIAM interaction in the cell. The issue with going down this path is that we need homogenous samples with clear and well-behaved photophysics. Each sample must only have two fluorescent lifetimes without too much noise, and these lifetimes cannot vary too much between sam-

ples. I have attempted to undertake such endeavours with the data I have collected. Still, with too few photons per pixel, attempting to fit this data onto a bi-exponential fitting algorithm is not wise. Doing so will almost certainly result in over-fitting, leading to conclusions being made on data it can not support.

The final question I wanted to answer involved understanding how intracellular force, precisely tension across vinculin, played a role in the interaction. Vinculin is a well-known mechanosensitive protein. Once bound to talin and actin in FAs and under mechanical load, vinculin extends, uncoiling its flexible neck domain, which alters the tertiary structure of the active protein compared to the inactive, autoinhibited conformation50. I was able to probe the mechanical force question using tension-sensing vinculin biosensors, which, once transfected into cells, fixed, and imaged, showed that little force was applied to the vinculin molecules in cells. As a loss of FRET is only observed in high-tension events, an event which produces a short lifetime is indicative of high FRET, which corresponds to low tension force acting on the biosensor as this does not separate the two FPs from one another sufficiently. This has presented a significant issue that I want to address and, hopefully, can be addressed by undertaking these measurements in live cells. Live cell experiments are needed as fixing cells first and then attempting to measure the intracellular tension in a cell fixed with PFA, permeabilised with detergent and then mounted in glycerol-based mounting media is not something I have been able to do.

Secondary to the issues surrounding fixed vs live imaging of the tension sensor is a much larger problem: how do we interrogate two different FRET interactions concurrently? Specifically, inter-molecular vinculin-RIAM interaction and the intra-molecular vinculin tension sensing FRET biosensor? Several practical solutions exist, but the most interesting and potentially exciting would be to develop a novel three-colour FRET model that would allow for the vinculin tension to be used in conjunction with an additional FRET acceptor mScarlet-RIAM. Three-colour FRET systems have been used in the past, but none have used two-photon TCSPC-FLIM and none so far have been used to investigate the spatial relationships of a FRET interaction and the temporal evolution whilst also multiplexing a force measurement.

4

RESULTS CHAPTER II:
THREE-COLOUR FRET CASCADE

4.1 Introduction to Three-Colour FRET Cascade

To start to answer questions such as: When RIAM binds to vinculin in developing focal adhesions, is vinculin in an open or closed state? Is mechanical force required for binding or does the addition of force on maturing adhesions occluded binding sites actively inhibit RIAM-vinculin binding? We needed to develop a new FRET-based assay that could determine whether multiple fluorescently labelled proteins are bound together in a single complex at a specific time point and location in a cell or if, alternatively, sub-complexes were formed first, which were then shuttled to a cellular location before being re-organised or dissembled.

This chapter will describe our methodology for determining multi-protein complex formation, FRET-Cascade. FRET-Cascade is an analytical approach used with TCSPC-FLIM to identify the induvial FRET components in a complex system and show which fluorescently tagged proteins are directly interacting at specific locations in the cell and how this evolves over time. To demonstrate how a three-colour FRET-Cascade could be achieved, I first designed eight different constructs consisting of fluorescent proteins, which would be expressed and purified as an *in vitro* model I could use as a starting point for a more complex *in vivo* assessment. The constructs and fluorescent proteins used individually, in pairs or triplets, are illustrated in figure 4.1-1 below. The FP mTurquoise2 (mTurq2) was chosen as the universal donor due to its high quantum yield (0.93), mono exponential lifetime decay, and long reported lifetime, 4.1 ns [162, 163]. Other options for the donor included Teal fluorescent protein (mTFP1), mCerulean2, or Cyan Fluorescent Protein (CFP), all of which are inferior choices, being dimmer, have lower quantum yield and generally have a multi-exponential decay [162, 163].

Once the donor was selected, the choice of first acceptor/second donor was easy as mVenus has been well documented in the literature as the

preferred acceptor for mTurq2 [162]. The final fluorophore, mScarlet-I, was chosen over other red fluorescent proteins such as mCherry, mRFP1 and mScarlet for several reasons; the most important was the size of the overlap integral between mTurq2 and the red acceptor and, by extension, the length of the Förster radius (R_0). The Förster radius is the distance at which there is 50% energy transfer between two fluorophores; for this reason, the Förster radius is often used over similar metrics to compare the efficiency of energy transfer (§4.2.6-2 for details). A longer Förster radius will yield a greater dynamic range for FRET, which is highly advantageous when considering how the FRET-Cascade model will be applied to living cells. Both mRFP1 and mCherry were disregarded as they are not as bright as either of the mScarlet fluorophores nor have particularly long Förster radii with mTurq2, 5.36 and 5.25 nm, respectively. Compared to mScarlet and mScarlet-I, which possess Förster radii of 5.66 and 5.65 nm, respectively. The bi-exponential decaying mScarlet-I was selected over the mono-exponential mScarlet as the I mutant is brighter and fluorescence decay characteristic, whilst not yet investigated, as for mCherry [164], should not significantly influence the radiative transfer as the final acceptor in the FRET-cascade. Studies of the EGFP-mCherry FRET pair have shown that whilst the FRET pair is highly effective, there are multiple energy transfer states between the two FPs which could over-complicate an already intricate model of interacting energy transfer states between three FPs.

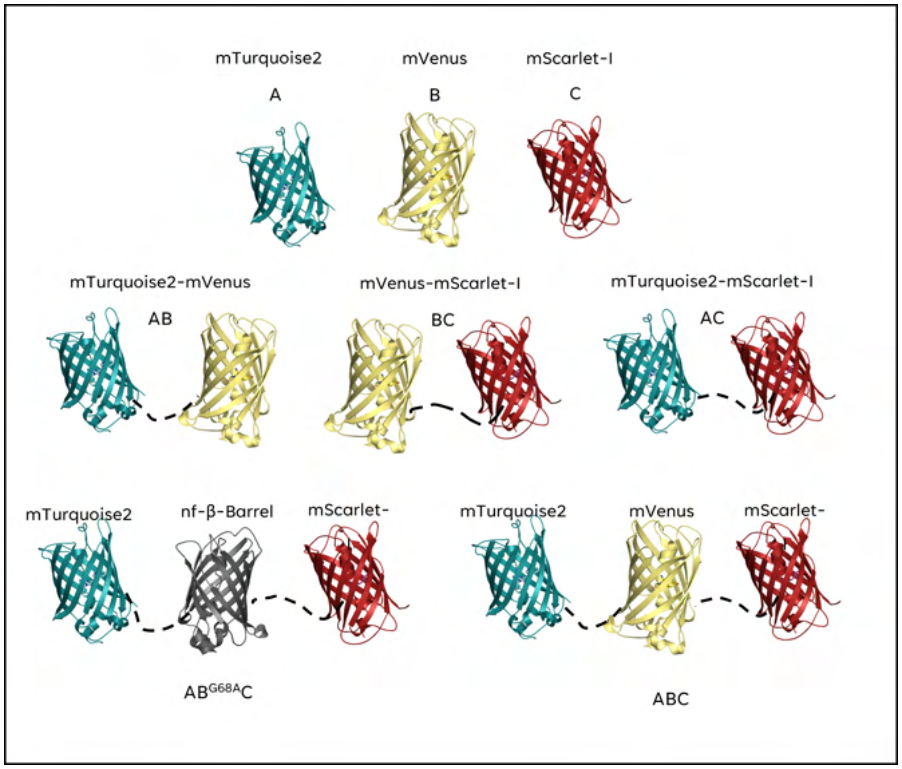

Figure 4.1.0.1: ***Cartoons of the chimeric fluorescent proteins:*** *Top row: The three induvial FPs mTurquoise2 , mVenus and mScarlet-I . Middle row: The three twin FPs; mTurquoise2-mVenus, mVenus-mScarlet-I, mTurquoise2-mScarlet I. Bottom row: The two triple FP constructs; The fully functional mTurquoise2-mVenus-mScarlet-I construct, and the mutated mTurquoise2-mVenusG68A-mScarlet-I construct. All images of the fluorescent proteins were created from their PDB accession codes and modelled in Pymol. Linkers shown in black are dotted lines for illustrative purposes, linker sequence GGSGGS for all twin and triplet constructs.*

4.1.1 Fluorophore Design

The fluorochrome found in GFP, isolated from *Aequorea victoria,* a bioluminescent jellyfish indigenous to the west coast of North America, is formed from a series of reactions involving only three amino acids, serine, tyrosine, and glycine in positions 65, 66, and 67 [165, 166] respectively of the 238 amino acid protein. There are three main biochemical steps involving these amino acids undergo; the first is a cyclisation reaction [165,166] that creates the five-membered nitrogenous-heterocycle, 4-imidazolinone, which sits at the centre of not only all GFP-like fluorescent protein chromophores but also most fluorochromes found in all fluorescent proteins [167]. The aromatic heterocycle is formed from the two amide moieties that connect residues 65 with 66 and 66 with 67 [168]. In the second step in forming a functional chromophore, the non-fluorescent intermediate compound undergoes a much slower oxidation step, where the saturated, carbon-carbon single bound joins the imidazolidinone ring to the phenol side chain of the tyrosine residue is oxidised, yielding an unsaturated carbon-carbon double bond. This forms the continuous delocalised system of electrons between the two aromatic moieties and is known as *p-Hydroxybenzylidene-imidazolinone* [168, 169]. Finally, a deprotonation step occurs, where a single proton is lost from the hydroxyl group of the phenol side chain, this causes relaxation of the delocalised system that leads to the formation of the green fluorochrome [166]. The GFP fluorochrome can exist as one of two equivalent structural isomers (figure 4.1.1-2).

For many species, the glycine in position 67 (relative to GFP) is highly conserved (Table 4.1.1). FPs isolated from distantly related organisms like Aequorea *victoria and Entacmaea quadricolor,* both members of the cnidaria phylum and lacking a common ancestor in approximately 600 million years [170], both possess a glycine in the third position of the three amino acids which form their chromophore. Early site-directed mutagenesis work [171] showed that a Gly-67-Ala mutation was sufficient to prevent the fully fluorescent chromophore forming in GFP. It was speculated that the cyclisation step was not possible due to the steric hindrance induced by the methyl group on the alanine [165, 171]. The equivalent mutation in mVenus is Gly-68-Ala; this was selected as a possible way to produce a "non-fluorescent beta barrel" or spacer, which could occupy the same physical space of the mVenus, but would not have any of the photophysical properties (visible absorption or emission) and, most importantly, would not FRET with the mTurquiose2 donor.

Table 7: *Table showing the composition of various chromophores within selected fluorescent proteins.*

Fluorophore	Chromophore†			Organism
	65	66	67	
CFP	Ser	Trp	Gly	*Aequorea victoria*
mCerulean2	Thr	Trp	Gly	*Aequorea victoria*
mTFP1	Ala	Tyr	Gly	*Clavularia* sp.
mTurq2	Ser	Trp	Gly	*Aequorea victoria*
GFP	Ser	Tyr	Gly	*Aequorea victoria*
mNeon	Gly	Tyr	Gly	*Branchiostoma lanceolatum*
mVenus	Gly	Tyr	Gly	*Aequorea victoria*
mCherry	Met	Tyr	Gly	*Discosoma sp.*
mScarlet	Met	Tyr	Gly	Synthetic
mRFP1	Glu	Tyr	Gly	*Discosoma sp.*
mKate	Met	Tyr	Gly	*Entacmaea quadricolor*
mEos	His	Tyr	Gly	*Lobophyllia hemprichii*
Dronpa	Cys	Tyr	Gly	*Echinophyllia sp*

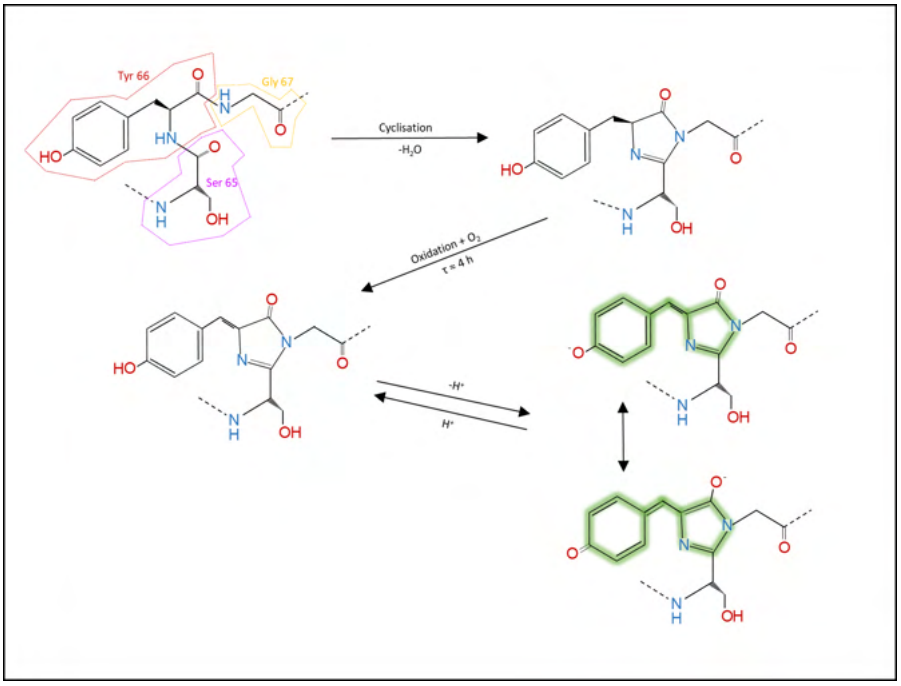

Figure 4.1.1.1: ***Maturation of the GFP core fluorochrome:*** *A schematic illustrating the three steps required for fluorochrome formation in GFP: Cyclisation, Oxidation, and deprotonation. All diagrams were drawn in PowerPoint.*

4.2 Protein Production & Purification

4.2.1 mTurquoise2-mVenus-mScarlet Design

The three-colour FRET cascade model required several constructs, initially, seven, which would be expressed in bacteria and then purified to allow for spectroscopic and biophysical characterisation of the three-colour FRET cascade system *in vitro*. Another seven constructs were made in a mammalian expression vector for *in vivo* expression and spectroscopic characterisation (figure 4.2-1). This required 14 different constructs with seven different inserts and two vector backbones. Once the three-colour construct in the mammalian expression vector was designed, it was purchased from VectorBuilder®. As this construct was already in a mammalian expression vector, the various combinations of FPs were produced through a series of digestions with restriction endonucleases (REases) which were used to excise specific FPs from the parent three-colour construct. The resulting linearised DNAs were then ligated together with T4 DNA ligase, creating the three dual-colour constructs, and then, after further digestion, the three separate single-colour constructs. The bacterial expression vectors were created by sub-cloning these constructs via PCR amplification into a pET-151 directional TOPO™ Expression system. Two different constructs were made by introducing a single point mutation via site-directed mutagenesis (SDM) in mVenus to create the non-fluorescent mVenus^{G68A} and the mono-exponential mScarlet^{I74T}.

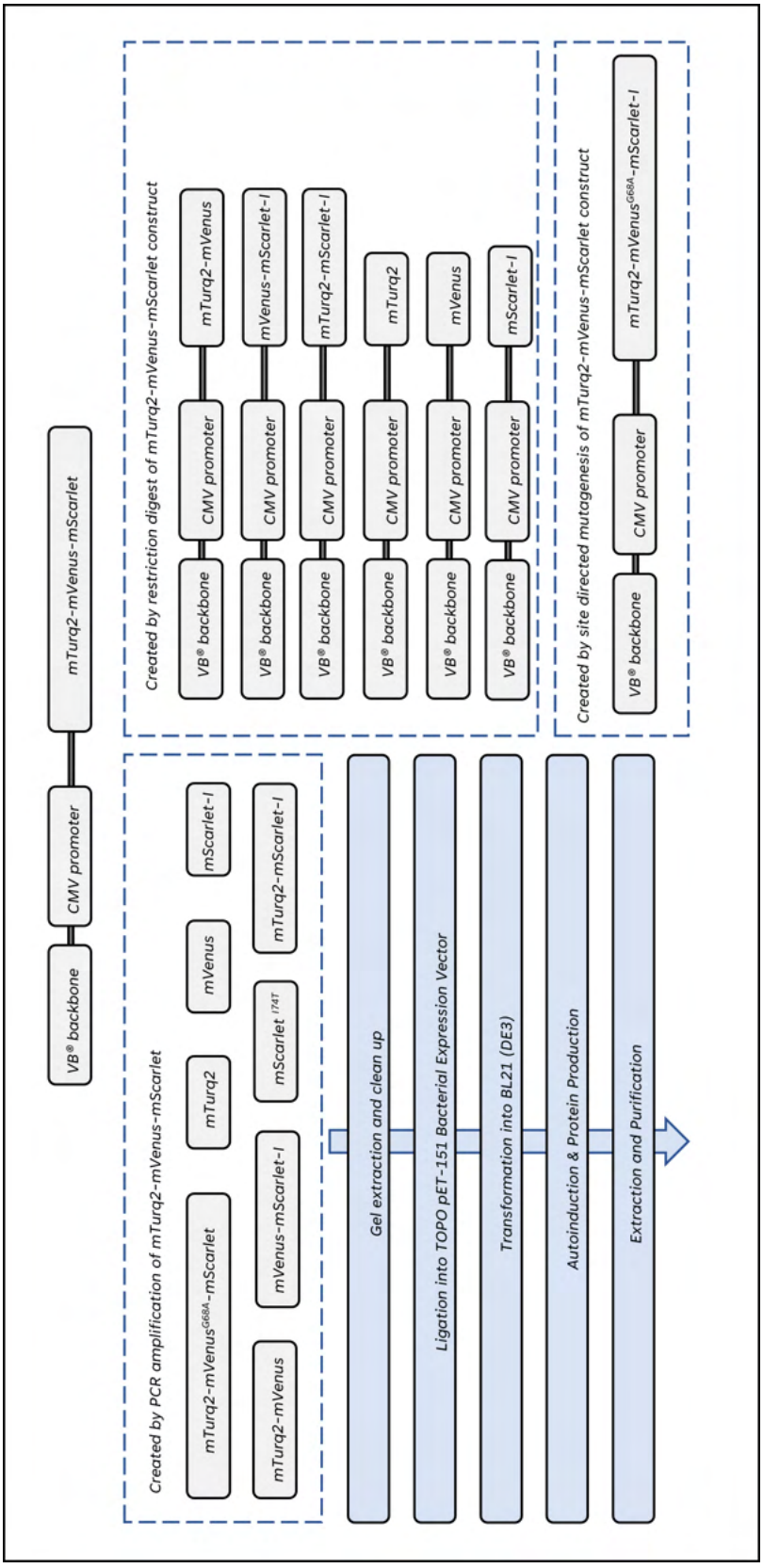

Figure 4.2.1.1: ***A scheme illustrating Cloning Workflow:*** *Overview of the in-vitro and in-vivo DNA constructs produced from the CMV-mTurq2-mVenus-mScarlet construct.*

4.2.2 DNA constructs

Table 8: *Table showing the composition of various chromophores within selected fluorescent proteins.*

	Construct	Prom.	Resist.	Size (Bp)	Vector	Expressed Protein
Bacterial Expression Vectors	pET151‡	T7	Amp	2.2	pET151	mTurquoise2 only
	pET151-B	T7	Amp	2.2	pET151	mVenus only
	pET151-C	T7	Amp	2.2	pET151	mScarlet-I only
	pET151-C^{I74T}	T7	Amp	2.2	pET151	mScarlet only §
	pET151-AB	T7	Amp	2.2	pET151	mTurquoise2-mVenus
	pET151-BC	T7	Amp	2.2	pET151	mVenus-mScarlet
	pET151-AC	T7	Amp	2.2	pET151	mTurquoise2-mScarlet-I
	pET151-ABC	T7	Amp	2.2	pET151	mTurquoise2-mVenus-mScarlet-I
	pET151-B^{G68A}	T7	Amp	2.2	pET151	Non-fluorescent mVenus with the *G68A* mutation
	pET151-AB^{G68A}	T7	Amp	2.2	pET151	mTurquoise2-nf-β-barrel
	pET151-AB^{G68A}C	T7	Amp	2.2	pET151	mTurquoise2-nf-β-barrel-mScarlet-I
Mammalian Expression Vectors	pVB-A¶	CMV	Amp	2.2	pVB	mTurquoise2 only
	pVB-B	CMV	Amp	2.2	pVB	mVenus only
	pVB-C	CMV	Amp	2.2	pVB	mScarlet-I only
	pVB-AB	CMV	Amp	2.2	pVB	mTurquoise2-mVenus
	pVB-BC	CMV	Amp	2.2	pVB	mVenus-mScarlet-I
	pVB-AC	CMV	Amp	2.2	pVB	mTurquoise2-mScarlet-I
	pVB-ABC	CMV	Amp	2.2	pVB	mTurquoise2-mVenus-mScarlet-I
	pVB- AB^{G68A}C	CMV	Amp	2.2	pVB	mTurquoise2-nf-β-barrel-mScarlet-I

4.2.3 Single Digestion of mTurquoise2-mVenus-mScarlet

Single digests of the mTurquoise2-mVenus-mScarlet construct were performed with either AgeI, XmaI or SalI, depending on the desired FP combination (figure 4.2.3-1) Digests were performed in 0.2 mL microfuge tubes

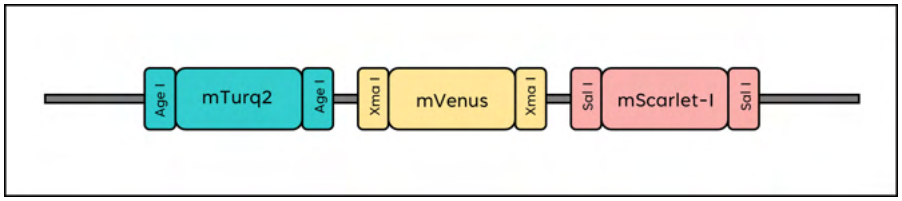

Figure 4.2.3.1: ***Plasmid Cloning Strategy:*** *Diagram of the positioning of the restriction sites within the fluorescent protein constructs.*

(Greiner) with approximately 100 ng of template DNA containing the mTurquoise2-mVenus-mScarlet insert, which was digested using a 10x Cutsmart® digestion buffer (NEB) and 0.5 μL of the selected REase, see table 2.2.3-1. The Digestion mixture was then incubated at 37°C for 2 hours in a thermocycler (Veriti™ 96 wall thermal Cycler, Thermo Fisher). The restriction endonuclease was denatured by heating the digestion mixture to 65°C for 20 minutes. Following digestion, the linearised vector was ligated using T4 DNA ligase and incubated for 16 hours (overnight) in the same thermocycler before being transformed into Top10 *E. coli* cells as described in §4.2.9.

Table 9: *Restriction Endonuclease Digestion of Plasmid DNA.*

Reagent	Vol. (µL)
ddH_2O	3.0
10x Cutsmart	0.5
XmaI	0.5
Template	1
Total	5.0

4.2.4 PCR Amplification

PCR reactions were performed in a single 0.2 mL microcentrifuge tube (Greiner) which was heated and cooled with the aid of a DNA Thermocycler (Veriti™ 96 wall thermal Cycler, Thermo Fisher). A premixed Q5 2x master mix (NEB) was used, which contained Q5 HF DNA polymerase, 200 μM dNTPs and 2.0 mM Mg^{2+}. Each PCR reaction contained 500 nM of the forward primer, 500 nM of the reverse primer and approximately 20 ng/μL of template plasmid to be amplified. All volumes and concentrations are outlined in Table 9.

Table 10: *PCR reagent volumes and concentrations.*

	Vol. (µL)	Final Concentration
Q5 HF 2x Master Mix	25	1x
10 µM forward primer	2.5	500 nM
10 µM reverse primer	2.5	500 nM
Plasmid DNA	0.3	20 ng/μL
ddH_2O	19.7	

Once the reagents were added and thoroughly mixed by pipetting, the micro-centrifuge tubes were placed in the thermocycler and the following program was loaded (see Table 11 below). Annealing temperatures varied due to the melting temperatures of the primers used for each amplification.

Table 11: *PCR reagent volumes and concentrations.*

Thermocycling programme		
	Temperature (°C)	Time (s)
Initial denaturation	98	30
Denaturation	98	20
Annealing	50-72	60
Extension	72	96
Final extension	72	300
Hold	4	∞

4.2.5 Site Directed Mutagenesis:mVenus^{G68A}& mScarlet^{I74T}

Site-directed mutagenesis (SDM) was used to introduce a single point mutation in mVenus FP of the three-colour construct at amino acid 68, glycine, which was mutated to an alanine. A pair of primers were designed containing a two-base-pair mismatch in the centre of the primer pair. Another SDM reaction was performed to introduce a point mutation into mScarlet-I at amino acid 74, where the Isoleucine found in mScarlet-I was mutated to a Threonine; this mutation causes the fluorescent lifetime of the mScarlet-I, which has a bi-exponential decay to become mono-exponential [172].

A PCR reaction was then carried out as described in §4.2.4 using Q5 DNA polymerase (NEB), which produced a linearised form of the double-stranded parental template. Following the PCR reaction, the linear plasmid was treated with KLD mix (NEB) as part of the SDM kit (NEB). The KLD mix is a Kinase, Ligase DpnI enzyme mix that circularises and ligates the amplified PCR product with the kinase and ligase while the DpnI restriction enzyme digests any methylated parental DNA from the PCR product (table 11).

Table 12: *Site-directed mutagenesis.*

Reagent	Vol. (µL)
ddH_2O	3.0
PCR Product	1.0
2x KLD Buffer	5.0
10x KLD Mix	1.0
Total	10.0

The KLD mix was incubated at room temperature for 60 minutes before 5 μL of the mix was transformed into Top10 *E. coli* cell as described in §4.2.9

4.2.6 Agarose Gel Electrophoresis

The volumes outlined in this protocol are sufficient to make a 50 mL 0.8 % agarose-TAE gel. First, 0.4 g of agarose (Sigma-Aldrich) was weighed and dissolved into 50 mL of Tris-Acetate-EDTA (TAE) buffer before being heated for 3 minutes in an 800 W microwave. Once the agarose was completely dissolved in the TAE solution, the gel solution was cooled to approximately 50°C before 5 μL of SYBR-safe gel stain (Fisher Scientific) was pipetted into the solution and mixed by gentle swirling. Once mixed, the 0.8 % agarose solution was poured into a gel mould, and a plastic comb was inserted. This will form the wells of the gel as it cools. Once set, the gel was placed in the electrophoresis tank, and more TAE buffer was poured in, covering the gel up to the max fill level. Samples were then loaded into the wells of the gel once diluted in 6x DNA loading buffer, and the gel was run at 80 V for 60 minutes. Once run, the gel was then imaged using a UVP Bio-imager.

4.2.7 Gel Extraction & Clean Up

Gel extraction was used to separate the cut DNA fragments from a double digest of a single plasmid or PCR product. The digested DNA and undigested DNA bands were separated on a 0.8 % agarose gel as described (§4.2.6),

and the DNA bands were visualised on a UV illuminator. The fluorescent bands corresponding to the empty cut vector and the cut gene of interest were excised from the gel block using a clean, sterile scalpel and placed in separate 1.5 mL microfuge tubes. The mass of the excised gel plugs was determined by weighing the tube before and after the gel plug was added. This was required as the volume of resuspension buffer, QG buffer from the QIAgen® gel extraction kit (Qiagen, 28706X4) to be added is based on the mass of the gel fragment. Three times the mass of the gel plug (in grams) of QG buffer (in μL) was added to the gel plug (see table 4.2.7-1 for volumes) and heated to 50°C on a heat block for 10 minutes. The QG buffer contains 5.5 M Guanidine Thiocyanate, a strong chaotropic reagent that breaks down the agarose gel and encapsulates the DNA fragments by denaturing the proteins in the agarose, disrupting the hydrogen bonding holding the aqueous gel together.

Once the gel had been fully incorporated into the QG buffer, one volume of isopropanol was added. Isopropanol is an organic solvent which causes the plasmid DNA to precipitate out of the solution. The QG-DNA solution was then passed through a QIAquick spin column and centrifuged at 17,100 g for 120 seconds. This caused the precipitated DNA to bind to the silicone membrane of the spin column. The column was washed twice with PE wash buffer and centrifuged at 17,100 g before 25 μL of pre-warmed elution buffer was added and incubated before centrifugation and elution. Following gel extraction, the isolated DNA was then analysed spectroscopically using the Nanodrop D-1000 spectrophotometer (Nanodrop technologies) before DNA ligation.

Table 4.2.7-1 Gel Extraction Values

Table 13: *Gel Extraction Values.*

	Empty Tube	Tube + plug	Gel plug	1x Volume	3x Volume
Digested insert	0.917	1.228	0.311 g	311 µL	933 µL
Digested vector	0.911	1.207	0.296 g	296 µL	888 µL

4.2.8 pET 151 TOPO Ligation

Directly following on from §4.2.7, ligation reactions (Table 13) were conducted. Two control reactions were also included. The first of which did not contain the T4 DNA ligase. This was done to determine if any uncut DNA had

been carried over from earlier steps. The second control did not contain the insert; this was done to determine if any partial digests of the backbone vector had also been carried over. The ligation reaction consisted of a 3:1 molar ratio of insert to the backbone DNA incubated with 2 μL of 10x T4 Buffer and 1 μL of T4 DNA Ligase. Moles of DNA were calculated from the concentrations determined by nanodrop, DNA length and volumes using equation 12 (see below). The total volume was made up to 20 μL with ddH_2O; all reactions were incubated overnight at 16°C in a thermocycler (Veriti™ 96 wall thermal Cycler, Thermo Fisher).

Table 14: *Ligation of the TOPO pET-151 vector and PCR products.*

Vector + Insert

	Vol. (µL)	Conc. (ng/µL)	Total mass (ng)	Size (bp)	fmol	Ratio
PCR product	8.11	36.95	299.7	2205	219.91	3.0
pET-151 vector	1.62	154.4	250.1	5535	73.13	1.0
T4 10x Buffer	2.00					
T4 DNA Ligase	1.00					
ddH2O	7.27					
Total volume	20.00					

No PCR Product Control

	Vol. (µL)	Conc. (ng/µL)	Total mass (ng)	Size (bp)	fmol	
pET-151 vector	1.62	154.4	250.1	5535	73.13	
T4 10x Buffer	2.00					
T4 DNA Ligase	1.00					
ddH2O	15.38					
Total volume	20.00					

No Ligase Control

	Vol. (µL)	Conc. (ng/µL)	Total mass (ng)	Size (bp)	fmol	Ratio
PCR product	8.11	36.95	299.7	2205	219.91	3.0
pET-151 vector	1.62	154.4	250.1	5535	73.13	1.0
T4 10x Buffer	2.00					
ddH2O	8.27					
Total volume	20.00					

$$\text{Moles of dsDNA} = \frac{\text{mass dsDNA (g)}}{(\text{Length dsDNA(bp)} \cdot 617.98) + 36.04} \qquad (12)$$

4.2.9 Transformation into Top10 Competent *E. Coli* Cells

For routine sub-cloning of plasmids, 0.5 μL of vector DNA was incubated with 25 μL of thawed TOP10 chemically competent *E. coli* cells (Invitrogen) for 30 minutes on ice. When transforming ligation products, 5 μL of ligation product was incubated on ice for 30 minutes with 50 μL of *E. coli* cells. Following incubation, the bacteria-DNA solution was heat shocked at 42°C for 45 seconds before being returned to the ice for 2 minutes, where 200 μL of SOC (Super Optimal broth with Catabolite repression) was added. The cell-DNA solution was incubated at 37°C, 180 rpm for one hour. The transformed cells were spread on to LB-agar (Sigma-Aldrich) plate containing either ampicillin 100 μg/mL or kanamycin 50 μg/mL (both from Thermofisher) using a sterile glass spreader and cultured at 37°C overnight. After 18 hours of incubation, the LB-Agar plates were checked for colonies.

4.2.10 Colony PCR

Following the successful transformation of the ligated PCR product into the pET-151 vector, approximately 10 colonies were picked for each construct with a sterile pipette tip. A single colony of bacteria was removed from the plate and used to inoculate a fresh, sterile LB-agar plate before the remaining collected bacterial mass was pipetted into a PCR microfuge tube containing 10 μL of sterile ddH_2O. This bacterial solution was then used as the starting material for a PCR reaction to screen the potentially successful colonies for the correct insert.

Table 15: *Colony PCR reaction details and thermocycler program*

Reaction mix

	Vol. (µL)	Final Concentration
Taq Polymerase	12.5	1x
10 µM forward primer	1.25	500 nM
10 µM reverse primer	1.25	500 nM
Bacterial solution	10	

Thermocycling programme

	Temperature (°C)	Time (s)
Initial denaturation	95	10 minutes
Denaturation	95	20
Annealing	56	60
Extension	72	60
Final extension	72	300
Hold	4	∞

4.2.11 Transformation into BL21 (DE3) *E. Coli* cells

Once the PCR products were confirmed to be correctly amplified and ligated within the pET-151 plasmids and verified through sequencing, the bacterial expression constructs were then transformed into BL21 (DE3) competent *E. coli* cells for protein production, following a heat shock protocol [173,174]. For each transformation, 50 μL of BL21 (DE3) *E. coli* cells were thawed on ice, to which 0.5 μL of construct DNA was added. The cells were then incubated for 30 minutes, after which they were heat shocked at 42°C for 45 seconds before returning to the ice for 3 minutes. Following this, 350 μL of unselective SOC was added, and the cells were then incubated at 37°C and 180 rpm for 60 minutes. Finally, the cells were plated out aseptically onto selective LB-agar containing 100 μg/mL Ampicillin and incubated at 37°C overnight.

4.2.12 Pre-culture & Autoinduction of BL21 (DE3) *E. Coli* cells

A single colony from a plate of the BL21 (DE3) *E. coli* cells containing one of the pET151 constructs were used to inoculate 10 mL of sterile unselective LB media (7-1 for composition) and incubated at 37°C and 180 rpm. After 6 hours, the pre-culture containing the desired pET151 plasmid was used to inoculate 200 mL of sterile selective ZYP-5052 autoinduction media (Table 18). The ZYP-5052 medium is specifically formulated for auto-induction, with glucose and α-lactose present in the medium [175]. Once the *E. coli*

have exhausted their limited supplies of glucose, they switch to α-lactose, inhibiting the lac repressor *LacI* allows for efficient expression of the downstream recombinant protein [176]. The auto-induction media (~200 mL) was inoculated with 5 mL of pre-culture, and the inoculated culture was incubated at 18°C and 180 rpm for 72 hours. After the long incubation period, OD_{600} was measured before the cell solution was centrifuged at 10,000 g for 30 minutes; the resulting pellets were collected while the supernatants were discarded. Pellets were weighed and then stored at -80°C.

4.2.13 Assessment of Over Expression

An expression test was carried out for each expressed protein before centrifugation and storage of the BL21 (DE3) *E. coli* cells, and this was done to determine whether the expression of the heterologous proteins had been successful. After only 4 hours of growth before glucose exhaustion, 1 mL of cell culture was removed and labelled as t_0. Once the protein overexpression procedure was completed, 1 mL of cell culture was removed from the 2,000 mL conical flask where the cells were grown.

The 1 mL samples (pre and post-induction) were first centrifuged at 10,000 g for 10 minutes at 4°C, supernatants were discarded, and the pelleted cells were re-suspended in a normalised volume of 10x BugBuster™ in buffer A (lysis buffer), (Table 18). The The normalisation formula below (equation 13) describes the dilution factor required to normalise the protein concentration across different bacterial culture densities, where OD_{600} is the optical density at 600 nm.

$$\text{Volume}_{lysisbuffer} = \frac{\text{OD}_{600} \cdot \text{Volume}_{removed}}{10} \tag{13}$$

The samples were incubated at room temperature for 10 minutes on a shaker plate. The samples were further analysed to determine the soluble and insoluble heterogeneous protein expression amounts. This was achieved by centrifuging the lysed/digested cells at 16,000 g for 10 minutes, the supernatants were removed and labelled as the soluble fractions and the pelleted cell debris was resuspended in a normalised volume of lysis buffer, which was labelled as the insoluble fraction. Analysis was completed by running a 20 μL sample on a 10% Bis-Tris SDS-PAGE (see §2.1.8 for details on running an SDS-PAGE). The gel ran for 60 minutes at 200 Volts and was stained in Coomassie brilliant blue stain for one hour.

4.2.14 Cell Lysis & Protein Extraction

The BL21 (DE3) cells containing the expressed protein of interest were thawed at room temperature from storage at -80°C. Once thawed, 8 mL of buffer A per gram of frozen cells was added to the cells (Table 18). The resulting suspension was thoroughly homogenised to a thick slurry through pipetting and mixing with the aid of a vortex. To this solution, 10 units/mL of benzonase (Novagen) was added to the slurry. Additionally, one tablet of the protease inhibitor cocktail (Roche) was added to prevent the degradation of the expressed protein of interest. The benzonase was used to help further the break-up of the genomic DNA that could otherwise clog up the narrow components of the purification system. The homogenised slurry of BL21 (DE3) cells in high-salt buffer A was then sonicated using a Sonics Vibra-cell VC 750 sonicator. The protocol consisted of cycles of 2 seconds of active sonication followed by 6 seconds of rest for 12 minutes, during which considerable heat was produced that could potentially denature the expressed protein. It was for this reason that the cell suspension was kept on ice for the duration of the sonication process. Once complete, the cell suspension was centrifuged at 18,750 g for 45 minutes at 4°C. The supernatant, containing all the expressed protein at this point, was removed and micro-filtered, first through a 0.45 μm and then a 0.22 μm pore disc filter.

4.2.15 Immobilised Metal-Ion Affinity Chromatography

The micro-filtered solution containing the expressed protein of interest was loaded onto a His-Trap HP 1 mL (GE) column in preparation for the first purification step, immobilised metal-ion affinity chromatography (IMAC) [177]. The His-Trap column consists of highly cross-linked agarose beads covalently attached to Ni^{2+} ions. These Ni^{2+} ions will chelate with the hexahistidine tag on the expressed proteins, which causes the expressed proteins of interest, which all have the same hexahistidine tags, to be retained on the column whilst endogenous *E. coli* proteins are washed off the column in the loading buffer (buffer A). Once these proteins had been eluted, a second buffer B (Table 18) with the same composition as buffer A, apart from 1M imidazole, was passed over the column. The addition of buffer B results in the histidine-tagged proteins being eluted much later than endogenous proteins. The eluted fractions with a significantly high absorbance at 280 nm from the chromatogram are assessed through SDS PAGE. Typically, 5 fractions, each with a volume of 1 mL, were pooled at this stage.

4.2.16 TEV Cleavage & His Tag Removal

The next step was to remove the hexahistidine tag from the expressed proteins using the TEV (Tobacco Etch Virus) cleavage enzyme (courtesy of *Dr M. Pfuhl, King's College London*). The TEV protease works by cutting the protein at the TEV cleavage site ENLYFG|G/S, which for the expressed proteins produced in this project sits between the hexahistidine tag and the start codon of the protein (see § 8.2.3 for sequence details). The eluted protein was first treated with 2 mM DTT before $\approx$ 750 μL of the purified protease was added to the protein solution, which was then incubated at RT for six hours. A 5 μL aliquot of the reaction was removed once every hour and then analysed by SDS-PAGE to follow the time course of TEV cleavage. Once the time course was complete, the cleaved-untagged fluorescent protein was transferred into a partially permeable membrane and dialysed for 24 hours in buffer A. This was done to reduce the concentration of imidazole still in the protein solution, which was vitally important in preparation for the next purification step – reverse immobilised metal-ion affinity chromatography.

4.2.17 Reverse Immobilised Metal-ion Affinity Chromatography

Before the protein solution was loaded onto the His-Trap column, the protein solution was filtered with 0.45 and 0.22 μm pore-size filters. Once completed, the protein solution was loaded onto the previously used His-Trap HP 1 mL column (§ 4.2.16). Crucially, in this case, the untagged protein was eluted in the flow through before the addition of buffer B, as only the negatively charged endogenous *E. coli* proteins can now bind to the His Trap column and not the now cleaved fluorescent protein. Once the desired fractions were verified to contain the expressed protein of interest, they were pooled and kept on ice before size exclusion chromatography. At this stage, the protein solution was analysed using a UV-spectrophotometer to determine an approximate protein concentration. An approximation of the protein concentration was determined by measuring the absorption at 260 nm and using the Beer-Lambert law described in Equation 14 below. The extinction coefficients for each purified protein were determined from sequencing data and the *Expasy Protparam* online tool.

$$\text{Abs} = \text{Concentration} \cdot \varepsilon \cdot \text{ł} \tag{14}$$

Where Abs is Absorbance measured in arbitrary units; Conc., concentration in Moles/dm^3; ε, the extinction coefficient in $M^{-1}.cm^{-1}$ and l, the path length of the cuvette in cm.

4.2.18 Size Exclusion Chromatography

The final stage of purification involved using a Supradex™ S75 16/600 HiLoad™ column to separate the larger expressed protein from smaller contaminants. This column has a maximum loading volume of 5 mL, which meant the pooled fractions from the reverse IMAC had to be concentrated down to a volume of less than or equal to 5 mL without precipitating the protein out of the solution. This was done using a 15 mL centrifugation filter (Merck) with a molecular weight cut-off of 10,000 Da that was spun at 3,750 g and 4°C for up to 60 minutes. Once complete, the concentrated protein solution was loaded onto the S75 16/600 column and washed with low salt -SEC buffer (Table 18 for composition) at a flow rate of 1.0 mL/min. The S75 16/600 column is packed with chemically inert porous Supradex™ beads, which have a fixed pore diameter, so those larger proteins are forced around the beads as smaller proteins are retained on the column for longer as they can travel through the beads. This column was selected as it can separate molecules with a molecular weight of between 3,000 Da and 70,000 Da, and since all the expressed proteins that were purified in this manner had a molecular weight between 30,000 and 40,000 Da, this column was appropriate. Finally, 20 μL from each of the fractions that gave particularly high absorbance readings at 280 nm were selected for analysis by SDS-PAGE. Once verified, these fractions were pooled and stored at 4°C.

4.2.19 Overlap Integral calculation

The size of the overlap integral, $J(\lambda)$, is an important measure of how efficient the energy transfer will be between the donor and the acceptor in a given FRET pair, as a larger overlap integral for one FRET pair compared to another implies higher efficiency of energy transfer at the same separation distance. This is of particular interest when choosing which fluorophores to use in a FRET experiment, as this directly relates to the dynamic range of the sensor, which is of paramount importance when investigating weak or transient interactions within multimeric complexes. The ability to use a sensor with a

sufficiently large dynamic range can be crucially significant when attempting to detect direct interactions at longer distances.

For the three-colour FRET Cascade system, the overlap Integrals were calculated for each FRET pair: *mTurquoise2-mVenus, mTurquoise2-mScarlet-I, mVenus-mScarlet-I*, the plots for the integrals were made by using equation 15 below.

$$J(\lambda) = \frac{\int_0^\infty F_D(\lambda) \cdot \varepsilon_A(\lambda) \cdot \lambda^4 d\lambda}{\int_0^\infty F_D\ (\lambda) d\lambda} \tag{15}$$

Where, $J(\lambda)$ is the overlap integral in M^{-1} cm^{-1} nm^4, $F_D(\lambda)$ is the fluorescence intensity of the donor with the total intensity of the donor normalised to unity, ε_A is the extinction coefficient of the acceptor in M^{-1} cm^{-1}, and λ is the wavelength in nm.

4.2.20 Excitation and Emission Spectroscopy

Excitation and emission spectra for the eluted purified proteins were performed in a 5 mL quartz cuvette, and measurements were taken on a Horiba FluoroMax® 4 spectrometer. Excitation spectra were recorded between 300 and 600 nm in 1 nm increments with a 5 nm spectral bandwidth, and the emission spectra were taken between 400 and 650 nm in 1 nm increments with a 5 nm spectral bandwidth. For all constructs, the same set of excitation and emission wavelengths were used; for the excitation spectra, the following emission wavelengths were used: 480, 530 and 600 nm. For the emission spectra, the following excitation wavelengths were used: 435, 515 and 590 nm.

4.2.21 Spectral unmixing

Direct excitation of acceptor fluorophores is spectroscopically indistinguishable from that observed from FRET and must be compensated. The emission spectra were observed by exciting the protein with a narrow range of wavelengths in the spectrofluorometer, for example, 435 +/- 2 nm. The spectrofluorometer scanned through a broad range of emission wavelengths (500-650 nm) by rotating a prism within one of the two monochromators while the intensity of the emitted light was recorded for each wavelength. This means that emissions will be detected for any wavelength that can excite the pro-

tein of interest, even at only 1-2% efficiency. This may not have much of an effect when the two fluorophores are spectrally distant, like with mTurq2 and mScarlet but with FPs which are spectrally closer together, such as mTurq2 and mVenus then the amount of mVenus emission detected at 515 nm when excited at 435 nm is not negligible,≈5%.

Each wavelength within the mixed spectrum can represent a combination of intensities from several known fluorophores. The measured spectrum at a given wavelength $I(\lambda)$ can be deconvolved into weighted coefficients (C_i) of each of the individual reference fluorophore spectra ($R_i(\lambda)$). The summed product for n component spectra yields the formula described in Equation 16.

$$I_{(\lambda)} = C_1 \cdot R_1(\lambda) + C_2 \cdot R_2(\lambda) + \ldots C_n \cdot R_n(\lambda) = \sum_i C_i \cdot R_i(\lambda) \quad (16)$$

4.2.22 Circular Dichroism Spectroscopy

Circular Dichroism (CD) is a photophysical phenomenon where certain solutions containing optically active substances that differentially absorb left and right-handed circular-polarised light [178, 179]. This is particularly interesting when investigating solutions containing chiral molecules, such as proteins with chiral amide groups between adjoining amino acids. Differences in CD spectra can give information regarding the amide bond orientation, specifically the dihedral angles and which secondary structures have been formed. Equation 4.2.22-1 below outlines the general concept of Circular Dichroism that describes the difference in absorbance of left circularly polarized (LCP) and right circularly polarized (RCP) light. The Beer-Lambert law can be applied to give the Molar Circular Dichroism $\Delta\,\varepsilon$.

$$\Delta\, Abs(\lambda) = Abs(\lambda)_{LCP} - Abs(\lambda)_{RCP} = [\varepsilon(\lambda)_{LCP} - \varepsilon(\lambda)_{RCP}] \cdot C \cdot\ L = \Delta\,\varepsilon(\lambda) \quad (17)$$

Where Abs = Absorption (*dimensionless*), λ = Wavelength (nm), ε Molar Extinction coefficient (mol^{-1} dm^3 cm^{-1}), C concentration (mol dm^{-3}), L = pathlength (cm).

Ultra-violet and Circular dichroism (CD) spectra of the *mTurquoise2-mVenus-mScarlet-I* and *mTurquoise2-mVenus^{G68A}-mScarlet-I* samples were acquired on the Chirascan Plus spectrometer (Applied Photophysics) using a Suprasil rectangular cuvette (Hellma UK & Starna Scientific Ltd). The instrument was flushed continuously with pure evaporated nitrogen throughout the experiment. For the UV-visible spectra, a wavelength range of 230-800 nm was used with a Spectral Bandwidth of 1 nm, a time per point of 0.5 s and a path length of 10 mm. The far-UV CD spectra used a wavelength range of 195-260 nm with a Spectral Bandwidth of 2 nm, a time per point of 1.5 s and a path length of 0.5 mm. Where appropriate, the CD spectra were smoothed with a window factor of 4 using the Savitzky-Golay method.

The far-UV CD spectra of the samples were recorded at 23°C, cooled to 6°C, heated to high temperature (94°C), and then cooled again to 23°C. The multi-wavelength melting profiles monitored between 195 and 260 nm were recorded during the heating process from 6 to 94°C. The instrument was equipped with a Quantum TC125 Peltier (NorthWest) set to change the temperature from 6 to 94°C at 1°C per minute and 1.5 s time-per-point CD measurement time. The total scan time was 2 minutes per spectrum, and a 1 nm step-size was employed in the 195 to 260 range with a 2 nm Spectral Bandwidth. The temperatures were measured directly with a thermocouple probe in the sample solution & buffer baseline auto-subtracted. Melting temperatures were determined from the derivative CD *vs* Temperature spectra and fitted using a Levenberg–Marquardt algorithm (LMA) on the Van't Hoff isochore. (Global 3, Global Analysis for T-ramp Version 1.2 built 1786, Applied Photophysics Ltd, 2007-2012).

4.2.23 Negative Staining for TEM of the Fluorescent Proteins

Sample preparation requires a buffer exchange before the protein can be sent for negative stain TEM imaging. This was because the matrix the protein was dissolved in, a PBS-based buffer, had to be exchanged for a non-phosphate buffer; a simple TBS-based buffer (20 mM Tris-Cl, 154 mM NaCl pH 7.4) was chosen. This was because excess phosphates tend to crystallise during the staining procedure, which not only creates aggregates but can also reduce the stain's overall contrast. Once a sample buffer exchange was completed on the purified mTurq2-mVenus-mScarlet-I protein, the sample was sent to the Centre for Ultrastructure Imaging (CUI) at King's College London for further preparation and imaging. Due to restrictions surrounding the ongoing

COVID pandemic, I was, unfortunately, unable to do the following sample preparations and subsequent imaging myself, but these were conducted on my behalf by staff at the CUI.

The first step conducted at the CUI was to prepare a protein-stain solution to be added to the EM grid. This was done by first preparing a 2% (w/v) solution of Uranyl acetate adjusted to pH 7.0 with 1M KOH; this was mixed at a 1:1 ratio with the protein sample. The protein-stain mixture was then added to the grid by placing a single drop of the solution onto the formvar grid for approximately 20 seconds and then removing the excess solution with filter paper. The grids were then left to air dry before the excess protein-stain solution was washed off the surface of the grid with double distilled water. The uranyl-acetate solution was used because it obstructs the beam path of the TEM's high-energy electrons, such that only those that reach the camera have not been obstructed by the Uranyl acetate, so they have travelled through the sample. Micrographs of the three-colour protein were taken on grids using the Transmission Electron Microscope (JEM 1400Plus, JEOL) between 60 and 120 kV. Images were acquired with a 2k x 2k format CCD camera (JEOL Ruby CCD Camera, JEOL, Japan).

4.3 Results II: Three-colour FRET Cascade

4.3.1 Assessment of Protein Expression

The FPs mVenus^{G68A}, mTurquoise2- mVenus^{G68A} and mTurquoise2- mVenus^{G68A}-mScarlet-I were successfully expressed (figure 4.3.1-1). Noticeably clear bands can be seen (highlighted in red boxes) at the expected sizes for each of the three proteins 27, 54 and 82 kDa corresponding to the molecular masses for the mVenus^{G68A}, mTurquoise2- mVenus^{G68A} and the mTurquoise2-mVenus^{G68A}-mScarlet-I proteins which indicated that the proteins were produced in the auto-induction culture successfully. Endogenous *E. coli* proteins which have been lysed are also observed; the goal of purification is to selectively isolate the proteins of choice from the endogenous *E. coli* proteins.

The mTurquoise2-mVenus^{G68A} and the mTurquoise2- mVenus^{G68A}-mScarlet-I proteins were found in the pellet and supernatant in roughly equal proportions of soluble and insoluble protein. This would normally be an area of concern, as we want as much of the protein of interest to be in the soluble fraction as this is by far the easiest to extract, purify and handle. The mVenus^{G68A} protein did not express well (figure 4.3.1), with little protein seen at 27 kDa compared to any other expressed proteins. However, the expressed protein was mostly found in the soluble fraction.

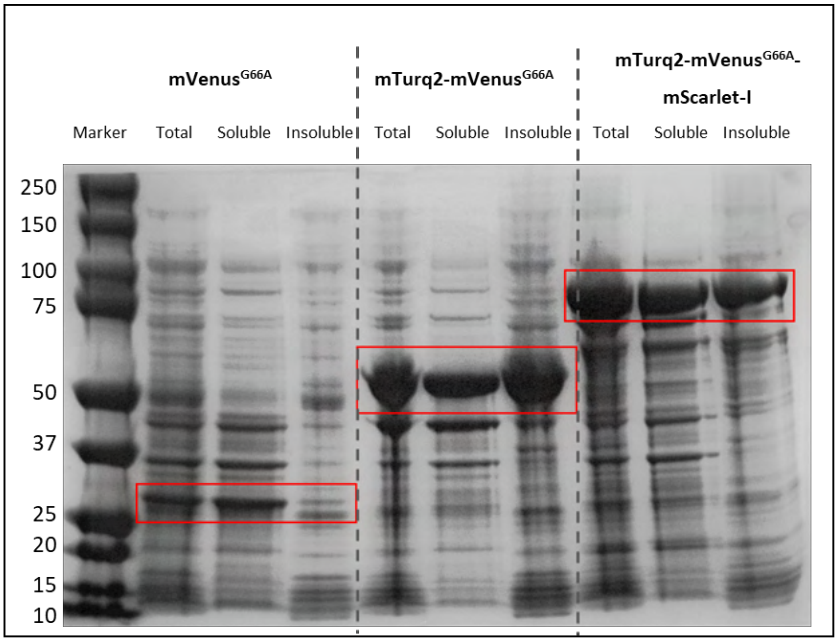

Figure 4.3.1.1: ***Expression test for the three constructs containing the mVenus^{G68A} mutation:*** *A gradient 4-12% Bis-Tris SDS-PAGE showing the total cell lysate, the soluble fraction, and the insoluble fraction from a 1 mL aliquot of BL21 (DE3)* E. coli *cells transformed with the pET-151 -mTurquiose2-mVenus construct and auto-induced over 72 hours.Expected molecular weights for the mVenus^{G68A}, 27 kDa; mTurq2-mVenus^{G68A}, 55 kDa and mTurq2-mVenus^{G68A}-mScarlet-I, 82 kDa.*

4.3.2 Immobilised Metal-ion Affinity Chromatography

Following the successful expression test outlined in §4.3.1, the mTurq2-mVenus constructs were successfully lysed and then purified by Immobilised Metal-ion Affinity Chromatography (IMAC), eluting from the 1 mL HP his-trap column at approximately 200 mM imidazole (figure 4.3.2-1A). Selected eluted fractions were chosen and run out on a 0.8% agarose gel (figure 4.3.2-1B); endogenous *E. coli* proteins are present in the total cell lysate and unbound fractions the two lanes differing by a large distinctive band in the total cell lysate lane at approximately 55 kDa, corresponding to the eluted protein. Selected eluted fractions were pooled before the hexahistidine tag was successfully cleaved by Tobacco Etch Virus (TEV) protease, a kind gift of Dr M. Pfuhl, King's College London. This was done as it allowed for a further Reverse-Immobilised Metal-ion Affinity Chromatography (Reverse-IMAC) purification step (figure 4.3.2-2).

A final purification step was to run a size-exclusion chromatography (SEC) on the pooled fractions from the Reverse-IMAC. This is achieved by passing the sample over a HiLoad® 16/600 Supradex® (Sigma) filtration column. The elution profile for the three-colour mTurq2-mVenus-mScarlet-I protein (figure 4.3.2-3A) shows a large peak at an elution volume of approximately 50 mL corresponding to high molecular weight contaminants filtered from the sample. The next peak on the elution profile is very broad and is found between 63 mL and 83 mL eluted volume. The width of this peak is likely due to endogenous *E. coli* proteins present in the sample of a similar size and weight to our protein of interest, as this peak does not include our protein of interest. This is further evidenced in the accompanying SDS-PAGE (figure 4.3.2-3B), which shows the presence of contaminants alongside a band at 82 kDa, corresponding to our three-colour, protein of interest. Whilst not ideal, if samples were prepared for structural studies such as NMR, X-Ray Crystallography or Cryo-EM, I would want to spend considerably more time ensuring that the samples were cleaner and free of other particulates and contaminants (e.g., Ion-Exchange chromatography). However, in the interests of expediency and as the intended use for these protein samples was primarily used for spectrofluorometry, TCSPC-FLIM, and circular dichroism, it was decided that further purification steps were unnecessary for this project.

Following purification, the concentration of the protein solutions was determined by the Lowry Protein Assay. A standard curve of BSA solutions of known

concentration was plotted (figure 4.3.2-4) in grey, and a linear trendline was fitted with an R^2 goodness-of-fit score of 0.9952 and a linear equation of y=0.1568x+0.061. The linear equation was used to calculate the concentration of the purified protein solutions. These are plotted on the same graph in (green diamonds). Table 16 contains a summary of the molecular weights (Da), Extinction coefficients (M^{-1} cm^{-1}) and concentrations in both units of mg/mL and μM for each purified fluorescent protein.

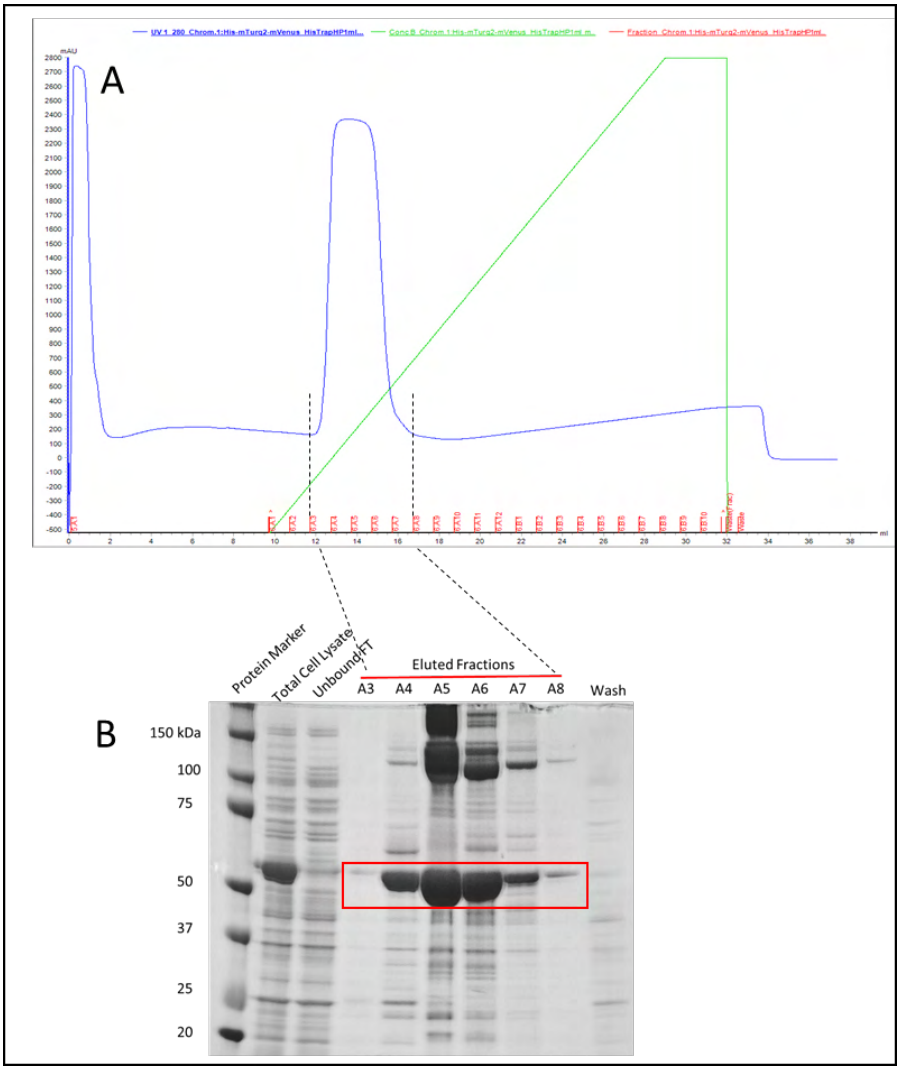

Figure 4.3.2.1: ***Immobilised Metal-ion Affinity Chromatography of the mTurquiose2-mVenus protein:*** *A 1 mL His-Trap HP column loaded with 25 mL of BL21 (DE3)* E. coli *cell lysate transformed with the pET-151 mTurquiose2-mVenus construct and auto-induced over 72 hours. A) the Chromatogram from the Äkta Pure software UNICORN 7 was produced for the IMAC purification of the mTurquiose2-mVenus protein. The chromatogram shows traces for the UV absorption at 280 nm (blue trace), the concentration of elution buffer, buffer B (green trace) and respective elution fractions and volumes (red). B). A 4-12% Bis-Tris SDS-PAGE showing the cell lysate, unbound fraction, eluted fractions, and the wash faction. The eluted fractions show the expected molecular weight of 55 kDa for the mTurquoise2-mVenus protein.*

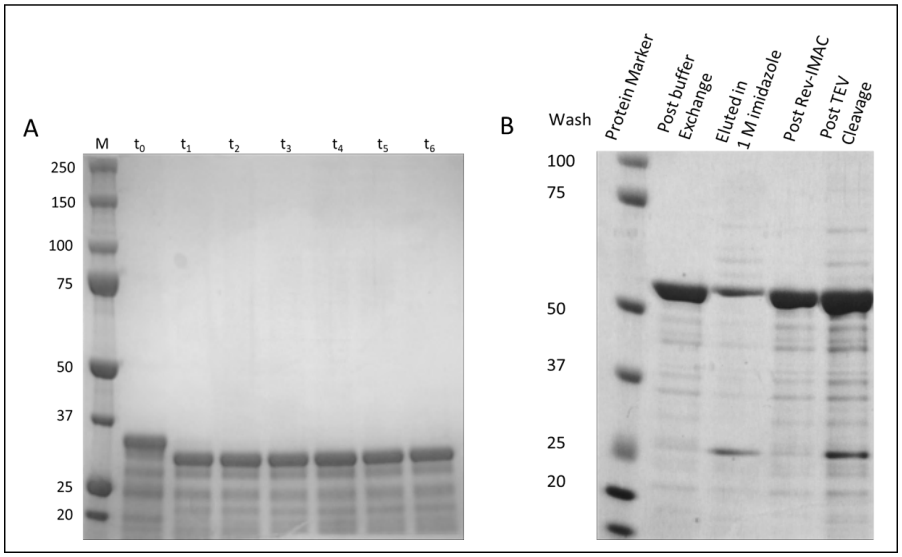

Figure 4.3.2.2: ***TEV Cleavage and Reverse Immobilised Metal-ion Affinity Chromatography of the mTurquiose2-mVenus protein:*** *A) 10% SDS-PAGE showing the samples removed from the TEV cleavage time course over a 6-hour time-period. B) a 4-12% gradient SDS-PAGE showing the progression of purification and clean up.*

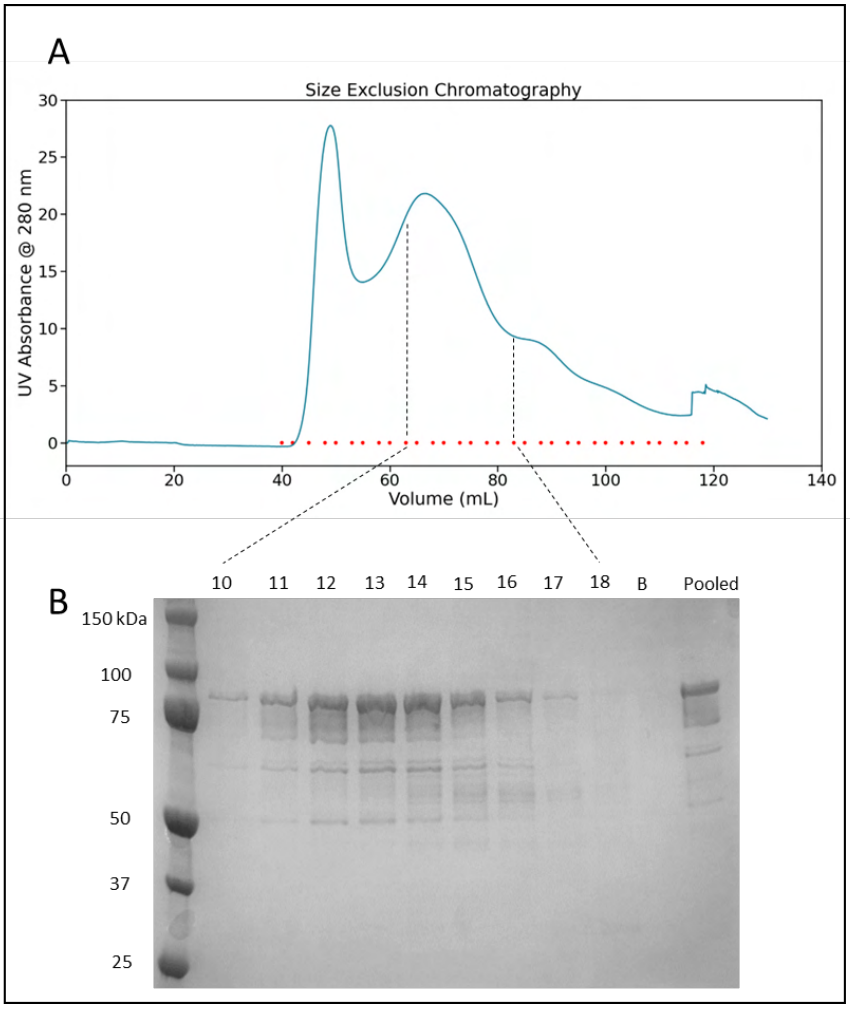

Figure 4.3.2.3: ***Size Exclusion Chromatography of the three-colour protein mTurq2-mVenus-mScarlet-I:*** *A) The elution profile for the purification of mTurq2-mVenus-mScarlet-I by SEC on a HiLoad® 16/600 Supradex® 200 pg column (Sigma). B) 4-12% gradient SDS-PAGE showing the eluted fractions (10-18), Wash (in Buffer B) and the pooled fractions.*

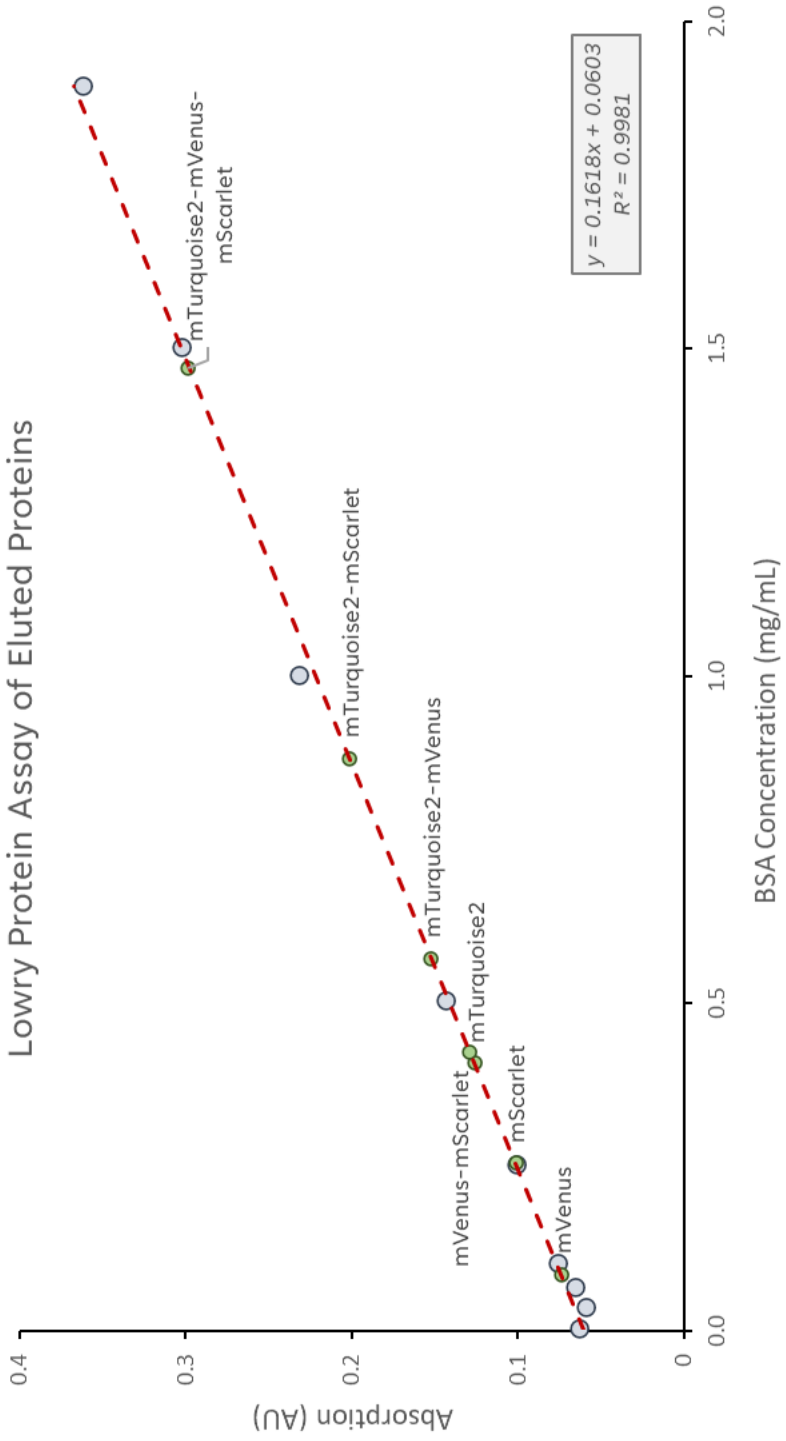

Figure 4.3.2.4: ***Expression test for the three constructs containing the mVenus^{G68A} mutation:*** *A gradient 4-12% Bis-Tris SDS-PAGE showing the total cell lysate, the soluble fraction, and the insoluble fraction from a 1 mL aliquot of BL21 (DE3)* E. coli *cells transformed with the pET-151 -mTurquiose2-mVenus construct and auto-induced over 72 hours.Expected molecular weights for the mVenus^{G68A}, 27 kDa; mTurq2-mVenus^{G68A}, 55 kDa and mTurq2-mVenus^{G68A}-mScarlet-I, 82 kDa.*

Table 16: *A table showing the Molecular weight, Extinction coefficient and concentration of the purified fluorescent proteins*

Protein of Interest	MW (Da)	ε_{280} (M^{-1} cm^{-1})	Conc. (μM)	Conc. (μg/mL)
mTurquoise2	26914.44	26025	9.76	262.61
mVenus	26892.44	23505	4.84	130.08
mScarlet-I	26363.86	34380	10.66	280.94
mTurquoise2-mVenus	54503.55	49530	11.19	609.76
mVenus-mScarlet-I	54009.03	57885	13.88	749.77
mTurquoise2-mScarlet-I	54561.57	60405	15.17	827.46
mTurquoise2-mVenus-mScarlet-I	81620.15	83910	10.70	872.93
mVenus^{G68A}	26878.44	23505	Not purified	
mTurquoise2- mVenus^{G68A}	54489.55	49530	Not purified	
mTurquoise2- mVenus^{G68A}-mScarlet-I	81606.15	83910	7.49	611.05

4.3.3 Overlap Integrals & FRET Efficiencies

The overlap integrals were calculated from the excitation and emission spectra as described in §4.2.19. The green shaded areas shared under the excitation and emission spectra (figure 4.3.3-1) are directly proportional to the size of the overlap integrals, panel D of the figure describe the numerical size of each of the overlap integrals along with the quantum yields of the donors (QY_D), and Förster radii are recorded. The mVenus-mScarlet-I FRET pair exhibit the largest overlap integral, approximately twice the size of the second largest overlap, mTurquoise2-mVenus. The mTurquoise2-mVenus overlap integral was approximately 20% larger than that of the least efficient FRET pair, mTurquoise2-mScarlet. This order is not surprising as we expect pairs of fluorophores that are closer spectrally to have larger overlaps. The product of the overlap integral with the donor-quantum yield is of great importance, as this describes the ability of the donor to transfer energy to an acceptor within a FRET pair. If we compare these values for the three FRET pairs, we see that mVenus-mScarlet-I has the largest corrected overlap integral followed by mTurq2-mVenus and then mTurq2-mScarlet-I.

FRET efficiency against distance for each of the FRET pairs was plotted (figure 4.3.3-2); this shows that even though the three FRET pairs have different overlap integrals and different donor quantum yields, which produce different Förster radii, all three of the FRET pairs have similar dynamic ranges of between 2-10 nm. The relative similarity in FRET sensitivity between the three FRET pairs is important to note.

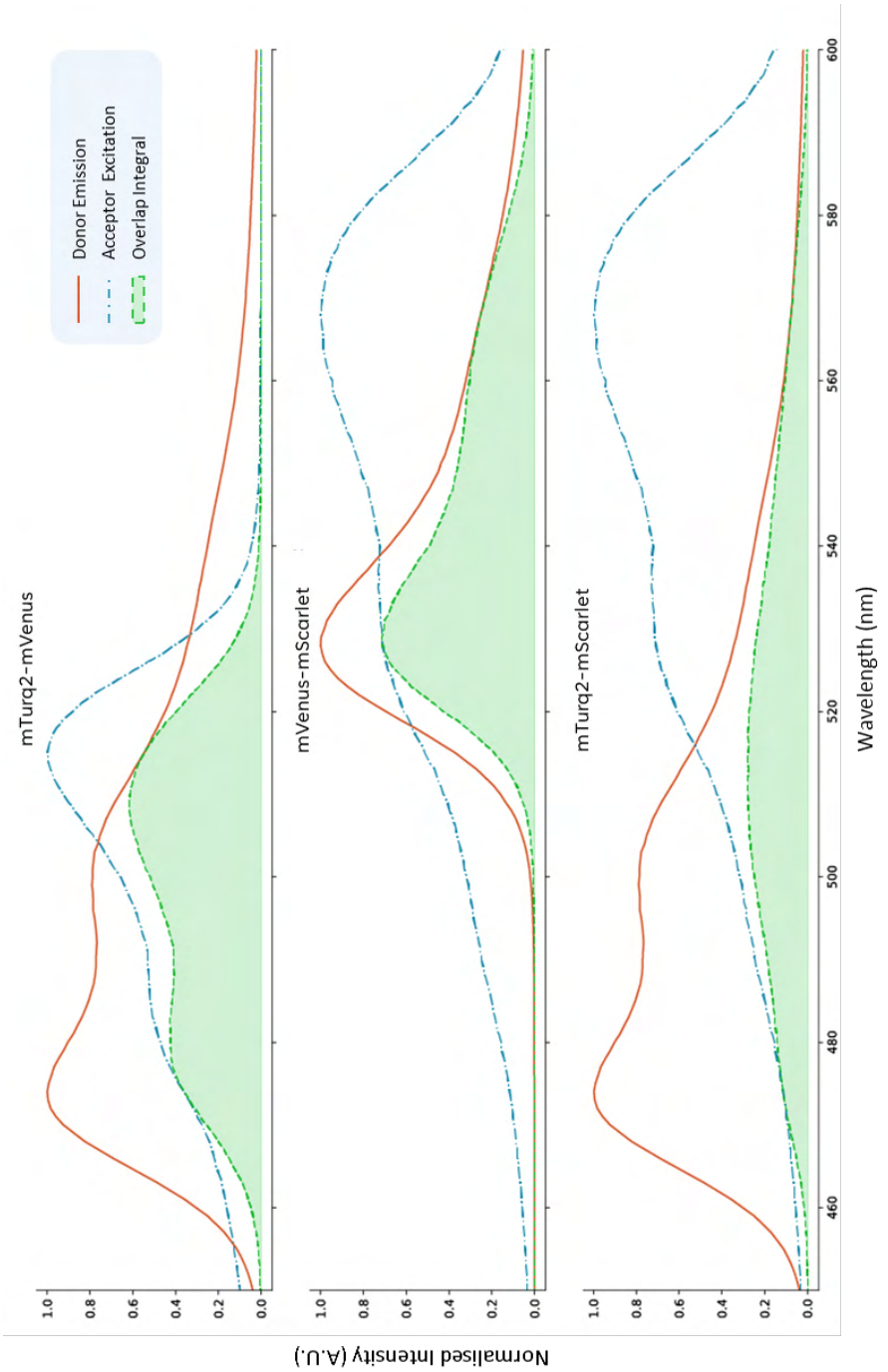

Figure 4.3.3.1: ***Overlap Integrals for the FRET pairs found in the purified FPs:*** *The donor emission spectra (red solid line), the acceptor excitation spectra (blue dot-dashed line) and area overlap integral (green shaded area under the green dotted line) that lies between the donor and acceptor. A) the mTurquoise2-mVenus FRET pair, B) the mVenus-mScarlet FRET pair and C) the mTurquoise2-mScarlet FRET pair. D) A summary table detailing the Quantum yield of the donor (QYD), the Förster radius of the FRET pair in nm, and the overlap integral (Jλ) in* M^{-1} cm^{-1} nm^4.

Table 17: *A summary table detailing the Quantum yields of the purified fluorescent proteins*

	mTurq2-mVenus	mTurq2-mScarlet	mVenus-mScarlet
QY_D	0.93	0.93	0.64
R_0 (nm)	5.83	5.08	5.53
$J\lambda$ (M^{-1} cm^{-1} nm^4)	$2.29x10^{15}$	$9.95x10^{14}$	$2.41x10^{14}$

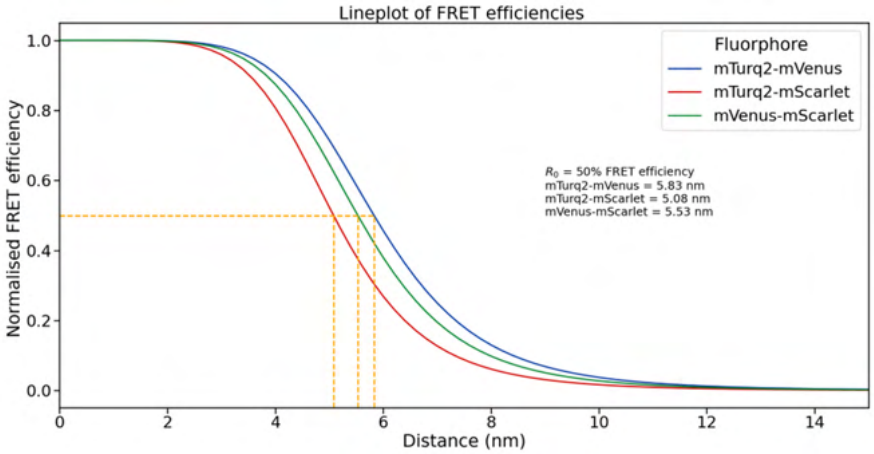

Figure 4.3.3.2: ***FRET Efficiency versus distance for the three FRET pairs:*** *Red line shows the distribution of FRET efficiencies for the mTurquoise2-mScarlet FRET pair, the green line shows the distribution of FRET efficiencies for the mVenus-mScarlet FRET pair and the blue line the mTurq2-mVenus FRET pair. The yellow dotted lines indicate R_0 the Förster radii for each FRET pair, this is where the FRET efficiency is equal to 50%. mTurq2-mVenus = 5.83 nm, mTurq2-mScarlet-I = 5.65 nm, and mVenus-mScarlet-I = 6.19 nm.*

4.3.4 Emission Spectra of the Fluorescent Protein FRET Pairs

For each purified protein, excitation and emission spectra were collected (figures 4.3.4-1 to 3); spectra for mTurq2, mVenus and mScarlet-I are shown across the three figures for reference. In figure 4.3.4-1, the three single FP spectra are compared with mTurquoise2-mVenus (mTurq2-mVenus) and mTurquoise2-mScarlet-I (mturq2-mScarlet). The mTurq2-mVenus FP shares very similar excitation spectra with the reference excitation spectra for mTurq2 alone; this is because, in both cases, only the mTurq2 was excited at its peak excitation wavelength of 435 nm. The difference between these two proteins can be seen in their emission spectra, especially considering the peak at approximately 530 nm corresponding to the mVenus emission spectra. It is important to note that this construct has no spectral features corresponding to mScarlet-I emission spectra. As there was very little direct excitation of the mVenus at 435 nm for the mTurq2-mVenus protein, we can conclude that the emission peak found at approximately 530 nm must be a direct consequence of the mTurq2 acting as a donor in the mTurq2-mVenus FRET pair, with the magnitude of the acceptor emission being a qualitative measure of ratiometric FRET.

A similar pattern also arises when examining the mTurquoise2-mScarlet-I protein; as with the previous example, only the donor, mTurq2, was excited (at 435 nm), and peaks corresponding to the emission of mTurq2 and mScarlet are observed, as expected. The relative heights of the emission peaks must also be proportional to the FRET efficiency between those two fluorophores.

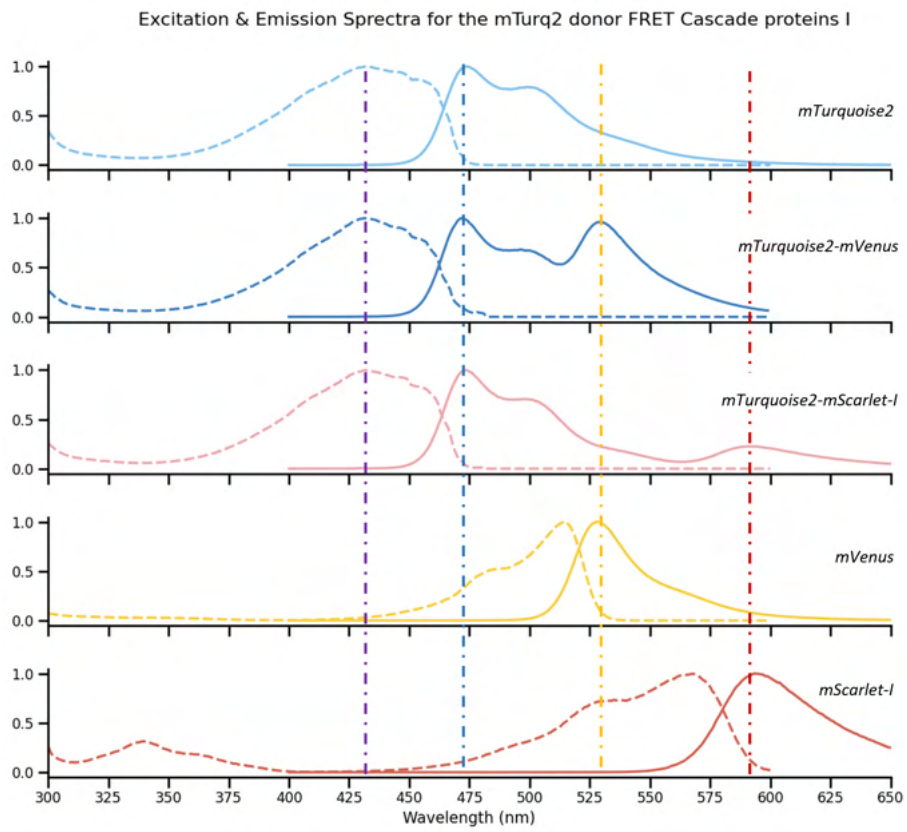

Figure 4.3.4.1: ***Excitation and Emission spectra for the three-colour mTurq2 Donor FRET Cascade fluorescent proteins II:*** *Spectroscopic measurements were taken on a FluoroMax®4 spectrofluorometer (Horiba), 2 mL of purified fluorescent protein was loaded into the spectrofluorometer in a quartz cuvette before the excitation and emission spectra were measured for each protein. Excitation spectra are in dashed lines and the emission spectra in solid lines, and all spectra are normalised to their peak intensities. The emission spectra were collected by exciting the mTurq2uoise2, mTurquoise2-mVenus^{G68A}-mScarlet-I and mTurquoise2-mVenus-mScarlet-I at 430 nm. For proteins consisting of three FPs, the donor measured is marked in bold. For comparison purposes, mVenus and mScarlet-I emission spectra are also shown in this panel, their emission spectra were collected by exciting at 510 and 560 nm respectively. Excitation spectra for the mTurquoise2, mTurquoise2-mVenus^{G68A}-mScarlet-I and mTurquoise2-mVenus-mScarlet-I proteins were also collected at an emission wavelength of 480 nm, the mVenus and mScarlet Emission spectra were collected 530 and 600 nm respectively.*

Comparing the emission spectra of the mTurq2 alone with the emission spectra of the three-colour protein mTurq2-mVenus-mScarlet-I (figure 4.3.4-2), we can see that by just exciting the mTurq2 FP in the three-colour protein at a wavelength of 435 nm, peaks in its emission spectra are observed that correspond to the emission peaks found in all three of the reference spectra. Furthermore, the relative heights of these peaks give a qualitative indication of FRET efficiency. A relatively high amount of FRET between the mTurq2 and mVenus fluorophores can be inferred due to the large peak in the three-colour protein emission spectra at 530 nm. We can also see in the same emission spectra that there is an additional peak at approximately 590 nm, which matches up with the emission spectra in the mScarlet-I. This peak has a lower intensity than the peaks observed at 480 and 530 nm, which may result from cascaded FRET. Only the mTurq2 FP in the three-colour protein was excited, so for there to be an emission peak at 590 nm, there must first have been a FRET transition between mTurq2 and mVenus followed by a second transition where the mVenus acted as the donor and was able to directly excite the mScarlet-I. There could also be a component of mTurq2-mScarlet FRET, but the increased separation due to mVenus being present would significantly reduce the efficiency compared to observed for the mTurq2-mScarlet-I construct.

The other tripartite protein is the mTurquoise2-mVenus^{G68A}-mScarlet-I protein; this differs from the previously discussed mTurq2-mVenus-mScarlet-I protein as this has the glycine-68-alanine mutation in the mVenus FP. This mutation prevents mVenus from acting as an acceptor, as it cannot form a complete chromophore and may be assumed to be a non-fluorescent beta-barrel (see §4.1.1 for more details) acts as a control for the FRET-Cascade model. As expected, the mTurquoise2-mVenus^{G68A}-mScarlet-I protein shares the same emission peak positions at 480 and 590 nm as the shorter mTurq2-mScarlet-I protein, but the intensity of the 590 nm peak in comparison to 480 nm is significantly different smaller for the longer, mTurquoise2-mVenus^{G68A}-mScarlet-I protein. This is because there is much less FRET occurring between the mTurq2 and mScarlet in the mTurquoise2-mVenus^{G68A}-mScarlet-I protein than in mTurq2-mScarlet-I. The increased separation distance between the mTurq2 and mScarlet is approximately twice that of the mTurq2-mScarlet-I construct due to adding a mutated "dark" mVenus.

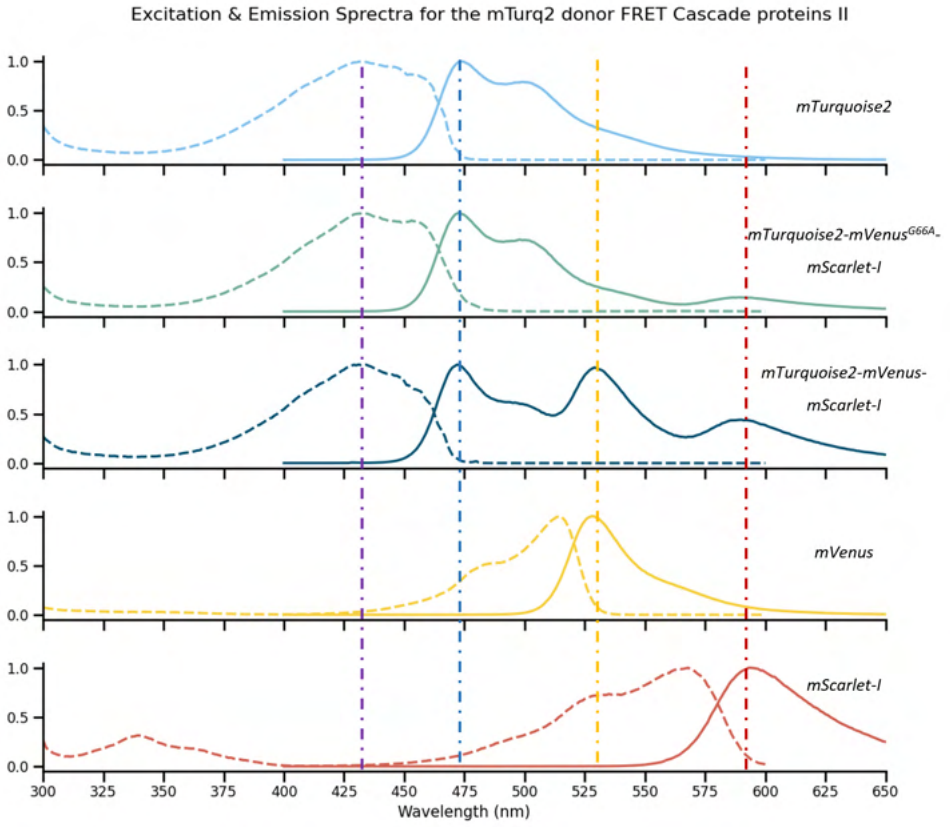

Figure 4.3.4.2: ***Excitation and Emission spectra for the three-colour mTurq2 Donor FRET Cascade fluorescent proteins II:*** *Spectroscopic measurements were taken on a FluoroMax®4 spectrofluorometer (Horiba), 2 mL of purified fluorescent protein was loaded into the spectrofluorometer in a quartz cuvette before the excitation and emission spectra were measured for each protein. Excitation spectra are in dashed lines, and the emission spectra are in solid lines, and all spectra are normalised to their peak intensities. The emission spectra were collected by exciting the mTurq2uoise2, mTurquoise2-mVenus^{G68A}-mScarlet-I and mTurquoise2-mVenus-mScarlet-I at 430 nm. For proteins consisting of three FPs, the donor measured is marked in bold. For comparison purposes, mVenus and mScarlet-I emission spectra are also shown in this panel, their emission spectra were collected by exciting at 510 and 560 nm respectively. Excitation spectra for the mTurquoise2, mTurquoise2-mVenus^{G68A}-mScarlet-I and mTurquoise2-mVenus-mScarlet-I proteins were also collected at an emission wavelength of 480 nm, the mVenus and mScarlet Emission spectra were collected 530 and 600 nm respectively*

A final set of observations and comparisons can be made for proteins with an mVenus donor (figure 4.2.7-3); for these proteins, the mVenus was directly excited at 510 nm, and the emission was measured at 530 and 590 nm for mVenus and mScarlet emission respectively. For the mVenus-mScarlet-I protein, the peaks observed in the emission spectra correspond with those found in mVenus and mScarlet-I FPs reference spectra as expected. From the relative heights of the peaks, it is possible to infer that energy transfer was particularly favourable with a peak height greater than half of the donor for the acceptor, mScarlet-I emission at 590 nm. As with the three-colour mTurq2-mVenus-mScarlet protein, the emission peak for the first acceptor, mVenus, at 530 nm was almost as intense as that of the mTurq2 (>90%). The mVenus then acts as a donor for mScarlet-I; however, the peak intensity for the mTurq2-mVenus-mScarlet-I protein at 590 nm is only around 60% of mVenus. However, the intensity of the mScarlet-I emission peak (when directly exciting mVenus) in both the *mTurq2-mVenus-mScarlet-I* and *mVenus-mScarlet-I* proteins should be almost identical. The fact that they are not may indicate that there is spectral bleed-through between donors and acceptors which are spectrally closer like mTurq2→mVenus and mVenus→mScarlet-I which have indicated larger energy transfers than more spectrally distance FRET pairs like the mTurq2→mScarlet-I transition either in the presence of or absence of mVenus. This would be logical, given the Stokes shift between mTurq2 and mScarlet-I.

Lastly, the three-colour fluorescent protein *mTurq2-mVenus-mScarlet-I* is shown with the mVenus FP used as the only donor, as it was excited at 510 nm instead of 435 nm. We can see that the excitation spectrum looks quite different compared to the mVenus-mScarlet-I protein due to the mTurq2 in the construct, which is why it can be seen in the excitation spectrum. As expected, the Emission spectrum has the same shape with peaks in the same positions as the mVenus-mScarlet-I protein. The height of the mScarlet emission peak at 590 nm is approximately the same as seen in the mVenus-mScarlet-I protein, which is expected, although it could be an indication of direct excitation of the acceptor, as previously mentioned.

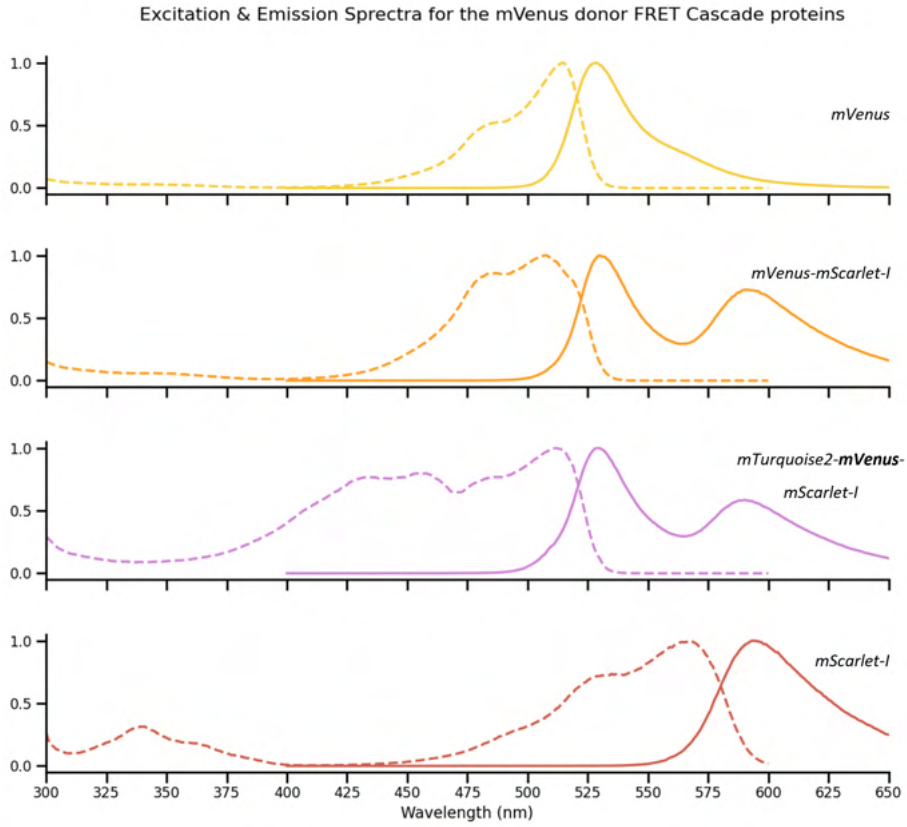

Figure 4.3.4.3: ***Excitation and Emission spectra for the mVenus Donor FRET Cascade fluorescent proteins :*** *Spectroscopic measurements were taken on a FluoroMax®4 spectrofluorometer (Horiba), 2 mL of purified fluorescent protein was loaded into the spectrofluorometer in a quartz cuvette before the excitation and emission spectra we measured for each protein. For all proteins, the excitation spectra are in dashed lines and the emission spectra in solid lines, the spectra are normalised to their peak intensities. For proteins consisting of three FPs, the donor measured is marked in bold. The emission spectra were collected by exciting the mVenus, mVenus-mScarlet, and mTurquoise2-mVenus-mScarlet-I at 510 nm. For comparison, the mScarlet-I emission spectrum is also shown in this panel, the emission spectrum was collected by exciting at 560 nm. Excitation spectra for the mVenus, mVenus-mScarlet, and mTurquoise2-mVenus-mScarlet-I proteins were collected at an emission wavelength of 530 nm, the mScarlet excitation spectra were collected at 600 nm.*

4.3.5 Spectroscopic Ratios

Spectra described in the previous section were further analysed to determine a parameter descriptive for FRET efficiency observed for the various combinations of fluorescent proteins. Unfortunately, the relative heights of the intensities of the emission peaks cannot be used directly to calculate the FRET efficiency. This is largely due to two reasons: a difference in quantum yield and molar extinction coefficients for the different FRET pairs and the second overlapping spectra need to be deconvolved or unmixed as the tail of one emission spectra will almost certainly run into the rising component of another emission spectra, examples of which can be seen in figures 4.3.4-1, 2 and 3. Spectra can, however, be deconvolved successfully by solving a simple linear algebra equation resulting in a series of component spectra.

Applying linear unmixing to the emission spectra (figures 4.3.4-1, 2 and 3) was relatively simple, as the component spectra are known, needing only the relative intensity weighting for each spectrum to be determined. This was accomplished with a linear algebra Solver toolkit in MS Excel. The ratio of donor-acceptor weighting coefficients was used to approximate the FRET efficiency between the various protein pairs. There are some discrepancies between the measured (blue) and the modelled (orange) spectra (figure 4.3.5-1), most notably in the region between 480 and 530 nm, where the measured spectrum dips significantly lower than that of the modelled spectrum. There are several possible reasons for this; there may be a non-linear scaling issue associated with the detector gain. However, the same dip is found in all the constructs with mTurq2 as the donor. The second possible cause could be because the two proteins are joined by very short linkers (6 amino acid GGSGGS), which may be causing some parts of the beta-barrels to flex or stretch in such a way that alters the emission spectra and, by extension the FRET ability of the donor. This may seem unlikely; however, studying the emission spectra for each FRET pair show a significantly diminished emission from mTurq2 in the 480-530 nm region compared to the mTurq2 alone spectra.

Finally, the photochemistry of the mTurq2 is likely more complex than we consider. For example, the two emission peaks observed for mTurq2 at 475 and 500 nm correspond to two distinct spectroscopic states of mTurq2, which may have different probabilities of resonant energy transfer. This could lead to a differential reduction in the peak heights. Similarly, the expected polarisation

changes in this region, due to increases in donor anisotropy due to the reduction in fluorescence lifetime (Perrin Equation [164]) and depolarisation of the acceptor may manifest in the uncorrected polarisation sensitivity of the spectrometer. This is beyond the scope of this thesis and will be explored through collaboration with Prof Angus Bain (UCL) using more advanced spectroscopic techniques. Unfortunately, the global COVID-19 pandemic prevented us from exploiting this collaboration during my PhD.

Even though this is a considerable deviation from the measured spectrum, it should not prevent us from calculating the weighted coefficients and subsequent donor/acceptor ratios. These ratios are a qualitative measure of FRET magnitude between the interacting pairs. These are related but not directly proportional to the FRET efficiency, which has not been calculated here. Indeed, a greater FRET ratio would indicate higher FRET efficiency, but quantitative measurements of fluorescence lifetime are more accurate than ratiometric measurements; an example is the FRET ratio shown above for the mTurq2-mVenus construct to be approximately 62 %, whereas the mTurq2-mScarlet-I was found to be 19.5%. These efficiencies should be approximately the same as both FRET pairs are the same distance apart, have similar R_0 values, and have the same donor. A more robust method is required, such as TCSPC-FLIM.

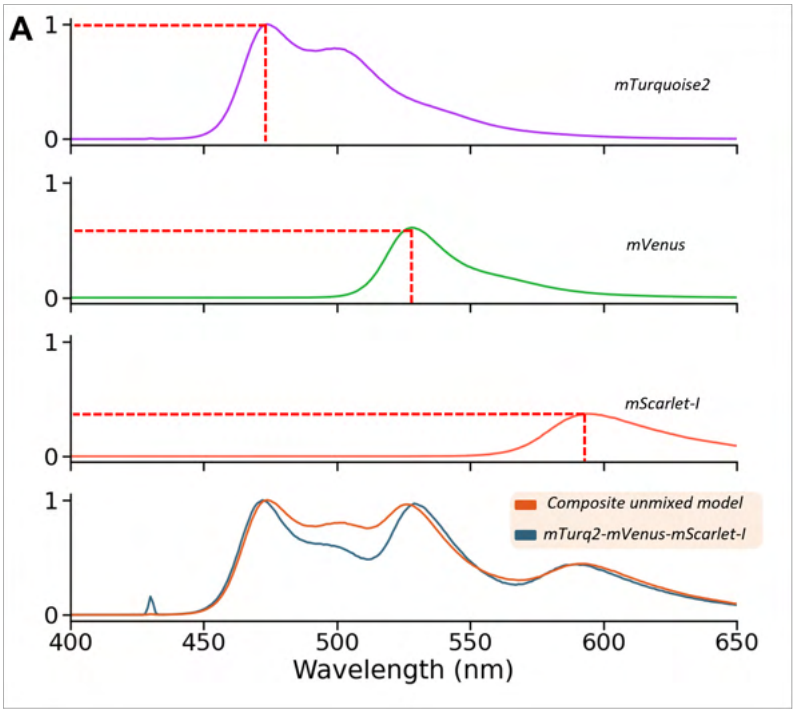

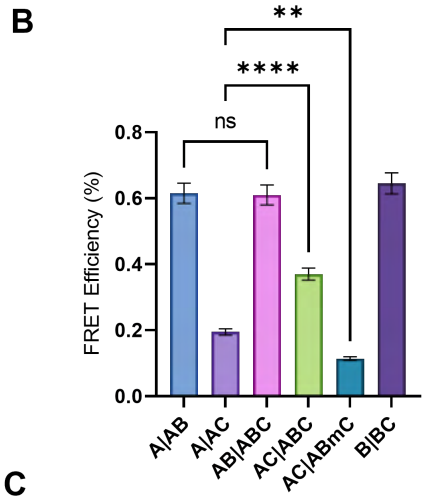

C

	mTurq2-mVenus	mTurq2-mScarlet-I	mVenus-mScarlet-I	mTurq2-mVenus^{G66A}-mScarlet-I	mTurq2-mVenus-mScarlet-I	
					mTurq2-mVenus	mTurq2-mScarlet-I
FRET (%)	61.50	19.49	64.5	11.40	61.05	37.45

Figure 4.3.5.1: ***Relative FRET Efficiencies calculated from the emission spectra of the FRET Cascade FPs:*** *FRET efficiencies were calculated for specific transitions by dividing the acceptor emission peak by the donor alone emission peak within the normalised emission spectra for that given FRET pair. The above graphs illustrate which FRET transitions are significantly different between the various proteins. A|AB represents the mTurq2-mVenus donor-acceptor pair, A|AC the mTurq2-mScarlet donor-acceptor pair and B—BC the mVenus-mScarlet donor-acceptor pair. AC|ABC represents the mTurq2-mScarlet-I FRET pair in the three colour protein and AC|AB^{G68A}C represents the same FRET pair but in the mutated mTurq2-mVenus^{G68A}-mScarlet-I protein. A One-way ANOVA with Dunn–Šidák correction was used to produce the pairwise comparisons. N=9 measurements cells per condition across three separate technical repeats, P-values $\geq$ 0.123 ns, $\leq$ 0.0332 (*), $\leq$ 0.0021 (**), $\leq$ 0.0002 (***), $\leq$ 0.0001 (****).*

4.3.6 Circular Dichroism Data

The difference between the two three-colour fluorescent protein constructs, mTurq2-mVenus-mScarlet-I and mTurq2-mVenus^{G68A}-mScarlet-I, is only a single point mutation within the mVenus on residue 68, which was mutated from glycine to an alanine. From the assessment of protein production (§4.2.1), we saw that when mVenus^{G68A} was produced in isolation, very little of the mutant was produced. Encouragingly though, the other two proteins contain the same mutation: mTurq2-mVenus^{G68A} and mTurq2-mVenus^{G68A}-mScarlet-I, were expressed in significant amounts. The reason for this is unclear, but we know it is possible to produce a single protein containing the mVenus^{G68A} mutation. A major concern is that the G68A mutation changes the overall tertiary structure of the beta-barrel in some way which prevents the mVenus^{G68A} from being used as an effective non-fluorescent spacer.

The near-UV spectrum (Figure 4.3.6-1) is particularly sensitive to changes in the overall shape of a protein, especially changes in the tertiary structures. The information collected in the 250–300 nm region is due to the absorption, dipole orientation and interactions with the surrounding environment of the aromatic amino acids: phenylalanine, tyrosine, and tryptophan [178]. The near-UV CD is also sensitive to cysteine residues and whether these pairs have formed disulphide bridges [179]. Unlike far-UV CD, the near-UV CD spectrum cannot be assigned to any singular 3D structure. Rather, the near-UV CD spectra can provide information on any changes to the 3D structure.

There is a large degree of similarity between the two near-UV CD spectra (4.3.6-1.A), with two notable exceptions being the 250-300 nm and 430-580 nm regions. The difference in the latter is simple to explain, as the absence of an active mVenus chromophore no longer has an absorbance peak at 515 nm in the mutant. This can also be seen in companion absorbance spectra (figure 4.3.6-1.B), wherein the absorbance spectra for the same proteins, a difference can be seen for the same region surrounding the 515 nm absorbance peak associated with mVenus; this is absent for the mVenus^{G68A} protein.

The 250-300 nm region in the near-UV CD spectra also looks significantly different between the two spectra, particularly at ~ 280 nm. This would most likely correspond to the absorption of Tryptophan and tyrosine, which are well known to strongly absorb at 280 nm and are routinely used to estimate protein concentration based on their absorption. The induced mutation is a simple swap between glycine and alanine and does not include

any aromatic residues; furthermore, the absorption spectra (figure 4.36-1 panel B) do not indicate any changes in aromatic residues within this region. This must mean that the environment, either a tyrosine or tryptophan residue in one of the three-colour fluorescent proteins, must be altered for the mVenus^{G68A}-containing construct. The simplest explanation is that for the mTurq2-mVenus-mScarlet-I constructs, the tyrosine in position 68 is successfully converted into the mature mVenus chromophore. This changes the structure of the tyrosine and its local environment, as it is now part of a larger delocalised system interacting with many more residues through intermolecular bonding.

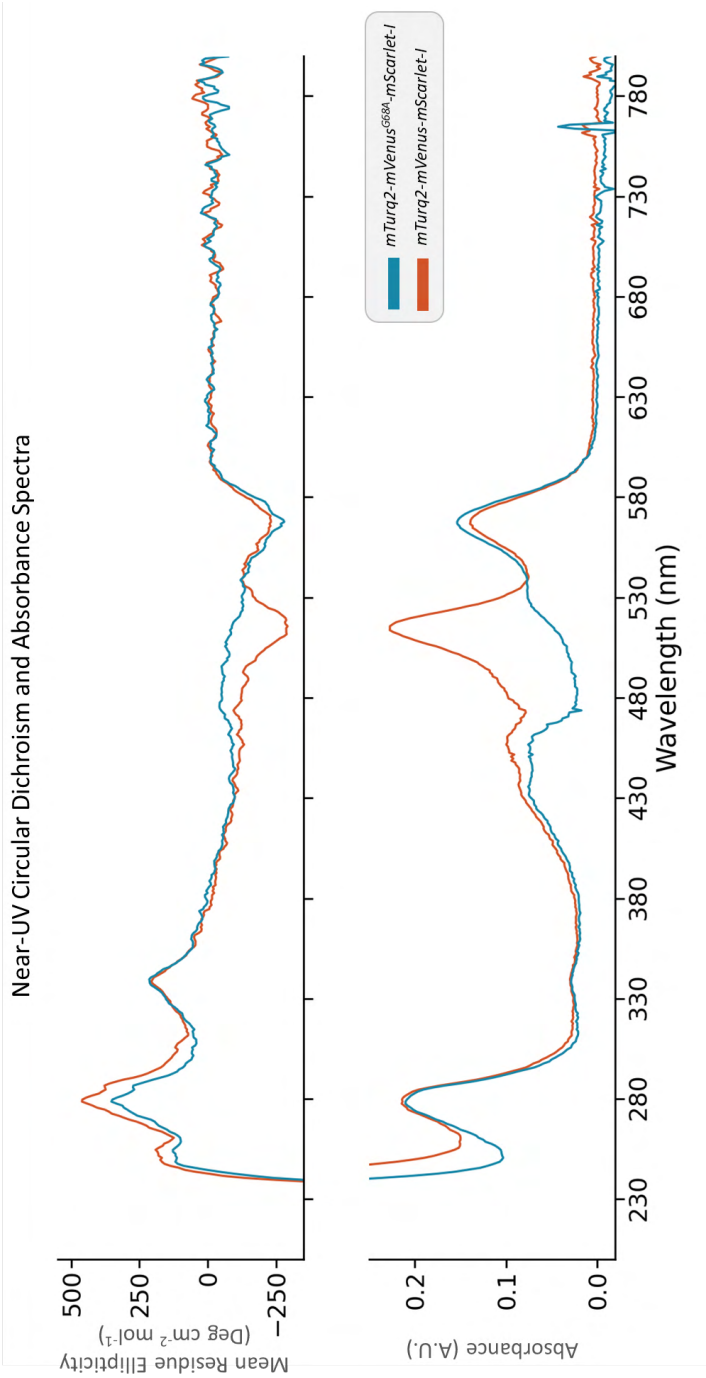

Figure 4.3.6.1: ***Near-UV Circular Dichroism and Absorbance Spectra:*** *The UV-vis absorption and near-UV Circular dichroism (CD) spectra of the mTurquoise2-mVenus-mScarlet-I and mTurquoise2-mVenus^{G68A}-mScarlet-I proteins were acquired on the Chirascan Plus spectrometer (Applied Photophysics) using a Suprasil rectangular cuvette (Hellma UK & Starna Scientific Ltd). A) shows the near-UV CD spectra and B) shows the near UV-vis absorption spectra for the two three-coloured FPs*

The far-UV spectra (figure 4.2.9-2 panel A) can reveal important characteristics of a protein's secondary structure. Electronic transitions associated with the chiral amide groups can be detected with far-UV CD. This is of particular interest, as only certain dihedral angles, ϕ and ψ, are permitted and can be used to predict the secondary structure of a peptide through the Ramachandran plot [179, 180]. Specifically, peaks found ≈190-200 nm correspond to $\pi \longrightarrow \pi^*$ transitions associated with the carbonyl bonds (C=O) within the amide and troughs ≈210-220 nm are $n \longrightarrow \pi^*$ transitions associated with amino bonds (N-C) within the amide group [178]. The relative size and position of these peaks and troughs can yield much information about the secondary structures and environments [178, 179, 181]. Far-UV spectra can be used to estimate the amount of each secondary structure within a protein; this can then be used to make some limited predictions about the 3D structure of the protein [181]. Alternatively, in our case, whether there are any significant structural changes between the mVenus^{G68A} or mVenus-containing constructs.

The three-colour fluorescent proteins share very similar spectra with minimal differences between the two proteins, mTurq2-mVenus-mScarlet-I and mTurq2-mVenus^{G68A}-mScarlet-I. The shape of the far-UV CD spectra (figure 4.3.6-2A) suggests that the proteins are mostly beta-sheets due to the broad trough around 190-220 nm and the rise towards a peak around 195-200 nm. This result confirms that the proteins are formed primarily from beta sheets, as we would expect, for a pair of proteins comprised of three beta-barrels, each consisting of 11 beta sheets and one coaxial helix per barrel [165].

Far-UV Spectra were also recorded over a range of temperatures (figure 4.3.6-2B (cut-out)); the change in Mean Residue Ellipticity (deg cm^2 dmol^{-1}) against temperature for a single wavelength at 205 nm was recorded for three-colour proteins. A single wavelength was chosen between the two transitional regions ($\pi \longrightarrow \pi^*$ and $n \longrightarrow \pi^*$) to best demonstrate changes in the dihedral angles and, by extension, changes in secondary and tertiary structure are caused as a function of temperature. The mVenus-containing protein (red) remains mostly unchanged until approximately 60°C, whereas the mVenus^{G68A}-containing protein (blue) has some major changes by 50°C. This suggests that there is a difference in thermal stability between the proteins and there may still be the possibility that the mutant is not as tightly folded in the absence of a mature chromophore.

The results of secondary structure analysis using the BeStSel (Beta Structure Selection) (Figure 4.2.9-2 panel C) demonstrate that the algorithm has predicted the same secondary structures for three-colour proteins. This is not surprising, as there is very little difference in their far-UV spectra. For comparison, I was able to input the CD spectra for the individual FPs, mTurq2, mVenus and mScarlet from reference spectra and calculate what we might expect to see for an average structure containing those FPs. The expected data (green bars) shows some moderate difference but nothing significant, apart from an overestimation of the anti-parallel (right-twisted) beta sheet and a slight underestimation of the unstructured region. This is a good indication overall that there is not a significant difference between the three-colour proteins in terms of the secondary and tertiary structures; the mutation may have reduced the overall stability of that protein, especially at higher temperatures which may be the reason during protein production and extraction, less of that protein was successfully extracted than the mVenus variant.

It is also possible that when produced as a single FP, mVenus^{G68A} was not sufficiently stable to be produced by *E. coli* growing at 30°C and could require a specialised strain of bacteria for culturing at a lower temperature, such as the ArcticExpress-DE3 (Agilent Technologies) commercial strain of *E. coli*. These are a B strain of *E. coli,* much like the BL21 (DE3) strain which I used to express the FPs used in this chapter, but crucially, they can be cultured between 4-12°C and express the GroEL/ES complex of chaperonins [182]. It has been shown [182] that these specialised low-temperature *E. coli* strains exhibit high protein refolding activities at the lower-growth temperatures, approximately 16-fold greater than cells grown at 30°C. If desired, the mVenus^{G68A} protein could be produced in isolation using the ArcticExpress-DE3 cells grown at 12°C.

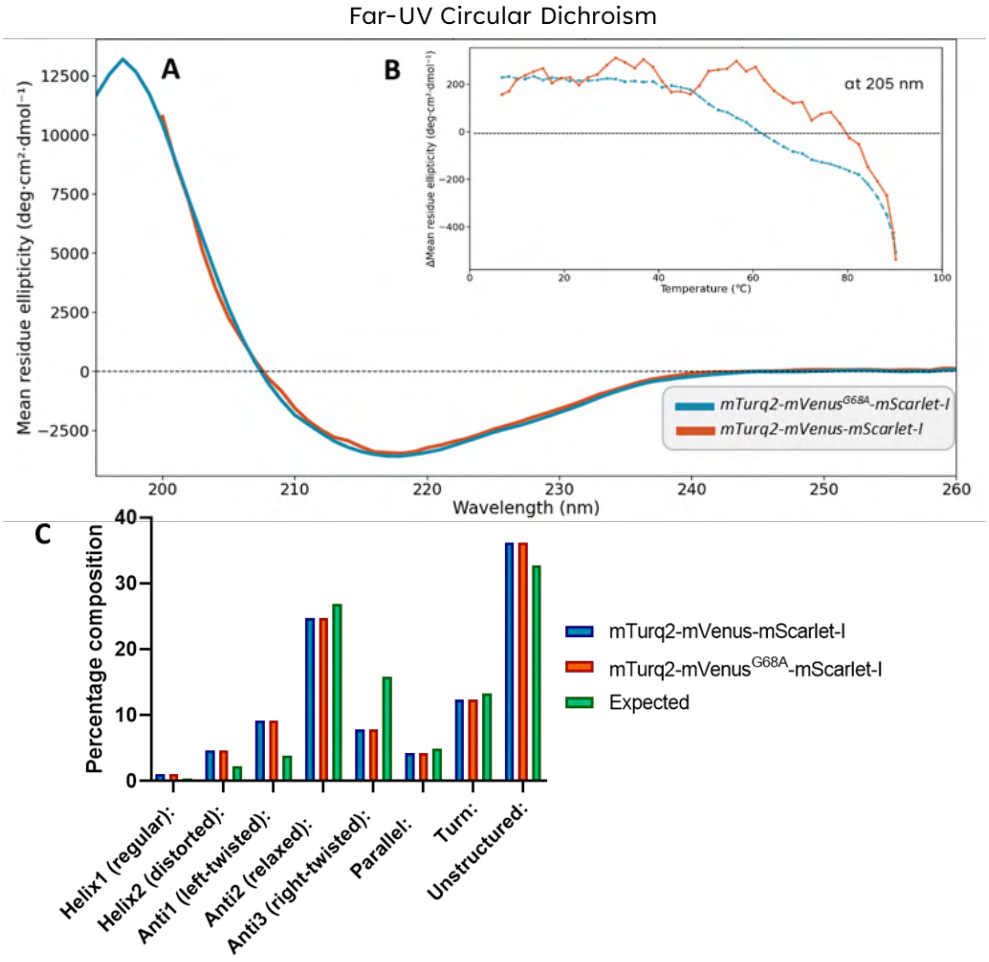

Figure 4.3.6.2: ***The Far-UV Circular Dichroism Spectra for the two three-coloured FRET Cascade FPs:*** *The far-UV CD spectra were collected using a Chirascan Plus spectrometer (Applied Photophysics), spectral measurements were taken between 195-260 nm with a Bandwidth of 2 nm, a time per point of 1.5s and a pathlength of 0.5 mm using a Suprasil rectangular cuvette (Hellma UK & Starna Scientific Ltd). A) shows the far-UV CD spectra and B) shows the change in Mean Residue Ellipticity as a function of heating at a specific wavelength of 205 nm. Multi–wavelength melting profiles was collected by first cooling the samples to 6° C before heating to 94° C using a Quantum TC125 Peltier (NorthWest). C) Percentage composition versus secondary structure type for the two three-colour FPs and the expected – average secondary structure for the three fluorophores. CD spectra analysis was performed using the BeStSel (Beta Structure Selection) single spectrum analysis online tool (https://bestsel.elte.hu/index.php)*

4.3.7 Average lifetimes for the FRET cascade model applied to Fluorescent Proteins Measured in Solution

Fluorescence lifetime measurements were recorded to quantify the resonance energy transfer between the FPs and novel constructs in the FRET-Cascade model. The average fluorescence lifetimes for the measured purified fluorescent proteins (figure 4.3.7-1 panel A) were recorded. The control mTurq2 fluorescence lifetime decay was measured as 4.18 ± 0.072 ns. When expressed as a FRET pair with either mVenus or mScarlet, a significant drop in fluorescence lifetime was observed, 2.71 ± 0.041 and 2.60 ± 0.068 ns, respectively. This reduction in fluorescence lifetime for both two-colour proteins was statistically significant (p-values of < 0.0001). Similar fluorescence lifetime reductions were observed for the two three-colour proteins mTurq2-mVenus-mScarlet-I and mTurq2-mVenus^{G68A}-mScarlet-I with lifetimes measured as 2.43 ± 0.081 and 3.21 ± 0.076 ns respectively (P-values <0.0001). For each transient, a mono-exponential decay function was used with Levenberg-Marquardt (LMA) fitting algorithm (figure 4.3.7-2). This was found to be a good fit as determined by the chi-squared goodness-of-fit test.

The mVenus alone control fluorescence lifetime was measured as 2.95 ± 0.025 ns, whereas the fluorescence lifetime for the mVenus-mScarlet FP was found to be 2.38 ± 0.055 ns which was determined to be statistically significant (P-value <0.0001) from the mVenus alone fluorescence lifetime. Additionally, the lifetime of the mVenus FP within the three-colour mTurq2-mVenus-mScarlet-I protein was also recorded; this was found to be 2.51 ± 0.074 ns, which is not significantly different (P-value 0.682) from the lifetime of the mVenus in the mVenus-mScarlet FP. This is as expected, as we would not expect the mTurq2 FP within the three-colour protein to have an appreciable effect on the mVenus-mScarlet interaction when only the mVenus is directly excited at 950 nm (two-photon excitation).

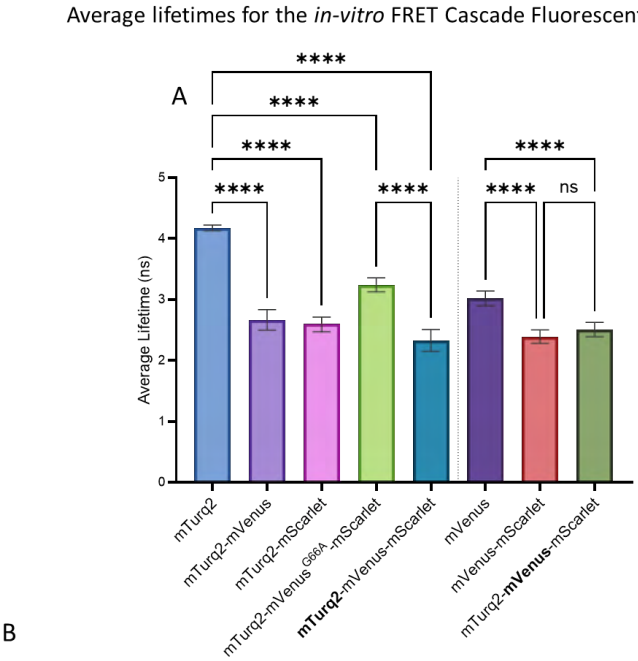

B

	mTurq2	mTurq2-mVenus	mTurq2-mScarlet	mTurq2-mVenus^{G66A}-mScarlet	**mTurq2**-mVenus-mScarlet	mVenus	mVenus-mScarlet	mTurq2-**mVenus**-mScarlet
LMA Fit	Mono	Mono	Mono	Mono	Mono	Mono	Mono	Mono
Average Lifetime (ns)	4.179	2.706	2.603	3.205	2.426	2.953	2.383	2.509
Average χ^2 / d.f.	0.949	1.095	0.908	0.991	1.089	1.159	1.058	1.075

Figure 4.3.7.1: ***Average lifetimes for the FRET Cascade Fluorescent Proteins Measured in Solution:*** *Lifetime measurements were taken with a home build TCSPC-FLIM imaging system built around a Nikon Ti-Eclipse microscope and Coherent chameleon Vision II Ti-Sapphire laser source. Donors were excited at 875 nm (TPE) for mTurq2 and 950 nm (TPE) for mVenus. For proteins consisting of three FPs, the fluorophore in bold is the donor. Lifetimes were determined using TRI2. Pixel binning (23x23) was used with a Levenberg-Marquardt Algorithm fitting for a mono-exponential decay curve for each transient recorded. A) A graph showing the average lifetime recorded for each FP; error bars indicate SD. B) A summary table of the values plotted in part A showing the average lifetime (ns), the type of Levenberg–Marquardt algorithm (LMA) fit used, and the average $\chi 2$/degrees of freedom score. N=9 measurements cells per condition across three different technical repeats, P-values $\geq$ 0.123 ns, $\leq$ 0.0332 (*), $\leq$ 0.0021 (**), $\leq$ 0.0002 (***), $\leq$ 0.0001 (****).*

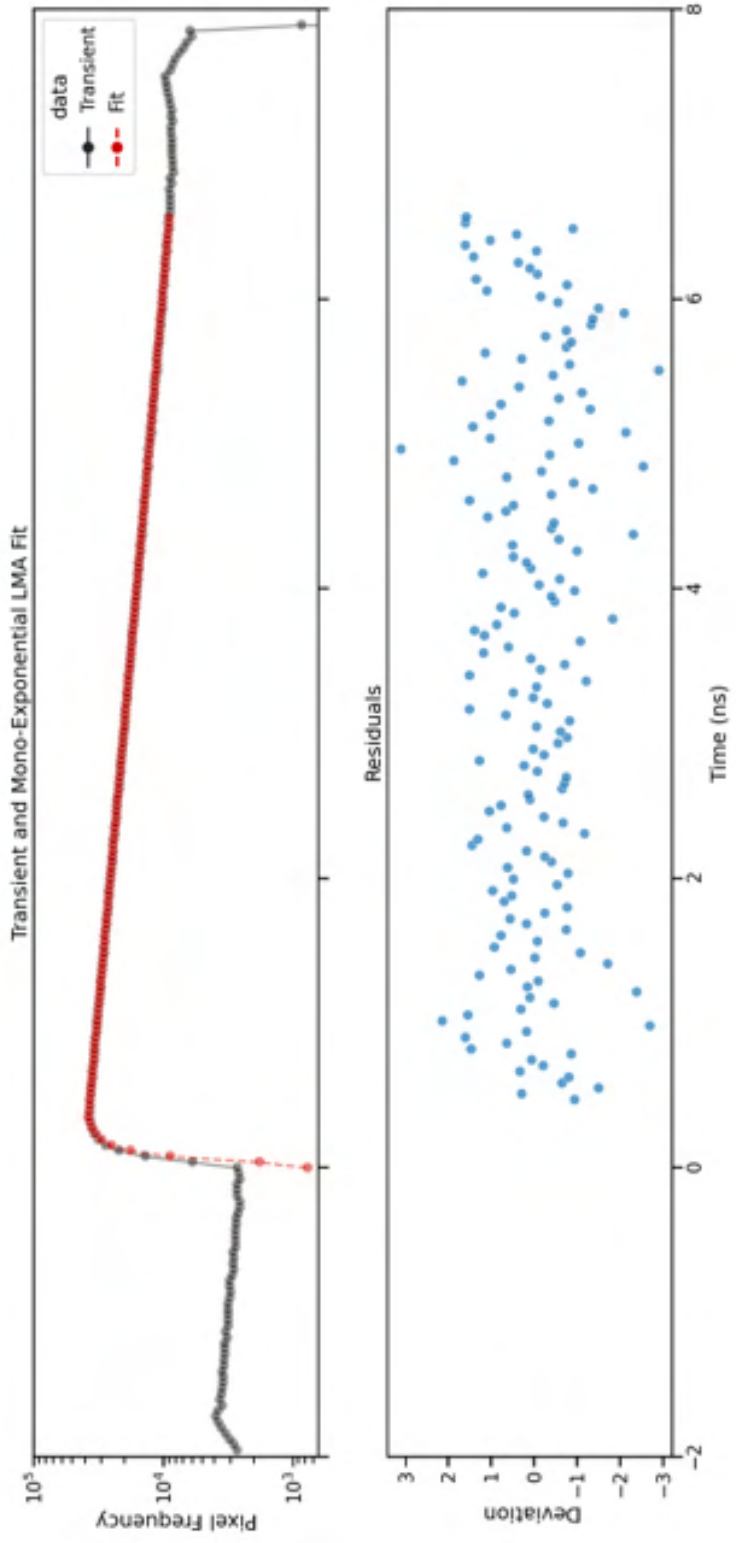

Figure 4.3.7.2: *Semi-log plot of a pixel frequency versus time:* *The transient lifetime decay (black) was recorded as part of the TCSPC-FLIM measurements taken for each FP, and data were fitted with a mono-exponential Levenberg-Marquardt fitting algorithm (red) with deviations from the fit are shown (blue).*

4.3.8 FRET Efficiencies and Energy Transfer Rates for the FRET Cascade Fluorescent Proteins Measured in Solution.

Fluorescence lifetime data of single FPs cannot tell us very much in isolation, as there are many factors, mostly environmental, which may alter the fluorescence lifetime of a fluorophore, only one of which is FRET. Furthermore, to better understand the complex interactions involved in the assembly of a multimeric system, then a metric that allows comparison of resonant energy transfer between any two close partners over time as the complex multimeric changes spatiotemporally are required.

For brevity, when explaining FRET transitions which require a donor and an acceptor to be named, I will use A, B and C to denote the proteins in the model FRET-Cascade, where A is mTurq2, B is mVenus, and C is mScarlet-I. When describing FRET transitions, it is often important to make clear which of the FPs in the FRET pair is the donor and which is the acceptor; I have produced my nomenclature to describe this. For example, A|AB would describe mTurq2 as the donor as this is the first letter before the vertical line and is in the mTurq2-mVenus protein, whereas B|ABC would be used to describe a transition where mVenus is the donor in the mTurq2-mVenus-mScarlet-I protein.

The FRET efficiency for the A|AB transition in the mTurq2-mVenus FRET pair was calculated as 38.51±1.95%, which significantly increases to 48.40±1.03% with the addition of mScarlet-I (for mTurq2-mVenus-mScarlet-I). This result is very much as anticipated, as we expect to see a high degree of FRET between the mTurq2 and mVenus due to their large spectral overlap and short separation distance. The decrease in fluorescence lifetime in the presence of mScarlet-I for the three-colour FP indicates an additional decay pathway from the mTurq2 excited state. No additional lifetime reduction from mTurq2 should be indicated if the energy cascades through mVenus to mScarlet-I, whereby the excited mVenus undergoes a second FRET transition with mScarlet-I. The additional lifetime reduction from mTurq2 in the mTurq2-mVenus-mScarlet-I FP must come from the FRET between the mTurq2 and mScarlet-I.

There are several possible FRET transitions for the mTurq2-mVenus^{G68A}-mScarlet-I, six in total, but only three will be discussed here. The individual FRET components must be isolated to build a sound theoretical model of all the possible transitions. The mTurq2-mVenus^{G68A}-mScarlet-I does not have a functional mVenus that could function as a potential acceptor for mTurq2,

and there is no conceivable way for FRET to cascade through the three-colour system. Any FRET transition determined must be due to a direct transition between the mTurq2 and mScarlet-I. We can see that a FRET efficiency of 22.4% was calculated for this transition (figure 4.2.11-1A and B). This is significantly (P-value < 0.0001) different from the non-mutant ABC protein, taken at face value, it would suggest that almost half of the FRET calculated for the ABC protein was due to direct FRET, whereas the other half was a result of FRET via mVenus.

One possible interpretation of these results could be that the mTurq2-mScarlet FRET efficiency within the three-colour mutant, A|AB^{G68A}C FRET was significantly lower than that of the mTurq2-mVenus FRET efficiency in the A|ABC and A|AB proteins. However, this is not the case, as the FRET efficiency for the A|AC (mTurq2-mScarlet-I) protein was calculated to be ≈38%. The FRET efficiency for the mTurq2-mScarlet-I protein was almost identical to the mTurq2-mVenus FRET pair with a P-value of only 0.0436 difference between the two populations. The separation distance is far more likely to be greater, resulting in a change in the measured FRET efficiency. The mVenus-mScarlet FRET efficiencies were also calculated from fluorescence lifetime data with the B|BC protein ≈20.8% FRET efficiency, and the B|ABC FRET efficiency, ≈16.9% was found not to be significantly different. These two FRET pairs essentially describe the same transition in different environments. The distances between the FRET pairs (figure 4.3.7-1B) were determined using the FRET efficiencies and the Förster radii and equation (18) below, which describes the relationship between separation distance, the Förster radius and FRET efficiency.

$$r = \sqrt[\frac{1}{6}]{\left(\frac{1-E}{E}\right) \cdot {R_0}^6} \tag{18}$$

A simplified diagram outlining the FRET transitions between the three fluorophores and the distances separating (figure 4.2.11-1D) suggests a non-linear, triangular 3D structure based on the calculations performed using equation (18). To calculate the transfer rates between each FP, we need to describe each process that depopulates the excited state of the mTurq2 donor. If we consider the lifetime of the mTurq2, approximately 4.18 ns. of the reciprocal transfer rate is the transfer rate K_A is equal to the reciprocal of the mTurq2 donor (where the subscript denotes the species A) lifetime and is

the sum of the radiative and non-radiative transfer rates (k_r, k_{nr}). Equation (19) below describes this formally.

$$\frac{1}{\tau_A} = K_A = (k_{nr} + k_r) \tag{19}$$

We can apply the same logic to the mTurq2-mVenus protein; in this scenario, the same radiative and non-radiative processes act on the mTurq2 donor as with the donor alone. The only difference now is that there is an acceptor within a sufficient distance of the mTurq2 donor to induce another non-radiative transition, FRET. For this protein, we will describe the FRET transfer between A and B as Γ_{AB}. Equation (20) below describes the energy transfers that occur for the FRET pair mTurq2-mVenus (AB)

$$\frac{1}{\tau_{A|AB}} = K_{A|AB} = (k_{nr} + k_r) + \Gamma_{AB} \tag{20}$$

Following on from the previous example, we can apply the same process for the mutated three-colour AB^{G68A}C protein where there is no longer an mTurq2-mVenus (A -> B) FRET interaction, but there is an mTurq2-mVenus (A -> C) FRET interaction but in the presence of the non-fluorescent β-barrel mVenus^{G68A}. Below, equation (21) describes the transfer rate between the mTurq2 and mScarlet in the mTurq2-mVenus^{G68A}-mScarlet protein.

$$\frac{1}{\tau_{A|AB^{G68A}C}} = K_{A|AB^{G68A}C} = (k_{nr} + k_r) + \Gamma_{AC} \tag{21}$$

Now that we have a method for describing the energy transfers and, in particular, the FRET transitions, we can assemble a series of energy transfers which would be equivalent to the energy transfers for the (mTurq2-mVenus-mScarlet-I protein. Equation (22) below outlines the energy transfer rate for the mTurq2-mVenus-mScarlet-I protein.

$$\frac{1}{\tau_{A|ABC}} = K_{A|ABC} = (k_{nr} + k_r) + \Gamma_{AB} + \Gamma_{AC} \tag{22}$$

This can be verified as we know the reciprocal of the donor alone lifetime is equal to the K_A The transfer rate and we can subtract the K_A rate away from the $K_{A|AB}$ and $K_{A|AB^{G68A}C}$ rates to give the Γ_{AB} and Γ_{AC} in isolation. Summing these as described in equations (22) will give a theoretical transfer rate, which can be experimentally checked by comparing it with the lifetime measured for the mTurq2 donor in the mTurq2-mVenus-mScarlet-I protein. The transfer rates were used to produce a calculated theoretical transfer rate of 4.44 x 10^8 s^{-1} which would correspond to a fluorescence lifetime of 2.25 ± 0.391 ns (figure 4.3.8-1C). Compared to the measured lifetime of 2.33 ± 0.27 ns with an associated transfer rate of 4.29 x10^8 $s^{-1,}$ this represents a discrepancy of only 3.4%, which is well within the margin of error. This indicates that our model and interpretation of the results are self-consistent, giving us confidence in our interpretation and measurements.

FRET Efficiencies for the *in-vitro* FRET Cascade Fluorescent Proteins

A

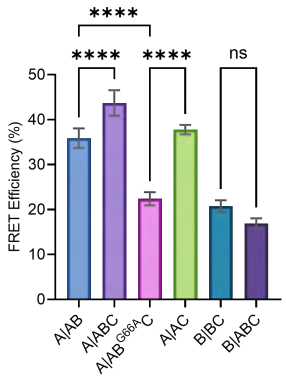

D

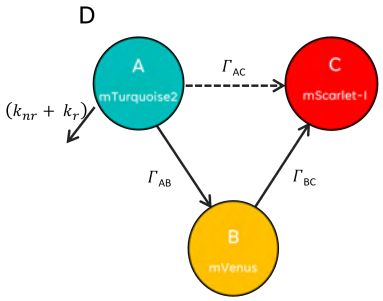

B

	A|AB	A|AB^{G68A}C	A|ABC	A|AC	B|BC	B|ABC
FRET Efficiency (%)	36.1%	22.4%	44.2%	37.8%	20.8%	16.9%
Standard deviation	0.413	0.230	0.410	0.155	0.423	0.444
R_0 (nm)	5.83	5.08		5.08	5.53	5.53
Distance, r (nm)	6.41	6.25		5.52	6.91	7.21

C

	K_TA	$K_TA\|AB$	Γ_{AB}	$K_TA\|AB^{G68A}C$	Γ_{AC}	$K_TA\|ABC$ Calculated	$K_TA\|ABC$ Measured	Diff (%)
Energy Transfer (s^{-1})	$2.39x10^8$	$3.75x10^8$	$1.35x10^8$	$3.08x10^8$	$6.91x10^7$	$4.44x10^8$	$4.29x10^8$	
Standard deviation	$1.09x10^7$	$6.35x10^7$	$2.29x10^7$	$3.52x10^7$	$4.65x10^6$	$7.70x10^7$	$4.89x10^7$	
Lifetime (ns)	4.178	2.668	7.382	3.242	14.464	2.253	2.332	3.40%

Figure 4.3.8.1: ***FRET Efficiencies for the in-vitro FRET Cascade Fluorescent Proteins:*** *FRET efficiencies were calculated using the FRET efficiency equation (see equation (22)). A) Shows the average FRET efficiencies for the various FRET pairs graphically. Where A=mTurquoise2, B=mVenus and C=mScarlet, for FRET pairs the letter before the line marks the donor, so A—ABC denotes the FRET efficiency measured where the donor is A, mTurquoise2 and B—ABC would denote the FRET efficiency measured where the donor is B, mVenus in the mTurq2-mVenus-mScarlet protein. B) A summary table describing the FRET efficiencies, standard deviation, the calculated Forster radii for each FRET pair and the calculated separation distance between the FRET pair. C)A summary table detailing the Energy transfer rates, standard deviation and the associated lifetime of each FRET component. D) A diagram showing the three fluorescent proteins joined by their short 6 amino acid linkers. The diagram shows the radiative, non-radiative and FRET transfers, along with a likely 2D conformation of the three-colour mTurq2-mVenus-mScarlet protein. N=9 measurements cells per condition across three separate technical repeats, P-values $\geq$ 0.123 ns, $\leq$ 0.0332 (*), $\leq$ 0.0021 (**), $\leq$ 0.0002 (***), $\leq$ 0.0001 (****).*

As described in the previous section, we now know the approximate FRET transfer rates for each FRET pair and have been able to use these to calculate estimates for the separation distances between the fluorophores. Thus, by making a simple calculation using the cosine rule, we can approximate the average angle, which subtends ABC, the separation angle. A diagram illustrating this is shown in panel D of Figure 4.3.8-1, along with the distances, FPs, and estimate for the calculated angle. The angle was calculated as described using the equation (23) and found to be $62.43 \pm 3.83^{\circ}$ ($1.09 \pm 0.067\pi$ radians)

$$\theta = \cos^{-1}\left(\frac{\overrightarrow{AB}^2 + \overrightarrow{BC}^2 - \overrightarrow{AC}^2}{2 \cdot \overrightarrow{AB} \cdot \overrightarrow{BC}}\right) \tag{23}$$

Where, $\overrightarrow{AB}$ is the length of the vector that lies between mTurq2 and mVenus, $\overrightarrow{BC}$ is the length of the vector that lies between mVenus and mScarlet and $\overrightarrow{AC}$ is the length of the vector that lies between mTurq2 and mScarlet. Figure 4.2.11-3A illustrates the relationship between the angle which subtends mTurq2-mVenus-mScarlet-I (θ) and the distance determined by FRET between mTurq2 and mScarlet-I as a polar plot (blue trace) where distance is shown radiating outwards from the centre, and the separation angle θ is shown in degrees anti-clockwise. The inner red circle outlines a separation distance of 2.5 nm (minimum diameter of a beta-barrel from an x-ray structure)54, and the associated shaded red sector in the graph corresponds to the angles which would bring the centres of the two beta-barrels closer than 2.5 nm. Circles drawn in yellow denote the distance determined by FRET between mTurq2 and mScarlet $\approx 7.14 \pm 0.166$ nm, where these lines meet the blue cardioid, marked in green, corresponds to the separation angle in degrees.

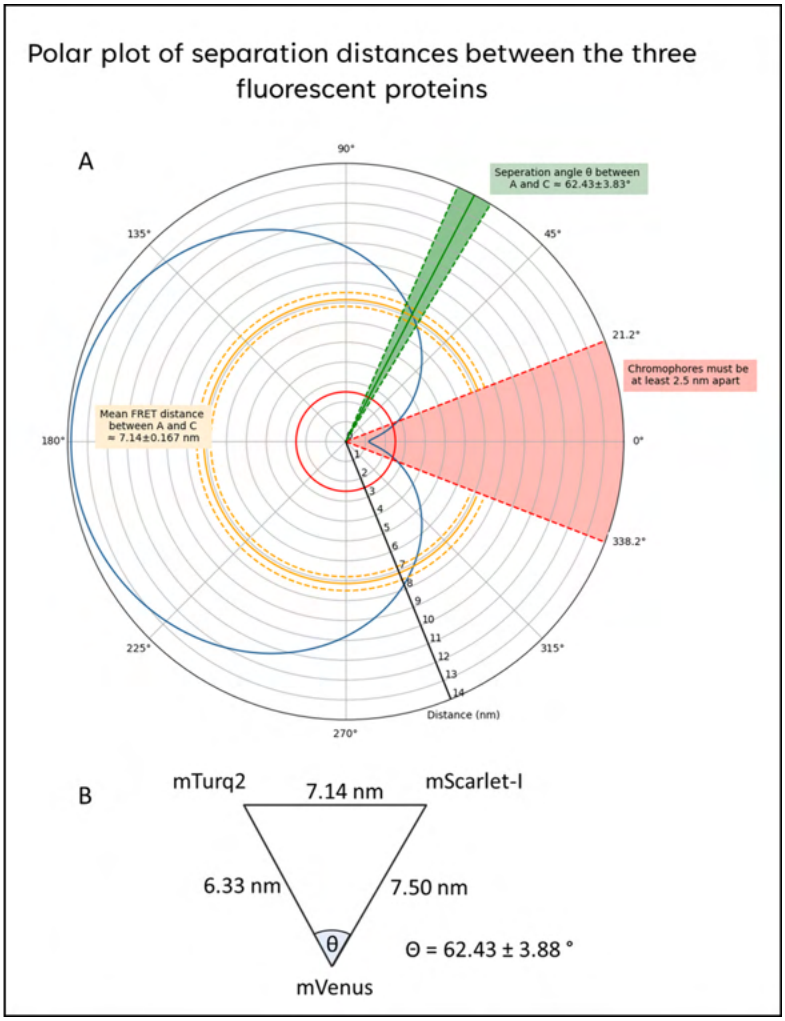

Figure 4.3.8.2: ***Polar plot of separation angle versus distance for the mTurq2-mVenus-mScarlet protein:*** *A) Shows a polar plot of theta. This separation angle lies between mTurq2 and mScarlet against the distance between mTurq2 and mScarlet. The angle theta was calculated using equation 4.3.7. B) Is a graphical representation of the distances between each fluorophore and the calculated separation angle.*

4.3.9 Average lifetimes for the FRET cascade model applied to Fluorescent Proteins expressed in MEFs

So far, the work was undertaken to describe the three-colour FRET The cascade system has been focused on *in vitro purified proteins* by either measuring excitation and emission spectra using a spectrofluorometer, measuring CD spectra or imaging droplets of concentrated protein solutions with our home-built TCSPC-FLIM system. One of the key directions that I wanted to push the development of this three-colour technique was to apply the *in vitro* model into an *in vivo* model, first applied to fixed cells and then, if successful, towards live cells. This next subsection deals with the same constructs mentioned before, but instead of purified proteins, DNA constructs containing the relevant genes for the fluorescent proteins were transiently transfected into MEFs and imaged using TCSPC-FLIM.

The average fluorescence lifetime for the mTurq2 alone transfected cells is lower than that of the *in vitro* protein measurements (figure 4.3.9-1), decreasing from 4.18 ns to 3.06 ns. It is not immediately obvious why this might be, only that the internal environment of a fixed, mounted cell is not the same as the well-buffered and, crucially, the well-defined composition of the protein solution. mTurq2, like many other fluorescent proteins tend to have different, often lower lifetimes in fixed and mounted samples compared to lifetimes measured in solution [183]. The mTurq2 FP is known to be particularly sensitive [183, 184] to alterations in pH and potentially the $NaBH_4$ treatment and mounting in Mowiol-488 (a glycerol-based mountant) may have had an undesirable impact on the the fluorescence lifetime of that specific fluorophore [183].

The lifetimes of the *in vivo* fluorescent proteins are comparable to the corresponding *in vitro* lifetimes, although with more variation; this is likely due to the added complexity of imaging through a cell at a considerably lower concentration than the protein solutions. In solution, individual molecules diffuse in and out of the focal plane due to Brownian motion, and no one fluorophore is directly excited for any considerable length of time. This is not the case with fixed cells as a smaller number of fluorophores are initially imaged and, when cycled through many more successive rounds of excitation and emission, are more likely to become irreversibly damaged through photo-bleaching.

The mVenus donor alone lifetime is significantly lower in cells (Figure 4.3.9-2) than in solution, a decrease of 2.95 ± 1.59 to 2.37 ± 0.067 ns, a reduction of approximately 500 ps. Again, it is not clear why the lifetimes of the donor-alone FPs are much shorter. A significant decrease in the lifetime of the mVenus alone constructs measured in cells compared to the purified construct has caused a large decrease in the overall amount of FRET calculated in the MEFs compared to the purified proteins measured in solution. This has resulted in much lower significance being reported between the average mVenus lifetime in the donor alone and the mVenus in the mVenus-mScarlet FRET pair. With a P-value of 0.0124 (only one *) for the mVenus + mVenus-mScarlet FRET pair. Encouragingly, the lifetimes of the mVenus-mScarlet construct and the lifetime of the mVenus as a donor in the mTurq2-mVenus-mScarlet three-colour FRET cascade construct are not significantly different, with a P-value of 0.7442.

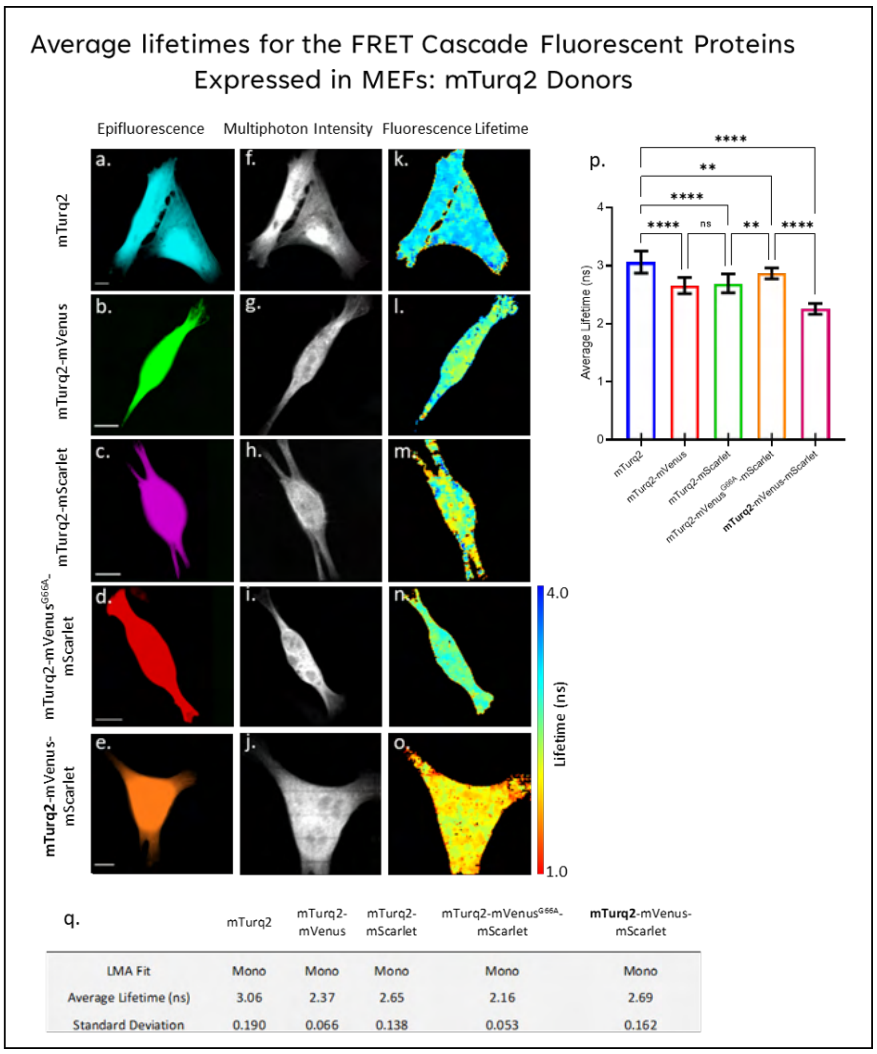

	mTurq2	mTurq2-mVenus	mTurq2-mScarlet	mTurq2-mVenus^{G66A}-mScarlet	**mTurq2**-mVenus-mScarlet
LMA Fit	Mono	Mono	Mono	Mono	Mono
Average Lifetime (ns)	3.06	2.37	2.65	2.16	2.69
Standard Deviation	0.190	0.066	0.138	0.053	0.162

Figure 4.3.9.1: ***Average lifetimes for the in-vivo FRET Cascade Fluorescent Proteins mTurq2 Donors:*** *A) Lifetime measurements were taken with a home build TCSPC-FLIM imaging system built around a Nikon Ti-Eclipse microscope and Coherent chameleon Vision II Ti:Sapphire laser source. Donors were excited at 875 nm (TPE) for mTurq2. Proteins consisting of three FPs, the fluorophore in bold is the donor. Lifetimes were determined using TRI2, a time-resolved analysis software package using a mono-exponential LMA fitting algorithm. A-O) TCSPC FLIM data for the MEFs transfected with plasmids encoding the FRET Cascade proteins. A-E) a widefield epi-fluorescence image of MEF transfected with an appropriate FRET Cascade plasmid. F-J) shows the Multiphoton Intensity image, and H-O) shows the lifetime distribution in a typical transfected cell. P) The average lifetimes for the FERT Cascade proteins expressed in MEFs, error bars show standard deviation. Q) A summary table of lifetimes, standard deviation and LMA fit. N=9 measurements per condition across three separate technical repeats, P-values $\geq$ 0.123 ns, $\leq$ 0.0332 (*), $\leq$ 0.0021 (**), $\leq$ 0.0002 (***), $\leq$ 0.0001 (****)*

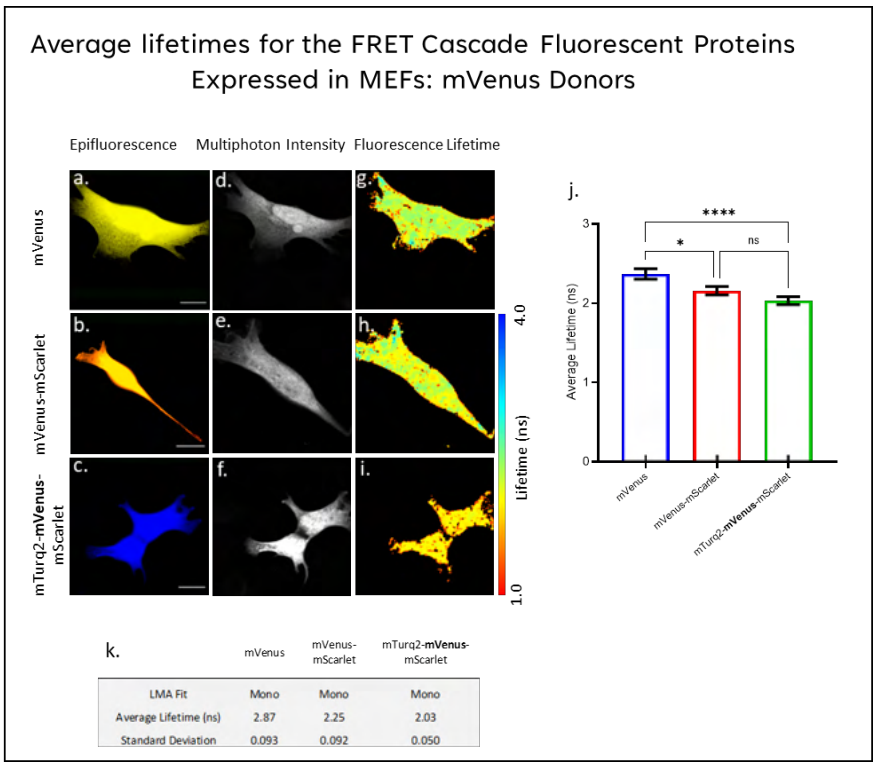

Figure 4.3.9.2: ***Average lifetimes for the in-vivo FRET Cascade Fluorescent Proteins: mVenus Donors:*** *A) Lifetime measurements were taken with a home build TCSPC-FLIM imaging system built around a Nikon Ti-Eclipse microscope and Coherent chameleon Vision II Ti:Sapphire laser source. Donors were excited at 875 nm (TPE) for mTurq2, and 950 nm (TPE) for mVenus. The proteins consist of three FPs, the fluorophore in* ***bold*** *is the donor. Lifetimes were determined using TRI2, a time-resolved analysis software package using a mono-exponential LMA fitting algorithm. A-I) TCSPC FLIM data for the MEFs transfected with plasmids encoding the FRET Cascade proteins. A-C) A widefield epi-fluorescence image of MEF transfected with an appropriate FRET Cascade plasmid. D-F) Multiphoton Intensity image. G-I) Cellular lifetime distributions in a transfected MEF. J) The average lifetimes for the FERT Cascade proteins expressed in MEFs, error bars show standard deviation. K) A summary table of lifetimes, standard deviation and LMA fit. N=12 measurements per condition across three separate technical repeats, P-values* $\geq$ *0.123 ns,* $\leq$ *0.0332 (*),* $\leq$ *0.0021 (**),* $\leq$ *0.0002 (***),* $\leq$ *0.0001 (****)*

4.3.10 FRET Efficiencies and Energy Transfer Rates for the FRET Cascade Fluorescent Proteins Expressed in MEFs

Following on from the description of the fluorescent lifetimes for the three-colour FRET cascade constructs transiently expressed in MEFs, this section is concerned with the calculated FRET efficiencies, transfer rates and the possibility of using the three-colour system accurately in fixed cells. There is an overall reduction in the amount of FRET compared to the in-solution measurements (figure 4.3.10-1), which detected up to 36% FRET efficiency for the mTurq2-mVenus FRET compared to the mTurq2 donor alone, whereas *in vivo* measurements of the same interaction suggests a more modest 13.2 % FRET efficiency. This trend continues, with the three-colour mTurq2-mVenus-mScarlet-I construct in-solution FRET efficiency measured at 43.7% but reduced to 26.3% in cells. This could be a serious and significant issue for this technique if the dynamic range of the FRET sensors is radically reduced. However, it is important to note that the general trends in the *in vitro* measurements are also found in the *in vivo* FRET calculations.

The Energy Transfer calculations (§ 4.3.7) showed that the difference between the calculated and measured lifetimes for the three-colour mTurq2-mVenus-mScarlet protein was still very small, with only a 9.82% deviation. This demonstrates that despite the added complexity of imaging in fixed cells and the general reduction in donor-alone lifetimes, it is still possible to assemble the individual FRET components measured in controlled experiments to construct a reliable estimate of the three-colour lifetime.

There is a consistent difference between the longer *in vitro* lifetime measurements and the shorter *in vivo* measurements (figure 4.3.10-2A). This is most significant for the mTurq2 donor alone, which significantly affects the calculated FRET efficiencies and the Energy Transfer rates. However, there are three constructs where the difference between the two populations is insignificant: mTurq2-mVenus, mTurq2-mScarlet-I and **mTurq2**-mVenus-mScarlet-I. As previously mentioned, significant changes in the lifetime of the donor will affect the apparent FRET efficiencies and the calculated energy transfer rates (figure 4.3.10-2B), where we can see a clear, constant discrepancy between the *in vivo* and *in vitro* FRET efficiencies.

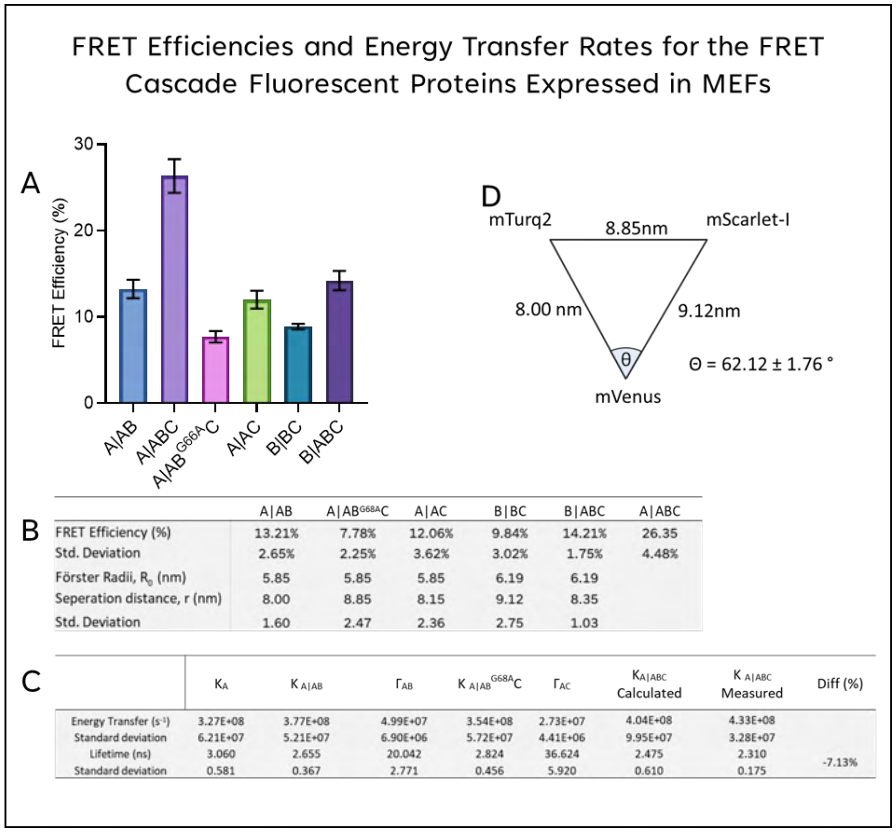

B

	A|AB	A|AB^{G68A}C	A|AC	B|BC	B|ABC	A|ABC
FRET Efficiency (%)	13.21%	7.78%	12.06%	9.84%	14.21%	26.35
Std. Deviation	2.65%	2.25%	3.62%	3.02%	1.75%	4.48%
Förster Radii, R_0 (nm)	5.85	5.85	5.85	6.19	6.19	
Seperation distance, r (nm)	8.00	8.85	8.15	9.12	8.35	
Std. Deviation	1.60	2.47	2.36	2.75	1.03	

C

	K_A	$K_{A\|AB}$	Γ_{AB}	$K_{A\|AB}{}^{G68A}C$	Γ_{AC}	$K_{A\|ABC}$ Calculated	$K_{A\|ABC}$ Measured	Diff (%)
Energy Transfer (s^{-1})	3.27E+08	3.77E+08	4.99E+07	3.54E+08	2.73E+07	4.04E+08	4.33E+08	
Standard deviation	6.21E+07	5.21E+07	6.90E+06	5.72E+07	4.41E+06	9.95E+07	3.28E+07	
Lifetime (ns)	3.060	2.655	20.042	2.824	36.624	2.475	2.310	-7.13%
Standard deviation	0.581	0.367	2.771	0.456	5.920	0.610	0.175	

Figure 4.3.10.1: ***FRET Efficiencies and Energy Transfer Rates for the FRET Cascade Fluorescent Proteins Expressed in MEFs:*** *FRET efficiencies were calculated using the FRET efficiency equation (see equation 4.2.10-1). A) Shows graphically the average FRET efficiencies for the various FRET pairs. Where, A=mTurquoise2, B=mVenus and C=mScarlet, for FRET pairs, the letter before the line marks the donor, so A—ABC denotes the FRET efficiency measured where the donor is A, mTurquoise2 and B—ABC would denote the FRET efficiency measured where the donor is B, mVenus in the mTurq2-mVenus-mScarlet protein. B) A summary table describing the FRET efficiencies, standard deviation, the calculated Forster radii for each FRET pair and the calculated separation distance between the FRET pair. C)A summary table detailing the Energy transfer rates, standard deviation and the associated lifetime of each FRET component. N=12 measurements per condition across three separate technical repeats P-values $\geq$ 0.123 ns, $\leq$ 0.0332 (*), $\leq$ 0.0021 (**), $\leq$ 0.0002 (***), $\leq$ 0.0001 (****)*

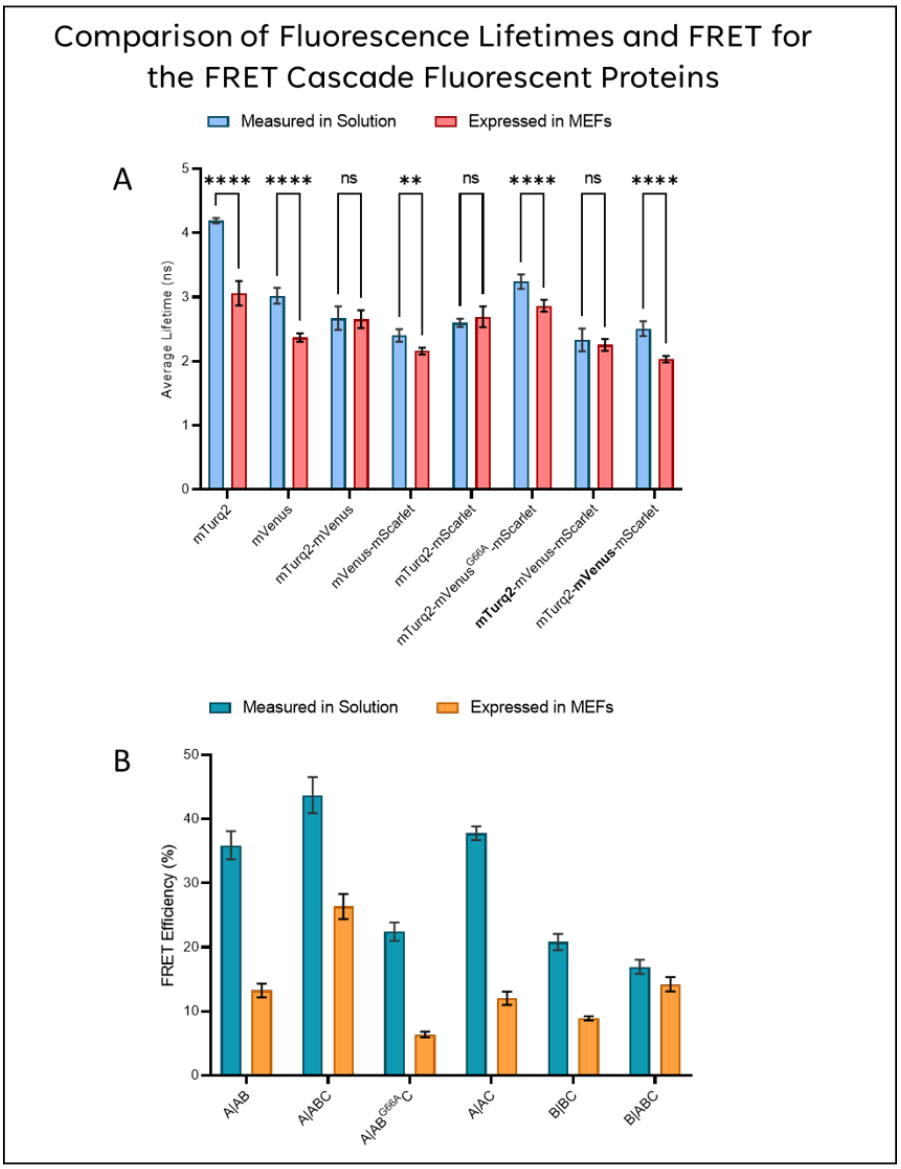

Figure 4.3.10.2: ***Comparison of In vivo and In vitro measurements for the FRET Cascade fluorescent proteins:*** *A) Comparison of fluorescence lifetimes against FP pair. B) Comparison of FRET against FP pair. N=12 measurements per condition across three separate technical repeats P-values* ≥ 0.123 *ns,* ≤ 0.0332 *(*),* ≤ 0.0021 *(**),* ≤ 0.0002 *(***),* ≤ 0.0001 *(****)*

4.3.11 Negative Stain TEM Images

Negative Staining for Transmission Electron Microscopy (TEM) was chosen as a quick and relatively simple technique for acquiring low-resolution (~2 nm) structural images of the three-colour mTurq2-mVenus-mScarlet-I protein. The rationale was to obtain structural information regarding the general shape or envelope of the three-colour protein. Specifically, I wanted to know if the predicted distances calculated from the FRET interactions and the energy transfer rates from the three-colour model could be independently validated.

A proposed orientation model of the β-barrels was produced by arranging the FPs such that they were the correct distance apart from one another (panel D of Figure 4.3.11-1). This model matches well with the negative stain images of the three-colour mTurq2-mVenus-mScarlet-I protein and the calculated FRET distances (table in figure 4.3.11-1). For simplicity, I have compared the shortest, middle, and longest sides of the measured triangular overlays (red) with the shortest, middle, and longest sides calculated for the mTurq2-mVenus-mScarlet protein using the FRET calculations. The differences between the measured and calculated distances are small, with an average approximately difference of only 1.26%; some of this error could be due to the relative orientation of three-colour protein, which may not be positioned completely flat on the surface.

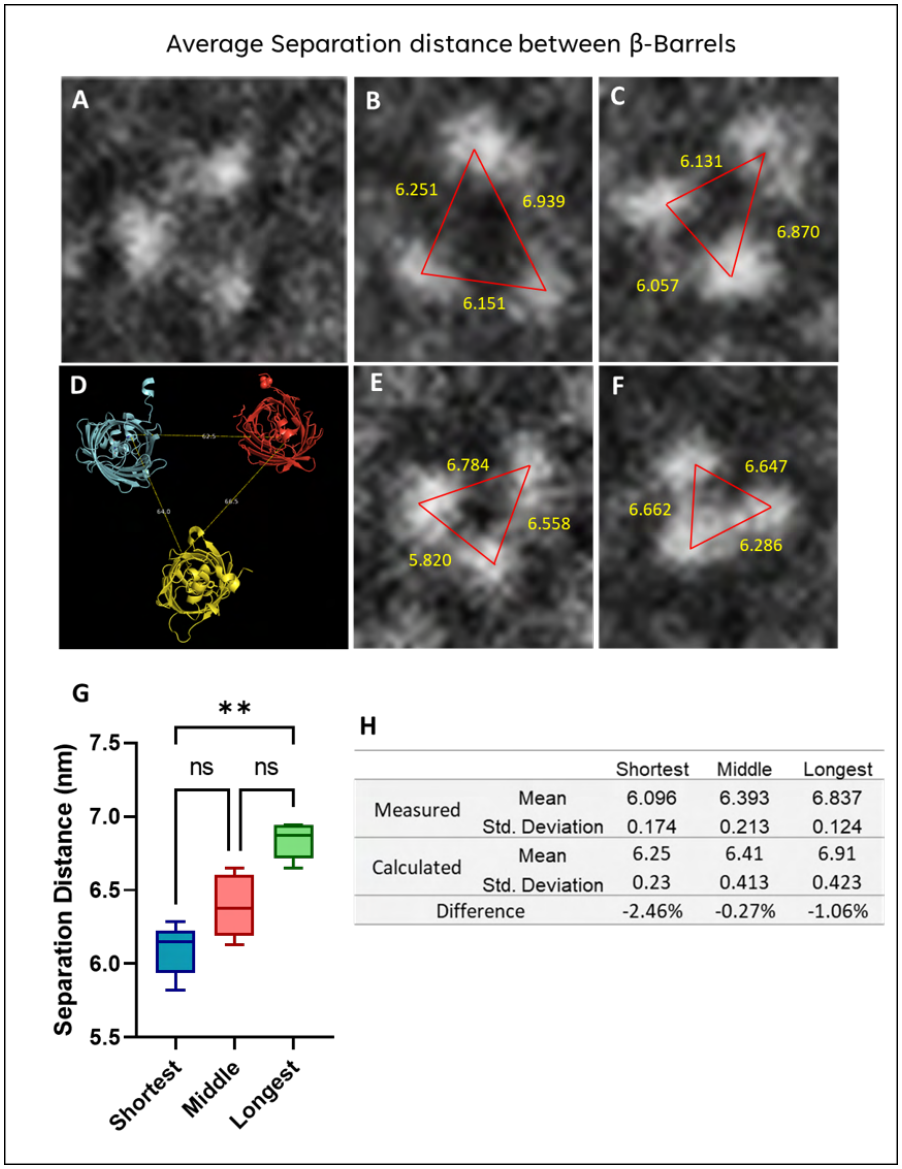

		Shortest	Middle	Longest
Measured	Mean	6.096	6.393	6.837
	Std. Deviation	0.174	0.213	0.124
Calculated	Mean	6.25	6.41	6.91
	Std. Deviation	0.23	0.413	0.423
Difference		-2.46%	-0.27%	-1.06%

Figure 4.3.11.1: ***Average Separation distance between*** *β*-***Barrels Determined by Negative Stain TEM:*** *A-E) Negative Stain TEM micrographs acquired at 120kV of the three colour mTurq2-mVenus-mScalet-I protein. Distances between beta-barrels measured in Fiji (ImageJ). F) Predicted model rendered in Pymol, a top-down projection for comparison with TEM data. G) Bar chart of average distances measured between β-barrels in the TEM micrographs. H) Summary statistics table outlines the mean and standard deviations for the distances measured (TEM micrographs) and calculated (FRET calculations), and the percentage difference between the two. N=3 measurements per condition across three separate technical repeats. P-values* ≥ 0.123 *ns,* ≤ 0.0332 *(*),* ≤ 0.0021 *(**),* ≤ 0.0002 *(***),* ≤ 0.0001 *(****)*

4.4 Conclusions of the Three-colour FRET cascade model

At the start of this chapter, I described a problem I wanted to solve, specifically how we could establish a novel method that would allow us to simultaneously probe the two-colour tension-sensing FRET biosensor with the putative vinculin-RIAM FRET interaction. In the previous chapter, I introduced evidence that shows the possibility of a vinculin-RIAM interaction within developing FAs; I also described how intracellular mechanical force is both key to vinculin activation and function. A more nuanced analytical FRET-based approach was required to understand this interaction and how intracellular force affects the vinculin-RIAM interaction.

The mVenus^{G68A} mutation was incorporated into the three-colour mTurq2-mVenus-mScarlet-I protein to produce a suitable control with the same separation distance between the mTurq2 and mScarlet-I. Alternative mutations could have been inserted instead of the *G68A* point mutation, such as the Q69M and F46L, both well-understood and characterised mutations found in many "dark" non-fluorescent versions of YFPs and GFPs such as ShadowY, ShadowG, and sREACh [185]. These mutations, which produce dark-FPs, only reduce the quantum efficiencies of the FPs and do not affect the formation of their chromophore—resulting in a fully functional acceptor/quencher with relatively weak emission. This is a fundamental difference from the *G68A* mutation, incapable of acting as an acceptor or quencher. I decided to try the *G68A* mutation, inserted using site-directed mutagenesis, and the resulting protein was shown not to have an excitation peak at 515 nm nor an emission peak at 530 nm, as we found with the functional mVenus.

Excitation and emission spectra confirmed that the purified proteins were as we had expected in terms of their spectra, with an indication of FRET observed in straightforward spectroscopic measurements with appropriate emission peak assignments. Some concerns regarding the secondary and tertiary structures of the mutant were relieved once the CD spectra revealed that the *G68A* point mutation had not caused any significant changes to the 3D structure of the protein. However, some stability is lost at higher temperatures with the mutant compared to the mVenus. The mVenus^{G68A} mutant likely requires lower temperatures to be expressed as a functional, fully folded protein. This may explain why earlier research conducted by the Tsien group [165, 171] concluded that when this mutation was inserted into

GFP, the protein expressed was not only non-fluorescent but also disordered. The inclusion of this mutation is a new finding, but as far as I am aware, no other researcher has used this specific mutation to create a non-fluorescent beta-barrel and has used it to control for FRET.

Once the structural integrity of the mutated three-colour protein had been confirmed, the purified proteins were imaged using our two-photon TCSPC-FLIM imaging system (detailed in figure 4.2.10-1). As expected, the mTurq2 had a very long fluorescent lifetime of 4.18 ± 0.072 ns which is very close to the published lifetime of 4.0 ns [183] (no error was given in the publication, and the published value was achieved with a widefield frequency-domain FLIM imaging system [183]). This result gives confidence that the correct FPs can be produced and fluorescence lifetimes that with the literature values. The same was true for the mVenus FP, which was determined to be 2.95 ± 0.026 ns, and the published value was stated as 2.9 ± 0.1 ns [186] which was again achieved with a widefield frequency-domain FLIM imaging system [183]. A significant decrease in the average lifetimes were observed for the two-FP proteins compared to the mTurq2 and mVenus, as the donor-alone controls, showed that FRET had indeed occurred between each of those two-part chimeric proteins. Another decrease in the average lifetime was also observed for the three-colour mTurq2-mVenus-mScarlet-I protein, as we would also expect. The mutated three-colour protein, mTurq2-mVenus^{G68A}-mScarlet-I, had a longer lifetime than the unmutated three-colour protein and the mTurq2-mScarlet protein, suggesting that the increased distance between the two FPs had made a significant difference while also giving further support to the idea that the mVenus, which separates the FPs in the mutated three-colour protein, truly, is both non-fluorescent and non-absorbing.

The average FRET efficiencies were calculated from the fluorescent protein lifetimes. The three-colour mTurq2-mVenus-mScarlet-I protein was determined to have the shortest fluorescence lifetime and, consequently, the greatest FRET efficiency of 48.4 ± 1.03 %. It is impossible to compare this or another FRET value to published work as these specific constructs with the six amino linkers have not been made previously. However, we can comment on the general trend between the six FRET pairs made and imaged. The two mTurq2 donors, mTurq2-mVenus and mTurq2-mScarlet, exhibited similar FRET efficiencies of 38.51 ± 1.95 % and 38.02 ± 2.07 %, respectively. Not too surprising as both FRET pairs have the same donor, the same linker length (presumably the same separation distance) and very similar Förster radii.

The fact that they are both similar in value is reassuring, as their agreement effectively acts as a control. Of the four FRET pairs with mTurq2 as the donor, the mTurq2-mVenus^{G68A}-mScarlet-I protein was found to have the least FRET. Not too surprising when we consider that the middle fluorophore was not involved in the FRET cascade at all.

Once the FRET efficiencies had been calculated, the energy transfer rates were then determined from their respective interactions to calculate and effectively predict the total energy transfer out of the mTurq2 donor and then used that total energy transfer rate to estimate the lifetime. From these calculations, I could use the model to predict a lifetime for the three-colour protein of 2.25 ± 0.39 ns, compared to the measured lifetime of 2.33 ± 0.27 ns; this represents only a 3.4 % discrepancy between my predicted and measured results. This again instils more confidence that the model is correct and that we can determine the distances between the fluorophores. If at this stage, we had found large discrepancies between the predicted and measured values, it would certainly give cause for concern that perhaps I had not performed either the lifetime measurements correctly, the photophysical model was too simplistic, or that perhaps the proteins themselves had deteriorated and, as such were no longer viable.

A prediction for the distances between the FPs was performed using the FRET efficiencies and equation 4.2.11-2, as detailed in figure 4.2.11-1 panel B; the distances between the mTurq2-mVenus, mTurq2-mScarlet, and mVenus-mScarlet FPs was determined to be 6.33 ± 0.12 nm, 7.14 ± 0.17 nm, and 7.50 ± 0.31 nm respectively. The most significant thing about these results is that the distance between the mTurq2 and mScarlet proteins is not twice that between mTurq2-mVenus or mVenus-mScarlet. This was surprising to find as I had not considered up until this point that the three-colour protein would be anything but a long cylindrical sausage in shape. However, from these results, all the distances are roughly the same, suggesting a triangular or globular shape to the three-colour FP. A simple formula for deducing the interior angle of a triangle when all three sides are known, the cosine rule, was used to calculate an approximate separation angle between the mTurq2 and mScarlet FPs. This was determined to be 62.43 ± 3.88°. I then measured the distances between the centres of β-barrels, which gave a range very close to the predicted distances calculated from the FRET efficiencies. This is not conclusive evidence that the three-colour protein is in a triangular/-

globular confirmation, but it does provide some validation of the predicted model.

Finally, the three-colour model was then applied to MEFs transfected with the mammalian expressing versions of the same proteins. This is a step towards using the model to predict dynamic multi-protein cellular interactions. There were some significant issues regarding lifetime measurements that generally did not agree with the lifetimes measured for the purified proteins. This led to reduced FRET efficiencies being calculated, which had larger standard deviations associated with them. The trend between the constructs is the same as with the purified proteins, which means that even though the absolute lifetime values measured were not the same, the FRET distances could still be calculated similarly as with the purified proteins. Distances were calculated to be 8.00 ± 1.60 nm, 9.12 ± 2.75 nm, and 8.85 ± 2.47 nm for the mTurq2-mVenus, mTurq2-mScarlet and mVenus-mScarlet FRET pairs respectively. The separation angle between mTurq2 and mScarlet in the mTurq2-mVenus-mScarlet-I protein was 62.12 ± 1.8°, which is still in agreement with the *in vitro* distances (albeit slightly longer) and, most importantly, the separation angle. It is likely that due to the reduced absolute protein concentration found in transfected cells, as opposed to a known μM concentration of purified proteins, the variation associated with the fluorescence lifetimes is much greater. This is compounded further when an additional error was possibly introduced through fixation and mounting of the cells, leading to cross-linking and potential modification of the FPs is why both the lifetimes were not as expected for all FPs, and the reason why the calculated FP separation distances were found to be longer for the *in vivo* measurements than the *in vitro* measurements.

A recent study has shown that some glycerol-based mounting media can significantly reduce the lifetime of *Aquorea victoria*-derived FPs such as mTurq2 and mVenus by as much as 20% [187]. They specifically showed that cells expressing mTurq2 in cells that were fixed in either PFA or methanol and then imaged in either TBS or PBS exhibited average fluorescent lifetimes of 4.08 ± 0.03 ns compared to cells fixed in PFA or methanol and mounted in Mowiol, or Vectashield which when imaged the average lifetimes were recorded as 3.70 ± 0.04 ns and 3.13 ± 0.02 ns respectively. This represents a 9.31% and 23.3% reduction in the fluorescence lifetime for Mowiol and Vectashield mounted samples. It would seem the best mounting media would be a simple physiological buffer comprising either TBS or PBS. The same study then

compared different solutions of glycerol ranging from 20% to 50%, which showed a reduction in the fluorescence lifetime of the more concentrated glycerol samples, solutions of which incidentally had higher refractive indices. The paper concluded that the relationship between fluorescent lifetime was inversely proportional to the square of the refractive index of the mounting media. Optimal imaging was found in solutions where the refractive index was close to that of water, 1.33. Additionally, it should be noted that most commercial mounting media have fluor-protectants like DABCO, typically found in Mowiol, which acts to prevent photobleaching. This may be ideal for widefield or confocal imaging where brighter samples are favoured but may also contribute to reduced lifetimes in FLIM imaging.

The mTurq2 *in vitro* lifetime was measured as 4.18 ± 0.072, and the *in vivo* lifetime was 3.06 ± 0.19, corresponding to a 26.78% reduction. Similarly, the mVenus *in vitro* lifetime was measured as 2.953 ± 0.025, and *in vivo,* the lifetime was measured as 2.369 ± 0.061, corresponding to a 19.77% reduction in the donor alone lifetime. All the fixed cell imaging was conducted on cells mounted in DABCO-supplemented Mowiol, whereas the purified proteins were dissolved in PBS. The use of a DABCO-supplemented glycerol-based mounting media could well be the reason for this discrepancy in fluorescent lifetimes; future work will need to be done with cells prepared in TBS, especially before the publication of this data.

5

RESULTS CHAPTER III:
APPLICATION OF THE THREE-COLOUR FRET MODEL TO LIVE AND FIXED CELLS

5.1 Introduction to the Application of the Three-colour FRET model

This chapter describes individual FRET exchanges that occur in the multi-colour FRET interactions between the vinculin tension sensor and mScarlet-RIAM using two-photon TCSPC-FLIM. The precise location of the vinculin-RIAM interaction is of great interest and importance and is explored within this chapter. The determination of whether there is a significant difference in donor lifetime for the vinculin tension sensor + mScarlet-RIAM between the mask regions (described in previous chapters) is of paramount interest. Furthermore, probing whether, within specific regions, a greater proportion of vinculin molecules are in a free or bound conformation with RIAM is an additional aim.

The relationship between the expression levels of mScarlet-RIAM and its colocalization with vinculin within FAs is investigated extensively in this chapter. In previous chapters, evidence has been presented that describes an interaction between vinculin and RIAM that likely occurs in the cytoplasm, although this interaction is still detectable within the FAs, as demonstrated by the many FRET experiments presented. However, there appears in some cells at least to be less mScarlet-RIAM expression at the very edge of the cell, where we see nascent adhesions being formed and where we would expect to see RIAM expression interacting with vinculin. We have seen a great deal of variability associated with some of the fixed cell FRET data, specifically relating to the large spread of lifetime values not limited to but including the conditions containing the mScarlet-RIAM acceptor. The increased spread in lifetime values could be due to the amount of expressed mScarlet-RIAM and whether it is effectively localised within the lamellipodium. It may be possible to separate the imaged cells into two groups, one with higher, well-localised

mScarlet-RIAM and another having lower expression levels and not as well localised in the lamellipodium.

5.2 Results III: Application of the Three-colour FRET model to live and fixed cells

5.2.1 MEFs transfected with teal-vinculin & mScarlet-RIAM in fixed cells

The individual FRET exchanges in the multi-colour FRET interaction between the vinculin Tension Sensor and mScarlet-RIAM in fixed transfected MEFs are described using two-photon TCSPC-FLIM. The first describes the interaction between teal-vinculin and mScarlet-RIAM (figure 5.2.1-1); the FLIM data were segregated using intensity masks into three specific compartments: Focal Adhesion only, Whole Cell, and Excluding Focal Adhesions.

Comparing the lifetime data for the co-transfected teal-vinculin + mScarlet-RIAM cells to the teal-vinculin donor alone control cells showed a significantly shorter fluorescence lifetime for the co-transfected teal-vinculin + mScarlet-RIAM imaged cells. This is evidenced both in terms of the warmer (red) colour of the FAs (panels A-F of Figure 5.2.1-1) and the calculated FRET efficiencies (approximately 20%) for each of the three masked teal-vinculin + mScarlet-RIAM regions compared to the teal-vinculin-only control cell (panels G-J). No significant difference was found between the FRET efficiencies of the different masked regions; this is not entirely surprising. As shown with GFP-vinculin and RIAM-mScarlet, the FRET interaction is not exclusively isolated to any one region of the cell. This data would suggest an interaction between vinculin and RIAM, but the interaction is not specific to FAs alone.

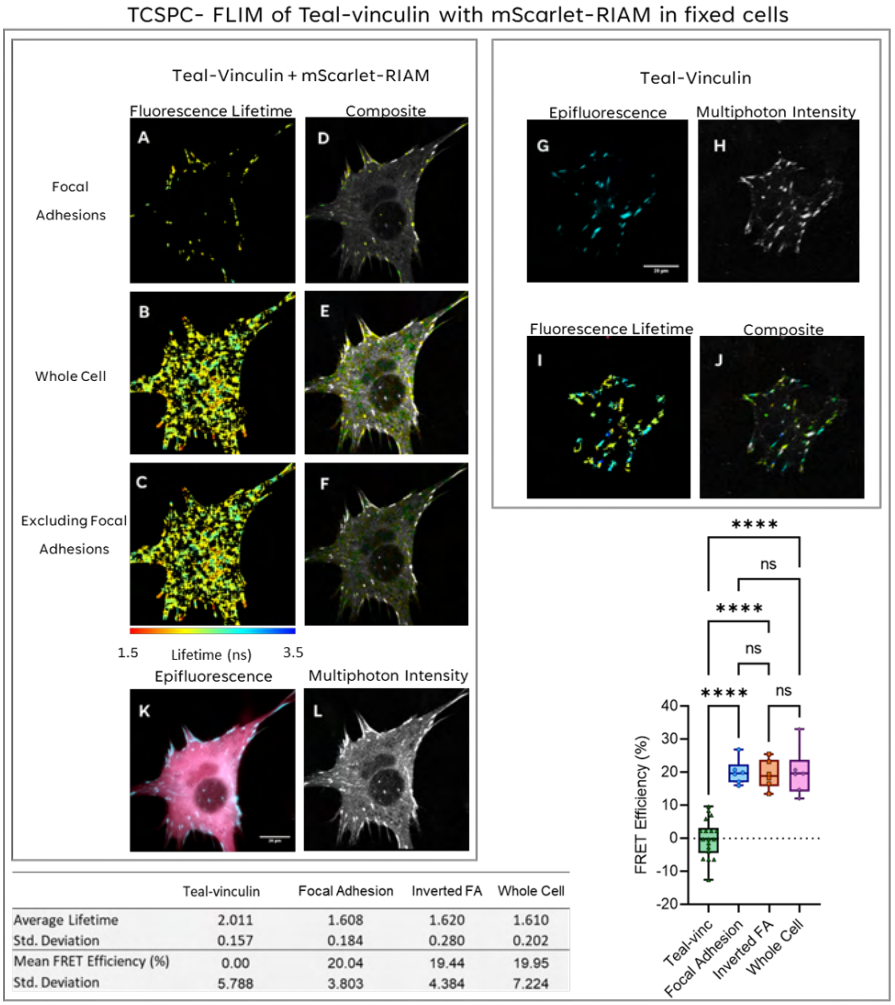

	Teal-vinculin	Focal Adhesion	Inverted FA	Whole Cell
Average Lifetime	2.011	1.608	1.620	1.610
Std. Deviation	0.157	0.184	0.280	0.202
Mean FRET Efficiency (%)	0.00	20.04	19.44	19.95
Std. Deviation	5.788	3.803	4.384	7.224

Figure 5.2.1.1: ***Average Separation distance between β-Barrels Determined by Negative Stain TEM:*** *A-C) show Fluorescence Lifetime images for the same cell masked through thresholding of the two-photon intensity map for the three separate conditions: Focal Adhesions only, Whole Cell and Focal Adhesions Excluded. Panels D-F) shows composite images for the Multiphoton Intensity images merged with the lifetime images. G and K) Show the epifluorescence widefield images of the Teal-Vinc donor alone and the teal-Vinc + mScarlet-RIAM donor + acceptor cells, respectively. H and L) show the Multiphoton Intensity images for the same cells. I) shows the fluorescence lifetime image for the donor cell, and J) shows the composite (colour merge of intensity and lifetime) image for the donor alone cell. M) Shows the average FRET efficiencies as a Box plot for each condition. Significance was determined through a one-way ANOVA with Tukey corrections for multiple tests. N) A summary table of lifetimes, standard deviation, and FRET efficiencies. N=8 measurements per condition across three separate technical repeats. Scale bar = 20μm. P-values $\geq$ 0.123 ns, $\leq$ 0.0332 (*), $\leq$ 0.0021 (**), $\leq$ 0.0002 (***), $\leq$ 0.0001 (****)*

5.2.2 MEFs Transfected with the Tensionless-Vinculin Biosensor & mScarlet-RIAM in Fixed Cells

The tensionless-vinculin control construct was used as a FRET control for the vinculin tension Sensing Biosensor; this construct has the two FPs at the C-terminus of the vinculin head domain do not contain the actin binding tail domain required of vinculin. A potential consequence is that vinculin remains in an autoinhibited inactive state that cannot be activated through the usual mechanism of talin and actin binding, which means that the vinculin-TL construct is permanently in a low-force, high FRET conformation. The following lifetime data (Figure 5.2.2-1) shows the fluorescence lifetime and FRET efficiency data for vinculin null MEFs transfected with either vinculin-TL only or co-transfected with vinculin-TL and mScarlet-RIAM.

The addition of the mScarlet-RIAM construct results in a lower average lifetime of the teal FP in the vinculin-TL transfected cells compared to the teal FP in cells only transfected with vinculin-TL. There was a significant reduction in the fluorescence lifetime and an increase in the FRET efficiency for all three masks used with very little difference between any of the three masked regions (see box plot diagram figure 5.2.2-1 panel M). Suggesting that when vinculin is in a low-tension autoinhibited state where it cannot bind to actin, the actin-binding domain is absent from the vinculin-TL construct while still forming an interaction with RIAM. This finding would suggest that the vinculin-RIAM interaction could be actin-independent. Additionally, there was no significant difference in average lifetimes between the three masked regions, which one might expect to see if the interaction was predominantly FA associated.

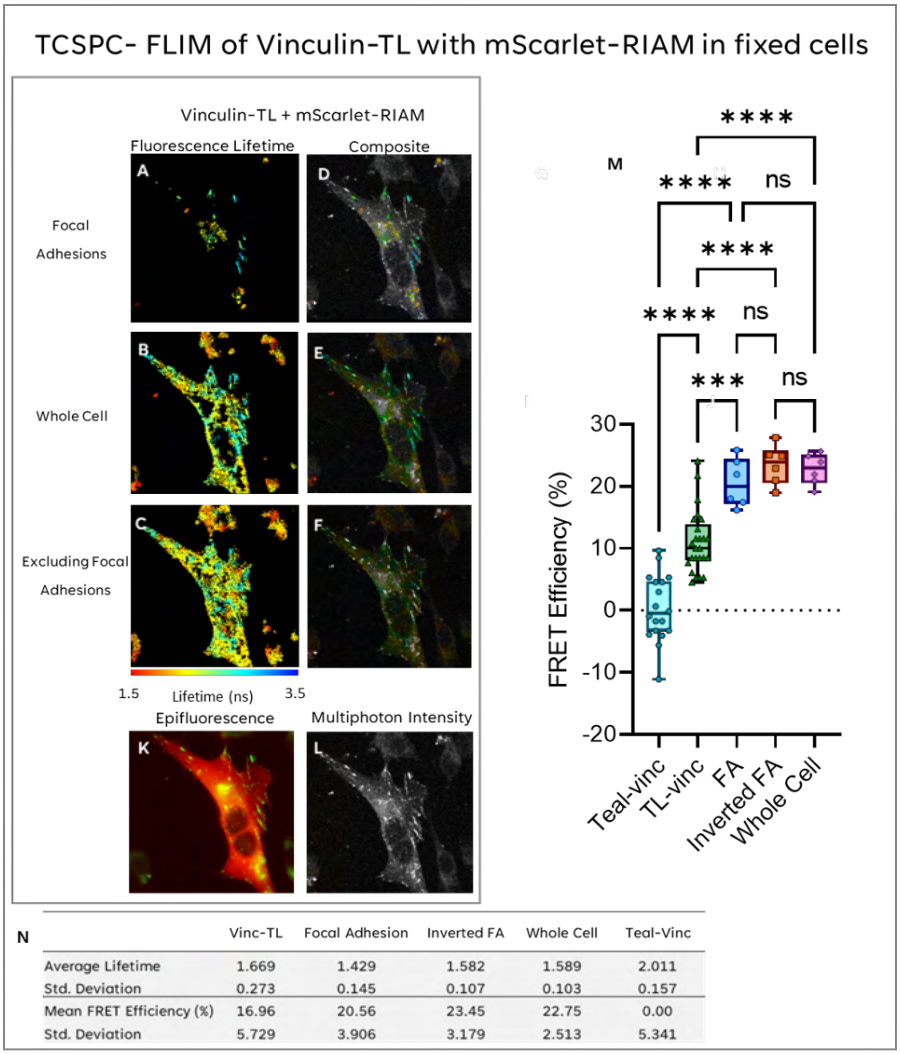

N

	Vinc-TL	Focal Adhesion	Inverted FA	Whole Cell	Teal-Vinc
Average Lifetime	1.669	1.429	1.582	1.589	2.011
Std. Deviation	0.273	0.145	0.107	0.103	0.157
Mean FRET Efficiency (%)	16.96	20.56	23.45	22.75	0.00
Std. Deviation	5.729	3.906	3.179	2.513	5.341

Figure 5.2.2.1: ***Vinculin-TL with mScarlet-RIAM in fixed cells:*** *A-C) show Fluorescence Lifetime images for the same cell masked through thresholding of the two-photon intensity map for the three separate conditions: Focal Adhesions only, Whole Cell and Focal Adhesions Excluded. Panels D-F) shows composite images for the Multiphoton Intensity images merged with the lifetime images. G and K) Show the epifluorescence widefield images of the mVenus-vinculin donor alone and the mVenus-vinculin + mScarlet-RIAM donor + acceptor cells, respectively. H and L) show the Multiphoton Intensity images for the same cells. I) shows the fluorescence lifetime image for the donor cell, and J) shows the composite (colour merge of intensity and lifetime) image for the donor alone cell. M) Shows the average FRET efficiencies as a Box plot for each condition. Significance is determined through a one-way ANOVA with Tukey corrections for multiple tests. N) A summary table of lifetimes, standard deviation, and FRET efficiencies. N=8 measurements per condition across three separate technical repeats. Scale bar = 20μm. P-values $\geq$ 0.123 ns, $\leq$ 0.0332 (*), $\leq$ 0.0021 (**), $\leq$ 0.0002 (***), $\leq$ 0.0001 (****)*

5.2.3 MEFs transfected with mVenus-vinculin & mScarlet-RIAM in fixed cells

The mVenus-vinculin construct was transfected into vinculin null MEFs with and without mScarlet-RIAM. The addition of the mScarlet-RIAM construct in the co-transfected cells reduced the average lifetime of the mVenus FP and an average FRET efficiency of approximately 22% for all three masked regions. A finding extremely similar to the teal-vinculin + mScarlet-RIAM data presented above is not very surprising, as we are probing the same interaction as described with the teal-vinculin + mScarlet-RIAM co-transfected cells, with the only the difference being the FP used to tag the vinculin. This is still an an important result, as the FRET transfer rates are needed to calculate the overall resonance energy transfer rates between all FPs in a three-colour model.

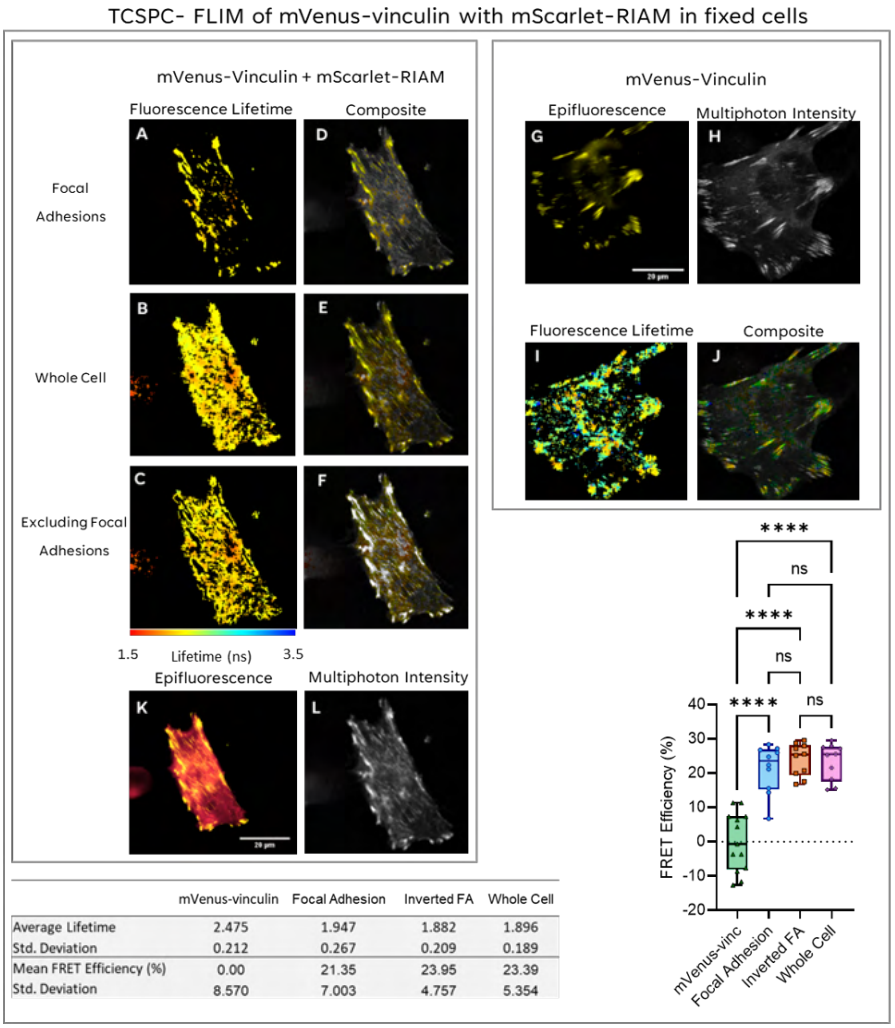

	mVenus-vinculin	Focal Adhesion	Inverted FA	Whole Cell
Average Lifetime	2.475	1.947	1.882	1.896
Std. Deviation	0.212	0.267	0.209	0.189
Mean FRET Efficiency (%)	0.00	21.35	23.95	23.39
Std. Deviation	8.570	7.003	4.757	5.354

Figure 5.2.3.1: ***mVenus-vinculin with mScarlet-RIAM in fixed cells:*** *A-C) show Fluorescence Lifetime images for the same cell masked through thresholding of the two-photon intensity map for the three separate conditions: Focal Adhesions only, Whole Cell and Focal Adhesions Excluded. Panels D-F) shows composite images for the Multiphoton Intensity images merged with the lifetime images. G and K) Show the epifluorescence widefield images of the mVenus-vinculin donor alone and the mVenus-vinculin + mScarlet-RIAM donor + acceptor cells, respectively. H and L) show the Multiphoton Intensity images for the same cells. I) shows the fluorescence lifetime image for the donor cell and J) shows the composite (colour merge of intensity and lifetime) Image for the donor alone cell. M) Shows the average FRET efficiencies as a Box plot for each condition. Significance is determined through a one-way ANOVA with Tukey corrections for multiple tests. N) N=8 measurements per condition across three separate technical repeats, Scale bar = 20μm. P-values $\geq$ 0.123 ns, $\leq$ 0.0332 (*), $\leq$ 0.0021 (**), $\leq$ 0.0002 (***), $\leq$ 0.0001 (****)*

5.2.4 MEFs Transfected with Tension Sensing-Vinculin Biosensor & mScarlet-RIAM in Fixed Cells

The vinculin-tension sensing biosensor was transfected into vinculin null MEFs with and without mScarlet-RIAM producing a three-coloured, multiplexed FRET experiment. The addition of the mScarlet-RIAM construct resulted in the reduction of the average lifetime of the teal FP in the vinculin-TS construct, from a FRET efficiency of approximately 12% to an average of approximately 30% with the addition of mScarlet-RIAM (panels N and M of Figure 5.2.4-1). This increase in average FRET efficiency of approximately 18% is a direct consequence of the mScarlet FP interacting with the teal FP within the TSMod in the vinculin-TS construct. The increase in FRET efficiency is indicative of an additional FRET interaction, which would suggest that while there is low tension acting on the vinculin-TS protein, yielding a high FRET efficiency between the teal and mVenus FPs, there is also a second energy transfer between the teal FP and the mScarlet FP. This increase in FRET efficiency for vinculin-TS with mScarlet-RIAM occurred for each of the three masked regions; however, a relatively large spread of lifetime values were observed. Most probably due to the binary nature of the biosensor, being constrained to either an open or closed conformation per vinculin molecule. However, only a single lifetime value is reported when averaged over the whole cell for all adhesions in that cell.

The presence of mScarlet-RIAM has resulted in a decrease in the lifetimes measured across the three segregated regions. The large spread of values likely corresponds, as mentioned above, to the Tension Sensing biosensor's open or closed state, which can be in either an open or closed form. Vinculin is thought to be in an autoinhibited state in the cytoplasm and is thought not to be able to fully open without first binding to talin and actin. This should correspond to a difference in average lifetimes between the cytoplasmic regions, where we expect to see a high amount of FRET. These regions will not have the mechanical force exerted on vinculin to separate the teal and mVenus FPs and so will exhibit a greater FRET efficiency compared to the FAs, where we would have expected to see either a larger variation in lifetimes or a general reduction corresponding to the open, active form of vinculin being in greater abundance compared to the cytoplasm.

Average lifetime distributions for the various donor-acceptor and donor-alone conditions were also produced (see Figure 5.2.4-2). For the three vinculin-TS

conditions co-transfected with mScarlet-RIAM, we can see two peaks in the distributions, which broadly line up with 1.3 and 1.6 ns (panel A of Figure 5.4.2-2). The shorter lifetime corresponds to the three-colour FRET transfer from the teal FP to the two FRET acceptors, mVenus and mScarlet, and the longer lifetime most likely corresponds to the teal-mVenus FRET transfer only. There may be a sizeable FRET transfer between teal and mScarlet is unlikely to occur without mVenus present due to the proximity of mVenus to teal in the tension-sensing construct. Cells imaged with the shortest lifetimes are likely to predominantly be vinculin-TS in the high FRET closed state and have mScarlet-RIAM present. This could indicate a preference for RIAM binding to the closed, inactive autoinhibited conformation of vinculin if it could also be shown that the mScarlet-RIAM construct does not associate with the open, active form of vinculin. The second, longer lifetime peak at approximately 1.6 ns represents the bulk of the cells imaged for this condition and likely shows the vinculin-TS construct in a closed, high FRET – low tension state without RIAM present. It could be speculated that this could be a transitional state within FAs where RIAM has dissociated from vinculin, and before vinculin activation through successful binding with talin and actin.

There is an additional peak illustrated by the teal-only donor, with a peak at approximately 2.0 ns. This is likely to be illustrative of a cell where the vinculin-TS construct was predominately found in the open state, where there was little FRET measured between the teal and mVenus FPs and where the mScarlet-RIAM protein did not associate sufficiently within the FAs to significantly reduce the lifetime. No cells were imaged with longer lifetimes associated with the vinculin-TS construct being in its fully open and active conformation. This is as we might expect if we were to believe that vinculin is only under tension when bound to talin and actin in the FAs. The two peaks seen in both masked conditions purport to a 1.4 and 1.6 ns lifetime as described above, most likely relating to a teal-mVenus configuration without mScarlet-RIAM and a lower lifetime configuration with the mScarlet-RIAM present.

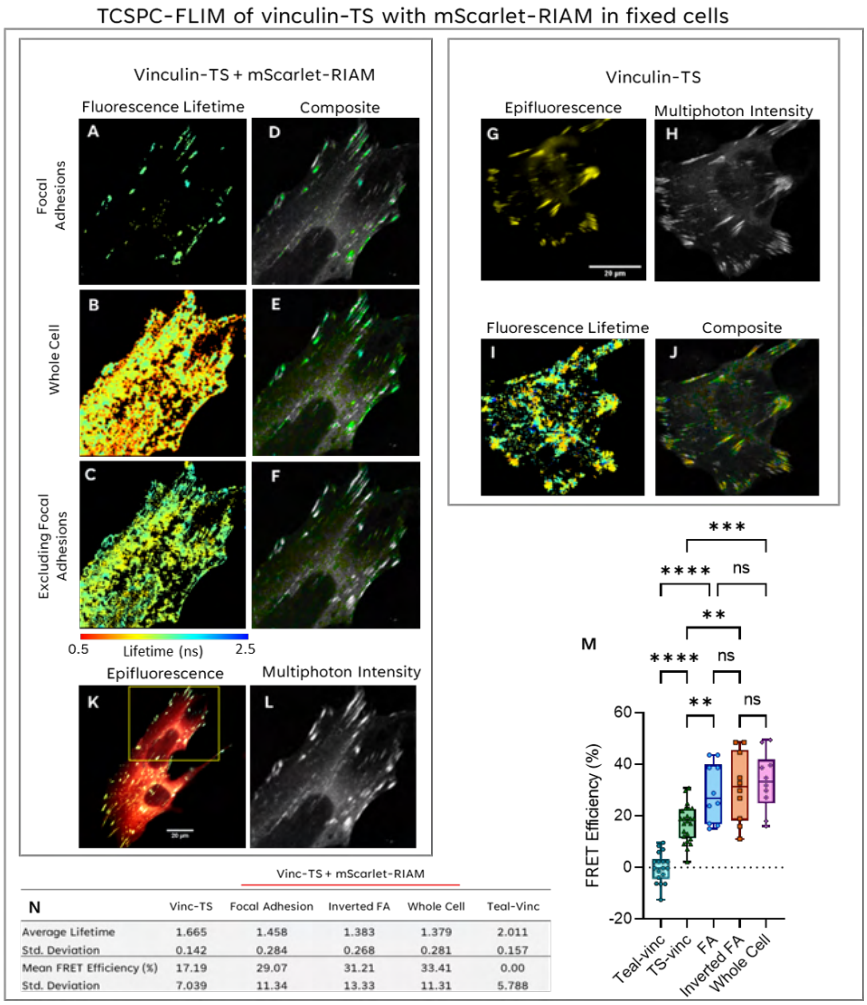

Figure 5.2.4.1: ***Vinculin-TS with mScarlet-RIAM in fixed cells:*** *A-C) show Fluorescence Lifetime images for the same cell masked through thresholding of the two-photon intensity map for the three separate conditions: Focal Adhesions only, Whole Cell and Focal Adhesions Excluded. Panels D-F) shows composite images for the Multiphoton Intensity images merged with the lifetime images. G and K) Show the epifluorescence widefield images of the mVenus-vinculin donor alone and the mVenus-vinculin + mScarlet-RIAM donor + acceptor cells, respectively. H and L) show the Multiphoton Intensity images for the same cells. I) shows the fluorescence lifetime image for the donor cell and J) shows the composite (colour merge of intensity and lifetime) image for the donor alone cell. M) Shows the average FRET efficiencies as a Box plot for each condition. Significance is determined through a one-way ANOVA with Tukey corrections for multiple tests. N) A summary table of lifetimes, standard deviation, and FRET efficiencies. N=8 measurements per condition across three separate technical repeats. Scale bar = 20μm. P-values $\geq$ 0.123 ns, $\leq$ 0.0332 (*), $\leq$ 0.0021 (**), $\leq$ 0.0002 (***), $\leq$ 0.0001 (****)*

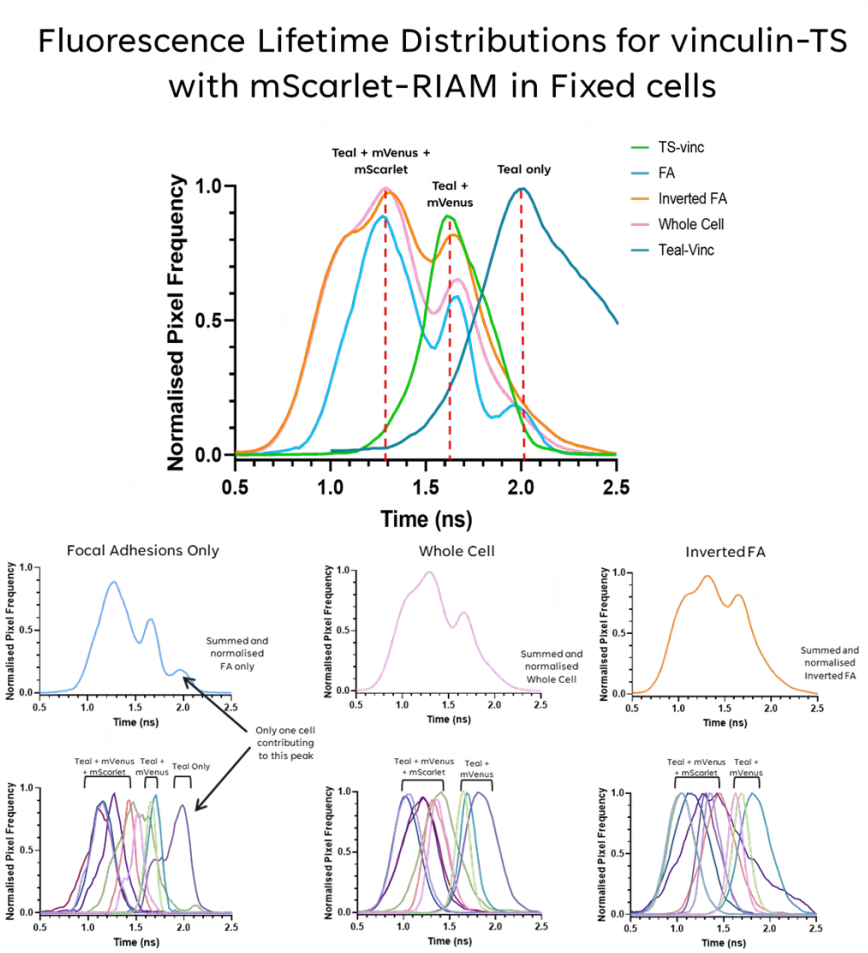

Figure 5.2.4.2: ***Fluorescence Lifetime Distributions for vinculin-TS with mScarlet-RIAM in Fixed cells:*** *A) Summed average lifetime plots for the various Vinc-TS+ mScarlet-RIAM conditions along with Vinc-TS alone and Teal-vinculin alone lifetime plots. B-D) Plots of normalised pixel frequency against lifetime for the three masked Vinc-TS + mScarlet-RIAM conditions. E-G) Individual plots of each cell imaged in each condition of normalised pixel frequency against lifetime for the three masked Vinc-TS + mScarlet-RIAM conditions.*

5.2.5 The effect of mScarlet-RIAM expression in nascent adhesion on the Three-colour FRET model

Colocalization was determined using *Coloc 2* ImageJ (FIJI) [188–191]; this was chosen as *Coloc2* utilises a one-to-one pixel assignment to determine colocalisation, a feature required for comparing widefield-epifluorescence and FLIM data. Two cells were selected for demonstration purposes, one with nominally higher mScarlet expression, especially in the lamellipodium, and another with lower mScarlet expression. Panels G and N show 2D histograms of the pixel intensities for the two images, showing little correlation between the two channels. Conversely, looking at panel N, we can see a better agreement between the two channels, but it is still far from a perfect linear relationship.

The Manders' coefficients for the lower expressing mScarlet-RIAM cell are much lower than that of the higher expressing cell, 0.054 and 0.102 opposed to 0.861 and 0.586. This would suggest a better cooccurrence between RIAM and vinculin for the higher-expressing cell than the lower-expressing RIAM cell. However, only 26.1% of the pixels in the green channel and 58.6% in the red channel are non-zero; this does not indicate a strong relationship between the two proteins within the FAs. On its own, low co-occurrence does not tell us much other than there are more structural similarities between the two channels in the higher expressing mScarlet-RIAM cells than the lower expressing cell.

Additionally, the Pearson Product Moment Correlation Coefficient (PPMCC) [189–191], and we can see in panel O from figure 5.2.5-1 that for the higher expressing mScarlet-RIAM cell, the Pearson correlation coefficient was calculated to be 0.07, and for the lower expressing cell was calculated to be -0.19. This would strongly suggest that for either of the cells analysed, there is little to no correlation between the localisation of mScarlet-RIAM and vinculin. However, when we look at the fluorescence lifetimes of the cells, we can see in the higher expressing mScarlet-RIAM cell that there is a shorter lifetime of 1.38 ns compared to 1.69 ns for the lower expressing mScarlet-RIAM cells. This would yield a FRET efficiency of 34.10 and 16.01 %, which span the lower and upper limits of the vinculin-TS + mScarlet-RIAM FRET efficiency range. This would mean that some cells with lower mScarlet-RIAM or miss-localised expression, the FRET interaction is scaled by the RIAM expression level; this is typical of intermolecular FRET experiments with uncontrolled stoichiom-

etry must be considered when aggregating data across multiple cells and repeats.

The interaction persists despite the lack of colocalization from the widefield epifluorescence images. One possible explanation is that RIAM is shuttling vinculin towards the lamellipodium and relinquishes its binding partner very early on in the FA complex formation process, just as vinculin begins to bind and associate with talin and the actomyosin cytoskeleton. This would reconcile the results of the numerous FRET experiments and the GFP-pull downs presented in earlier chapters. Interestingly, without the FRET data, one might assume there was no interaction between these proteins purely based on the lack of colocalization. A reminder that the colocalization of images taken in widefield epifluorescence is diffraction limited, with optimal resolutions no better than 250-300 nm. FRET and, by extension, FLIM is not limited in the same way in terms of interaction detection and can report on interactions between proteins as close as 2 nm away. A correlation between mScarlet-RIAM and lower fluorescence lifetimes may exist, but without extending the scope of this investigation, single molecules would be very difficult to achieve with the technology that we have at present.

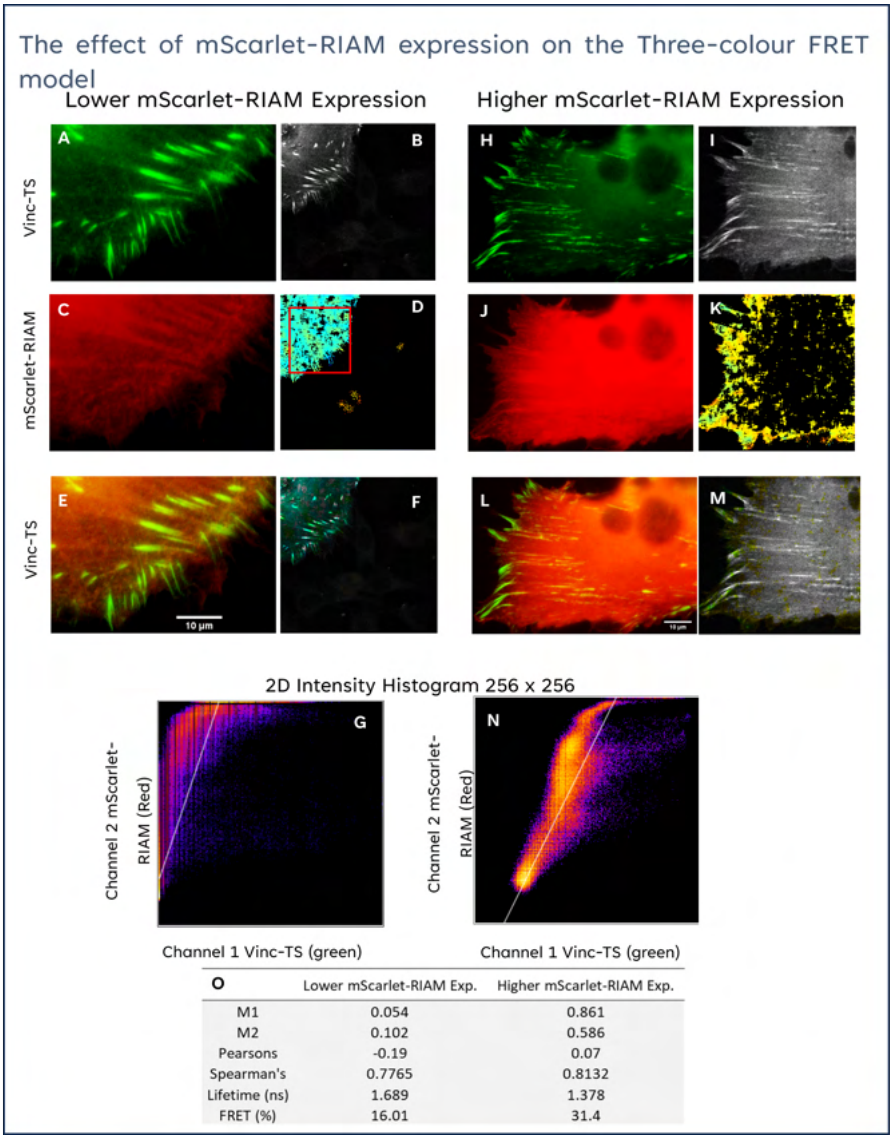

O	Lower mScarlet-RIAM Exp.	Higher mScarlet-RIAM Exp.
M1	0.054	0.861
M2	0.102	0.586
Pearsons	-0.19	0.07
Spearman's	0.7765	0.8132
Lifetime (ns)	1.689	1.378
FRET (%)	16.01	31.4

Figure 5.2.5.1: ***The effect of mScarlet-RIAM expression in nascent adhesion on the Three-colour FRET model:*** *A-F Low mScaret-RIAM expressing cell. H-M high expressing mScalret-RIAM cell. G and N show 2D histograms of the pixel intensities for the two images, with the Vinc-TS (green) channel plotted against the mScarlet-RIAM (red) channel. O contains a table showing the result from the colocalization analysis along with lifetime and FRET efficiency data for the two cells. Scale bar = 10 µm.*

5.2.6 Three-colour FRET model Applied to the Vinculin Tension Sensing Biosensor with mScarlet-RIAM in Fixed MEFs

The fluorescence lifetimes for the various FRET pairs between the vinculin-TS and mScarlet-RIAM transfected and co-transfected cells were used to produce the three-colour FRET model (figure 5.2.6-1. panel A) from the distribution of FRET efficiencies recorded for the various FPs encoded within each of the constructs. Large variations in FRET efficiencies can be observed for several different constructs, but still, a significant increase in the FRET efficiencies can be seen when mScarlet-RIAM is included as an additional acceptor in all cases compared to when it is not there. Vinculin-TL increases its FRET efficiency from 17.0 ± 5.73 % to 28.9 ± 3.29 % by adding mScarlet-RIAM in the FA-only masked cells. The same trend can be seen in the more variable vinculin-TS condition with the addition of mScarlet-RIAM increases the FRET efficiency of the multi-colour FRET cascade in the FAs from 12.28 ± 6.04 % to 29.07 ± 8.75 %. The general trend that the addition of mScarlet-RIAM across all the constructs is positive, but variability in the data is probably a reflection of the heterogeneity in the samples imaged. There is very little difference between the FRET efficiencies of the FAs only and the whole cell, only minor differences in averages and variance but otherwise, the same and not statistically different.

The separation distances for the three fluorophores were for the teal-mVenus pair 8.31 ± 4.06 nm, mVenus-mScarlet 7.03 ± 2.34 nm and teal-mScarlet 7.13 ± 1.35 nm. An assumed stoichiometry between the teal and mVenus FPs was taken as 1:1, which I believe is sensible as they are encoded on the same biosensor. I have, however, not made any assumptions regarding the stoichiometry of the mScarlet-RIAM protein within the RIAM-vinculin complex. The distance measurements were then subsequently used to calculate the average intramolecular force acting on an average vinculin molecule was determined within the fixed MEFs imaged and was calculated to be 1.06 ± 0.51 pN (equation 3.2.7-1).

The energy transfer rates between the different fluorophores used in the vinculin-TS + mScarlet-RIAM experiments can be used to ascertain if the vinculin-RIAM interaction occurs when the tension sensor is in the open or closed configuration and to deduce whether this interaction is more likely to be found within the cytoplasm or just found in focal adhesions. However, the large spread of fluorescence lifetimes makes it difficult to reach a definitive

conclusion. Increased variance in the lifetime data propagates to a larger standard deviation and lower confidence in the calculated separation distances.

Here we can see how the FRET transfer rates Γ_{AB}, Γ_{AC} and Γ_{BC} were used to estimate the lifetime of the three-colour vinculin-TS + mScarlet-RIAM interaction. The difference between the actual measured and predicted values was only -0.87% indicating that the model likely represents the interaction well between the vinculin TS and the RIAM-mScarlet construct, despite the large uncertainty in the FRET data. The whole cell masked data were also analysed similarly (data not presented here). However, there was very little difference between the FRET averages of the whole cell and FA-only masked cells. The only difference was found in the variance, which is likely to be more a symptom of relatively small samples and cellular heterogeneity, whether sample prep driver or otherwise.

Further experiments are needed to fully understand this interaction between RIAM and vinculin. Some evidence, but mostly conjecture at this point, suggests that the interaction is a transient shuttling. Global analysis [124] on the FLIM data would be beneficial, as this could quantify which areas of the cell exhibit more FRET. Unfortunately, this cannot be used effectively on this data set as there are just too much heterogeneity and low photon count in the sample data, which has hampered my ability to undertake bi-exponential fitting using the LMA algorithm and to show the relative proportions of FRET between multiple donor acceptors in a fractional sense.

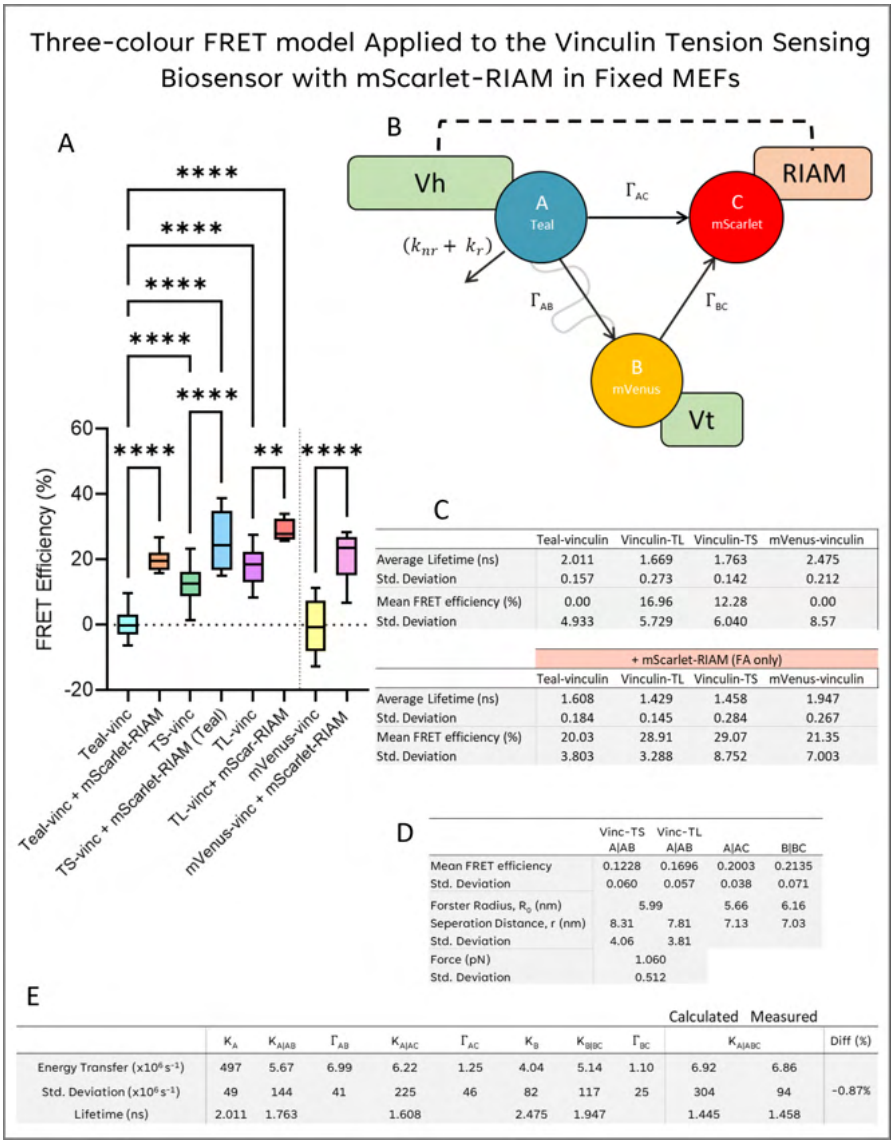

	Teal-vinculin	Vinculin-TL	Vinculin-TS	mVenus-vinculin
Average Lifetime (ns)	2.011	1.669	1.763	2.475
Std. Deviation	0.157	0.273	0.142	0.212
Mean FRET efficiency (%)	0.00	16.96	12.28	0.00
Std. Deviation	4.933	5.729	6.040	8.57

+ mScarlet-RIAM (FA only)				
	Teal-vinculin	Vinculin-TL	Vinculin-TS	mVenus-vinculin
Average Lifetime (ns)	1.608	1.429	1.458	1.947
Std. Deviation	0.184	0.145	0.284	0.267
Mean FRET efficiency (%)	20.03	28.91	29.07	21.35
Std. Deviation	3.803	3.288	8.752	7.003

	Vinc-TS A|AB	Vinc-TL A|AB	A|AC	B|BC
Mean FRET efficiency	0.1228	0.1696	0.2003	0.2135
Std. Deviation	0.060	0.057	0.038	0.071
Forster Radius, R_0 (nm)	5.99		5.66	6.16
Seperation Distance, r (nm)	8.31	7.81	7.13	7.03
Std. Deviation	4.06	3.81		
Force (pN)	1.060			
Std. Deviation	0.512			

									Calculated	Measured	
	K_A	$K_{A\|AB}$	Γ_{AB}	$K_{A\|AC}$	Γ_{AC}	K_B	$K_{B\|BC}$	Γ_{BC}	$K_{A\|ABC}$		Diff (%)
Energy Transfer ($x10^6 s^{-1}$)	497	5.67	6.99	6.22	1.25	4.04	5.14	1.10	6.92	6.86	
Std. Deviation ($x10^6 s^{-1}$)	49	144	41	225	46	82	117	25	304	94	-0.87%
Lifetime (ns)	2.011	1.763		1.608		2.475	1.947		1.445	1.458	

Figure 5.2.6.1: ***Three-colour FRET model Applied to the Vinculin Tension Sensing Biosensor with mScarlet-RIAM in Fixed MEFs:*** *A) Shows the average FRET efficiencies for the various FRET pairs graphically. Where A=mTFP1 (Teal), B=mVenus and C=mScarlet, for FRET pairs, the letter before the line marks the donor, so A—ABC denotes the FRET efficiency measured where the donor is A, Teal and B—ABC would denote the FRET efficiency measured where the donor is B, mVenus in the Vinc-TS + mScarlet-RIAM complex. B) A diagram showing the three fluorescent proteins in the vinculin head (VH) and tail (Vt) domains along with the placement of the tension sensor and mScarlet-RIAM. C) D) A summary table detailing the FRET efficiencies, Forster radii and separation distances for the various energy transfers and force calculation for the vinculin Tension Sensor. E) Energy transfer rates, standard deviation, and the associated lifetime of each FRET component.*

5.3 Conclusion for the Application of the Three-colour FRET model

Previously, in Chapter 3, I described the vinculin-RIAM association in isolation and showed that I could not only detect a biological interaction between the two proteins via pull-downs but also by using fluorescently tagged versions of the proteins, I could show a direct association. In the same chapter, I also introduced the vinculin Tension Sensor, which can report on the intramolecular tensile force applied to vinculin through FRET. Chapter 4 dealt with the development of a three-colour FRET approach allowing a combination of the two FRET interactions into a single experiment where I can simultaneously report on the two independent FRET interactions. This chapter is the culmination of the previous chapters, where I set out to combine the two approaches, simultaneously reporting on the tensile forces applied to vinculin and whether RIAM is also bound to vinculin, achieved with some compartmental segregation to give crude spatial resolution between the interactions occurring in the cytoplasm and FAs.

FRET efficiencies calculated from the fluorescent lifetimes of vinculin-TS and vinculin-TL constructs yielded an average separation distance between the teal and mVenus FPs of 8.31 ± 4.06 nm and 7.81 ± 3.81 nm for the tension sensor constructs, respectively. The vinculin-TL construct is considered the high FRET, low tension, and control and should represent the relaxed position the two FPs occupy when little to no tension is applied. We then consider the vinculin-TS construct, which can respond to intramolecular forces acting on vinculin by extending the 40 amino acid nanospring, which separates the two FPs to observe a loss of FRET as an indication of applied force. The difference between the separation distance for the vinculin-TL and vinculin-TS imaged cells describe the average increase in separation distance measured by the tension sensor. The average increase in distance was found to be 0.51 ± 0.22 nm. The nanospring has previously been found to have a stiffness of 0.478 nm/pN [130, 149], which yields an average applied mechanical force to vinculin to be 1.06 ± 0.52 pN.

It is important to realise that 10 cells were imaged for each condition, each containing 50-100 resolved focal adhesions, each associated with hundreds or thousands of vinculin molecules. The average separation distance is a bulk measurement, so it cannot tell us much about what is happening at the individual adhesion level, but only the average experienced across all

the cells imaged. This is why there are much variation in the vinculin-TS measurements, and it is challenging to draw a more valid and significant conclusion from this experiment. However, this tells us that the vinculin-TS construct does, for many cells, record a value for the applied force to vinculin, and that force can be detected on vinculin with the FAs.

The second area of focus, relating to the colocalization of vinculin and RIAM showed that most of the vinculin is detected in the FAs and RIAM is predominantly localised to the cytoplasm where there is very little cooccurrence and colocalization between the two proteins. Even so, there is an interaction that can be detected by TCSPC-FLIM/FRET.

The three-colour model applied to the vinculin-RIAM interaction accurately predicted the lifetime of the vinculin-TS + mScarlet-RIAM interaction. From this, a simple model can be made; it is likely that the teal-mVenus FRET pair is in a closed, high-FRET configuration in the cytoplasm and only separates when vinculin is localised in FA and bound to both talin and actin. It is understood that mechanical forces originating from the actomyosin cytoskeleton engage the force-dependent extension of vinculin. Despite the lack of a significant difference between the teal-vinculin fluorescence lifetimes associated with the cytoplasmic and focal adhesion fractions, there is still likely to be a difference. Measuring that difference accurately through fixed-cell traditional TCSPC-FLIM is a significant challenge. Faster methods, which allow for data to be acquired in tens of seconds and not hundreds, would be of particular interest, as would super-resolved FLIM techniques that would allow for the interrogation of single adhesions *in vivo*.

From the evidence presented thus far, it is becoming increasingly apparent that the vinculin-RIAM interaction is not a focal adhesion-associated reaction and is not likely to play a vital role in the maturation or preservation of FAs within the lamellipodium. What is more likely, is that RIAM performs a shuttling role. We know RIAM has a role in shuttling talin molecules from elsewhere in the cytoplasm and is also able, under the right conditions to associate with vinculin and, therefore, likely to perform a similar task for Vinculin. In future experiments, it would be interesting to better understand the effect truncated or knocked down RIAM cells have on focal adhesion assembly and whether mutations in RIAM can lead to cells with diminished or fewer adhesions as the recruitment and assembly apparatus is lost.

6

DISCUSSION

6.1 Discussion of Results

6.1.1 The vinculin-RIAM Interaction

The data presented in this manuscript in chapter three relates specifically to elucidating a physiological vinculin-RIAM interaction. A previous study64 had shown that the D1 subdomain of the vinculin head domain (amino acids 1-258) and the N-terminal of RIAM (amino acids 1-250) and that, at high concentrations, the N-terminus of RIAM can displace vinculin from a talin-vinculin interaction and instead RIAM can bind to vinculin. The two N-terminal domains were also crystallised, and a structure for this interaction was published37. However, no in vivo study of the interaction or evidence of biological function for the interaction has been published yet; a core objective of this thesis is to show that vinculin-RIAM interaction is physiological and to elucidate a possible biological function of the interaction.

Co-immunoprecipitation studies of EGFP-vinculin (described in §3.2.1) showed that pulling both talin and RIAM from a GFP-trap is possible. Talin, a known binding partner to vinculin data, shows that RIAM is also present in the vinculin complex. This alone is not conclusive as RIAM is an established binding partner of talin, so being able to probe for RIAM on a vinculin pull-down when talin is shown to be present may not be convincing of a direct interaction. Following this, the putative interaction was further probed using two FRET pairs, one where RIAM was genetically encoded to the N-terminus of RIAM and the other where mScarlet was placed at the C-terminus of RIAM with EGFP-vinculin as the donor in both cases. These experiments supported the theory that the N-terminus of RIAM is more likely to be in direct contact with the N-terminus of vinculin as FRET efficiencies for the GFP-vinculin + RIAM-mScarlet and GFP-vinculin + mScarlet-RIAM equated to a separation distance of 7.23 nm for the two N-terminally labelled proteins compared to 7.91 nm for EGFP-vinculin + RIAM-mScarlet. This is encouraging as this result is consistent with the proposed N-terminal interaction [37].

Once I had established that the two proteins directly interacted and that this could be measured through FLIM, I wanted to establish the function of this interaction. It is well documented that RIAM associates with talin35,37 and acts to shuttle the auto-inhibited conformation of talin from the cytoplasm to inactive integrins on the plasma membrane54,61,63. I wanted to investigate whether this was also true for vinculin. I set out to investigate the location of the vinculin-RIAM interaction; I wanted to know if the interaction was primarily FA based or also occurred in the cytoplasm. In §3.2.3, I described using different thresholds to mask high and low-intensity regions, excluding different background levels to isolate pixels from the whole cell and FAs. I then inverted the FA mask maintaining the low-intensity threshold to remove any extra-cellular background. The FRET efficiencies calculated for the separate regions were all approximately the same, with very little difference between the three masked areas.

I wanted to see if the interaction formed Indepentently in the cytoplasm or if the interaction also occurred within FAs. Evidence already suggested that it was predominantly in the cytoplasm, but I wanted to see if I could drive the interaction by increasing the FA turnover rate by adding nocodazole. Nocodazole disrupts microtubules, which causes the enlargement of FAs203 as more FA-associated proteins assemble at the leading edge of the cell203. I wanted to see if we could get a change in the proportion of vinculin molecules interacting with RIAM when nocodazole is present. The FRET efficiency showed that the untreated cells had an average FRET efficiency of 16.83 ± 3.95 %, and the nocodazole-treated cells had an average of 18.03 ± 2.36 %. A very modest increase in the degree of FRET between the two proteins was found not to be significant, suggesting that the interaction does not primarily occur in the adhesion. However, driving the formation of new adhesions has caused a very modest increase in the measured FRET efficiency.

To determine if vinculin-RIAM interaction required actin, a ROCK (Rho protein associated Kinase) inhibitor, H-1152, was used. Inhibition of ROCK decreases LIMK activity204, preventing cofilin phosphorylation, causing actin filaments to destabilise, and resulting in a loss of the actomyosin cytoskeleton and FAs. Vinculin-RIAM FRET efficiency data (§3.2.5) showed that untreated cells had an average FRET efficiency of 25.09 ± 2.67 %, whereas the treated cells had an average lifetime of 26.75 ± 2.56 %. Again, no significant difference between the two was found, further supporting the idea that the vinculin-RIAM

interaction was not formed in the FAs but elsewhere in the cell, most likely in the cytoplasm.

6.1.2 Three-Colour Cascade FRET

Another core objective of this thesis was to develop an in vitro multicolour FRET cascade methodology that could elucidate the precise order of formation, re-organisation and turn-over of a multimeric protein complex in a spatiotemporal manner. This involved producing and purifying the fluorescent proteins mTurquoise2, mVenus and mScarlet-I. This was achieved in isolation and as the three different two-fluorophores and two different three-fluorophore proteins. This specific mutation had not been used before to achieve an mVenus that did not absorb or emit light. Still, a related mutation in EGFP, G67A, was shown to prevent chromophore formation and possibly could lead to the misfolding of the protein. Excitation and emission spectra confirmed that the purified proteins behaved as expected in their spectra, indicating FRET observed in spectroscopic measurements with appropriate emission peak assignments. The G68A mutation inserted in mVenus did not have an excitation peak at 515 nm nor an emission peak at 530 nm, indicating that the mutation had prevented the formation of the mVenus fluorochrome. The secondary and tertiary structures of the mutant were undamaged, as shown by CD spectra. Some stability is lost at higher temperatures compared to the mVenus. The mVenus-G68A mutant may require lower temperatures to be expressed as a functional, fully folded protein. This may explain why earlier research conducted by the Tsien group [?, ?] concluded that this mutation in EGFP produced a protein that was not only non-fluorescent but also disordered. Including this mutation is not a new finding, but as far as I am aware, no other researcher has used this specific mutation to create a non-fluorescent beta-barrel or control for FRET.

Imaging the purified proteins using a 2-photon TCSPC-FLIM imaging system showed that the average mTurq2 and mVenus fluorescence lifetimes were similar to the published lifetime [?] measured by a widefield frequency-domain FLIM imaging system [?]. The average lifetimes observed for the two-FP proteins were significantly decreased compared to the relevant single-FP controls, confirming that FRET had occurred between each of those two-part chimeric proteins. A further decrease in the average lifetime was observed for the three-colour, mTurq2-mVenus-mScarlet-I protein, indicating that the construct had functioned as expected. The mutated three-colour protein,

mTurq2-mVenusG68A-mScarlet-I, had a longer lifetime than the unmutated mTurq2-mScarlet protein, suggesting that the increased distance between the two FPs had made a significant difference while also giving further support to the idea that the mVenus which separates the FPs in the mutated three-colour protein, truly is both non-fluorescent and non-absorbing. FRET efficiencies were calculated from the lifetime data, and the energy transfer rates were determined.

The individual FRET transfer rates determined from their respective interactions were used to calculate and effectively predict a lifetime for the three-colour protein of 2.25 ± 0.391 ns, compared to the measured lifetime of 2.33 ± 0.266 ns; this represents only a 3.40% discrepancy between the predicted and measured results. This result validates both our theory and experimental methodology.

The distances between the mTurq2-mVenus, mTurq2-mScarlet and mVenus-mScarlet FPs were found to be 6.33 ± 0.12 nm, 7.14 ± 0.17 nm, and 7.50 ± 0.31 nm, respectively. A key finding was determining the distances between the mTurq2 and mScarlet FPs, and between the mTurq2 and mVenus FPs, in the mTurq2-mVenus-mScarlet-I protein were approximately the same distance. If the mTurq2-mVenus-mScarlet protein were in an open/linear configuration, we would expect to see the distance between mTurq2 and mScarlet exactly twice the distance between mTurq2 and mVenus. This was not the case, which would suggest a triangular or globular shape to the three-colour FP and not a cylindrical one. Next, we used the cosine rule to calculate an approximate separation angle between the mTurq2 and mScarlet FPs of 62.43 ± 3.88 nm. Lastly, structural validation was attempted through negative stain TEM, which successfully produced low-resolution screening images of the three-colour, mTurq2-mVenus-mScarlet protein in the negative stain. Distances between the centres of what are likely to be beta-barrels, a range of distances very close to the predicted distances calculated from the FRET efficiencies. This is not conclusive evidence that the three-colour protein is in a triangular/globular confirmation, but it does provide some validation of the predicted model.

6.1.3 Application of the Three-Colour FRET Model

At the end of Chapter 3, I discussed how the vinculin-tension Sensing construct (vincTS) could determine whether mechanical force was applied to

vinculin. To recap briefly, vinculin-TS has two FPs, teal and mVenus; when force is applied to vinculin, these FPs will pull apart from one another, such that a loss of FRET compared to a control is indicative of a high force FA. From calculated FRET efficiency data, separation distances could be calculated, and by using the specific stiffness of the nanospring, an applied force acting on the vincTS could be deduced. This showed that approximately 1.57 ± 0.97 pN force was applied to fixed, stationary vinculin molecules within the FAs imaged. Incidentally, the same construct had been used in a previous study, and they found that the applied force was approximately 2.5 pN (error not stated in the paper) in stationary FAs [149]. This is broadly in agreement with the published data using the same construct. However, as previously stated, improvements could have been made regarding mounting fixed samples, especially when using mounting media with a mismatched refractive index, as this could have effectively reduced the dynamic range of the teal FP, which in turn could have led to the reduced FRET efficiencies measured and lower-than-expected force measurement.

In Chapter 5, I revisited this topic again but with the addition of mScarlet-RIAM in a three-colour FRET experiment. Here, we saw a reduction in the fluorescent lifetime of the teal donor when mScarlet-RIAM was added, which was analysed using the three-colour model. This indicated that an energy transfer from the teal donor to an mVenus acceptor in the biosensor occurred in addition to an energy transfer between the teal donor and an mScarlet-RIAM acceptor. This indicated that the teal-mVenus FPs were likely in the closed, low-force conformation of the biosensor, as the measured lifetimes for the vinculin-TS and vinculin-TL (the high FRET control) were very similar at 1.763 ± 0.14 ns and 1.669 ± 0.27 ns for the vinculin-TS and vinculin-TL constructs respectively. In both cases, adding the mScarlet-RIAM construct further reduced the teal lifetime to 1.458 ± 0.28 ns and 1.429 ± 0.15 ns again for the vinculin-TS and vinculin-TL constructs. This would strongly indicate that, on average, the force detected on vinculin was lower compared to both the published values and the data set previously collected and studied when calculated, this was found to be 1.06 ± 0.51 pN in the absence of mScarlet-RIAM. The additional FRET observed when the mScarlet-RIAM construct was co-transfected with the vincTS construct can be explained by the mScarlet-RIAM protein associating with the vincTS biosensor in its closed, high FRET state or potentially the mScarlet-RIAM binds at very close range to the teal FP within the sensor as the sensor opens. The former is far more likely than the

latter, but a potential problem with the model is presented here. The model is straightforward in comprising two equally weighted FRET transfers between teal and mVenus and teal and mScarlet (§5.2.4 and §5.3). In this instance, I have given equal weighting to the two FRET transfers, which may not be correct, as this would suggest a 1:1:1 stoichiometry between the three FPs. While it is probably safe to assume that for every teal FP, there will also be a mVenus FP as these are both encoded within the same gene, assuming there is little misfolded or partially folded biosensor in the cell. However, it is not likely that there will always be a RIAM protein interacting with every single biosensor. Without any data reporting on the concentration of mScarlet-RIAM, it is challenging to make assertions about the frequency of vinculin-RIAM interaction.

A significant reduction in the fluoresce lifetime was measured with the addition of the mScarlet-RIAM construct, indicating a direct between the mScarlet-RIAM and the vinculin-TS biosensor. Colocalization was attempted and outlined in §5.2.5; however, this was not particularly fruitful as the vinculin-TS biosensor and mScarlet-RIAM were not to be colocalized in the FAs despite the FRET interaction being reported there. The co-localization images were diffraction-limited, with a resolution of $\approx$ 250-300 nm. FRET and, by extension, FLIM is not limited in the same way in terms of interaction detection and can report on interactions between proteins as close as 2 nm away. A correlation between mScarlet-RIAM and lower fluorescence lifetimes probably does exist. However, using single-molecule imaging techniques such as FCCS or Single-Molecule Three-Colour FRET would require determining the correlation between mScarlet-RIAM and the vinculin-TS biosensor within developing adhesions.

The data presented in Chapter 5, and partially reviewed above, demonstrates that FRET occurs between the teal and mVenus FPs within the vinculin-TS construct as evidenced by 1.76 $\pm$ 0.14 ns lifetime and associated FRET efficiency of 12.28 $\pm$ 6.04 %. The FRET efficiency measured in FAs increases to 31.21 $\pm$ 13.33 % when the mScarlet-RIAM construct is co-transfected into the same cells with the vinculin-TS biosensor. Applying the three-colour model (described in §4.2.11) allowed for the calculation of the separation distances for the three fluorophores, which were found to be as follows: Teal-mVenus 8.31 $\pm$ 4.06 nm, mVenus-mScarlet 7.03 $\pm$ 2.34 nm and Teal-mScarlet 7.13 $\pm$ 1.35 nm.

6.2 Proposed RIAM-Vinculin Model

The current model of nascent adhesion assembly is thought to be initiated by signalling pathways that activate Rap1-GTPase in an "inside-out" signalling mechanism54,61,63. To briefly recap, this involves the activation Rap1-GTPase, which in its active state, binds to the RA-PH (Ras-association Pleckstrin Homology) double domain on RIAM [?]. The Rap1-RIAM complex binds to talin while in its autoinhibited conformation in the absence of force through its FERM domain and R2/3 of the rod domain of talin [?, ?]. It is likely that in the autoinhibited conformation of talin, both domains are accessible to Rap1-RIAM, which, once bound to talin, translocates to the plasma membrane. At the plasma membrane, talin engages with integrin tails and plasma membrane proteins like PIP2 through its FERM domain, forming the nascent adhesion [?] and activating integrin [?]. It has also been suggested that the talin-RIAM-Rap1 complex may recruit other proteins that regulate actin polymerisation at the leading edge and may even pre-complex with vinculin [?, ?, 192]. Once talin is bound to integrins, the Rap1-RIAM complex is thought to dissociate, allowing vinculin to bind to talin. RIAM and vinculin binding via the R2/3 domains on talin are mutually exclusive. However, there are other vinculin binding sites (VBS) on talin (11 in total); four of these are located within the R2/3 domain, and it is thought that this is where vinculin first associates [?]. Vinculin binding is thought to initiate a conformational change in the structure of talin, which allows for cryptic VBS to be revealed, accelerating the rate of vinculin association with talin [?, ?]. As both talin and vinculin also bind actin, actin association induces mechanical forces on both vinculin and talin, further changing the 3D tertiary structures of these two proteins and allowing for further vinculin to bind to talin. Once talin is in the full-extended confirmation, none of the 5 RIAM molecules is bound, but 11 vinculins can potentially be bound [35, 37].

The data presented in this thesis has culminated in a new proposed model of vinculin and possibly talin recruitment by Rap1-activated RIAM. I have shown a physiological interaction between vinculin and RIAM further to the proposed *in vitro* interaction proposed earlier and shown in figures 6.2-1 and 6.2-2. Once Rap1-RIAM has been associated with the auto-inhibited conformation of vinculin, much like activated Rap1-RIAM associates with talin, the complex is then translocated to the plasma membrane (panel 1 of Figure 6.2-1). It is also possible that these two complexes also form a larger pre-complex. The

literature has already postulated that vinculin could associate with the R8 domain of talin without mechanical force205. This is interesting as we know the mechanical force is required for vinculin binding to the R2/3 domains of talin, and it is thought that force-induced re-modelling of talin is a prerequisite for vinculin binding.

Once talin has been recruited to the plasma membrane by RIAM, talin associates with and activates integrins (panel 2 of Figure 6.2-1). This stage of my proposed model is the same as the current recruitment theory. However, The following step does differ, as my data suggests that activated Rap1-RIAM mediates vinculin recruitment. In the previous section, I discussed how mScarlet-RIAM binds to the vincTS construct when that construct is reporting high FRET and low mechanical force on vinculin. Therefore, the lack of change in FRET interaction between GFP-vinculin and mScarlet-RIAM when adding nocodazole and ROCK strongly indicates that RIAM does not associate with active vinculin. The activated Rap1-RIAM-vinculin complex (panel 3 of figure 6.2-2) dissociates from vinculin, where vinculin then binds to talin and is further activated through a force-dependent mechanism [?,?].

My hypothetical model differs from the established model in how vinculin is recruited to the plasma membrane/lamellipodium. I have shown evidence of a RIAM-vinculin interaction where RIAM acts to recruit and translocates vinculin in the same manner as the established talin recruitment.

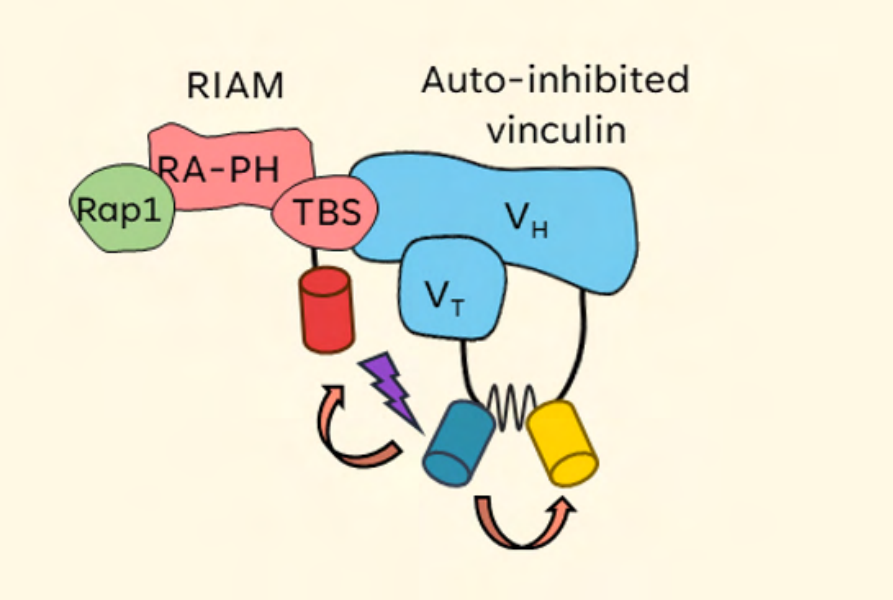

Figure 6.2.0.1: ***Three-colour FRET between vincTS and mScarlet-RIAM:*** *A scheme illustrating the hypothesised three-colour FRET interaction between the vincTS and mScarlet-RIAM proteins.*

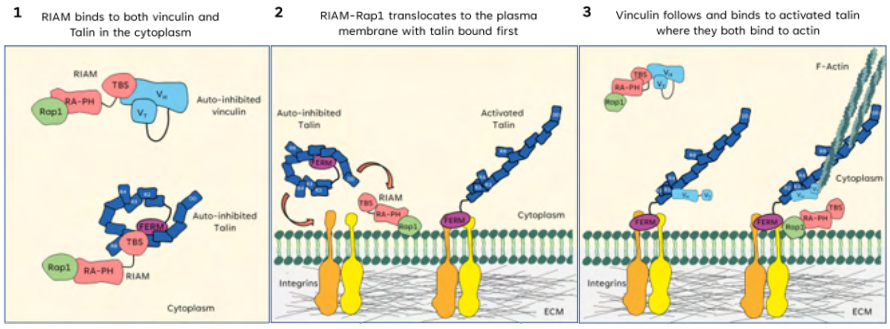

Figure 6.2.0.2: ***Proposed Model of vinculin and talin recruitment by RIAM:*** *A scheme detailing the key events in my proposed model for vinculin and talin recruitment by RIAM.*

6.3 Future work

Live Cell FLI-SWARM imaging

A significant issue that I feel detrimentally affected this project was the choice to predominantly use fixed cells for the FLIM imaging. This caused two problems. The first, while it made imaging much easier, as using fixed samples are far less challenging than keeping cells alive while being imaged. Nonetheless, it limited what I could achieve in imaging the dynamic interactions with the vinculin TS biosensor and force-induced FA remodelling. The second issue I found was decreased fluorescence lifetime with fixed cells mounted in a glycerol-based mounting medium198.

If I had the time, I would undoubtedly endeavour to complete the same vinculinTS + mScarlet-RIAM series of experiments as outlined in chapter 5 of this thesis again. However, I would want to do it with live cells as this would most likely alleviate the issue surrounding decreased lifetime, drastically improving the confidence associated with the in vivo measured lifetimes for the vinculin biosensor with mScarlet-RIAM. A significant barrier to imaging live cells with conventional TCSPC-FLIM is that it is much slower to acquire lifetime data (300 seconds) than other FLIM methods, such as Frequency-Domain FLIM, which can image live cells in real-time albeit with significantly poorer spatial resolution125. Within the Ameer-Beg group, we have already developed a much faster approach to TCSPC-FLIM, FLI-SWARM (Fluorescence Lifetime Imaging SWept Array Microscopy), which massively parallelises the data acquisition bottle-neck by using an array of 1024 beamlets to scan the sample which allows for real-time acquisition. Disruption relating to the ongoing COVID pandemic meant I could not use this new, unpublished technique.

Another benefit to using the FLI-SWARM to acquire fast FLIM data is that Image Correlation Spectroscopy (ICS) data can also be acquired simultaneously. Several related techniques can be used to determine how quickly a fluorescent signal is changing, either in space or time. Fluorescence Correlation Spectroscopy (FCS) is a popular method in which temporal changes in the fluorescence emission intensity caused by single fluorophores passing through the detection volume are recorded over time from a stationary excitation spot [193]. This allows the diffusion coefficient to be calculated for that specific fluorophore but has very little spatial information [123,193–195]. ICS is a popular extension where the sample is observed via a camera instead

of a detector with FCS [194, 195]. Three-colour FRET model to determine the spatiotemporal relationship between Talin, Vinculin and RIAM A simple extension of the work I have presented in this thesis would be to label the three proteins, talin, vinculin and RIAM, with mTurq2, mVenus and mScarlet and then to use the three-colour model to determine which proteins were interacting where in the cell. If coupled with live cell imaging, this could also be extended to identify when the interaction(s) are most prevalent in the cell cycle. This could be attempted using the FLI-SWARM system as described above but could prove difficult without some super-resolved imaging. As previously discussed in §6.1.3, FRET-based techniques can detect interactions between fluorescently labelled proteins as close together as 2 nm; however, their precise local concentrations must be known to fully describe the interplay between the three labelled proteins. This would be a challenge to do accurately with diffraction-limited imaging techniques, as observed in the colocalization section presented in this manuscript. For that reason, this would most likely need to be done at the single-molecule level using super-resolved single-molecule localisation techniques such as STORM (STochastic Optical Reconstruction Microscopy) or PALM (Photo-Activatable Localisation Microscopy) imaging techniques.

Super-Resolved Compressed Sensing of Vinculin Tension Sensing Biosensor

As a PhD student, I was involved in developing a separate FLIM-based imaging technique known as Super-Resolved Compressive-Sensing FLIM (SRCS-FLIM). This side project involved the development of an innovative imaging technique that combined super-resolved single-Molecule Localisation imaging with TCSPC-FLIM by utilising an image reconstruction technique called Compressed Sensing. SRCS-FLIM can produce super-resolved images of single molecules at resolutions approaching 40 nm with fluorescence lifetime data. This system is still in its proof-of-concept stage but could be used to image individual FAs in cells expressing the vinculin-TS biosensor. A version of the vinculin-TS biosensor has been made, with the photoactivatable FP Dronpa and mScarlet cloned in as the donor and acceptor, respectively. PALM experiment could be conducted with the Dronpa-mScarlet vinculin-TS construct expressed in cells and imaged with SRCS-FLIM. This would yield in vivo information regarding forces applied to individual vinculin molecules, not just the ensembled average described in this manuscript.

Single-molecule Three-colour FRET studies.

Over the last 20-25 years [?,?,?], there has been a growing interest in using *in vitro* single molecule three-colour FRET experiments to probe nanoscale molecular interactions. This can be achieved by attaching three separate fluorophores to either a single protein, multiple proteins, or short oligonucleotide sequences and observing the three-dimensional conformational changes that occur as the molecules of interest interact with known binding partners or respond to specific cellular signalling molecules. This information can be beneficial as it can report on the precise mechanism of protein remodelling210. As a potential next step, it could be very interesting to label talin, vinculin and RIAM with dyes that allowed for the detection of conformational changes to be monitored as the three proteins interacted with one another. This would not have to be limited to just those three proteins as any protein that binds to other proteins in a complex or even dimerises with itself could be investigated similarly.

6.4 Conclusion

At the start of this thesis, I stated three core aims that I was determined to research, explore, and investigate; these were:

1. To determine if the *in vitro* interaction between RIAM and vinculin can be detected and characterised *in vivo* using a range of biochemical and biophysical assays.
2. To develop a new FRET-based assay that would be used to determine whether multiple fluorescently labelled proteins are bound together in a single complex at a specific time point and location in a cell.
3. To merge the last two objectives and apply the multi-colour FRET model to solve specific questions regarding intracellular tension across vinculin in developing focal adhesions:
   (a) Is the vinculin Tension Sensor in an open or closed conformation when RIAM is bound to vinculin?
   (b) Does RIAM only associate with the auto-inhibited form of cytoplasmic vinculin?
   (c) Does the putative vinculin-RIAM require other FA proteins, such as actin?

There does appear to be evidence to support the idea of a biologically relevant interaction between vinculin and RIAM. I have shown that interaction can be determined through pull-down assays and FLIM imaging. I successfully produced and purified the fluorescent protein constructs of individual pairs and three FPs, which I used to establish a three-colour FRET model. I then used this model to determine that RIAM likely binds to vinculin in its inactive state and is likely to occur predominantly in the cytoplasm. I also detected an interaction in the focal adhesions, but the vinculin-RIAM interaction appears to occur independently of actin. This provided further evidence to suggest that the interaction is not likely to occur within the focal adhesions per se. However, RIAM could perform a similar role in shuttling talin to the cell's leading edge when activated by Rap1-GTPase.

A

APPENDIX A

A.1 Buffers & Reagents

Table 18: *Buffers Table A*

Buffers	Composition
Buffer A	150 mM NaCl, 50 mM Tris-Cl, 20 mM Imidazole pH 8.0
Buffer B	150 mM NaCl, 50 mM Tris-Cl, 1M Imidazole pH 8.0
Catalase solution	17 mg of Catalase dissolved into 50 mM phosphate buffer pH8.0
Complete Growth Media	Dulbecco's Modified Eagle's Medium (DMEM), 10% FCS, 1% Penicillin-Streptomycin, 1% L-Glutamine and 1% Non-Essential Amino Acids.
cTBS (Cytoskeletal Tris Buffered Saline)	20 mM Tris-Cl, 154 mM NaCl, 2 mM EGTA, 2 mM $MgCl_2$, pH 7.4
cTBS-Tx	0.2% Triton-X 100 in cTBS
Dilution buffer	50 mM Tris-Cl, 150 mM NaCl, 500 µM EDTA, 0.1% IGEPAL, 25 mM NaF, and 1 mM PMSF
Glucose Oxidase (Glox) Mix	35 mg Glucose oxidase dissolved into 100 µL of Catalase solution
Imaging Buffer	FluoroBrite® DMEM, 10% FCS, 1% Penicillin-Streptomycin, 1% L-Glutamine and 1% Non-Essential Amino Acids.
Laemmli buffer (2x)	50% 4x NuPAGE LDS sample buffer, 10 mM DTT and 40% ddH_2O
LB media	Yeast Extract 5g/L, Tryptone 10 g/L and NaCl 5g/L
Lysis buffer	50 mM Tris-Cl, 150 mM NaCl, 500 µM EDTA, 0.1% IGEPAL, 25 mM NaF, 0.5% Triton-X 100, and 1 mM PMSF
Milk Blocking solution (5%)	5% (w/v) Skimmed milk powder dissolved in TBS
MOPS SDS PAGE Running Buffer	50 mM MOPS, 50 mM Tris -base, 1 g/L SDS, 300 mg/L EDTA, pH 7.7
NuPAGE transfer buffer	25 mM Bicine, 25 mM Bis-Tris, 1 mM EDTA, 20% Methanol and pH 7.2
PBS (Phosphate Buffer Saline)	137 mM NaCl, 2.7 mM KCl, 10 mM Na_2HPO_4, 1.8 mM KH_2PO_4, pH 7.4
PFA Fixing solution	4% (v/v) Paraformaldehyde in PBS
PFA-PHEM Fixing solution	4% PFA dissolved in PHEM buffer
PHEM Buffer	60 mM **P**IPES, 25 mM **H**EPES, 10 mM **E**GTA, 2 mM **M**$gCl_2.6H_2O$, 120 mM Sucrose, pH 7.4
STORM imaging Buffer	200 mM MEA, 10% Glucose (v/v), 50 mM Tris-Cl, 10 mM NaCl, 1x Glox mix and pH 8.0.
TAE Buffer	40 mM **T**ris-base, 20 mM **A**cetic acid and 1 mM **E**DTA
TBS (Tris Buffer Saline)	20 mM Tris-Cl, 154 mM NaCl pH 7.4
TBS-Tw	0.1% Tween 20 in TBS
Tris-Acetate SDS PAGE running buffer	50 mM Tricine, 50 mM Tris-Cl, 0.1% SDS and pH = 8.24
Wash buffer	50 mM Tris-Cl, 150 mM NaCl, and 500 µM EDTA
ZYP-5052 Autoinduction media	1% (w/v) N-Z-amine, 0.5% (w/v) Yeast extract, 50 mM Na_2HPO_4, 50 mM KH_2PO_4, 25 mM $(NH_4)_2SO_4$, 2mM $MgSO_4$, 0.5% (v/v) Glycerol, 0.05% (w/v) Glucose, 0.2 % (w/v) Lactose

Table 19: *Antibodies & dyes Table B*

Antibodies		Clone	Dilution	Supplier
Primary				
	Mouse-talin1	8d4 monoclonal	1/500	Merck
	Rabbit-RIAM	EPR2806 monoclonal	1/50	Abcam
	Rabbit-GFP	ab290 polyclonal	1/1000	Abcam
	Mouse αTubulin	DM1A Monoclonal	1:500	Merck
Secondary				
	Goat-anti-Mouse-IRDye® 680RD		1/5,000	Li-Cor
	Goat-anti-Rabbit-IRDye® 800CW		1/10,000	Li-Cor
	Goat anti-mouse Atto647N		1:500	Merck
	Phalloidin-AlexaFluor® 647		1:40	Thermofisher
	DAPI		1:1000	Thermofisher

B

APPENDIX B

B.1 Python Code

The following script I wrote in Python to compile, sum and average individual lifetime histograms which were then used to determine the average fluorescence lifetime for each image. This script then graphs a number of parameters while producing a summary data spreadsheet for each process step. Lastly, this script calculates the transfer rates between fluorescent protein pairs in the three colour cascade model.

```
import timeit
import os
import pandas as pd
import seaborn as sns
import matplotlib.pyplot as plt
import scipy.stats as stats
import sys
from statannot import add_stat_annotation

### Set of functions written to return practical FRET-based
    calculations

class Calcs:
    def __init__(self, t_D, t_DA):
        self.t_D = t_D
        self.t_DA =  t_DA

    def fret_eff(self):
        return (1-(self.t_DA/self.t_D))

    def dist_D_DA(self, r0):
        return (((1-self.fret_eff())/self.fret_eff())**(1/6))*r0

    def et_rate(self):
        return ((1/(self.t_DA*1E-9))- (1/(self.t_D*1E-9)))

start = timeit.default_timer()
FP_order = ['GFP-vinc','GFP-vinc + mScar-RIAM', 'GFP-vinc + mScar
    -RIAM + Noc']
```

```
28
29 Donor = FP.order[0]
30 Acc = FP.order[1:]
31 stdout_fileno = sys.stdout
32 sys.stdout = open("Summary Statistics.txt", "w")
33
34 all_dfs = []
35 for folder_name in FP.order:
36     for filename in os.listdir(folder_name):
37         df = pd.read_csv(folder_name + "/" + filename, sep="\t",
       skiprows=1, names=['time', 'count'])
38         df['filename'] = filename
39         df['Fluorophore'] = folder_name
40         all_dfs.append(df[['Fluorophore', 'filename', 'time', '
       count']])
41
42 df = pd.concat(all_dfs, axis=0).fillna(0)
43 df['norm_cc'] = df.groupby('filename')['count'].transform(lambda
       x : x / x.max())
44 df['per_sample'] = df.groupby('Fluorophore')['count'].transform(
       lambda x : x / x.max())
45 summary = df.groupby(['Fluorophore', 'time'])['norm_cc'].sum().
       to_frame('sum').reset_index()
46 summary['norm_sum_per_fp'] = summary.groupby('Fluorophore')['sum'
       ].transform(lambda x : x / x.max())
47 peak_summary = df.groupby(['filename', 'Fluorophore']).apply(
       lambda x : x.sort_values('count', ascending=False)['time'].
       iloc[0]).to_frame('mean lifetime').reset_index()
48 tau = peak_summary.groupby('Fluorophore')['mean lifetime'].
       describe().sort_values('Fluorophore', ascending=True)
49 Ave_lifetime = pd.DataFrame(data=tau)
50 summary['FRET_E'] = summary.groupby('Fluorophore')['time'].
       transform(lambda x : (1-(x /(Ave_lifetime.loc[Donor, 'mean'])
       ))*100)
51 peak_summary['FRET_E'] = peak_summary.groupby('Fluorophore')['
       mean lifetime'].transform(lambda x : (1-(x /(Ave_lifetime.loc
       [Donor, 'mean'])))*100)
52 print('----------//General Notes//----------"n"n"n"n')
53 print('----------//Mean lifetime Summary Statistics//----------
       ')
54 print(Ave_lifetime.to_string())
55
56 #Grpahs
57 sns.axes_style("whitegrid", -'axes.grid' : False")
58 sns.set_context("notebook", font_scale=1.5)                #poster
       , paper, notebook, talk
```

```
59 #colors = 'Set1'                                    #Set1,
       Set2, white, binary, deep
60 colors = ['#1163ab', '#ba1146', 'blue']
61 width = 3
62
63 ax1 = sns.relplot(
64     data = summary,
65     x = 'FRET E',
66     y = 'norm sum per fp',
67     kind = 'line',
68     hue = 'Fluorophore',
69     style = 'Fluorophore',
70     linewidth = width,
71     hue order=(FP order),
72     palette= colors,
73     #legend=False,
74     )
75
76 ax1.set(xlabel = 'FRET Efficiency (%)', ylabel = 'Normalised
       summed average pixel frequency', title = 'Lineplot of FRET
       Efficiencies', xlim=(-50, 50))
77 #plt.tight layout()
78 plt.subplots adjust(left=0.06, bottom=0.076, right=0.97, top
       =0.95)
79 plt.legend(bbox to anchor=(1.05, 1), loc=2, borderaxespad=0.)
80
81 ax2 = sns.relplot(
82     data = summary,
83     x = 'time',
84     y = 'norm sum per fp',
85     kind = 'line',
86     hue = 'Fluorophore',
87     style = 'Fluorophore',
88     linewidth = width,
89     hue order=(FP order),
90     palette= colors,
91     aspect=1.8,
92     height = 8
93     )
94 ax2.set(xlabel = 'Time (ns)', ylabel = 'Normalised summed pixel
       frequency', title = 'Average Lineplot for each condition')
95 plt.tight layout()
96 plt.subplots adjust(left=0.06, bottom=0.076, right=0.97, top
       =0.95)
97
98
99 ax3 = sns.relplot(
```

```
100     data = df,
101     x = 'time',
102     y = 'norm_cc',
103     kind='line',
104     linewidth = width,
105     hue = 'Fluorophore',
106     style = 'Fluorophore',
107     palette= colors,
108     aspect=1.8,
109     height = 8
110 )
111 ax3.set(xlabel = 'Time (ns)', ylabel = 'Summed Average Pixel
        frequency', title = 'Lineplot for each cell')
112 plt.tight_layout()
113 plt.subplots_adjust(left=0.06, bottom=0.076, right=0.97, top
        =0.95)
114
115 ax4 = sns.relplot(
116     data = df,
117     x = 'time',
118     y = 'norm_cc',
119     kind='line',
120     aspect=3,
121     height = 8,
122     hue = 'filename',
123     row='Fluorophore',
124     legend=True,
125     ci=95
126 )
127 ax4.set(xlabel = 'Time (ns)', ylabel = '', xlim=(1.4, 2.8))
128 plt.text(0.3, 1.5, 'Normalised Pixel frequency', ha='center',
        rotation=90, size='medium', color='black')       #, weight='
        semibold'
129 plt.subplots_adjust(left=0.045, bottom=0.07, right=0.96, top
        =0.933, wspace=0.20, hspace=0.20)
130
131
132 #Average lifetime per condition
133 plt.figure()
134 ax5 = sns.catplot(
135     data = peak_summary,
136     x = 'Fluorophore',
137     y = 'mean lifetime',
138     kind='violin',
139     inner = 'point',
140     order=FP_order,
141     saturation =0.5,
```

```
142     palette= colors,
143     aspect=1.8,
144     height = 8
145 )
146 ax5 = sns.swarmplot(
147     data = peak_summary,
148     x = 'Fluorophore',
149     y = 'mean lifetime',
150     order=FP_order,
151     color= 'white',
152     edgecolor='gray'
153     )
154 ax5.set(xlabel = 'Fluorophore', ylabel = 'Mean Lifetime (ns)',
        title = 'Violin plot')
155 plt.tight_layout()
156 plt.subplots_adjust(left=0.06, bottom=0.076, right=0.97, top
        =0.95)
157
158
159 plt.figure()
160 ax6 = sns.catplot(
161     data = peak_summary,
162     x = 'Fluorophore',
163     y = 'FRET_E',
164     kind='violin',
165     order=FP_order,
166     saturation =0.5,
167     palette= colors,
168     edgecolor='gray',
169     aspect=1.8,
170     height = 8
171 )
172 ax6 = sns.swarmplot(
173     data = peak_summary,
174     x = 'Fluorophore',
175     y = 'FRET_E',
176     order=FP_order,
177     color= 'white',
178     edgecolor='gray'
179     )
180
181 ax6.set(xlabel = 'Fluorophore', ylabel = 'FRET Efficiency (%)',
        title = 'Violin plot of FRET Efficiency')
182 plt.tight_layout()
183 plt.subplots_adjust(left=0.06, bottom=0.076, right=0.97, top
        =0.95)
184
```

```
185 plt.figure()
186 ax8 = sns.boxplot(
187     data = peak_summary,
188     x = 'Fluorophore',
189     y = 'mean lifetime',
190     order=FP_order,
191     saturation =0.9,
192     palette= colors
193     )
194
195 add_stat_annotation(
196     ax8,
197     data=peak_summary,
198     x='Fluorophore',
199     y = 'mean lifetime',
200     order=FP_order,
201     box_pairs=[(Donor, Acc[0])], #, (Donor, Acc[1]), (Acc[0], Acc
        [1])],
202     test='t-test_ind',
203     text_format='star',
204     loc='inside')
205
206 ax8.set(xlabel = 'Fluorophore', ylabel = 'Mean Lifetime (ns)',
        title = 'Mean Lifetime Box plot')
207 plt.tight_layout()
208 plt.subplots_adjust(left=0.06, bottom=0.076, right=0.97, top
        =0.95)
209
210 plt.figure()
211 ax9 = sns.boxplot(
212     data = peak_summary,
213     x = 'Fluorophore',
214     y = 'FRET_E',
215     order=FP_order,
216     saturation =0.9,
217     palette=colors
218     )
219
220 add_stat_annotation(
221     ax9,
222     data=peak_summary,
223     x='Fluorophore',
224     y = 'FRET_E',
225     order=FP_order,
226     box_pairs=[(Donor, Acc[0])], #, (Donor, Acc[1]), (Acc[0], Acc
        [1])],, (Donor, Acc[1]), (Acc[0], Acc[1])],
227     test='t-test_ind',
```

```
228     text_format='star',
229     loc='inside')
230 
231 ax9 = sns.swarmplot(
232     data = peak_summary,
233     x = 'Fluorophore',     y = 'FRET_E',
234     order=FP_order,
235     color= 'white',
236     edgecolor='black',
237     size= 4,
238     linewidth = 1
239     )
240 
241 ax9.set(xlabel = 'Fluorophore', ylabel = 'FRET Efficiency (%)',
        title = 'FRET Efficiency Box plot')
242 plt.tight_layout()
243 plt.subplots_adjust(top=0.938,
244 bottom=0.109,
245 left=0.085,
246 right=0.98,
247 hspace=0.2,
248 wspace=0.2)
249 
250 df.to_csv(r'df.csv')
251 peak_summary.to_csv(r'peak_summary.csv')
252 Ave_lifetime.to_csv(r'Ave_lifetime.csv')
253 summary.to_csv(r'summary.csv')
254 
255 #----Speedrun---
256 x = True        #True / False
257 if x == True:
258     peak_summary.to_csv(r'peak_summary.csv')
259     plt.savefig('lineplot-average[FRET_E].svg',  dpi=600)
260     plt.savefig('lineplot-average[Time].svg',  dpi=600)
261     plt.savefig('lineplot-ind.svg',  dpi=600)
262     plt.savefig('lineplot-average_ci.svg', dpi=600)
263     plt.savefig('violin.svg', dpi=600)
264     plt.savefig('violin[FRET_E].svg', dpi=600)
265     plt.savefig('Mean Lifetime box.svg', dpi=600)
266     plt.savefig('FRET Efficiency box.svg', dpi=600)
267 plt.show(block=False)
268 
269 #Stats on the peak lifetime measurement from each histogram
270 print("\n----------//Statistics//----------")
271 print("H0: There is no statistically significant difference
    between the Donor and Acceptor populations")
```

```
272 print("H1: There is a statistically significant difference
        between the Donor and Acceptor populations")
273
274 D=summary[summary['Fluorophore'] == Donor].loc[:, '
        norm_sum_per_fp']
275 ci = 0.05
276 D_stat, D_p = stats.shapiro(D)
277
278 #Wilk-Shapiro test for normality
279 print('"n ---------- #Wilk-Shapiro test for Normality
        ----------')
280 print("WS-Stat for ", Donor, "is =", round(D_stat, 5), " and the
        P-value for the", Donor, " is =", D_p)
281 if D_p ¡= ci:
282     print("The", Donor, "data is not normally distributed")
283 else:
284     print("The", Donor, "data is normally distributed")
285 for i in Acc:
286     A = summary[summary['Fluorophore'] == i].loc[:, '
        norm_sum_per_fp']
287     A_stat, A_p = stats.shapiro(A)
288     print("WS-Stat for ", i, "is =", round(A_stat, 5), " and the
        P-value for the", i, "is =", A_p)
289     if A_p ¡= ci:
290         print("The", i, "data is not normally distributed")
291     else:
292         print("The", i, "data is normally distributed")
293
294 #Kolmogrov-Smirnov 2 sample test
295 print('"n"n---------- #Kolmogrov-Smirnov 2 sample test
        ----------')
296 for i in Acc:
297     A = summary[summary['Fluorophore'] == i].loc[:, '
        norm_sum_per_fp']
298     KS_stat, KS_p = stats.ks_2samp(D, A)
299     if KS_p ¡ ci:
300         result = "reject"
301     else:
302         result = "accept"
303
304     print("KS-Stat for", Donor, "and", i, "=", round(KS_stat,4),
        ",the P-value for", Donor, "and", i, "=", KS_p,
305           "'nWe", result.upper(), "the null Hypothesis at the",
        ci, "confidence interval'n")
306
307 #Wilcoxson Rank Sum Test
308 print('"n"n---------- #Wilcoxson Rank Sum Test ----------')
```

```
for i in Acc:
    A = summary[summary['Fluorophore'] == i].loc[:, 'norm_sum_per_fp']
    WRS_stat, WRS_p = stats.ranksums(D, A)
    if WRS_p ¡ ci:
        result = "reject"
    else:
        result = "accept"

    print("The Wilcoxson Ranked Sum statistic for", Donor, "and", i, "is =", round(WRS_stat,4),
          "“nThe P-value for for", Donor, "and", i, "is =", WRS_p,
          "“nWe", result.upper(), "the null Hypothesis at the", ci, "conferdence interval“n")

#FRET Efficiency
print('“n“n---------- #FRET Efficiency ----------')
tau=[]
eff =[]
tau_D = (Ave_lifetime.loc[Donor, 'mean'])*1E-9
tau.append(tau_D)
E_D = round(1-(tau_D/tau_D),4)
eff.append(E_D)
for i in Acc:
    tau_A =(Ave_lifetime.loc[i, 'mean'])*1E-9
    j = Calcs(tau_D, tau_A)
    tau.append(tau_A)
    eff.append(100*j.fret_eff())
    print("FRET Efficiency for", Donor, "&", i, "is", round(100*j.fret_eff(),4), "%")

E_data ={'Fluorophore': FP_order, 'Mean Lifetime (s)':tau, 'FRET E (%)': eff"
post_summary = pd.DataFrame(E_data).set_index('Fluorophore')
print(post_summary)


#FRET Distance Calculations
print('“n“n---------- #FRET Distance Calculations ----------')
r0_AB = 5.85*1E-9                          #mTurq2-mVenus
r0_AC = 5.08*1E-9                          #mTurq2-mScarlet
r0_BC = 5.45*1E-9                          #mVenus-mScarlet
r0_gfpmScar = 5.689*1E-9                   #GFP-mScarlet
r0_tok = 5.466*1E-9                        #mTFP1-mOK2
r0_tmv = 5.987*1E-9                        #mTFP1-mVenus
r0_grf = 5.236*1E-9                        #GFP-mRFP
```

```
350
351
352 for i in Acc:
353     tau_A =(Ave_lifetime.loc[i, 'mean'])*1E-9
354     j = Calcs(tau_D, tau_A)
355     print("The average distance between", Donor, "and", i, "is",
        round((j.dist_D_DA(r0_gfpmScar)*1E9), 3),"nm")
356
357 sys.stdout.close()
358 sys.stdout = stdout_fileno
359 print('Finished')
360 stop = timeit.default_timer()
361 print('Time:', stop-start)
```

Listing 1: *PyFLIM code for the compilation of individual histograms*

[1] Jonathan D. Humphrey, Eric R. Dufresne, and Martin A. Schwartz. Mechanotransduction and extracellular matrix homeostasis. *Nature Reviews Molecular Cell Biology*, 15:802–812, 2014.

[2] Mazvita Maziveyi and Suresh K. Alahari. Cell matrix adhesions in cancer: The proteins that form the glue. *Oncotarget*, 8:48471–48487, 2017.

[3] Takatsugu Okegawa, Rey Chen Pong, Yingming Li, and Jer Tsong Hsieh. The role of cell adhesion molecule in cancer progression and its application in cancer therapy. *Acta Biochimica Polonica*, 51:445–457, 2004.

[4] Mariliis Klaas, Triin Kangur, Janeli Viil, Kristina Mäemets-Allas, Ave Minajeva, Krista Vadi, Mikk Antsov, Natalia Lapidus, Martin Järvekülg, and Viljar Jaks. The alterations in the extracellular matrix composition guide the repair of damaged liver tissue. *Scientific Reports*, 6(1), June 2016.

[5] Pia Ringer, Georgina Colo, Reinhard Fässler, and Carsten Grashoff. Sensing the mechano-chemical properties of the extracellular matrix. *Matrix Biology*, 64:6–16, 2017.

[6] Armando Del Rio, Raul Perez-Jimenez, Ruchuan Liu, Pere Roca-Cusachs, Julio M. Fernandez, and Michael P. Sheetz. Stretching single talin rod molecules activates vinculin binding. *Science*, 323:638–641, 2009.

[7] Jonathan D. Humphries, Pengbo Wang, Charles Streuli, Benny Geiger, Martin J. Humphries, and Christoph Ballestrem. Vinculin controls focal adhesion formation by direct interactions with talin and actin. *Journal of Cell Biology*, 2007.

[8] Boris Martinac. The ion channels to cytoskeleton connection as potential mechanism of mechanosensitivity. *Biochimica et Biophysica Acta (BBA) - Biomembranes*, 1838(2):682–691, February 2014.

[9] Markus Moser, Kyle R. Legate, Roy Zent, and Reinhard Fässler. The tail of integrins, talin, and kindlins. *Science*, 324:895–899, 2009.

[10] José Luis Alonso and Wolfgang H Goldmann. Cellular mechanotransduction. *transport*, 1, 2016.

[11] Peter M. Thompson, Caitlin E. Tolbert, and Sharon L. Campbell. Vinculin and metavinculin: Oligomerization and interactions with f-actin. *FEBS Letters*, 587:1220–1229, 2013.

[12] Paul Atherton, Ben Stutchbury, Devina Jethwa, and Christoph Ballestrem. Mechanosensitive components of integrin adhesions: Role of vinculin. *Experimental Cell Research*, 343:21–27, 2016.

[13] Matteo Parri and Paola Chiarugi. Rac and rho gtpases in cancer cell motility control. *Cell communication and signalling: CCS*, 8:23, September 2010.

[14] Anne J Ridley. Special issue: Membrane dynamics rho gtpases and actin dynamics in membrane protrusions and vesicle trafficking rac and rho gtpases in cancer cell motility control. *Trends Cell Biol.*, 10:522–9, October 2006.

[15] Ho Sup Lee, Chinten James Lim, Wilma Puzon-McLaughlin, Sanford J. Shattil, and Mark H. Ginsberg. Riam activates integrins by linking talin to ras gtpase membrane-targeting sequences. *Journal of Biological Chemistry*, 284:5119–5122, 2009.

[16] Elisabetta Ada Cavalcanti-Adam, Tova Volberg, Alexandre Micoulet, Horst Kessler, Benjamin Geiger, and Joachim Pius Spatz. Cell spreading and focal adhesion dynamics are regulated by spacing of integrin ligands. *Biophysical journal*, 92:2964–2974, April 2007.

[17] Herbert B. Schiller, Caroline C. Friedel, Cyril Boulegue, and Reinhard Fäsignssler. Quantitative proteomics of the integrin adhesome show a myosin ii-dependent recruitment of lim domain proteins. *EMBO Reports*, 12:259–266, 2011.

[18] Herbert B Schiller and Reinhard Fässler. Mechanosensitivity and compositional dynamics of cell-matrix adhesions. *EMBO reports*, 14:509–519, June 2013.

[19] Rishita Changede and Michael Sheetz. Integrin and cadherin clusters: A robust way to organize adhesions for cell mechanics. *BioEssays*, 39:1–12, 2017.

[20] Sabina E. Winograd-Katz, Reinhard Fässler, Benjamin Geiger, and Kyle R. Legate. The integrin adhesome: From genes and proteins to human disease. *Nature Reviews Molecular Cell Biology*, 15:273–288, 2014.

[21] R. Zaidel-Bar, M. Cohen, L. Addadi, and B. Geiger. Hierarchical assembly of cell–matrix adhesion complexes. *Biochemical Society Transactions*, 32(3):416–420, June 2004.

[22] D. R. Critchley. Cytoskeletal proteins talin and vinculin in integrin-mediated adhesion. *Biochemical Society Transactions*, 32:831–836, 2004.

[23] Ingo Thievessen, Peter M. Thompson, Sylvain Berlemont, Karen M. Plevock, Sergey V. Plotnikov, Alice Zemljic-Harpf, Robert S. Ross, Michael W. Davidson, Gaudenz Danuser, Sharon L. Campbell, and Clare M. Waterman. Vinculin-actin interaction couples actin retrograde flow to focal adhesions, but is dispensable for focal adhesion growth. *Journal of Cell Biology*, 202:163–177, 2013.

[24] Gerold Diez, Vera Auernheimer, Ben Fabry, and Wolfgang H Goldmann. Head/tail interaction of vinculin influences cell mechanical behavior. *Biochemical and biophysical research communications*, 406:85–88, 2011.

[25] Edward R. Horton, Adam Byron, Janet A. Askari, Daniel H.J. Ng, Angélique Millon-Frémillon, Joseph Robertson, Ewa J. Koper, Nikki R. Paul, Stacey Warwood, David Knight, Jonathan D. Humphries, and Martin J. Humphries. Definition of a consensus integrin adhesome and its dynamics during adhesion complex assembly and disassembly. *Nature Cell Biology*, 17:1577–1587, 2015.

[26] Haguy Wolfenson, Alexander Bershadsky, Yoav I. Henis, and Benjamin Geiger. Actomyosin-generated tension controls the molecular kinetics of focal adhesions. *Journal of Cell Science*, 124:1425–1432, 2011.

[27] Grégory Giannone. Super-resolution links vinculin localization to function in focal adhesions. *Nature cell biology*, 17:845–847, July 2015.

[28] Michiel Fokkelman, Hayri E. BalcloGlu, Janna E. Klip, Kuan Yan, Fons J. Verbeek, Erik H.J. Danen, and Bob Van De Water. Cellular adhesome screen identifies critical modulators of focal adhesion dynamics, cellular traction forces and cell migration behaviour. *Scientific Reports*, 6:1–14, 2016.

[29] B Geiger. A 130k protein from chicken gizzard: its localization at the termini of microfilament bundles in cultured chicken cells. *Cell*, 18:193–205, September 1979.

[30] B M Jockusch and M Rüdiger. Crosstalk between cell adhesion molecules: vinculin as a paradigm for regulation by conformation. *Trends in cell biology*, 6:311–315, August 1996.

[31] Ruth M. Saunders, Mark R. Holt, Lisa Jennings, Deborah H. Sutton, Igor L. Barsukov, Andrey Bobkov, Robert C. Liddington, Eileen A. Adamson, Graham A. Dunn, and David R. Critchley. Role of vinculin in regulating focal adhesion turnover. *European Journal of Cell Biology*, 85(6):487–500, June 2006.

[32] Constantina Bakolitsa, Daniel M. Cohen, Laurie A. Bankston, Audrey A. Bobkov, Gregory W. Dadwell, Lisa Jennings, David R. Crithcley, Susan W. Craig, and Robert C. Liddington. Structural basis for vinculin activation at sites of cell adhesion. *Nature*, 430:583–586, 2004.

[33] Annette R. Menkel, Martina Kroemker, Peter Bubeck, Melanie Ronsiek, Gerd Nikolai, and Brigitte M. Jockusch. Characterization of an f-actin-binding domain in the cytoskeletal protein vinculin. *Journal of Cell Biology*, 126:1231–1240, 1994.

[34] Robert P. Johnson and Susan W. Craig. An intramolecular association between the head and tail domains of vinculin modulates talin binding. *Journal of Biological Chemistry*, 269:12611–12619, 1994.

[35] Clémence Vigouroux, Véronique Henriot, and Christophe Le Clainche. Talin dissociates from riam and associates to vinculin sequentially in response to the actomyosin force. *Nature Communications*, 11:3116, 2020.

[36] Dumbauld David W., Lee Ted T., Singh Ankur, Scrimgeour Jan, Gersbach Charles A., Zamir Evan A., Fu Jianping, Chen Christopher S., Curtis Jennifer E., Craig Susan W., and García Andrés J. How vinculin regu-

lates force transmission. *Proceedings of the National Academy of Sciences*, 110:9788–9793, June 2013. doi: 10.1073/pnas.1216209110.

[37] Benjamin T. Goult, Thomas Zacharchenko, Neil Bate, Ricky Tsang, Fiona Hey, Alexandre R. Gingras, Paul R. Elliott, Gordon C.K. Roberts, Christoph Ballestrem, David R. Critchley, and Igor L. Barsukov. Riam and vinculin binding to talin are mutually exclusive and regulate adhesion assembly and turnover. *Journal of Biological Chemistry*, 288:8238–8249, 2013.

[38] Hiroaki Hirata, Hitoshi Tatsumi, Chwee Teck Lim, and Masahiro Sokabe. Force-dependent vinculin binding to talin in live cells: a crucial step in anchoring the actin cytoskeleton to focal adhesions. *American Journal of Physiology-Cell Physiology*, 306:C607–c620, January 2014. doi: 10.1152/ajpcell.00122.2013.

[39] Alex Carisey, Ricky Tsang, Alexandra M. Greiner, Nadja Nijenhuis, Nikki Heath, Alicja Nazgiewicz, Ralf Kemkemer, Brian Derby, Joachim Spatz, and Christoph Ballestrem. Vinculin regulates the recruitment and release of core focal adhesion proteins in a force-dependent manner. *Current Biology*, 23:271–281, 2013.

[40] Rolle Rahikainen, Magdaléna Von Essen, Markus Schaefer, Lei Qi, Latifeh Azizi, Conor Kelly, Teemu O. Ihalainen, Bernhard Wehrle-Haller, Martin Bastmeyer, Cai Huang, and Vesa P. Hytönen. Mechanical stability of talin rod controls cell migration and substrate sensing. *Scientific Reports*, 7:1–15, 2017.

[41] Tina Izard and Clemens Vonrhein. Structural basis for amplifying vinculin activation by talin. *Journal of Biological Chemistry*, 279:27667–27678, 2004.

[42] Olivier Pertz, Louis Hodgson, Richard L. Klemke, and Klaus M. Hahn. Spatiotemporal dynamics of rhoa activity in migrating cells. *Nature*, 440:1069–1072, 2006.

[43] K. Burridge and L. Connell. A new protein of adhesion plaques and ruffling membranes. *The Journal of cell biology*, 97:359–367, 1983.

[44] Paul R Elliott, Benjamin T Goult, Petra M Kopp, Neil Bate, J Günter Grossmann, Gordon C K Roberts, David R Critchley, and Igor L Barsukov. The structure of the talin head reveals a novel extended conformation

of the ferm domain. *Structure (London, England : 1993)*, 18:1289–1299, October 2010.

[45] Benjamin T Goult, Mohamed Bouaouina, Paul R Elliott, Neil Bate, Bipin Patel, Alexandre R Gingras, J Günter Grossmann, Gordon C K Roberts, David A Calderwood, David R Critchley, and Igor L Barsukov. Structure of a double ubiquitin-like domain in the talin head: a role in integrin activation. *The EMBO Journal*, 29:1069–1080, March 2010. https://doi.org/10.1038/emboj.2010.4.

[46] Mohamed Bouaouina, Yatish Lad, and David A Calderwood. The n-terminal domains of talin cooperate with the phosphotyrosine binding-like domain to activate beta1 and beta3 integrins. *The Journal of biological chemistry*, 283:6118–6125, March 2008.

[47] A. Wayne Orr, Brian P. Helmke, Brett R. Blackman, and Martin A. Schwartz. Mechanisms of mechanotransduction. *Developmental Cell*, 10:11–20, 2006.

[48] Marco Mainardi, Sajikumar Sreedharan, Nicoletta Berardi, and Benjamin T Goult. The mechanical basis of memory – the meshcode theory. *Hypothesis And Theory*, page 25, 2021.

[49] Alexandre R Gingras, Wolfgang H Ziegler, Ronald Frank, Igor L Barsukov, Gordon C K Roberts, David R Critchley, and Jonas Emsley. Mapping and consensus sequence identification for multiple vinculin binding sites within the talin rod. *The Journal of biological chemistry*, 280:37217–37224, November 2005.

[50] Abhishek Kumar, Mingxing Ouyang, Koen Van den Dries, Ewan James McGhee, Keiichiro Tanaka, Marie D. Anderson, Alexander Groisman, Benjamin T. Goult, Kurt I. Anderson, and Martin A. Schwartz. Talin tension sensor reveals novel features of focal adhesion force transmission and mechanosensitivity. *Journal of Cell Biology*, 213:371–383, 2016.

[51] David A. Calderwood, Iain D. Campbell, and David R. Critchley. Talins and kindlins: Partners in integrin-mediated adhesion. *Nature Reviews Molecular Cell Biology*, 14:503–517, 2013.

[52] Evangelos Papagrigoriou, Alexandre R. Gingras, Igor L. Barsukov, Neil Bate, Ian J. Fillingham, Bipin Patel, Ronald Frank, Wolfgang H. Ziegler, Gordon C.K. Roberts, David R. Critchley, and Jonas Emsley. Activation

of a vinculin-binding site in the talin rod involves rearrangement of a five-helix bundle. *EMBO Journal*, 23:2942–2951, 2004.

[53] Alexander W. M. Haining, Tyler J. Lieberthal, and Armando del Río Hernández. Talin: a mechanosensitive molecule in health and disease. *The FASEB Journal*, 30(6):2073–2085, February 2016.

[54] Esther M Lafuente, Andrfile:///C:/Users/conor/Downloads/S0021925818396315.risé A F L van Puijenbroek, Matthias Krause, Christopher V Carman, Gordon J Freeman, Alla Berezovskaya, Erica Constantine, Timothy A Springer, Frank B Gertler, and Vassiliki A Boussiotis. Riam, an ena/vasp and profilin ligand, interacts with rap1-gtp and mediates rap1-induced adhesion. *Developmental Cell*, 7:585–595, October 2004. doi: 10.1016/j.devcel.2004.07.021.

[55] Kira S Ermekova, Nicola Zambrano, Hillary Linn, Giuseppina Minopoli, Frank Gertler, Tommaso Russo, and Marius Sudol. The ww domain of neural protein fe65 interacts with proline-rich motifs in mena, the mammalian homolog of drosophilaenabled*. *Journal of Biological Chemistry*, 272:32869–32877, 1997.

[56] Andrea Jenzora, Barbara Behrendt, J Victor Small, Jürgen Wehland, and Theresia E B Stradal. Prel1 provides a link from ras signalling to the actin cytoskeleton via ena/vasp proteins. *FEBS letters*, 579:455–463, January 2005.

[57] H Kitayama, Y Sugimoto, T Matsuzaki, Y Ikawa, and M Noda. A ras-related gene with transformation suppressor activity. *Cell*, 56:77–84, January 1989.

[58] Johannes L Bos, Johan de Rooij, and Kris A Reedquist. Rap1 signalling: adhering to new models. *Nature Reviews Molecular Cell Biology*, 2:369–377, 2001.

[59] Nils Cordes. Overexpression of hyperactive integrin-linked kinase leads to increased cellular radiosensitivity. *Cancer Research*, 64:5683–5692, August 2004.

[60] Nikolaos Patsoukis, Kankana Bardhan, Jessica D. Weaver, Duygu Sari, Alvaro Torres-Gomez, Lequn Li, Laura Strauss, Esther M. Lafuente, and Vassiliki A. Boussiotis. The adaptor molecule riam integrates signalling events critical for integrin-mediated control of immune function and cancer progression. *Science Signaling*, 10, 2017.

[61] Frederic Lagarrigue, Chungho Kim, and Mark H. Ginsberg. The rap1-riam-talin axis of integrin activation and blood cell function. *Blood*, 128:479–487, July 2016.

[62] Benjamin T. Goult, Neil Bate, Nicholas J. Anthis, Kate L. Wegener, Alexander R. Gingras, Bipin Patel, Igor L. Barsukov, Iain D. Campbell, Gordon C.K. Roberts, and David R. Critchley. The structure of an interdomain complex that regulates talin activity. *Journal of Biological Chemistry*, 284:15097–15106, 2009.

[63] Joseph P Wynne, Jinhua Wu, Wenjuan Su, Adam Mor, Nikolaos Patsoukis, Vassiliki A Boussiotis, Stevan R Hubbard, and Mark R Philips. Rap1-interacting adapter molecule (riam) associates with the plasma membrane via a proximity detector. *The Journal of cell biology*, 199:317–330, October 2012.

[64] Jun Yang, Liang Zhu, Hao Zhang, Jamila Hirbawi, Koichi Fukuda, Pallavi Dwivedi, Jianmin Liu, Tatiana Byzova, Edward F Plow, Jinhua Wu, and Jun Qin. Conformational activation of talin by riam triggers integrin-mediated cell adhesion. *Nature Communications*, 5:5880, 2014.

[65] Hao Zhang, Yu-Chung Chang, Mark L Brennan, and Jinhua Wu. The structure of rap1 in complex with riam reveals specificity determinants and recruitment mechanism. *Journal of molecular cell biology*, 6:128–139, April 2014.

[66] Yu-Chung Chang, Hao Zhang, Janusz Franco-Barraza, Mark L Brennan, Tejash Patel, Edna Cukierman, and Jinhua Wu. Structural and mechanistic insights into the recruitment of talin by riam in integrin signalling. *Structure (London, England : 1993)*, 22:1810–1820, December 2014.

[67] Bo Yang, Zi Zhao Lieu, Haguy Wolfenson, Feroz M. Hameed, Alexander D. Bershadsky, and Michael P. Sheetz. Mechanosensing controlled directly by tyrosine kinases. *Nano Letters*, 16:5951–5961, 2016.

[68] Paul Atherton, Ben Stutchbury, De Yao Wang, Devina Jethwa, Ricky Tsang, Eugenia Meiler-Rodriguez, Pengbo Wang, Neil Bate, Roy Zent, Igor L. Barsukov, Benjamin T. Goult, David R. Critchley, and Christoph Ballestrem. Vinculin controls talin engagement with the actomyosin machinery. *Nature Communications*, 6:1–12, 2015.

[69] Baihao Su and Jinhua Wu. Phosphorylation of riam activates its adaptor function in mediating integrin signaling. *Journal of cellular signalling*, 2:103–110, 2021.

[70] Frédéric Lagarrigue and Alexandre R. Gingras. Src-mediated phosphorylation of riam promotes integrin activation. *Structure*, 29:305–307, 2021.

[71] Duygu Sari-Ak, Alvaro Torres-Gomez, Yavuz-Furkan Yazicioglu, Anthos Christofides, Nikolaos Patsoukis, Esther M Lafuente, and Vassiliki A Boussiotis. Structural, biochemical, and functional properties of the rap1-interacting adaptor molecule (riam). *Biomedical journal*, 45:289–298, April 2022.

[72] Eun-Ah Cho, Pingfeng Zhang, Vikas Kumar, Mikhail Kavalchuk, Hao Zhang, Qingqiu Huang, James S Duncan, and Jinhua Wu. Phosphorylation of riam by src promotes integrin activation by unmasking the ph domain of riam. *Structure (London, England : 1993)*, 29:320–329.e4, April 2021.

[73] Jeffrey D Bjorge, Andrew Jakymiw, and Donald J Fujita. Selected glimpses into the activation and function of src kinase. *Oncogene*, 19(49):5620–5635, November 2000.

[74] Rosalyn B Irby and Timothy J Yeatman. Role of src expression and activation in human cancer. *Oncogene*, 19(49):5636–5642, November 2000.

[75] Nicholas J. Anthis, Kate L. Wegener, David R. Critchley, and Iain D. Campbell. Structural diversity in integrin/talin interactions. *Structure*, 18:1654–1666, 2010.

[76] James E Bear and Frank B Gertler. Ena/vasp: towards resolving a pointed controversy at the barbed end. *Journal of cell science*, 122:1947–1953, June 2009.

[77] J. A. Cooper. Effects of cytochalasin and phalloidin on actin. *The Journal of cell biology*, 105:1473–1478, 1987.

[78] P Forscher and S J Smith. Actions of cytochalasins on the organization of actin filaments and microtubules in a neuronal growth cone. *The Journal of cell biology*, 107:1505–1516, October 1988.

[79] I Spector, N R Shochet, Y Kashman, and A Groweiss. Latrunculins: novel marine toxins that disrupt microfilament organization in cultured cells. *Science (New York, N.Y.)*, 219:493–495, February 1983.

[80] Elena G. Yarmola, Thayumanasamy Somasundaram, Todd A. Boring, Ilan Spector, and Michael R. Bubb. Actin-latrunculin a structure and function. *Journal of Biological Chemistry*, 275(36):28120–28127, September 2000.

[81] Kirsi Riento and Anne J Ridley. Rocks: multifunctional kinases in cell behaviour. *Nature Reviews Molecular Cell Biology*, 4:446–456, 2003.

[82] M. Hawkins, B. Pope, S. K. Maciver, and A. G. Weeds. Human actin depolymerizing factor mediates a pH-sensitive destruction of actin filaments. *Biochemistry*, 32(38):9985–9993, September 1993.

[83] S M Hayden, P S Miller, A Brauweiler, and J R Bamburg. Analysis of the interactions of actin depolymerizing factor with g-and f-actin'. *Biochemistry*, $32:9994--10004, 1993$.

[84] Erick O Fuentes, Jost Leemhuis, G Bjōrn Stark, and Eva M Lang. Rho kinase inhibitors y27632 and h1152 augment neurite extension in the presence of cultured schwann cells. *Journal of brachial plexus and peripheral nerve injury*, 3:19, September 2008.

[85] Mami Ikenoya, Hiroyoshi Hidaka, Takamitsu Hosoya, Masaaki Suzuki, Naoki Yamamoto, and Yasuharu Sasaki. Inhibition of rho-kinase-induced myristoylated alanine-rich c kinase substrate (marcks) phosphorylation in human neuronal cells by h-1152, a novel and specific rho-kinase inhibitor. *J. Neurochem*, 81:9–16, 2002.

[86] E Lazarides and K Burridge. Alpha-actinin: immunofluorescent localization of a muscle structural protein in nonmuscle cells. *Cell*, 6:289–298, November 1975.

[87] J.J. Campbell and M.M. Knight. An improved confocal FRAP technique for the measurement of long-term actin dynamics in individual stress fibers. *Microscopy Research and Technique*, 70(12):1034–1040, 2007.

[88] M Chrzanowska-Wodnicka and K Burridge. Rho-stimulated contractility drives the formation of stress fibers and focal adhesions. *Journal of Cell Biology*, 133(6):1403–1415, June 1996.

[89] Kazuo Katoh, Yumiko Kano, Mutsuki Amano, Kozo Kaibuchi, and Keigi Fujiwara. Stress fiber organization regulated by mlck and rho-kinase in cultured human fibroblasts. *American Journal of Physiology - Cell Physiology*, 280:1669–1679, 2001.

[90] J.E. Estes. The polymerization of actin. *International Cell Biology 1980–1981*, pages 336–345, 1981.

[91] L M Coluccio and L G Tilney. Phalloidin enhances actin assembly by preventing monomer dissociation. *The Journal of cell biology*, 99:529–535, August 1984.

[92] Phillip Crews, Lawrence V. Manes, and Mark Boehler. Jasplakinolide, a cyclodepsipeptide from the marine sponge, jaspis sp. *Tetrahedron Letters*, 27:2797–2800, January 1986.

[93] Michael R. Bubb, Adrian M.J. Senderowicz, Edward A. Sausville, Kimberly L.K. Duncan, and Edward D. Korn. Jasplakinolide, a cytotoxic natural product, induces actin polymerization and competitively inhibits the binding of phalloidin to f-actin. *Journal of Biological Chemistry*, 269:14869–14871, 1994.

[94] Balázs Visegrády, Dénes Lőrinczy, Gábor Hild, Béla Somogyi, and Miklós Nyitrai. The effect of phalloidin and jasplakinolide on the flexibility and thermal stability of actin filaments. *FEBS Letters*, 565(1-3):163–166, April 2004.

[95] Michael R. Bubb, Ilan Spector, Bret B. Beyer, and Katina M. Fosen. Effects of jasplakinolide on the kinetics of actin polymerization. an explanation for certain in vivo observations. *Journal of Biological Chemistry*, 275:5163–5170, 2000.

[96] Robert J Vasquez, Bonnie Howell, Anne-Marie C Yvon, Patricia Wadsworth, and Lynne Cassimeris. Nanornolar concentrations of nocodazole alter microtubule dynamic instability in vivo and in vitro. *Molecular Biology of the Cell*, 8:973–985, 1997.

[97] Hye Joung Choi, Masayuki Fukui, and Bao Ting Zhu. Role of cyclin b1/cdc2 up-regulation in the development of mitotic prometaphase arrest in human breast cancer cells treated with nocodazole. *PLoS ONE*, 6, 2011.

[98] Mikhail V. Blagosklonny. The power of chemotherapeutic engineering: Arresting cell cycle and suppressing senescence to protect from mitotic inhibitors. *Cell Cycle*, 10:2295–2298, 2011.

[99] Beth A. Weaver. How taxol/paclitaxel kills cancer cells. *Molecular Biology of the Cell*, 25(18):2677–2681, September 2014.

[100] P B Schiff, J Fant, and S B Horwitz. Promotion of microtubule assembly in vitro by taxol. *Nature*, 277:665–667, February 1979.

[101] N Kumar. Taxol-induced polymerization of purified tubulin. mechanism of action. *The Journal of biological chemistry*, 256:10435–10441, October 1981.

[102] Robert M Clegg. The history of fret : From conception through the labors of birth. *Reviews in Fluorescence*, 3:1–45, 2006.

[103] George Gabriel Stokes. Xxx. on the change of refrangibility of light. *Philosophical Transactions of the Royal Society of London*, 142:463–562, January 1852. doi: 10.1098/rstl.1852.0022.

[104] Joseph R. Lakowicz. Energy transfer. In *Principles of Fluorescence Spectroscopy*, pages 443–475. Springer US, 2006.

[105] Georgi Valchanov, Anela Ivanova, Alia Tadjer, Dennis Chercka, and Martin Baumgarten. Understanding the fluorescence of tadf light-emitting dyes. *The Journal of Physical Chemistry A*, 120:6944–6955, September 2016. doi: 10.1021/acs.jpca.6b06680.

[106] W Pauli. Über den zusammenhang des abschlusses der elektronengruppen im atom mit der komplexstruktur der spektren. *Zeitschrift für Physik*, 31:765–783, 1925.

[107] W Becker. Fluorescence lifetime imaging – techniques and applications. *Journal of Microscopy*, 247:119–136, August 2012. https://doi.org/10.1111/j.1365-2818.2012.03618.x.

[108] Badri Maliwal, Sangram Raut, Rafal Fudala, Sabato D'Auria, Vincenzo Marzullo, Alberto Luini, Ignacy Gryczynski, and Zygmunt Gryczynski. Extending fōrster resonance energy transfer measurements beyond 100 using common organic fluorophores: enhanced transfer in the presence of multiple acceptors. *Journal of biomedical optics*, 17:11006, January 2012.

[109] Th. Fōrster. Zwischenmolekulare energiewanderung und fluoreszenz. *Annalen der Physik*, 437:55–75, January 1948.

[110] W Russ Algar, Niko Hildebrandt, Steven S Vogel, and Igor L Medintz. Fret as a biomolecular research tool – understanding its potential while avoiding pitfalls. *Nature Methods*, 16:815–829, 2019.

[111] B. Wieb Vandermeer. Kappaphobia is the elephant in the fret room. *Methods and Applications in Fluorescence*, 8, 2020.

[112] Wlodek M Bujalowski and Maria J Jezewska. *Spectroscopic Methods of Analysis*, volume 875. Humana Press, 2012.

[113] Daniel Axelrod. Fluorescence excitation and imaging of single molecules near dielectric-coated and bare surfaces: A theoretical study. *Journal of Microscopy*, 247:147–160, 2012.

[114] B.W. van der Meer. Kappa-squared: from nuisance to new sense. *Reviews in Molecular Biotechnology*, 82(3):181–196, January 2002.

[115] Suman Ranjit, Kaushik Gurunathan, and Marcia Levitus. Photophysics of backbone fluorescent dna modifications: Reducing uncertainties in fret. *Journal of Physical Chemistry B*, 113:7861–7866, 2009.

[116] M S Wranne, A F Füchtbauer, B Dumat, M Bood, A H El-Sagheer, T Brown, H Gradén, M Grøtli, and L M Wilhelmsson. Toward complete sequence flexibility of nucleic acid base analogue fret. *Journal of the American Chemical Society*, 139:9271–9280, 2017.

[117] Eitan Lerner, Anders Barth, Jelle Hendrix, Benjamin Ambrose, Victoria Birkedal, Scott C Blanchard, Richard Bōrner, Hoi Sung Chung, Thorben Cordes, Timothy D Craggs, Ashok A Deniz, Jiajie Diao, Jingyi Fei, Ruben L Gonzalez, Irina V Gopich, Taekjip Ha, Christian A Hanke, Gilad Haran, Nikos S Hatzakis, Sungchul Hohng, Seok-Cheol Hong, Thorsten Hugel, Antonino Ingargiola, Chirlmin Joo, Achillefs N Kapanidis, Harold D Kim, Ted Laurence, Nam Ki Lee, Tae-Hee Lee, Edward A Lemke, Emmanuel Margeat, Jens Michaelis, Xavier Michalet, Sua Myong, Daniel Nettels, Thomas-Otavio Peulen, Evelyn Ploetz, Yair Razvag, Nicole C Robb, Benjamin Schuler, Hamid Soleimaninejad, Chun Tang, Reza Vafabakhsh, Don C Lamb, Claus A M Seidel, and Shimon Weiss. Fret-based dynamic structural biology: Challenges, perspectives and an appeal for open-science practices. *eLife*, 10:e60416, 2021.

[118] Eitan Lerner, Thorben Cordes, Antonino Ingargiola, Yazan Alhadid, Sang Yoon Chung, Xavier Michalet, and Shimon Weiss. Toward dynamic structural biology: Two decades of single-molecule fōrster resonance energy transfer. *Science*, 359, 2018.

[119] Timothy D. Craggs, Marko Sustarsic, Anne Plochowietz, Majid Mosayebi, Hendrik Kaju, Andrew Cuthbert, Johannes Hohlbein, Laura Domicevica, Philip C. Biggin, Jonathan P.K. Doye, and Achillefs N. Kapanidis. Substrate conforma-

tional dynamics facilitate structure-specific recognition of gapped dna by dna polymerase. *Nucleic Acids Research*, 47:10788–10800, 2019.

[120] Rupsa Datta, Tiffany M Heaster, Joe T Sharick, Amani A Gillette, and Melissa C Skala. Fluorescence lifetime imaging microscopy: fundamentals and advances in instrumentation, analysis, and applications. *Journal of Biomedical Optics*, 25:1–43, May 2020.

[121] Robert S. Knox and Herbert van Amerongen. Refractive index dependence of the förster resonance excitation transfer rate. *The Journal of Physical Chemistry B*, 106(20):5289–5293, April 2002.

[122] Enrico Gratton. Fluorescence lifetime imaging for the two-photon microscope: time-domain and frequency-domain methods. *Journal of Biomedical Optics*, 8:381, 2003.

[123] Michelle A. Digman, Valeria R. Caiolfa, Moreno Zamai, and Enrico Gratton. The phasor approach to fluorescence lifetime imaging analysis. *Biophysical Journal*, 94:L14–l16, 2008.

[124] P. R. Barber, S. M. Ameer-Beg, J. Gilbey, L. M. Carlin, M. Keppler, T. C. Ng, and B. Vojnovic. Multiphoton time-domain fluorescence lifetime imaging microscopy: Practical application to protein-protein interactions using global analysis. *Journal of the Royal Society Interface*, 6, 2009.

[125] Marion Peter and Simon M. Ameer-Beg. Imaging molecular interactions by multiphoton flim. *Biology of the Cell*, 96:231–236, 2004.

[126] Gertrude Bunt and Fred S. Wouters. Fret from single to multiplexed signalling events. *Biophysical Reviews*, 9:119–129, 2017.

[127] Mathew Tantama, Juan Ramón Martínez-François, Rebecca Mongeon, and Gary Yellen. Imaging energy status in live cells with a fluorescent biosensor of the intracellular atp-to-adp ratio. *Nature communications*, 4:2550, 2013.

[128] Alex J. Pollock, Shivam A. Zaver, and Joshua J. Woodward. A sting-based biosensor affords broad cyclic dinucleotide detection within single living eukaryotic cells. *Nature Communications*, 11:1–13, 2020.

[129] Greta Faccio and Stefan Salentinig. Enzyme-triggered dissociation of a FRET-based protein biosensor monitored by synchrotron SAXS. *Biophysical Journal*, 113(8):1731–1737, October 2017.

[130] Michael D. Brenner, Ruobo Zhou, Daniel E. Conway, Luca Lanzano, Enrico Gratton, Martin A. Schwartz, and Taekjip Ha. Spider silk peptide is a com-

pact, linear nanospring ideal for intracellular tension sensing. *Nano Letters*, 16(3):2096–2102, February 2016.

[131] Emilia Galperin, Vladislav V. Verkhusha, and Alexander Sorkin. Three-chromophore fret microscopy to analyze multiprotein interactions in living cells. *Nature Methods*, 1:209–217, 2004.

[132] Yuansheng Sun, Horst Wallrabe, Cynthia F. Booker, Richard N. Day, and Ammasi Periasamy. Three-color spectral fret microscopy localizes three interacting proteins in living cells. *Biophysical Journal*, 99:1274–1283, 2010.

[133] Alen Piljic and Carsten Schultz. Simultaneous recording of multiple cellular events by fret. *ACS chemical biology*, 3:156–160, April 2008.

[134] Amicia Elliott, Noah Bedard, Alessandro Ustione, Michelle Baird, Michael Davidson, Tomasz Tkaczyk, and David Piston. Hyperspectral imaging for simultaneous measurements of two fret biosensors in pancreatic β-cells. *Plos One*, 12:e0188789, December 2017.

[135] Sean C Warren, Anca Margineanu, Matilda Katan, Chris Dunsby, and Paul M W French. Homo-fret based biosensors and their application to multiplexed imaging of signalling events in live cells. *International Journal of Molecular Sciences*, 16, 2015.

[136] Heather M. Watrob, Chia Pin Pan, and Mary D. Barkley. Two-step fret as a structural tool. *Journal of the American Chemical Society*, 125:7336–7343, 2003.

[137] Xianglong Hu, Yang Li, Tao Liu, Guoying Zhang, and Shiyong Liu. Intracellular cascade FRET for temperature imaging of living cells with polymeric ratiometric fluorescent thermometers. *ACS Applied Materials &amp Interfaces*, 7(28):15551–15560, July 2015.

[138] Sungchul Hohng, Chirlmin Joo, and Taekjip Ha. Single-molecule three-color fret. *Biophysical Journal*, 87:1328–1337, 2004.

[139] Stephan Uphoff, Seamus J Holden, Ludovic Le Reste, Javier Periz, Sebastian van de Linde, Mike Heilemann, and Achillefs N Kapanidis. Monitoring multiple distances within a single molecule using switchable FRET. *Nature Methods*, 7(10):831–836, September 2010.

[140] Horst Wallrabe, Yuansheng Sun, Xiaolan Fang, Ammasi Periasamy, and George S. Bloom. Three-color confocal förster (or fluorescence) resonance energy transfer microscopy: Quantitative analysis of protein interactions in

the nucleation of actin filaments in live cells. *Cytometry Part A*, 87(6):580–588, March 2015.

[141] Valerică Raicu. Efficiency of resonance energy transfer in homo-oligomeric complexes of proteins. *Journal of biological physics*, 33:109–127, April 2007.

[142] Nicoletta I. Petridou, Zoltán Spiró, and Carl Philipp Heisenberg. Multiscale force sensing in development. *Nature Cell Biology*, 19:581–588, 2017.

[143] Diana E Jaalouk and Jan Lammerding. Mechanotransduction gone awry. *Nature reviews. Molecular cell biology*, 10:63–73, January 2009.

[144] Benoit Ladoux and René-Marc Mège. Mechanobiology of collective cell behaviours. *Nature Reviews Molecular Cell Biology*, 18:743–757, 2017.

[145] Lisa S. Fischer, Srishti Rangarajan, Tanmay Sadhanasatish, and Carsten Grashoff. Molecular force measurement with tension sensors. *Annual Review of Biophysics*, 50:595–616, 2021.

[146] Sharonda LeBlanc, Hunter Wilkins, Zimeng Li, Parminder Kaur, Hong Wang, and Dorothy A. Erie. *Using Atomic Force Microscopy to Characterize the Conformational Properties of Proteins and Protein–DNA Complexes That Carry Out DNA Repair*. Elsevier, 2017.

[147] Claude N. Holenstein, Unai Silvan, and Jess G. Snedeker. High-resolution traction force microscopy on small focal adhesions - improved accuracy through optimal marker distribution and optical flow tracking. *Scientific Reports*, 7(1), February 2017.

[148] Nicolas Schierbaum, Johannes Rheinlaender, and Tilman E. Schäffer. Combined atomic force microscopy (AFM) and traction force microscopy (TFM) reveals a correlation between viscoelastic material properties and contractile prestress of living cells. *Soft Matter*, 15(8):1721–1729, 2019.

[149] Carsten Grashoff, Brenton D. Hoffman, Michael D. Brenner, Ruobo Zhou, Maddy Parsons, Michael T. Yang, Mark A. McLean, Stephen G. Sligar, Christopher S. Chen, Taekjip Ha, and Martin A. Schwartz. Measuring mechanical tension across vinculin reveals regulation of focal adhesion dynamics. *Nature*, 466:263–266, 2010.

[150] Anna-Lena Cost, Pia Ringer, Anna Chrostek-Grashoff, and Carsten Grashoff. How to measure molecular forces in cells: A guide to evaluating genetically-encoded fret-based tension sensors. *Cellular and molecular bioengineering*, 8:96–105, 2015.

[151] Fanjie Meng and Frederick Sachs. Visualizing dynamic cytoplasmic forces with a compliance-matched fret sensor. *Journal of Cell Science*, 124:261–269, 2011.

[152] Nathan Becker, Emin Oroudjev, Stephanie Mutz, Jason P. Cleveland, Paul K. Hansma, Cheryl Y. Hayashi, Dmitrii E. Makarov, and Helen G. Hansma. Molecular nanosprings in spider capture-silk threads. *Nature Materials*, 2:278–283, 2003.

[153] U K Laemmli. Cleavage of structural proteins during the assembly of the head of bacteriophage t4. *Nature*, 227:680–685, 1970.

[154] H. Towbin, T. Staehelin, and J. Gordon. Electrophoretic transfer of proteins from polyacrylamide gels to nitrocellulose sheets: procedure and some applications. 1979. *Biotechnology (Reading, Mass.)*, 24:145–149, 1979.

[155] O. H. LOWRY, N. J. ROSEBROUGH, A. L. FARR, and R. J. RANDALL. Protein measurement with the folin phenol reagent. *The Journal of biological chemistry*, 193:265–275, 1951.

[156] William H Kruskal and W Allen Wallis. Use of ranks in one-criterion variance analysis. *Journal of the American Statistical Association*, 47:583–621, December 1952. doi: 10.1080/01621459.1952.10483441.

[157] Wolfgang H. Ziegler, Robert C. Liddington, and David R. Critchley. The structure and regulation of vinculin. *Trends in Cell Biology*, 16:453–460, 2006.

[158] Betty P. Liu, Magdalena Chrzanowska-Wodnicka, and Keith Burridge. Microtubule depolymerization induces stress fibers, focal adhesions, and dna synthesis via the gtp-binding protein rho. *Cell Adhesion and Communication*, 5:249–255, 1998.

[159] Alexander Bershadsky, Alexander Chausovsky, Eitan Becker, Anna Lyubimova, and Benjamin Geiger. Involvement of microtubules in the control of adhesion-dependent signal transduction. *Current Biology*, 6:1279–1289, 1996.

[160] Kenneth Levenberg and Frankford Arsenal. A method for the solution of certain non-linear problems in least squares. *Quarterly of Applied Mathematics*, 1:536–538, 1943.

[161] Donald W Marquardt. An algorithm for least-squares estimation of nonlinear parameters. *Journal of the Society for Industrial and Applied Mathematics*, 11:431–441, 1963.

[162] Marieke Mastop, Daphne S. Bindels, Nathan C. Shaner, Marten Postma, Theodorus W.J. Gadella, and Joachim Goedhart. Characterization of a spectrally diverse set of fluorescent proteins as fret acceptors for mturquoise2. *Scientific Reports*, 7, December 2017.

[163] Talley J Lambert. Fpbase: a community-editable fluorescent protein database. *Nature Methods*, 16:277–278, 2019.

[164] Thomas S Blacker, Weiyue Chen, || *Edward Avezov, Richard J Marsh, Michael R Duchen, Clemens F Kaminski, a resolved f luorescenceandanisotropy. Acs*, 2016.

[165] Mats Ormo and Andrew Cubitt. Crystal structure of the aequorea victoria green fluorescent protein. *Science*, 273:1392–1395, 1996.

[166] Roger Heim, Douglas C Prasheret, Roger Y Tsien, and Eric R Kandel. Wavelength mutations and posttranslational autoxidation of green fluorescent protein (aequorea victoria/blue fluorescent protein/escherichia coli/imidazolidinone) communicated by. *Biochemistry*, 91:12501–12504, 1994.

[167] Olesya V. Stepanenko, Olga V. Stepanenko, Irina M. Kuznetsova, Vladislav V. Verkhusha, and Konstantin K. Turoverov. *Beta-Barrel Scaffold of Fluorescent Proteins*. Elsevier, 2013.

[168] O. Shimomura. Structure of the chromophore of i$$aequorea$$/i$$ green fluorescent protein. *FEBS Letters*, 104(2):220–222, August 1979.

[169] Chris W. Cody, Douglas C. Prasher, William M. Westler, Franklyn G. Prendergast, and William W. Ward. Chemical structure of the hexapeptide chromophore of the aequorea green-fluorescent protein. *Biochemistry*, 32:1212–1218, 1993.

[170] Eunji Park, Dae Sik Hwang, Jae Seong Lee, Jun Im Song, Tae Kun Seo, and Yong Jin Won. Estimation of divergence times in cnidarian evolution based on mitochondrial protein-coding genes and the fossil record. *Molecular Phylogenetics and Evolution*, 62:329–345, January 2012.

[171] Andrew B. Cubitt, Roger Heim, Stephen R. Adams, Aileen E. Boyd, Larry A. Gross, and Roger Y. Tsien. Understanding, improving and using green fluorescent proteins. *Trends in Biochemical Sciences*, 20:448–455, 1995.

[172] Daphne S Bindels, Lindsay Haarbosch, Laura van Weeren, Marten Postma, Katrin E Wiese, Marieke Mastop, Sylvain Aumonier, Guillaume Gotthard, Antoine Royant, Mark A Hink, and Theodorus W J Gadella. mscarlet: a bright monomeric red fluorescent protein for cellular imaging. *Nature Methods*, 14:53–56, 2017.

[173] M. Mandel and A. Higa. Calcium-dependent bacteriophage dna infection. *Journal of Molecular Biology*, 53:159–162, 1970.

[174] Douglas Hanahan. Studies on transformation of escherichia coli with plasmids. *Journal of Molecular Biology*, 166:557–580, 1983.

[175] F William Studier. Protein production by auto-induction in high-density shaking cultures. *Protein Expression and Purification*, 41:207–234, 2005.

[176] W. Gilbert and B. Muller-Hill. Isolation of the lac repressor. *Proceedings of the National Academy of Sciences*, 56:1891–1898, 1966.

[177] Jerker Porath, Jan Carlsson, Ingmar Olsson, and Greta Belfrage. Metal chelate affinity chromatography, a new approach to protein fractionation. *Nature*, 258:598–599, 1975.

[178] K E Van Holde, W C Johnson, C Johnson, P S Ho, and W S Ho. *Principles of Physical Biochemistry*. Prentice Hall, 1998.

[179] G D Fasman. *Circular Dichroism and the Conformational Analysis of Biomolecules*. Springer US, 1996.

[180] G. N. Ramachandran, C. Ramakrishnan, and V. Sasisekharan. Stereochemistry of polypeptide chain configurations. *Journal of Molecular Biology*, 7:95–99, 1963.

[181] András Micsonai, Frank Wien, Linda Kernya, Young-Ho Lee, Yuji Goto, Matthieu Réfrégiers, and József Kardos. Accurate secondary structure prediction and fold recognition for circular dichroism spectroscopy. *Proceedings of the National Academy of Sciences*, 112:E3095–e3103, June 2015.

[182] Teresa San-Miguel, Pedro Pérez-Bermúdez, and Isabel Gavidia. Production of soluble eukaryotic recombinant proteins in e. coli is favoured in early log-phase cultures induced at low temperature. *SpringerPlus*, 2(1), March 2013.

[183] Joachim Goedhart, Laura van Weeren, Mark A Hink, Norbert O E Vischer, Kees Jalink, and Theodorus W J Gadella. Bright cyan fluorescent protein variants identified by fluorescence lifetime screening. *Nature Methods*, 7(2):137–139, January 2010.

[184] Joachim Goedhart, David von Stetten, Marjolaine Noirclerc-Savoye, Mickaël Lelimousin, Linda Joosen, Mark A. Hink, Laura van Weeren, Theodorus W.J. Gadella, and Antoine Royant. Structure-guided evolution of cyan fluorescent

proteins towards a quantum yield of 93%. *Nature Communications*, 3(1), March 2012.

[185] Hideji Murakoshi and Akihiro C.E. Shibata. Shadowy: A dark yellow fluorescent protein for flim-based fret measurement. *Scientific Reports*, 7, December 2017.

[186] Gert Jan Kremers, Joachim Goedhart, Erik B. Van Munster, and Theodorus W.J. Gadella. Cyan and yellow super fluorescent proteins with improved brightness, protein folding, and fret fōrster radius. *Biochemistry*, 45:6570–6580, 2006.

[187] T.W.J. Gadella L. Joosen, M.A. Hink and J. Goehardt. Effect of fixation procedures on the fluorescence lifetimes of aequorea victoria derived fluorescent proteins. *Journal of Microscopy*, 256(3):166–176, September 2014.

[188] Sylvain V. Costes, Dirk Daelemans, Edward H. Cho, Zachary Dobbin, George Pavlakis, and Stephen Lockett. Automatic and quantitative measurement of protein-protein colocalization in live cells. *Biophysical Journal*, 86:3993–4003, 2004.

[189] Qi Li, Anthony Lau, Terence J. Morris, Lin Guo, Christopher B. Fordyce, and Elise F. Stanley. A syntaxin 1, gα o, and n-type calcium channel complex at a presynaptic nerve terminal: Analysis by quantitative immunocolocalization. *Journal of Neuroscience*, 24:4070–4081, 2004.

[190] Verbeek F. J. Manders E. M. M. and Aten J. A. Measurement of co-localization of objects in dual-colour confocal images. *Journal of Microscopy*, 169:375–382, March 1993.

[191] Stephen M Stigler. Francis galton's account of the invention of correlation. *Statistical Science*, 4:73–79, May 1989.

[192] Sangyoon J Han, Evgenia V Azarova, Austin J Whitewood, Alexia Bachir, Edgar Guttierrez, Alex Groisman, Alan R Horwitz, Benjamin T Goult, Kevin M Dean, and Gaudenz Danuser. Pre-complexation of talin and vinculin without tension is required for efficient nascent adhesion maturation. *eLife*, 10, March 2021.

[193] Elliot L Elson and Douglas Magde. Fluorescence correlation spectroscopy. i. conceptual basis and theory. *Biopolymers*, 13:1–27, January 1974. https://doi.org/10.1002/bip.1974.360130102.

[194] Michelle A Digman and Enrico Gratton. Scanning image correlation spectroscopy. *BioEssays*, 34:377–385, May 2012. https://doi.org/10.1002/bies.201100118.

[195] George W. Ashdown and Dylan M. Owen. Spatio-temporal image correlation spectroscopy and super-resolution microscopy to quantify molecular dynamics in t cells. *Methods*, 140-141:112–118, May 2018.